ALMA MATER STUDIORUM
UNIVERSITÀ DI BOLOGNA

DOTTORATO DI RICERCA IN
ASTROFISICA

CICLO 37

Settore Concorsuale: 02/C1 - ASTRONOMIA, ASTROFISICA, FISICA DELLA TERRA E DEI PIANETI

Settore Scientifico Disciplinare: FIS/05 - ASTRONOMIA E ASTROFISICA

Tracing star cluster formation and evolution with stellar kinematics

Presentata da: Alessandro Della Croce

Coordinatore Dottorato
Andrea Miglio

Supervisore
Emanuele Dalessandro

Co-supervisore
Francesco Rosario Ferraro

Esame finale anno 2025

Abstract

It is well established that star clusters are valuable probes in Astronomy across a wide range of disciplines from cosmology to stellar evolution. Indeed, star clusters are efficient tracers of intense star formation episodes across cosmic time and rich cradles of stellar-mass black holes (BHs), which are prime sources of gravitational waves. They are also important witnesses of the epoch of cosmic reionization, and the formation of the first structures in the early Universe. Finally, star clusters are potentially efficient tracers of the assembly process of galaxies in a cosmological context. However, fundamental questions about the possible unifying principles governing their formation are yet unanswered. In addition, whether clusters form through the monolithic collapse of the gas cloud or the hierarchical merger of clumps is still an intense matter of debate. Despite tremendous observational and theoretical efforts, our understanding of star cluster formation and the actual role of the different underlying physical processes is still in its infancy.

This thesis explores this long-standing problem with a multi-faceted approach, largely based on the dynamical study of very young clusters and associations in nearby star-forming regions and old massive clusters in the Galactic halo. Local star clusters represent the ideal laboratory for constraining the physical mechanisms at the basis of cluster formation as they can be resolved into individual stars, and thus they can be studied with a level of detail that cannot be achieved for distant systems.

To this aim, this thesis uses a multi-diagnostic, and multi-instrument approach, which is largely based on *Gaia*, *Hubble Space Telescope* (*HST*), and properly selected spectroscopic surveys (such as observations from the *Multi Unit Spectroscopic Explorer*, *MUSE*). Complementary, we used tailored N-body and Monte Carlo simulations to interpret the observed stellar cluster properties and constrain the initial physical conditions for cluster formation and evolution.

Establishing the link between the progenitor gas clouds and the gas-free stellar populations is essential to address key questions about cluster formation and evolution. We considered quantities that are expected to be inherited from and linked to the very early stages, including dynamical (such as velocity anisotropy, expansion, and rotation), and structural (e.g., mass segregation) properties. The *fil rouge* of this thesis is thus stellar kinematics as the critical tool to study cluster formation and evolution. We are indeed in the golden era for star cluster dynamical studies, thanks to all-sky astrometric surveys and large-scale spectroscopic campaigns. This is even more timely, as GPU-accelerated numerical simulations approach real star cluster complexities, providing the community with simulation surveys.

The analysis focused on two main aspects. The first is the study of the early phases of cluster assembly and survival, and their dependence on the environment. The second targeted the long-term evolution of star clusters and the role of massive compact objects, such as BHs.

To address the early stages of cluster evolution, we characterized the internal dynamical state of virtually the full population of young clusters known in the Milky Way. We focused, in the first place, on the expansion state, providing for the first time an estimate of the star cluster expansion timescale, in response to gas expulsion and out-of-equilibrium dynamics. Secondly, since increasing evidence shows that star clusters do not form or evolve in isolation, we studied the properties of a group of young clusters in the Perseus complex. A comparison between observations and numerical simulations suggests that these star clusters are part of a

larger system, probably in the process of forming a more massive cluster-like system through hierarchical mergers. We named this structure LISCA II as it is the second of its kind identified so far in our Galaxy. Finally, we characterized the star-forming complex that hosts such hierarchical structures. We first investigated the stellar content in the W3/W4/W5 complex. We then zoomed out studying the Perseus complex evolution in a Galactic framework, to shed further light on the formation and evolution of the Perseus region as a cluster nursery.

As a complementary approach to constrain the initial conditions of massive cluster formation, we also followed to route of reverse-engineering the present-day kinematic and structural properties of multiple populations (MPs) in a representative sample of Galactic old ($\sim$ 12 Gyr) globular clusters (GCs). In this context, we present here the first 3D kinematic analysis of MPs with a particular focus on their rotation and relative differences. We found that second-population stars tend to have typically a larger rotation than first-population ones with differences decreasing for increasing cluster dynamical ages. Interestingly, these results appear to suggest that globular clusters experienced multiple events of star formation and self-enrichment processes.

Recent years witnessed a renewed interest in the role of exotic objects in the long-term evolution of star clusters. We first studied (through numerical simulations) the role of stellar-mass BHs within massive GCs. In particular, we discuss the possible degeneracies in inferring such an elusive population concluding that multi-dimensional approaches are needed. We also introduce a set of measurable parameters that nicely allow us to break these degeneracies and we compare them with photometric and astrometric data of Galactic GCs. Within a similar context, we present the dynamical modeling of the central kinematics of the GC NGC 104 (commonly known as 47 Tucanae) to probe the presence of a central intermediate-mass BH (IMBH), as claimed by previous studies. The synergy between 3D kinematic data in the central region and individual star modeling through distribution function-based models allowed us to put the most stringent upper limit on the putative IMBH mass.

Thesis Outline

The thesis is organized as follows:

- ✧ Chapters 1 and 2 start introducing cluster formation and evolution, and the related open questions. First, the physical processes involved in the early stages are discussed, for example, stellar feedback, subsequent evolution. It follows a discussion about the long-term evolution due to stellar interactions, galaxy tidal field, and the presence of exotic objects. In addition, the puzzle of the multiple populations is briefly introduced. Finally, the thesis methodology as well as an overview of the different datasets and numerical simulations used throughout the thesis are presented (Chapter 2);

- ✧ Chapter 3 analyzes the internal kinematics of young star clusters with a particular focus on their expansion properties. It starts with a preliminary analysis to update the cluster member catalogs. It then follows the kinematic characterization of the star clusters and numerical simulation results. Finally, a comparison with previous works is presented;

- ✧ Chapter 4 focuses on the LISCA II hierarchical structure. After a preliminary data analysis, the physical properties of the newly identified system were studied. The structural and kinematical properties of the stellar halo embedding the star clusters are presented. Finally, a detailed comparison with numerical simulation following the hierarchical assembling of star clusters is performed;

- ✧ Chapter 5 characterizes the Perseus complex which hosts LISCA II. First, the W3/W4/W5 star-forming complex is studied, focusing on the star clusters within the region (some of which are partially embedded), and the young stellar objects population. Finally, the complex kinematics and evolution are traced using the six-dimensional phase-space information available for the clusters and complementing previous studies on the subject;

- ✧ Chapter 6 investigates the differences between MP kinematics in Galactic GCs as relics of their formation mechanism. The kinematic analysis is first introduced. After that, results concerning the differences in rotation are thoroughly discussed. It follows a comparison with the literature;

- ✧ Chapter 7 shifts the focus on old stellar systems, discussing the role of stellar mass BHs within GCs. Observational proxies for the total mass in BHs are investigated through a survey of Monte Carlo simulations. Particular attention is devoted to the degeneracies widely used parameters might be prone to. Finally, the comparison between numerical simulation results and observations is presented;

- ✧ Chapter 8 presents the dynamical modeling of the GC NGC 104 to constrain the mass of the claimed IMBH. The dynamical models along with the fitting methodology are carefully presented. After that, the structural and kinematical data sets are introduced. Finally, the results of a large Monte Carlo exploration of the parameter space and the comparison with previous studies are performed;

- ✧ Chapter 9 finally concludes with an overview of future projects.

The main reference articles for this thesis are summarized below:

- ✧ **Della Croce**, et al., *"Tracing the W3/W4/W5 and Perseus complex dynamical evolution with star clusters"*, submitted to A&A;
- ✧ Dalessandro, Cadelano, **Della Croce**, et al., *"A 3D view on multiple population kinematics in Galactic globular clusters"*, (2024, A&A, **691**, A94);
- ✧ **Della Croce** et al., *"Inference of black-hole mass fraction in Galactic globular clusters: a multi-dimensional approach to break initial-condition degeneracies"*, (2024c, A&A, **690**, A179);
- ✧ **Della Croce** et al., *"Young, wild and free: the early expansion of star clusters"*, (2024b, A&A, **683**, A10);
- ✧ **Della Croce** et al., *"The most stringent upper limit set on the mass of a central black hole in 47 Tucanae using dynamical models"*, (2024a, A&A, **682**, A22);
- ✧ **Della Croce** et al., *"Ongoing hierarchical massive cluster assembly: the LISCA II structure in the Perseus complex"*, (2023, A&A, **674**, A93).

Contents

I General Background **1**

1 Introduction **1**
1.1 Setting the scene . . . 1
1.2 Star cluster formation and early evolution . . . 4
1.2.1 The onset of star formation in giant molecular clouds . . . 4
1.2.2 Stellar feedback, gas expulsion, and cluster survival . . . 6
1.2.3 The violent relaxation phase . . . 9
1.2.4 Stellar interactions and dynamical feedback . . . 10
1.2.5 The hierarchical formation scenario . . . 11
1.3 The long-term evolution of bound stellar systems . . . 14
1.3.1 More than just rigid balls: stellar evolution . . . 15
1.3.2 Two-body relaxation theory in a nutshell . . . 15
1.3.3 Two-body relaxation driven cluster evolution . . . 17
1.3.4 Clusters orbit within galaxies: the role of the tidal field . . . 18
1.3.5 Exotic objects in GCs . . . 20
1.4 Chemical abundance variations in massive stellar clusters: a puzzle for "standard" cluster formation . . . 22

2 Stellar kinematics as a tool to unveil cluster formation and evolution **25**
2.1 Observations of cluster internal kineamtics . . . 26
2.1.1 The *Gaia* astrometric mission . . . 26
2.1.2 The Hubble Space Telescope . . . 31
2.1.3 The Multi Unit Spectroscopic Explorer . . . 32
2.2 Numerical simulations of cluster internal dynamics . . . 33

II Formation and early evolution of star clusters **35**

3 Young star cluster kinematics **37**
3.1 Data analysis . . . 38
3.1.1 Revisiting cluster member catalogs . . . 38
3.1.2 Measuring cluster expansion . . . 40
3.2 Results on the expansion of young star clusters . . . 41
3.3 Comparison with numerical simulations . . . 46
3.3.1 N-body simulations of cluster formation . . . 46
3.3.2 Distribution of $\langle v_{\rm R} \rangle / \sigma_{\rm R}$ for star clusters in equilibrium . . . 47

3.4 Testing the impact of different age estimates . . . 48
3.5 Comparison with previous works . . . 48
3.6 Summary and conclusions . . . 51

4 LISCA II: a hierarchical structure in the Perseus complex 53
4.1 Preliminary data analysis . . . 54
4.1.1 The starting catalogs . . . 54
4.1.2 Searching for star clusters in the region . . . 54
4.1.3 Completeness of the Gaia catalog . . . 57
4.2 Physical properties of the observed area . . . 58
4.2.1 Differential reddening . . . 58
4.2.2 Cluster and halo ages . . . 61
4.2.3 Line-of-sight velocity distribution and iron content . . . 62
4.3 Structural and kinematic properties of the diffuse stellar halo . . . 65
4.3.1 Density distribution . . . 65
4.3.2 Kinematic properties . . . 65
4.3.3 Multi-mass structural and kinematic analyses . . . 68
4.4 Star cluster properties . . . 72
4.5 Total system mass . . . 76
4.6 Comparison with N-body simulations of early cluster evolution . . . 77
4.6.1 Mass segregation and bulk internal motion . . . 79
4.6.2 Dynamics of subclusters . . . 80
4.7 Summary and conclusions . . . 81

5 Tracing the W3/W4/W5 and Perseus complex dynamical evolution with star clusters 83
5.1 Identifing star clusters in the W345 region . . . 84
5.2 Properties of star clusters in the W3/W4/W5 region . . . 87
5.2.1 Structure . . . 87
5.2.2 Differential reddening and cluster ages . . . 90
5.2.3 Kinematics . . . 91
5.3 Young stars in the W3/W4/W5 region: their link with star clusters . . . 94
5.3.1 The YSO population . . . 94
5.3.2 Bright-rimmed cloud ionizing sources . . . 96
5.4 The kinematics of the Perseus complex . . . 97
5.4.1 3D cluster positions and velocities . . . 97
5.4.2 The projected kinematics . . . 100
5.4.3 Orbits in an axisymmetric potential . . . 102
5.4.4 Orbits in a spiral-perturbed potential . . . 105
5.5 Summary and conclusions . . . 108
5.6 Supplementary material . . . 109
5.6.1 Perseus star cluster orbits in an axisymmetric potential . . . 109
5.6.2 Testing the impact of the Galactic bar . . . 112
5.6.3 Exploring different f values . . . 114

6 Multiple population kinematics in Galactic GCs: a window on the complex processes of massive cluster formation 117
6.1 Kinematic analysis of internal rotation differences . . . 118
6.1.1 1D velocity dispersion and rotation profiles . . . 118
6.1.2 Full 3D kinematic analysis . . . 121
6.2 Results . . . 123
6.2.1 Observational evidence of internal rotation differences . . . 123
6.2.2 Exploring the link between MP ellipticity and rotation . . . 128
6.2.3 Numerical simulations of rotating MP clusters . . . 129
6.3 Comparison with the literature . . . 131
6.4 Summary and conclusions . . . 133
6.5 Supplementary material . . . 134
6.5.1 Sample definition and observational datasets . . . 134
6.5.2 Additional table . . . 139
6.5.3 Incompleteness effects . . . 139
6.5.4 Global kinematics and comparison with the literature . . . 139

III The long-term evolution of massive stellar systems 145

7 Black hole subsystems in Galactic globular clusters 147
7.1 Monte Carlo simulations of star cluster evolution . . . 148
7.2 Results from numerical simulations . . . 149
7.3 Observations . . . 152
7.3.1 Properties of Galactic GCs . . . 153
7.3.2 Accounting for incompleteness . . . 154
7.3.3 Comparison with simulations . . . 156
7.4 Summary and conclusions . . . 158
7.5 Supplementary material . . . 159
7.5.1 Density distribution and velocity dispersion profiles for nine GCs 159
7.5.2 Table of Δ and velocity dispersion ratio values . . . 161

8 Quest for an intermediate-mass BH in NGC 104 165
8.1 Dynamical models . . . 166
8.1.1 Model for the stellar component . . . 167
8.1.2 The gravitational potential . . . 167
8.1.3 Observable properties from a DF . . . 168
8.2 The observable datasets . . . 169
8.3 Results from the dynamical model . . . 170
8.4 Comparisons with previous works . . . 173
8.5 Summary and conclusions . . . 175
8.6 Supplementary material . . . 175
8.6.1 Model and data comparison . . . 175

IV Conclusions **179**

9 Final remarks **181**
9.1 Thesis summary and conclusions 181
9.2 Future instruments 183
9.3 Future projects 184
9.3.1 Probing rotation in young clusters 184
9.3.2 The search for hierarchical structures in the Galaxy 185
9.3.3 Cluster formation and evolution: from high-z to the local Universe 186

Part I

General Background

Chapter 1

Introduction

"[...] non erigeremo nuovi idoli, non ordineremo la società secondo inedite forme di stratificazione sociale. Edificheremo un unico tempio e lo dedicheremo al solo faro che deve illuminare la strada di ogni essere umano: la libertà"

L'Organizzazione,
CR Edizioni

This introduction presents the observational and theoretical state-of-the-art of star cluster formation and evolution, focusing in particular on topics investigated during the three years of the PhD program. The introduction aims to provide the reader with all the necessary notions to read the thesis fluently without being verbose. At the same time, it is meant to navigate the reader through the complex and multi-disciplinary field of star cluster formation and evolution.

The Introduction is structured as follows: section 1.1 introduces star clusters in general, their importance across astronomy, and discusses open questions in cluster formation and evolution. Section 1.2 introduces star cluster formation from the onset of star formation in gas clouds to stellar feedback and cluster survival. Section 1.3 continues discussing the processes involved in the long-term evolution of stellar clusters.

1.1 Setting the scene

The star formation process in galaxies primarily takes place in giant molecular clouds (GMCs, Kennicutt & Evans, 2012). In particular, in denser regions of GMCs, usually referred to as clumps. Turbulence is nowadays thought to be the main driver of the density enhancements allowing the locally gravitationally unstable clumps to collapse and ultimately produce stars (see Mac Low & Klessen, 2004; Ballesteros-Paredes et al., 2007; McKee & Ostriker, 2007; Girichidis et al., 2020, for reviews on the role of supersonic turbulence and, more in general, on the physics of star formation).

During the collapse, the gas cloud fragments in several star-forming regions, resulting in groups of stars (Lada & Lada, 2003; Kruijssen, 2012). During this stage (referred to as embedded phase), the proto star cluster accretes gas from the natal cloud. The details of the gas accretion are strongly dependent on the surrounding environment (e.g., the availability of gas and its relative position and speed, Girichidis et al., 2011; Kruijssen et al., 2012) and also on the onset of star formation and stellar feedback (e.g., Geen et al., 2015a,b). Such processes

regulate whether direct accretion onto the central object is favored (forming more massive stars in gas-richer areas, e.g., Bonnell et al., 2001), or whether the gas becomes gravitationally unstable on its way toward the center, forming more stars (Peters et al., 2010). Nearby gas cloud observations revealed that star formation in clumps could account for nearly all (70% − 90%) stars formed in GMCs (Lada & Lada, 2003). However, the exact fraction of stars forming in dense environments is still debated (e.g., Bressert et al., 2010; Ward et al., 2020), and the paradigm is shifting toward a more complex and hierarchical formation process in which feedback plays a non-trivial role (see e.g., Krause et al., 2018). Nonetheless, most stars in galaxies form in clustered environments within GMCs, making star clusters the building blocks of galaxies and foundation pillars of modern Astronomy.

Despite more than four centuries since their first reported observations by Galileo Galilei (in 1610 in the *Sideriur Nuncius*) and the tremendous observational and theoretical efforts of recent years, the physical processes and ingredients driving cluster formation and evolution are only poorly constrained so far and it remains an active research field (as pointed out from the number of recent reviews on the topic, Renaud, 2018; Forbes et al., 2018a; Bastian & Lardo, 2018; Krumholz et al., 2019; Gratton et al., 2019; Krause et al., 2020; Adamo et al., 2020). One of the main reasons for our lack of understanding is the intrinsic multi-scale, and multi-physics nature of star cluster formation and evolution (see Renaud, 2018, for an interesting review on the subject). The formation and evolution of GMCs (where clusters form) are regulated by galactic-scale processes, such as the development of density perturbations like spiral arms (Roberts, 1969), which may be triggered by tidal interactions with satellite galaxies (Toomre & Toomre, 1972; Tully, 1974; Bottema, 2003; Oh et al., 2008; Dobbs & Baba, 2014). At the other end of the ladder, there is star formation. Shortly after the gas collapsed, stars spring to life, injecting mass, energy, and momentum into the gas through feedback processes: from pre-stellar outflows (Bally, 2016), ionizing radiation (Stahler et al., 1980), stellar winds (Rogers & Pittard, 2013), up to the end of massive-stars life with supernova explosion (Smartt, 2009), possibly shaping the cloud evolution. The precise role of stellar feedback depends on the specifics of the star formation process, such as the relative gas and stellar distributions and the chemical composition of the gas. In addition, feedback from star-forming regions plays a role in regulating the star-formation rate of galaxies, driving galactic outflows (van der Kruit & Freeman, 2011). This is even more critical at high redshift for the formation of present-day globular clusters (GCs) since the hierarchical assembly of galaxies was likely still in process (see for example the GC formation model by Kruijssen, 2015) and the lower metal content in primordial gas allowed for more massive stars (Abel et al., 2002; Bromm et al., 2002; Yoshida et al., 2006) resulting in more extreme feedback.

Star clusters, in particular the more massive ones, are thus intimately linked to the host, and over the years they have proved powerful tools in studying the host properties and evolution. Figure 1.1 shows a collage of star cluster images ordered by age: from the still-forming Orion Nebula Cluster (ONC) to GCs (NGC 6535, 47 Tuc) through some open clusters (OCs), highlighting the huge variety of properties and apperances of Galactic star clusters.

In our Galaxy, the population of young star clusters (historically identified with OCs) was used to trace the Galactic spiral arms, studying their structure, and pattern speed in relation to the Galactic rotation curve (Naoz & Shaviv, 2007; Bobylev & Bajkova, 2014, 2023; Junqueira et al., 2015; Dias et al., 2019; Castro-Ginard et al., 2021; Hao et al., 2021; Joshi &

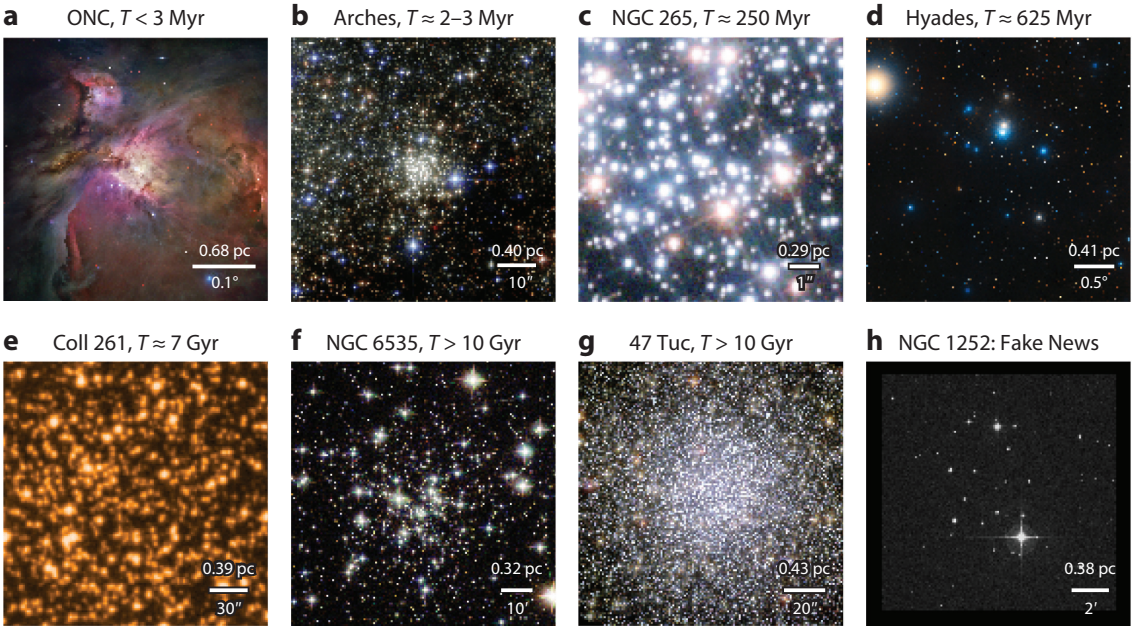

FIGURE 1.1: Images of different star clusters spanning a wide range in ages (~ 1 Myr to > 10 Gyr) and masses ($10^2 - 10^6$ $M_\odot$). NGC 1252 is also shown, an object previously classified as a cluster but now known to be an asterism thanks to *Gaia* data (see discussion in section 2.1.1). Each field of view in all frames is 3 pc $\times$ 3 pc, and angular sizes are indicated by scale bars. Figure is reproduced from Krumholz et al. (2019).

Malhotra, 2023). Possible age gradients along the arm (He et al., 2021) would allow testing different formation theories (i.e., the long-lived scenario, Lin & Shu 1964; Shu 2016, opposed to the one in which spiral arms are short-lived, and co-rotating with the Galactic disk, Toomre 1964). In addition, OCs allowed us to study non-axisymmetric perturbations in the disk, like the bar pattern speed (Thomas et al., 2023). In addition, the present-day spatial distribution of young OCs in the Galactic disk could help us study the chemical enrichment history of the Galaxy (see e.g., Yong et al., 2012; Reddy et al., 2016; Cunha et al., 2016; Donor et al., 2020; Casamiquela et al., 2021; Spina et al., 2021; Myers et al., 2022; Ray et al., 2022; Gaia Collaboration, 2023d).

Similarly, the old cluster population is intimately linked with its host (Brodie & Strader, 2006). GCs co-evolve with the Galaxy (see e.g., Reina-Campos et al. 2023 for an attempt to model the galaxy-cluster population co-evolution for a Hubble time), and witnessed the Galaxy assembly history possibly helping us to reconstruct it (Massari et al., 2019). In addition, their orbits in the Galactic halo trace the dark-matter mass distribution and the Galactic total mass distribution (Eadie et al., 2015; Vasiliev, 2019b).

On extra-galactic scales, the connection between the galaxy and the GC population is reflected in several scaling relations between the properties of the two: for instance between the total mass in GCs and the galaxy halo mass that was found to be largely independent of the galaxy type or environment (Spitler & Forbes, 2009; Hudson et al., 2014; Harris et al., 2015; Forbes et al., 2018b). This suggests that the galaxy-star cluster population co-evolution is a ubiquitous and fundamental process in galaxy formation and evolution. Therefore, it

is of primary importance to study the formation and evolution of massive star clusters in fully galactic and cosmological frameworks (Boley et al., 2009; Kravtsov & Gnedin, 2005; Kruijssen, 2015; Forbes et al., 2018a; Calura et al., 2022; Grudić et al., 2023), and also to study the initial properties of the GCs. In this respect, recent observations by the James Webb Space Telescope (*JWST*) of lensed field provided the first observational evidence of massive star-cluster formation at high redshift (Vanzella et al., 2022a,b, 2023b). Such observations will allow us in the coming years to assess the initial GC properties and their formation environments using larger and larger samples of proto-GCs.

The above discussion highlights the prominent relevance of star clusters in Astrophysics across many fields: from stellar theory, galaxy formation, and dynamics, to cosmology. However, to properly use star clusters to trace such a variety of physical processes we need to understand how star clusters form in the first place. Yet, many critical questions are still open. Did young star clusters form differently from old ones? Or stated in another way, is the star cluster formation process universal, and if so, how do star clusters form? What is the role of the galactic and cosmological environment in shaping their initial properties and evolution? Will young massive star clusters evolve into GC-like systems?

1.2 Star cluster formation and early evolution

The formation of star clusters involves a variety of physical processes acting at different scales and characteristic times, as briefly touched upon in section 1.1.

We now delve deeper into the physics of star cluster formation. In particular, section 1.2.1 presents the early stages of star formation and cluster formation environments, section 1.2.2 continues with stellar feedback and its implication for gas removal and cluster survival. Section 1.2.3 presents the subsequent phase of violent relaxation, where stellar interactions (further discussed in section 1.2.4) already play an important role. Finally, section 1.2.5 concludes by discussing the hierarchical formation scenario in more detail.

1.2.1 The onset of star formation in giant molecular clouds

GMCs are the densest gas regions of the interstellar medium. Also, they show complex, hierarchical morphologies (Elmegreen & Falgarone, 1996), meaning that the densest regions are embedded in sparser, lower-density ones and so on. The cloud properties and their evolution are instrumental in determining the structure and kinematics of the cluster forming out of it, and its evolution in the earliest stages when stars are still embedded in the natal gas (Klessen et al., 2000; Klessen & Burkert, 2000; Offner et al., 2009b; Vázquez-Semadeni et al., 2017).

Since the early 70s, line width observations revealed that GMCs are dominated by supersonic motion (Wilson et al., 1970). Given that GMCs are typically much more massive than their Jean mass (Blitz, 1993), the first, and simplest, interpretation was line broadening due to large-scale radial motion, as a direct consequence of gravitational instability (Liszt et al., 1974; Goldreich & Kwan, 1974). However, this explanation was soon rejected in favor of small-scale supersonic turbulence (Zuckerman & Evans, 1974; Klessen et al., 2000). Indeed the overall collapse of the region would predict star formation rates to be significantly higher than the observed ones. Also, cloud-scale radial motions would produce redshifted emission lines to the main star-forming region, that were not observed (Zuckerman & Palmer, 1974).

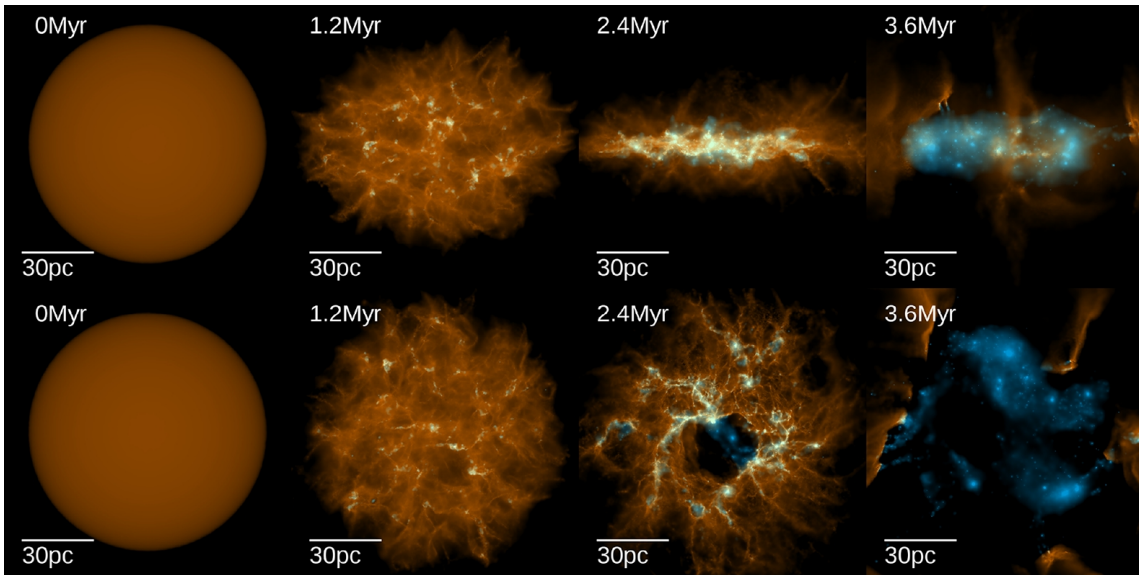

FIGURE 1.2: Evolution of the gas surface density (in orange) and young stars (in blue) for a simulated GMC of 3×10^7 $M_\odot$ and an initial radius of 50 pc. The leftmost panels show the initial conditions. Moving rightward, time increases to 3.6 Myr, which is about three times the initial free-fall time scale. The top row is showing the edge-on view of the disc and the bottom row, the face-on view. Star formation starts within a free-fall time (here 1.2 Myr) and stops after a few Myr, when the gas has been completely blown out by feedback. Figure is taken from Grudić et al. (2018a).

On the other hand, turbulence provides pressure support against the gravitational collapse, accounting for the small (of the order of 1%) star formation efficiencies per free-fall time (i.e., the fraction of gas mass converted into star per free-fall time, see e.g., Zuckerman & Evans 1974; Zuckerman & Palmer 1974; Krumholz et al. 2019). Indeed, such low star formation efficiencies imply GMC lifetimes much larger than the free-fall time scale, whereas in the absence of any form of pressure support the cloud should collapse in about a free-fall time scale (Jeans, 1902). In this scenario, turbulence thus plays a dual role: preventing the GMC from rapid gravitational collapse by providing global pressure support and producing density fluctuations on smaller scales that may become gravitationally unstable, thereby triggering star formation (Klessen et al., 2000; Mac Low & Klessen, 2004; Ballesteros-Paredes et al., 2007; Bergin & Tafalla, 2007; McKee & Ostriker, 2007; Hennebelle & Falgarone, 2012).

Numerical simulations of GMC formation and evolution showed that turbulence generation is a natural outcome of the GMC formation process itself (Audit & Hennebelle, 2005; Heitsch et al., 2005, 2006; Vázquez-Semadeni et al., 2006, 2007, 2019; Hennebelle et al., 2008; Banerjee et al., 2009). Gas clouds grow in mass by accreting gas from the surrounding diffuse environment. This convergence of gas toward denser regions develops turbulence through the super-linear growth of perturbations driven by various instabilities, such as thermal (Field, 1965) and Kelvin-Helmholtz instabilities (Heitsch et al., 2006; Klessen & Hennebelle, 2010). Local density perturbations could thus become gravitationally unstable (approaching the Jeans mass) and collapse, evolving with their own free-fall time scale set by the local density.

The formation of GMC through nearby gas accretion coupled with turbulence-driven density fluctuations makes the GMC collapse inherently non-homogeneous. Furthermore, given that denser areas collapse faster (due to a shorter free-fall time scale) while accreting gas from its surroundings, the process naturally produces a hierarchy of collapsing scales. "Thus, the cloud becomes a system of collapses within collapses" (quote from Krause et al., 2020). Figure 1.2 presents a possible scheme of the evolution of a massive (3×10^7 $M_\odot$) GMC including turbulence and feedback mechanisms (further discussed in section 1.2.2). As the cloud evolves, turbulence seeds density fluctuations which in turn trigger gravitational instability. Such unstable regions condense into filaments and clumps, forming the first stars. Star formation could also start within the accreting filaments, possibly forming a sparser population of lower-mass (given the smaller gas reservoir) stars. This process could naturally lead to primordial mass segregation and age gradients across the star-forming region (Vázquez-Semadeni et al., 2017; Getman et al., 2018), regardless of whether dynamical interactions were already efficient at this stage. Finally, the star formation rate accelerates (due to the continuous accretion of gas) until feedback comes into play, eroding the surrounding gas and regulating the star-formation rate by expelling the gas (e.g., Grudić et al., 2018a, but see also discussion in section 1.2.2).

In conclusion, the hierarchical and filamentary nature of GMC formation and evolution is imprinted in the nascent star cluster which might show a fractal-like morphology (Vázquez-Semadeni et al., 2017). Observations of embedded star clusters revealed non - homogeneous morphologies (see e.g., Lada et al., 1996; Piche, 1993). However, centrally concentrated clusters were also observed (Horner et al., 1997; Hillenbrand & Hartmann, 1998), although it is yet not clear whether that is the manifestation of a later stage of the embedded evolution of star clusters (Lada & Lada, 2003).

1.2.2 Stellar feedback, gas expulsion, and cluster survival

During their lifetime, stars inject energy, momentum, and matter into the surrounding medium (out of which they might still be accreting) through several physical processes (Dale, 2015). The stellar feedback is believed to have a profound impact on the natal gas cloud, exposing the stars within the first tens of million years (Adamo et al., 2020, and see also figure 1.2).

Massive stars are the main feedback sources, although low-mass ones can contribute significantly during their formation phase (or before the formation of more massive stars). Indeed, a fraction of the gravitational energy of the infalling matter is converted into radiation that may be absorbed by the surrounding gas and dust. Before massive stars are formed, this is the main source of feedback in GMC (Offner et al., 2009a). Furthermore, during the accretion phase, a disk forms and collimated, high-velocity ($100 - 1000$ km s^{-1}) jets are launched, likely by magnetic interactions between the star and disk magnetic fields (Frank et al., 2014).

After the accretion phase ends, stars emit ionizing radiation, heating the surrounding gas and driving its expansion at supersonic speed. The boundary at which recombination balances ionization is called Strömgren (1939) sphere. Also, the over-pressured gas causes an expanding shock in the surrounding medium (Spitzer, 1978). Photons carry momentum beside energy, which can be transferred to the ambient gas. This process may be crucial in dense clouds hosting massive stars (Krumholz & Matzner, 2009; Fall et al., 2010), although assessing the fraction of momentum that is transferred to the gas is challenging.

During the main sequence and post-main sequence evolution, large fluxes from the stellar interiors launch winds from the stellar surfaces. Therefore, stars lose a fraction of their mass which is deposited into the surrounding gas thereby carrying mechanical and thermal energy. How much energy is radiated away strongly depends on the thermodynamics of the surrounding gas. Also, the ejection velocities and mass-loss rates depend on the star mass, metallicity, and evolutionary stage: from high speed (up to 10^3 km s^{-1}), low mass loss rate (10^{-5} M$_\odot$ yr^{-1}) for massive main sequence stars, to lower speed ($\lesssim$ 100 km s^{-1}) and higher mass loss ($10^{-4} - 10^{-3}$ M$_\odot$ yr^{-1}) for Wolf Rayet or luminous blue variable stars (see e.g., Lamers & Cassinelli 1999, although there is no consensus on massive star evolution theories yet).

Finally, massive (roughly > 8 M$_\odot$) stars explode as supernovae at the end of their core hydrogen-burning phase. Supernovae launch at $> 10^3$ km s^{-1}metal-enriched material carrying about 10^{51} erg of total energy.

The above discussion highlights that while we have an overall, qualitative understanding of the physical processes involved in stellar feedback, their precise impact on the surrounding gas, and the consequent response of the stellar system to the gas expulsion are far from clear. For example, the gas might be exhausted or expelled from the center of dense clumps before the first supernovae. Also, precise time scales for the hydrogen-burning phase of massive stars and a self-consistent picture of stellar explosions are still a matter of debate. Possibly even more critical, most of our understanding of stellar evolution is based on single, isolated evolution models, despite being known that a large fraction of massive stars is in binaries, preferentially with other massive stars (Langer 2012, although recent year efforts boosted binary evolution modeling especially in numerical simulations, see e.g., Hurley et al. 2002; Iorio et al. 2023).

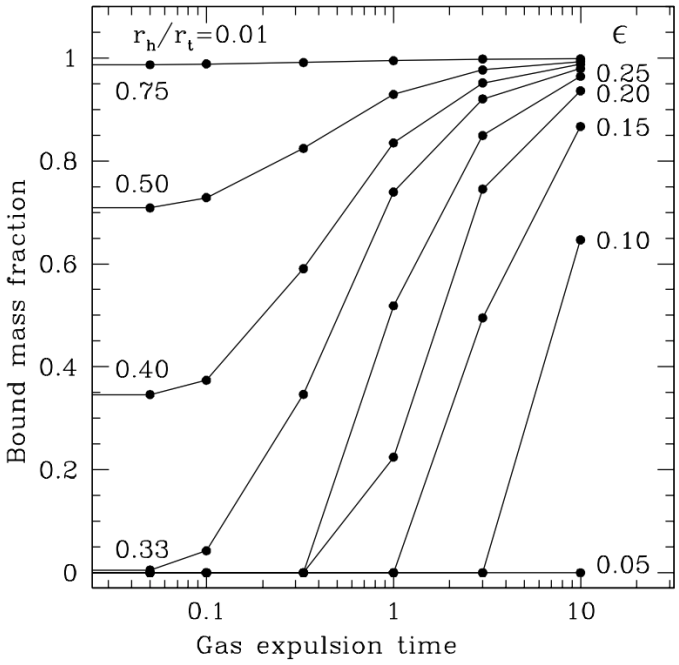

FIGURE 1.3: Bound mass fraction after the gas removal as a function of the gas expulsion time scale (scaled to the system t_{cr}). Different curves are for different star formation efficiencies (ϵ). The figure is adapted from Baumgardt & Kroupa (2007, see their figure 2) and shows a simulation with an initial filling factor of 0.01 (top-left corner). As could be seen, the slower the gas removal or the higher ϵ, the higher the final bound mass fraction.

Whether the nascent star cluster could survive as a bound stellar system strongly depends on the cloud star formation efficiency (i.e., the fraction of the available gas mass that was converted into stars) and the gas expulsion time (t_g, compared to the crossing time, $t_{cr} \sim$

$2r/\sigma$, with r the typical cluster size and σ the cluster velocity dispersion). In addition, their roles are intertwined. Figure 1.3 presents the interplay between gas expulsion time scale and star-formation efficiency on the final bound mass fraction. Put simply, the stellar system evolves due to changes in the gravitational potential driven by the gas being pushed away by stellar feedback. Hence, the higher the gas mass (i.e., lower star formation efficiency at fixed initial cloud mass) the more profound the changes in the gravitational potential. At the same time, the stellar system response depends on how fast (compared to the crossing time) the gas expulsion time is. In case $t_{\rm g} \gg t_{\rm cr}$, stars evolve through quasi-equilibrium states which minimizes the impact of gas expulsion. Indeed, if $t_{\rm g} \gg t_{\rm cr}$ the stellar system has enough time to readjust to the gravitational potential changes due to gas removal. In summary, energetic feedback sources are needed to sweep out the gas on short time scales, which translates into the need for more (or more massive) stars, which in turn translates into higher star formation efficiencies (i.e., lower final gas mass). Therefore, the two should balance for the gas expulsion to disrupt the gas cloud.

Finally, the non-homogeneous nature of star-forming regions in GMCs is central to determining the impact of gas expulsion on the stellar system. For example, the expelled gas could be collected into a nearby stellar clump or trigger a second episode of star formation by compressing a nearby gas cloud (Crowther et al., 2016; Zeidler et al., 2018).

In the past years, several numerical studies of gas expulsion, focussing on the stellar system response, were carried out (Kroupa et al., 2001; Baumgardt & Kroupa, 2007; Pelupessy & Portegies Zwart, 2012; Banerjee & Kroupa, 2013; Pfalzner & Kaczmarek, 2013; Brinkmann et al., 2017; Farias et al., 2017; Li et al., 2019a; Leveque et al., 2022a). In particular, N-body simulations exploring a wide range of initial cluster properties, star-to-gas mass ratios, and expulsion timescales showed that most clusters are likely disrupted due to gas removal, while the surviving ones significantly expand (Baumgardt & Kroupa, 2007) and may lose large fractions (up to 80%) of their stars (Lada et al., 1984). However, most of these simulations suffer a few critical limitations: *i)* the star cluster is assumed to be spherical and in virial equilibrium; *ii)* the gas is modeled as an external, and time-varying potential; *iii)* they require strong assumptions about the initial gas distribution (typically assumed to be reminiscent or the same as the stellar one). More recent simulations tackled these limitations: for example, Smith et al. (2013) and Farias et al. (2015) studied the response of fractal stellar systems to a time-decaying external potential finding that the survival or disruption of the stellar system is a highly stochastic process. Shukirgaliyev et al. (2017, 2021) extended previous investigations by allowing the gas to have a different density distribution than stars. Finally, Farias et al. (2018) introduced gas dynamics and found substructured embedded star clusters are more likely to survive gas expulsion than a virialized and spherical system, thereby concluding that gas removal may not be the main driver for young star cluster dissolution. These recent findings challenge the scenario that all stars form in bound star clusters the majority of which is then disrupted by gas expulsion (Lada & Lada, 2003), favoring the picture that star formation occurs across different density and spatial scales (Bastian et al., 2007; Sun et al., 2018; Rodríguez et al., 2019) and in highly sub-structured environments.

On the observational side, evidence of cluster expansion was hard to derive directly, and until very recently most of our understanding was based on indirect evidence resulting from cluster size-density or density-age anticorrelations (e.g., Pfalzner et al., 2014; Getman et al.,

2018). Thanks to the *Gaia* satellite (see Chapter 2), we are now able to directly probe expansion in star-forming regions and young star clusters with unprecedented detail (Cantat-Gaudin et al., 2019a,c; Román-Zúñiga et al., 2019; Damiani et al., 2019; Wright et al., 2019; Lim et al., 2020, 2021, 2022; Buckner et al., 2020; Armstrong et al., 2020, 2022; Schoettler et al., 2020, 2022; Kuhn et al., 2020; Swiggum et al., 2021; Maíz Apellániz et al., 2022; Miret-Roig et al., 2022; Guilherme-Garcia et al., 2023). In addition, we can study stellar feedback in external galaxies (McLeod et al., 2018; Chevance et al., 2016, 2020).

1.2.3 The violent relaxation phase

The response of the stellar systems to the gas expulsion is largely governed by the time scale and the gas mass swept out (see discussion in section 1.2.2). Right after the gas is expelled, the gravitational potential changes with time due to large-scale variations of the mass distribution rather than locally because of multiple stellar encounters (as in two-body relaxation theory, see e.g., section 1.3). During this process (named violent relaxation), individual stellar energies are not conserved given the time-dependent nature of the gravitational potential $\phi(\boldsymbol{x}, t)$. We can thus define the characteristic time scale $t_{\rm vr}$ through the logarithmic derivative of the potential (averaged over the spatial coordinates)

$$t_{\rm vr} \propto \left\langle \left(\frac{d \ln \phi(\boldsymbol{x}, t)}{dt} \right)^2 \right\rangle_{\boldsymbol{x}}^{1/2} . \tag{1.1}$$

The concept of violent relaxation was first introduced by Lynden-Bell (1967) in the context of galaxy evolution, and a few results of this theory are of primary relevance for star clusters. First, the energy gain or loss does not depend on the individual stellar mass. Hence violent relaxation itself would not lead to any form of segregation or equipartition, in contrast with the two-body relaxation theory (see section 1.3.2). Secondly, during the evolution, the system converts kinetic into potential energy and back again, possibly evolving toward an equilibrium configuration. Such system oscillations are strongly damped, and the system reaches equilibrium in a few dynamical time scales. Also, $t_{\rm vr}$ (equation 1.1) was found to typically be on the order of a few orbital periods (Lynden-Bell, 1967).

Since Lynden-Bell's seminal paper, violent relaxation has become a central process in the early evolution and formation of star clusters, especially in the context of the response to gas expulsion (see the discussion in section 1.2.2 and references therein). Recently, Leveque et al. (2022a) modeled the long-term dynamical evolution of star clusters starting from the embedded phase, accounting for gas expulsion and the subsequent violent relaxation phase. Finally, many theoretical works studied violent relaxation considering different scenarios, such as initial fractal distributions: Banerjee & Kroupa (2014, 2015) performed N-body simulations of both initially homogeneous and fractal systems tailored at reproducing the young (1 Myr) star cluster NGC 3603. They found that fractal systems may achieve lower central velocity dispersion than the homogeneous configuration. Also, they found that, under specific initial conditions, a spherical and monolithic configuration could be reached in the initially fractal system before stellar feedback sets in. Livernois et al. (2021) explored the role of dynamical interactions in hierarchical structures during the violent relaxation phase, finding that they

play an important role in the system evolution. In the following section, we shall discuss the details of stellar encounters in the early stages of cluster formation.

1.2.4 Stellar interactions and dynamical feedback

Dynamical interactions are usually invoked in the long-term evolution of star clusters (see section 1.3 for a more in-depth discussion). The relaxation time scale due to two-body interactions (Spitzer 1987) is indeed generally larger than young star cluster ages, hence they have been classified as dynamically-young systems (i.e., systems in which stellar encounters between stars were not effective in altering the distribution function of the system yet). However, this picture has been challenged by many observations of mass segregated young star clusters (Hillenbrand & Hartmann, 1998; de Grijs et al., 2002; Littlefair et al., 2003; Gouliermis et al., 2004; Stolte et al., 2006; Harayama et al., 2008; Bontemps et al., 2010; Gennaro et al., 2011; Evans & Oh, 2022). The interpretation could be threefold: the observed mass segregation is a by-product of the star formation process, it has a dynamical origin, or a combination of the twos. Competitive gas accretion during the star formation process naturally favors massive stars in stronger gravitational potentials (see e.g., Bonnell et al., 2001; Kirk et al., 2014; Vázquez-Semadeni et al., 2019, although feedback from massive stars could halt the accretion, Parker et al. 2015). On the other hand, the presence of a mass spectrum within a stellar system is known to lead to mass segregation if the system had sufficient time to evolve or if dynamical interactions were effective enough. It is yet unclear whether mass segregation in young star clusters is primordial or not. Also, disentangling between the two scenarios is a non-trivial task in observations.

Numerical simulations thus focused on the development of mass segregation in short time scales. The first finding was that star clusters forming from the merger of mass-segregated systems, inherit mass segregation from the parent clusters (McMillan et al., 2007). Hence the focus shifted toward clusters forming through the hierarchical merger of smaller stellar clumps: McMillan et al. (2007) and Allison et al. (2009) found that the high densities reached in low-mass clumps allow for stellar interactions to be efficient even on short (i.e., comparable to the free-fall) time scale, resulting in mass-segregated young stellar clusters (see e.g., Polak et al., 2024, but see also Vesperini & Chernoff 1996; Dorval et al. 2017; Cournoyer-Cloutier et al. 2024a,b for the evolution of binaries in these early evolutionary phases). Figure 1.4 qualitatively shows the development of mass segregation within merging sub-clusters: while the clusters approach each other massive stars start sinking in the center, then the two clusters merge (by about 7.5×10^5 yr after the start of the simulation) resulting in a mass segregated cluster.

Besides mass segregation, efficient dynamical interactions affect star-forming regions and new-born clusters in many ways. Efficient binary-single and binary-binary interactions would eject massive stars from the higher-density regions (given that massive stars are preferentially found in binaries, Sana et al. 2012, and dynamical interactions are more frequent in denser environments). Removing massive stars thus lowers the impact of feedback in the central part, and may result in off-centered feedback. Also, stellar interactions in dense clumps of stars would result in a dependence of the stellar velocity distribution on the stellar mass, a process known as energy equipartition (Heggie & Hut, 2003, see also Livernois et al. 2021 for a study on young, violent-relaxing systems). Therefore, recent years witnessed a renewed interest in the role of stellar dynamical interactions and stellar evolution in setting the

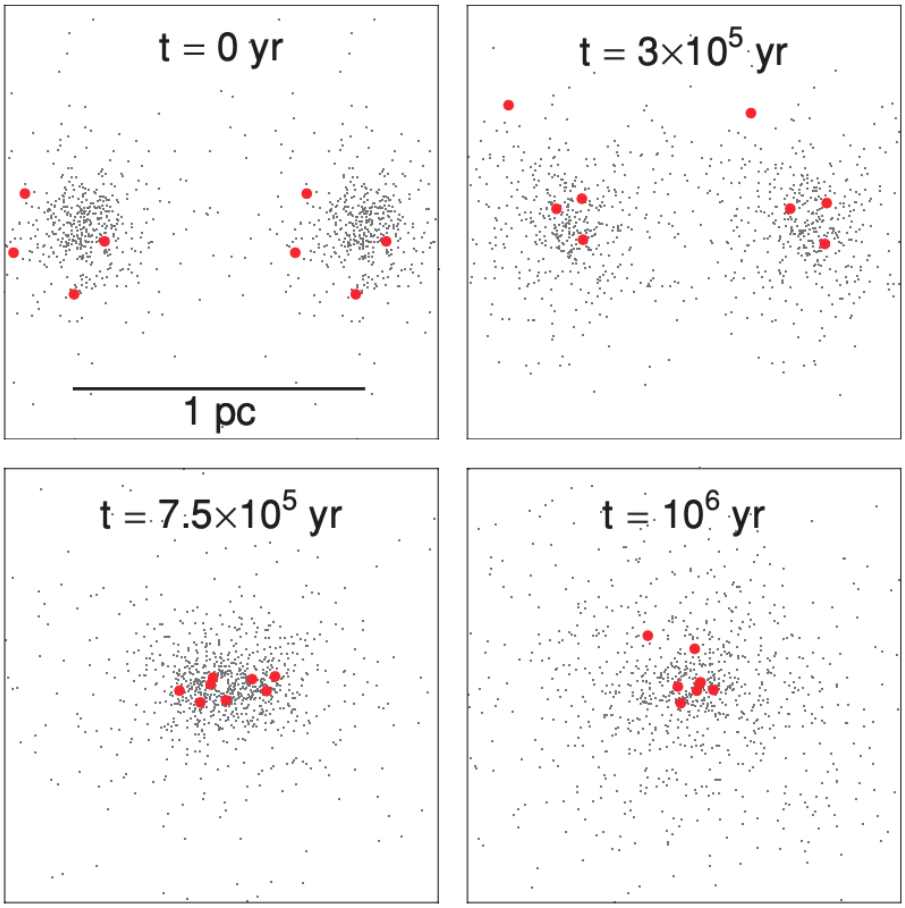

FIGURE 1.4: N-body simulation of two merging clusters (initialized as identical Plummer sphere, with 500 particles each, and at rest to each other at about a distance of 1 pc). Red dots show the location of the eight more massive stars in the simulations. Snapshots at different times are presented. By the end of the simulation (roughly 1 Myr) the two clusters merged and massive stars sunk in the potential well. The figure is reproduced from Moeckel & Bonnell (2009).

emerging properties of star clusters (see for example Goodwin & Whitworth, 2004; Moeckel & Bonnell, 2009; Vesperini et al., 2014; Parker & Wright, 2016; Parker et al., 2016; Sills et al., 2018; Ballone et al., 2020).

1.2.5 The hierarchical formation scenario

Numerical simulations of star formation in GMCs revealed that stars form with a fractal spatial distribution and that the initial properties of stars are inherited from (or at least linked to) those of the parent gas (see e.g., Dale & Bonnell, 2011; Grudić et al., 2018a; Ballone et al., 2020). Consequently, the formation of star clusters through the merger of smaller stellar clumps formed within the same GMC but in different locations, possibly at slightly different times and conditions raised much attention in recent years (see de Oliveira et al., 1998; Bonnell et al., 2003; Goodwin & Whitworth, 2004; Fujii et al., 2012; Gavagnin et al., 2016;

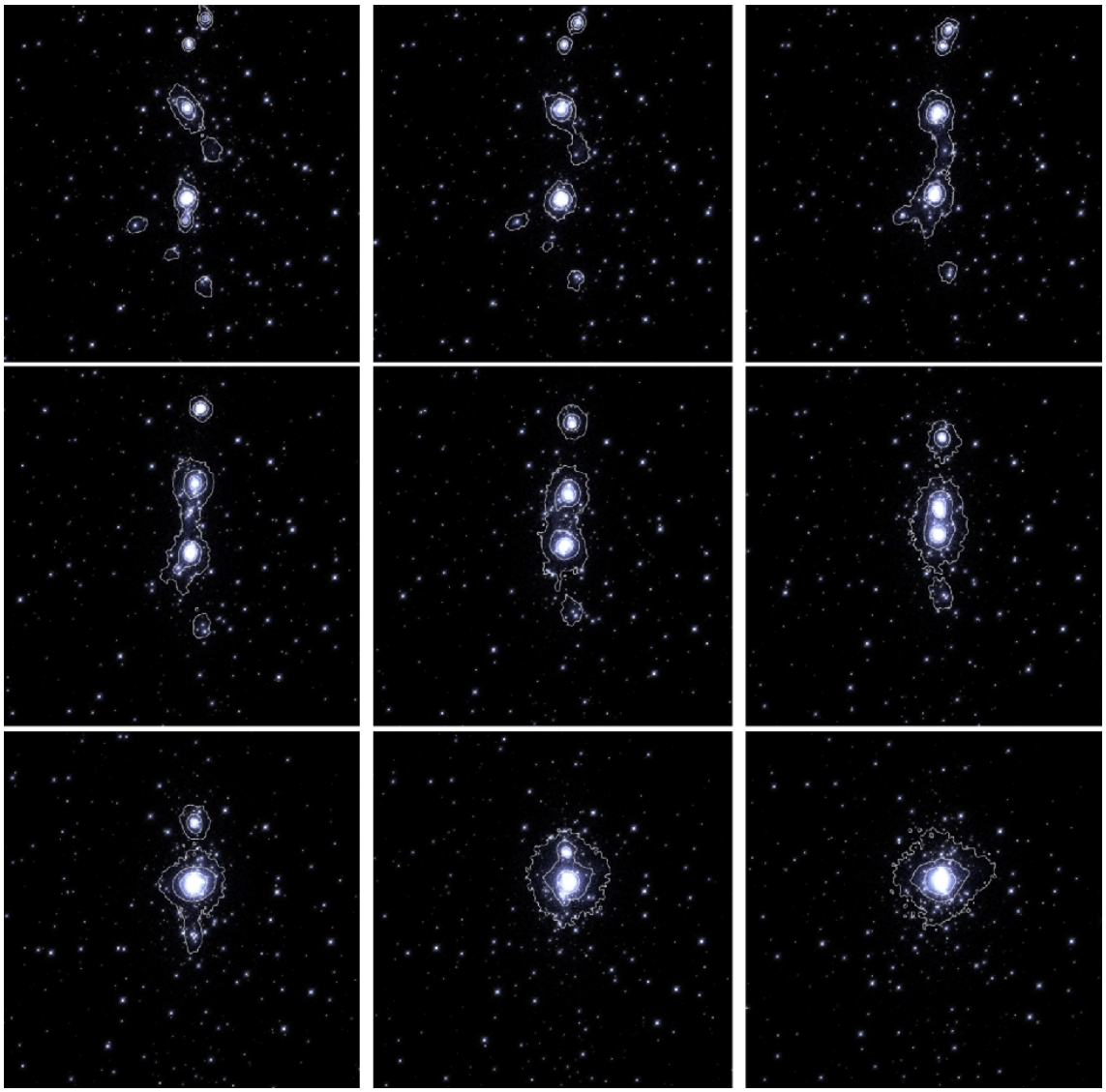

FIGURE 1.5: Evolution of the DR21 region (see Sills et al. 2018 for details on the initial conditions). Each snapshot presents the spatial distribution (5 pc wide) of stars (depicted in blue-white) and gas (represented by iso-density contours). Time proceeds from the top left to the bottom right panel: the first snapshot is after 0.1 Myr the simulation started, and each subsequent snapshot is taken after 0.1 Myr. The system (composed of stars and gas) quickly collapses (on the order of a Myr) to a nearly spherical configuration. The figure is taken from Sills et al. (2018).

Hong et al., 2017; Mapelli, 2017; Sills et al., 2018; Grudić et al., 2018b; Ballone et al., 2020; Livernois et al., 2021, for a non-exhaustive list of works). This scenario is generally referred to as the hierarchical cluster formation scenario, as opposed to the so-called monolithic formation scenario in which a dense star cluster forms at the center of a gravitationally unstable GMC in a starburst-like star formation episode (see e.g., Longmore et al., 2014; Banerjee & Kroupa, 2014). This section reviews the results and implications of the hierarchical formation scenario in the emerging properties of star clusters.

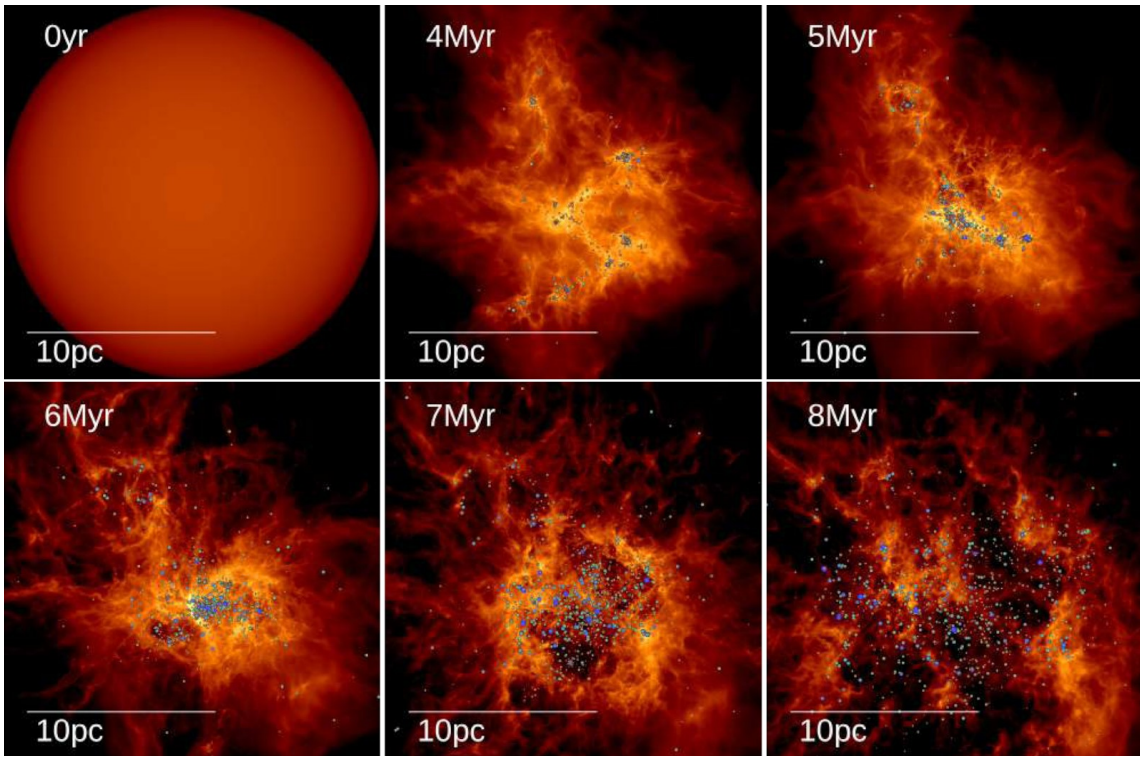

FIGURE 1.6: Surface density maps of a collapsing GMC with total mass 2×10^4 $M_\odot$. Different snapshots are at different times until cloud disruption. Circles represent sink particles (i.e., stars) in the simulation whose size increases with the stellar mass. The figure is part of the STARFORGE simulation set and was reproduced from Guszejnov et al. (2022).

In their seminal study, Bonnell et al. (2003) studied the fragmentation of GMCs and the evolution of the stellar system. They found that the substructuring played a key role in developing the forming star cluster. In particular, the local density at the center of clumps rises sharply due to infalling gas being converted into stars or accreted by proto-stars contributing to the formation of massive stars. They found that clumps can reach local densities 100 times higher than for a monolithic collapse (Bonnell et al., 2003). Such high densities had significant implications for the stellar interaction rates (see e.g., the discussion in section 1.2.4), resulting in closer and stronger interactions than would otherwise occur (Scally & Clarke, 2002), and thus hardening binaries, ejecting stars, truncating circumstellar disks, and favoring stellar mergers by direct collisions. The median local density then decreases due to dynamical ejections of stars from the subclusters, and the kinetic heating during subcluster interactions (Bonnell et al., 2003).

Subcluster mergers erase the initial clumpy distribution rather quickly (in a few initial free-fall time scales) resulting in a spherical-like configuration (see e.g., figure 1.5 from Sills et al., 2018). Also, the final density structure resulting from multiple mergers resembles the smooth density distributions observed in young massive clusters (Grudić et al., 2018b).

Despite eventually producing typical clusters, the lively evolution of hierarchical systems leaves imprints on the newly born cluster. Star-star scatterings in dense clumps may result in mass-segregated systems (McMillan et al., 2007; Allison et al., 2009; Livernois et al., 2021).

Also, hierarchical cluster formation boosts massive black hole (BH) formation and retention: repeated stellar mergers could produce very massive stars that will promptly collapse into BHs of, possibly, intermediate mass (Rantala et al., 2024; Fujii et al., 2024). Low-metallicity (< 0.1 $Z_{\odot}$) clusters may retain such BHs even after multiple mergers (Fujii et al., 2024). Besides stellar encounters, clump-clump interactions (ultimately culminating in mergers) have also a dominant role in shaping the early cluster properties. For instance, they could produce high ellipticity and rotating star clusters due to large-scale torques (de Oliveira et al., 1998; Mapelli, 2017). Some of the clumps are disrupted by multiple tidal interactions, developing a diffuse and lower-density population of stars orbiting around more massive clumps (Livernois et al., 2021). Finally, it has been suggested that multiple populations (MPs, widely observed in massive star clusters, e.g., Bastian et al. 2007; Gratton et al. 2019) can arise as a natural by-product of the cluster formation process, when accounting for initial substructuring and cluster mergers (see e.g., Hong et al., 2017; Howard et al., 2019). Given the topic's scientific relevance, the chemical enrichment evolution of hierarchical systems certainly deserves further investigation.

However, the dynamical evolution and the emerging properties of hierarchically forming star clusters have been poorly (or not at all) explored. The time scale hierarchical systems reach a monolithic configuration is a key ingredient in determining the survival chances after the gas expulsion phase (Fellhauer et al., 2009). Such time scale is largely unconstrained observationally, while theoretical studies found that it depends on many physical processes, such as the details of the initial sub-structuring (Fellhauer et al., 2009), rotation (Livernois et al., 2021), relative clump distances (Banerjee & Kroupa, 2015) and speeds (Karam & Sills, 2022). Also, Fellhauer et al. (2009) found that prompt mergers (i.e., before gas expulsion) boost the effective star formation efficiency of the cluster. On the other hand, Guszejnov et al. (2022) found that clumps do not merge fast enough and stellar feedback disrupts the cluster by blowing out the gas (see e.g., the simulation snapshots presented in figure 1.6).

Despite the efforts (e.g., Bonnell et al., 2003; Banerjee & Kroupa, 2015; Karam & Sills, 2024), the study of the dynamical evolution of hierarchically assembling systems is still in its infancy. This may be due to the lack of detailed observations of hierarchical cluster systems to compare numerical simulations with. However, this picture is likely changing.

1.3 The long-term evolution of bound stellar systems

After the left-over gas has been dispersed and the cluster settled to an equilibrium state, its evolution is governed by gravity (regulating the interaction rate between stars and the formation and evolution of binaries) and stellar evolution. Besides internal processes, the evolution of star clusters over billion-year time scales is affected by the cluster orbit in the galaxy. For instance, encounters with GMCs (Spitzer, 1958; Theuns, 1991; Gieles et al., 2006, that are more frequent for clusters with in-plane orbits), and repeated passages through the galactic disk (Chernoff et al., 1986; Weinberg, 1994) tidally perturb the cluster over short (i.e., shorter than $t_{\rm cr}$) time scales. Tidal shocks accelerate stars in the cluster center, thus increasing the cluster energy and causing expansion (Spitzer, 1958). Also, they may significantly speed up cluster dynamical evolution and dissolution (see e.g., Gnedin et al., 1999).

In this section, we first briefly discuss the implications of stellar evolution (section 1.3.1). we then move to the role of stellar encounters (sections 1.3.2-1.3.3) and tidal field (section 1.3.4),

before concluding with the critical role of BH retention in the long-term evolution of massive stellar systems (section 1.3.5).

1.3.1 More than just rigid balls: stellar evolution

After a few million years, stars may suffer significant mass loss due to stellar winds and supernova explosions, likely affecting the early cluster evolution. Several numerical studies showed that star clusters expand as a consequence of mass loss which in turn weakens the gravitational potential, possibly completely dissolving the cluster. In particular, clusters with lower initial concentration (Chernoff & Shapiro, 1987) or with flatter initial mass function (i.e., with a higher fraction of massive stars, Chernoff & Weinberg 1990) are more prone to disruption due to stellar evolution-driven mass loss. Fukushige & Heggie (1995) found that cluster dissolution may occur rapidly, suggesting that a loss of equilibrium causes the disruption. A more in-depth analysis revealed that the ratio $r_{\rm h}/r_{\rm t}$ (with $r_{\rm h}$, and $r_{\rm t}$ being the half-mass and the tidal radii, respectively) increases during the expansion, reaching values for which equilibrium is not possible (Fukushige & Heggie, 1995).

Stellar mass loss and disruption are intimately related to the host galaxy's tidal field (see e.g., Chernoff & Shapiro, 1987; Fukushige & Heggie, 1995; Vesperini, 2010) which strips stars to the cluster. The role of the tidal field in cluster evolution is presented in section 1.3.4.

1.3.2 Two-body relaxation theory in a nutshell

At the beginning of the 20th century, it was suggested that stellar interactions could be relevant in dense stellar systems by Jeans (1913) which first applied gas kinetic theory to stellar systems. After realizing that inter-star distances were small enough to allow for frequent dynamical interactions, studying the role of stellar scatterings within dense stellar systems became central in the field of star clusters (as highlighted by the many reviews and textbooks on the topic in past years, see e.g., Elson et al., 1987; Spitzer, 1987; Heggie & Hut, 2003; McMillan, 2008; Vesperini, 2010).

Focusing on individual stars, multiple and distant two-body encounters cause stars to lose energy in a process called dynamical friction (see e.g., Heggie & Hut, 2003). Indeed, due to the long-range nature of the gravitational force, multiple and distant encounters overwhelm close ones in perturbing the initial stellar orbit (Spitzer, 1987). From dynamical-friction theory: *i)* slower stars (i.e., stars with negative relative velocity to the test star, meaning that they are approaching the star in its reference frame) are responsible for the deceleration; *ii)* the higher the stellar mass, the stronger the energy loss of the star. Dynamical friction thus removes energy from massive stars, which sink toward the central part of the system, and transfer energy to lower-mass ones, developing mass segregation within the system.

On the other hand, considering a self-gravitating collection of interacting stars (i.e., a star cluster), two-body encounters cause evolution toward thermal equilibrium. The time scale for cumulative stellar interactions to alter the system's dynamical state significantly referred to as the two-body relaxation time scale, $t_{\rm relax}$ (see e.g., Spitzer, 1987)

$$t_{\rm relax} = 0.065 \frac{\langle v^2 \rangle^{3/2}}{G^2 \langle m \rangle^2 n \ln \Lambda}, \tag{1.2}$$

with $\langle v^2 \rangle$, G, $\langle m \rangle$, n, and $\ln \Lambda$ the local mean square root velocity of stars, the Gravitational constant, the local average stellar mass, the local stellar density, and the Coulomb logarithm (reminiscent of the analogy with kinetic plasma theory where the interactions are electrostatic), respectively. From equation 1.2 emerges that interactions are more effective (i.e., lower $t_{\rm relax}$) in denser areas (i.e., higher n as could be expected), but also for smaller $\langle v^2 \rangle$, meaning that, on average, relative star speeds are lower, thus allowing gravity for longer times to act on the stellar orbit.

The time scale in equation 1.2 varies significantly within the cluster: it is shorter in the center, due to higher densities and decreases moving outward as expected. Indeed, assuming virial equilibrium $\sigma^2 \sim GM/R \sim GM^{2/3}\rho^{1/3}$ (where we used the scaling $\rho \sim M/R^3$), which yields $t_{\rm relax} \sim N/\ln\Lambda \times 1/(G\rho)^{1/2}$ (assuming $M \sim N\langle m \rangle$ for a system with N particles). Hence, the density contribution dominates and the more massive the system (higher N) the slower the evolution.

To compare with observations it is useful to provide an integrated estimate of $t_{\rm relax}$ defined as the half-mass relaxation time scale, $t_{\rm rh}$ (Spitzer, 1987)

$$t_{\rm rh} = 0.0138 \frac{N r_{\rm h}^{3/2}}{G^{1/2}\langle m \rangle^{1/2} n \ln\Lambda} = 1.7 \times 10^5 \text{ yr } \frac{N^{1/2}(r_{\rm h}[\rm pc])^{3/2}}{(M[\rm M_\odot])^{1/2}}. \tag{1.3}$$

This allows us to separate between collisional ($t_{\rm rh} <$ age) and collisionless systems ($t_{\rm rh} >$ age). For Galactic GCs, on average $t_{\rm rh} \simeq 1.2$ Gyr (Harris, 1996, 2010 edition), making them collisional systems. Young star clusters in the disk of our Galaxy are on the other hand classified as collisionless systems according to the former definition. However, as discussed in section 1.2.4, stellar interactions do play a role even in very young systems depending on the cluster formation history. This makes the aforementioned separation blurry and in some respects, wrong. The reason is that equation 1.3 provides us an estimate of the present-day relaxation time and an answer to the question "On what time scale will stellar interactions change the stellar phase-space distribution assuming that the system structure and mass are not changing?". Therefore, the separation in collisional and collisionless systems according to equation 1.3 does not account for previous cluster evolution. From the above discussion, it also follows that $t_{\rm rh}$ is a function of time although it does not change as dramatically as the local relaxation time (see equation 1.2) evaluated for example at the center (Spitzer, 1987).

For a system in dynamical equilibrium, it can be shown that (Heggie & Hut, 2003)

$$t_{\rm rh} \sim \frac{N}{\log\Lambda} t_{\rm cr} = \frac{N}{\ln(0.02N)} t_{\rm cr} > t_{\rm cr}, \tag{1.4}$$

where we assumed the Coulomb logarithm by Giersz & Heggie (1996, which accounts for a mass spectrum within the system). According to the final relation in equation 1.4, stars orbit many times within the system practically unaffected by two-body relaxation, hence the system can evolve through equilibrium states under the effect of stellar encounters (Heggie & Hut, 2003).

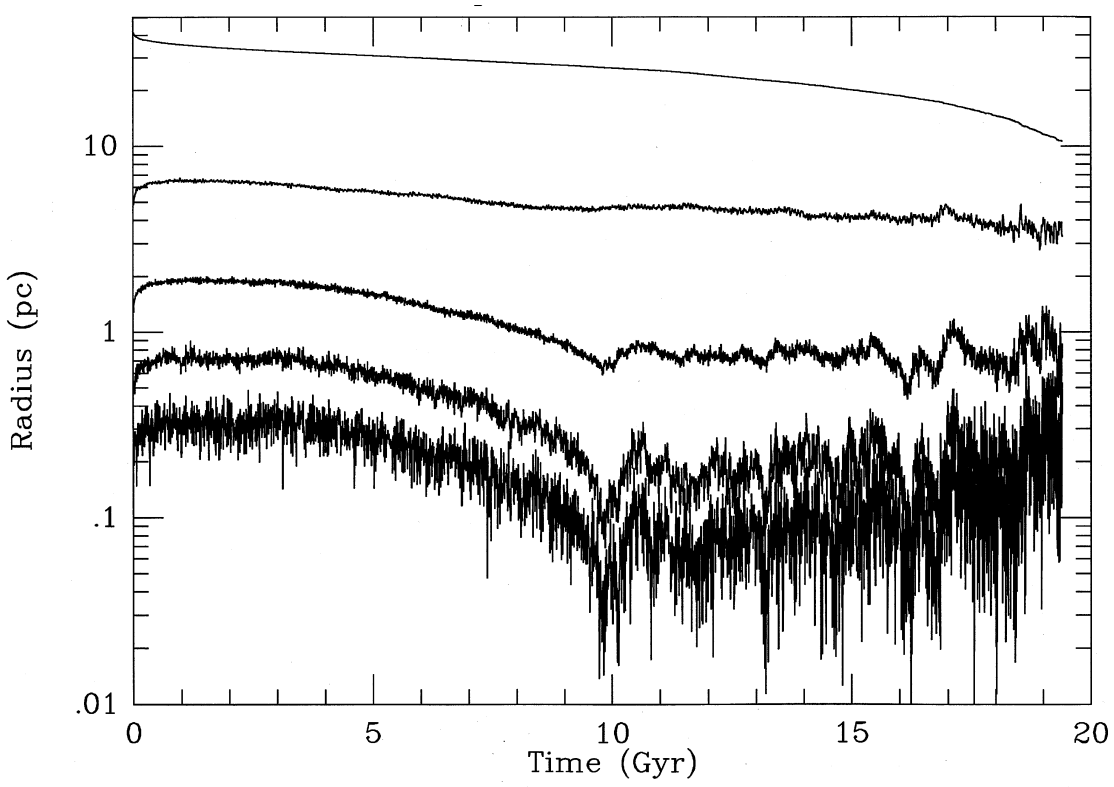

FIGURE 1.7: Time evolution of the 0.1%, 1%, 10%, and 50% Lagrangian radii (i.e., the radii enclosing a given fraction of the total cluster mass) and tidal radius r_t from an N-body simulation following the dynamical evolution of a star cluster orbiting at 4 kpc from the Galactic center and with an initial mass of $M_{cl} = 1.49 \times 10^5$ $M_\odot$ (reproduced from Aarseth & Heggie, 1998).

1.3.3 Two-body relaxation driven cluster evolution

This section briefly presents some well-established consequences of the two-body relaxation process (see section 1.3.2). Despite being known for many years, they are intense research fields. Indeed, the increasing wealth of data and detailed observations collected over the past years (Fabricius et al., 2014; Watkins et al., 2015; Bellini et al., 2017; Boberg et al., 2017; Bianchini et al., 2018; Kamann et al., 2018; Sollima et al., 2019) call for further theoretical efforts to explore the interplay between many different processes and perform more realistic simulations of cluster formation and evolution.

The relaxation process driven by stellar interactions alters the stellar energy distribution. We can think of the system evolving through quasi-equilibrium states given that two-body encounters-driven relaxation acts on a much longer time scale than t_{cr} (see the relation in equation 1.4).

One of the physical manifestations of multiple two-body encounters in star clusters is the tendency toward equipartition of kinetic energies (see Heggie & Hut, 2003, for an in-depth review on the topic). A balance between the relaxation process (on average lowering the cluster energy) and dynamical friction (increasing the mean cluster energy on average) is only possible if more massive stars (say with mass m_1 and velocity v_1) move slower than low-mass ones (say with mass m_2 and velocity v_2), translating into the condition for complete

energy equipartition: $m_1\langle v_1^2\rangle = m_2\langle v_2^2\rangle$.

The tendency toward energy equipartition has multiple implications: *i)* massive stars lose energy sinking toward the cluster center, while lighter stars (being more energetic) populate the external regions. Hence the system becomes segregated in mass; *ii)* the stellar velocity distribution (and in particular the velocity dispersion) is mass dependent with higher mass stars showing smaller velocity dispersion; *iii)* the velocity distribution evolves toward a Maxwellian distribution. Implications of the relaxation process were investigated by many theoretical studies (see e.g., Baumgardt & Makino, 2003; Khalisi et al., 2007; Bianchini et al., 2016; Aros & Vesperini, 2023) and also directly tested by observations of (extra-)Galactic GCs (see e.g., Heyl et al., 2017; Libralato et al., 2018; Watkins et al., 2022).

Complete equipartition is never achieved in real stellar systems and the reason is dual. First, a Maxwellian stellar velocity distribution allows for infinitely fast-moving stars, which will then escape the system even not considering the external tidal field (although this is not a physically motivated assumption, see discussion in section 1.3.4). Second, as relaxation proceeds, heavier stars tend to lose energy and sink into the potential well of the lighter stars. Assuming for simplicity that the system is composed of only two populations of masses $m_1 > m_2$ (following Heggie & Hut, 2003), the two populations exchange energy until the kinetic energies balance. However, while sinking toward the center, the self-gravity of the massive population may become important if $M_1 \gtrsim M_2\,(m_2/m_1)^{3/2}$ (with M_1 and M_2 being the total local masses of the two populations). If this is the case, stellar encounters subtract energy from the more massive population, which in turn contracts, and heats up: hence this system is moving away from energy equipartition (Heggie & Hut, 2003). The impossibility of reaching complete equipartition in stellar systems was first introduced by Spitzer (1969, and then extended to systems with realistic initial mass function by Vishniac 1978; Trenti & van der Marel 2013).

Finally, the progressive contraction of the cluster core leads to divergent central density in a finite time (as first studied by Hénon 1961; Antonov 1962), a process known as the gravothermal catastrophe. Binary systems both primordial or dynamically formed can prevent the ultimate collapse of the core by rapidly sinking in the center and injecting energy into the system through multi-body stellar encounters (Heggie & Hut, 2003). The post-core-collapse evolution may be characterized by large core oscillations driven by gravothermal effects (e.g., Makino, 1996). Figure 1.7 presents the time evolution of different Lagrangian radii of a star cluster toward and after (roughly > 10 Gyr) core-collapse (figure reproduced by Aarseth & Heggie, 1998). The inner regions are slowly contracting during the evolution until the core collapses and the post-core-collapse phase starts. On the other hand, $r_{\rm h}$ (corresponding to the Lagrangian radius enclosing 50% of the mass) remains roughly constant during the evolution.

Delving into the details of multi-body (> 2) encounters, energy generation, and the core collapse phase is beyond the scope of this introduction. We refer the interested reader to reviews on cluster evolution, for instance, Elson et al. (1987); Heggie & Hut (2003).

1.3.4 Clusters orbit within galaxies: the role of the tidal field

In addition to internal processes like stellar evolution (briefly presented in section 1.3.1), and two-body encounters (discussed in section 1.3.2), external processes, for example, the cluster orbit within the host galaxy, shape the cluster evolution over long time scales. Indeed, the

galaxy tidal field truncates the cluster size (defined by the tidal radius $r_{\rm t}$, i.e., the distance from the cluster beyond which the galaxy gravitational force becomes larger than the cluster self-gravity), and lowers the cluster escape speed (or in other words, the cluster escape energy $\equiv -3GM_{\rm cl}/2r_{\rm t}$), thereby enhancing mass loss. The evolution of tidally-limited star clusters was reviewed by Heggie (2001).

Assuming that the cluster is on a circular orbit at a distance $r_{\rm G}$ from the Galactic center, the two Lagrangian points lie at a cluster-centric distance of (Spitzer, 1987)

$$r_{\rm L} \equiv \left(\frac{1}{3}\frac{M_{\rm cl}}{M_{\rm G}(<r_{\rm G})}\right)^{1/3} r_{\rm G}, \tag{1.5}$$

with $M_{\rm cl}$ being the total cluster mass, and $M_{\rm G}(<r_{\rm G})$ the total host-galaxy mass enclosed within a sphere of radius equal to the circular orbit one (see e.g., Binney & Tremaine, 2008a). At first order, we can assume $r_{\rm t} \equiv r_{\rm L}$. Stars can thus escape the cluster only through the Lagrangian points of the galaxy–cluster system, developing extended tidal tails whose shape and stellar content were deeply investigated both using numerical simulations (Combes et al., 1999; Dehnen et al., 2004; Küpper et al., 2008; Ernst et al., 2009; Mastrobuono-Battisti et al., 2012) and by observations (Leon et al., 2000; Odenkirchen et al., 2003; Grillmair & Dionatos, 2006; Piatti & Carballo-Bello, 2020; Yang et al., 2022). For example, figure 1.8 presents the well-known case of Palomar 5, a sparse ($r_{\rm h} = 20$ pc) and low mass (about 10^4 $M_\odot$) clusters in the Galactic halo. Palomar 5 exhibits tidal tails extending for more than 20° on the sky (Erkal et al., 2017) resulting from the escape of stars through the cluster Lagrangian points. These features make Palomar 5 the best target for studying and understanding tidal tail formation. Recently in this context, Gieles et al. (2021) suggested that Palomar 5 was previously dense enough to retain BHs which efficiently ejected stars due to dynamical interactions hence resulting in extended tidal tails (see the discussion on BHs within star clusters in section 1.3.5).

Due to the tidal boundary defined by the galaxy's gravitational field, the cluster dissolution time is significantly shorter than without the external tidal field (see e.g., Baumgardt et al., 2002, who found that it may take up to 10^3 initial half-mass relaxation times for a cluster to lose about half of its mass in absence of the external tidal field). Also, due to the dependence of $r_{\rm t}$ on the cluster mass (equation 1.5), as stars leave the cluster, the tidal radius shrinks, further enhancing the mass loss (a process referred to as induced mass loss by Heggie, 2001). Gieles & Baumgardt (2008) extensively studied cluster dissolution in the presence of galactic tidal fields. They found that the dissolution time scale strongly depends on the initial $r_{\rm h}/r_{\rm t}$ ratio. Interestingly though, it does not depend on $r_{\rm h}$ for $r_{\rm h}/r_{\rm t} > 0.05$, but instead it scales with the cluster orbital properties as $\sim N^{0.65} r_{\rm G}/v_{\rm circ}$ (with $v_{\rm circ}$ being the circular velocity, Gieles & Baumgardt 2008): the smaller and shorter the cluster orbit within the host galaxy, the faster the evaporation.

Stars may acquire high enough energy through dynamical interactions in the central regions of the cluster on a $t_{\rm relax}$ (equation 1.2) time scale (which is typically lower than the strong interaction time scale, proportional to $N t_{\rm cr} \sim \ln\Lambda\, t_{\rm relax}$, Heggie 2001). Stars kicked out of the core at super-escape speeds leave the system on a $t_{\rm cr}$ time scale. However, this simple picture was challenged by direct orbit integration of possible escaping stars, finding that unbound stars (i.e., stars with energy equal or slightly above the escape one) may orbit within $r_{\rm t}$ for a time even longer than a Hubble time (Fukushige & Heggie, 2000). Hence,

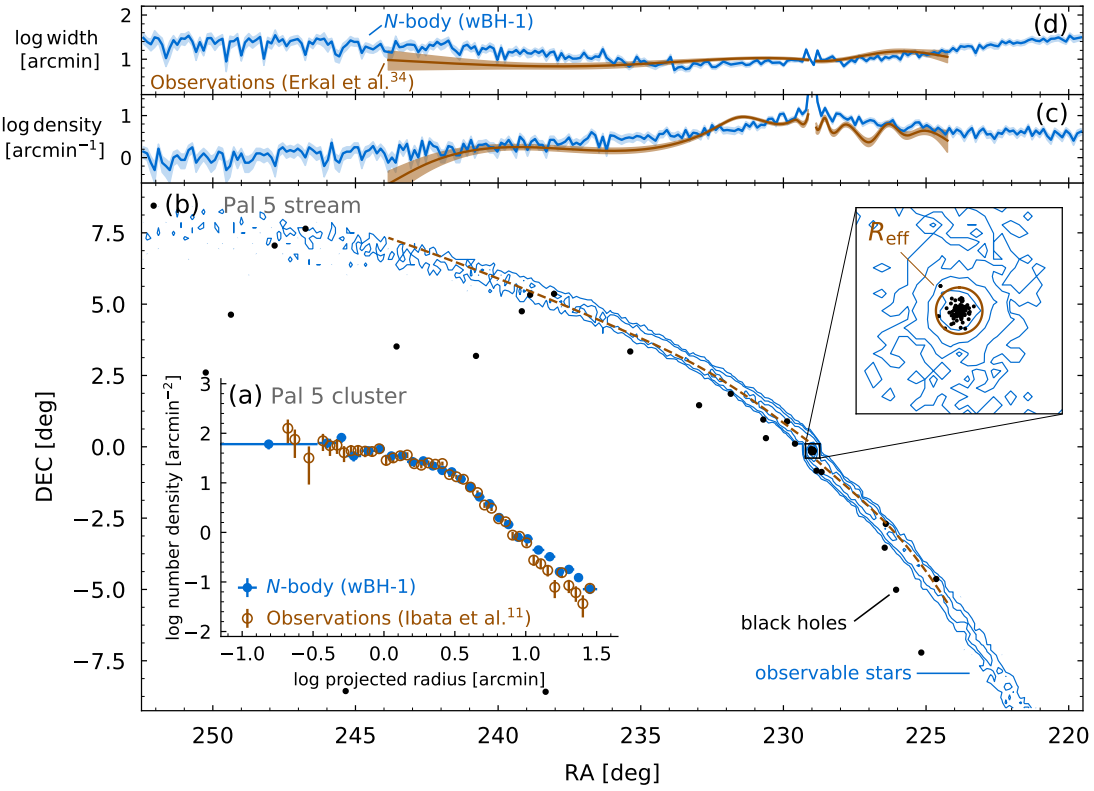

FIGURE 1.8: Comparison between the N-body simulation (in light blue) and observations of Palomar 5 (in brown). Panel (a) shows the density profile of observable stars; panel (b) presents the stream spatial distribution in the sky, while the stream density and width are shown in panels (c) and (d) respectively. In particular, the narrow stream width provides clues on the velocity dispersion of stars in the tidal tail. The figure is reproduced from Gieles et al. (2021), with data from Erkal et al. (2017).

they may never really leave the cluster.

Concerning the tidal tail's stellar content, low-mass stars populate higher-energy (less bound) orbits due to multiple stellar encounters (see sections 1.2.4, 1.3.3) It follows that *i)* tidal tails would be mainly of low-mass stars, and *ii)* the observed mass function flattens in the tidal tails (e.g., Vesperini & Heggie, 1997; Baumgardt & Makino, 2003).

1.3.5 Exotic objects in GCs

As high-density environments, star clusters facilitate high rates of dynamical encounters (Heggie & Hut, 2003), which can lead to the formation of various stellar exotica, including low-mass X-ray binaries, millisecond pulsars, blue stragglers, cataclysmic variables, and BHs. Within this context, the increasing number of BH detections in Galactic GCs, along with recent developments in terms of gravitational wave detections and results obtained with the LISA/Virgo detectors (Maccarone et al., 2007; Strader et al., 2012; Chomiuk et al., 2013; Miller-Jones et al., 2015; Giesers et al., 2018), has sparked renewed interest in understanding

the formation, and evolution of BHs in GCs, making them ideal testbeds for gravitational wave astrophysics (Rodriguez et al., 2015; Hong et al., 2018).

Several works addressed the role and impact of a population of BHs in the long-term dynamical evolution of a stellar system. They showed that the presence of BHs, specifically the heating from dynamically formed binary BHs, can significantly delay the mass segregation of visible stars and the core collapse of GCs (see e.g., Mackey et al., 2007, 2008; Breen & Heggie, 2013; Chatterjee et al., 2013; Morscher et al., 2015; Alessandrini et al., 2016; Peuten et al., 2016; Weatherford et al., 2018; Kremer et al., 2018, 2020). Also, these studies have shown that a sizeable population of BHs could be retained at the center of GCs for timescales longer than the Hubble time (Morscher et al., 2013; Sippel & Hurley, 2013; Heggie & Giersz, 2014; Arca Sedda et al., 2018; Askar et al., 2018). Only after dynamical ejections deplete the stellar-mass BH population significantly, the evolution towards core collapse can start (Kremer et al., 2020). Eventually, stellar binaries become efficient in generating energy preventing the ultimate collapse. Figure 1.9 presents the time evolution of a simulated stellar system that retained several hundred BHs for more than a Hubble time. The presence of binary BHs sustains the core from collapsing (as shown by the slowly increasing 1% Lagrangian and core radii) while inflating the external parts (see the steady increase of $r_{\rm h}$). Also, the observable cluster dynamical age is low ($0.7 - 0.8$) even after 15 Gyr of evolution.

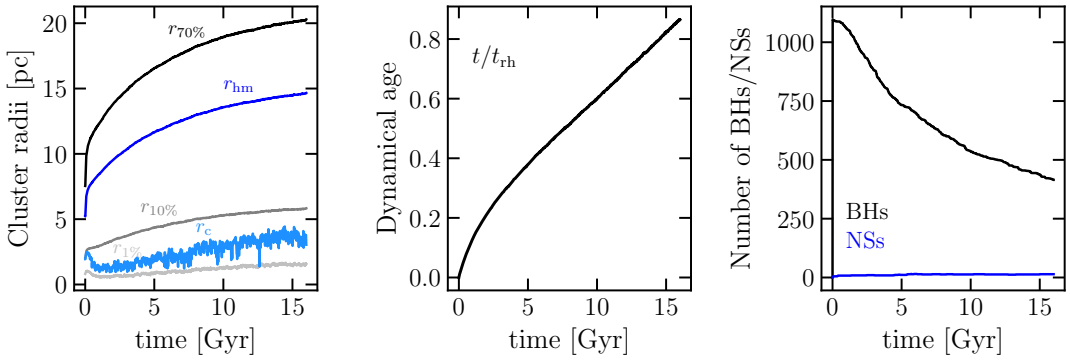

FIGURE 1.9: Time evolution of intrinsic cluster radii (left panel), observed cluster dynamical age (middle panel), and the number of bound BHs and neutron stars (NSs). The simulation is part of the set presented by Bhat et al. (2024, and further analyzed in Della Croce et al. 2024c). We refer to those papers for details on the simulation's initial conditions.

However, the BH retention in GCs and the distribution of kick velocities after their formation are still matters of intense investigation (Belczynski et al., 2002; Repetto et al., 2012; Janka, 2013; Mandel, 2016; Repetto et al., 2017; Giacobbo & Mapelli, 2020; Andrews & Kalogera, 2022). Due to asymmetric supernova explosion, indeed, BHs experience natal kicks (Janka, 2013; Mandel, 2016): if the kick amplitude is larger than the local escape speed, the BH is promptly ejected.

The search for stellar-mass BHs in Galactic GCs, therefore, opens up a window on many fundamental and timely science cases, including the constraint of the early BH retention and natal kicks, the study of stellar dynamical interactions, up to the BH-BH merging in

dense stellar systems as a source of gravitational wave emission (Moody & Sigurdsson, 2009; Banerjee et al., 2010; Rodriguez et al., 2015, 2016b,a, 2018; Antonini & Rasio, 2016; Hurley et al., 2016; Askar et al., 2017; Fragione & Kocsis, 2018; Hong et al., 2018; Samsing & D'Orazio, 2018; Samsing et al., 2018; Zevin et al., 2019; Arca Sedda et al., 2023, 2024a,b; Marín Pina et al., 2024; El-Badry, 2024).

1.4 Chemical abundance variations in massive stellar clusters: a puzzle for "standard" cluster formation

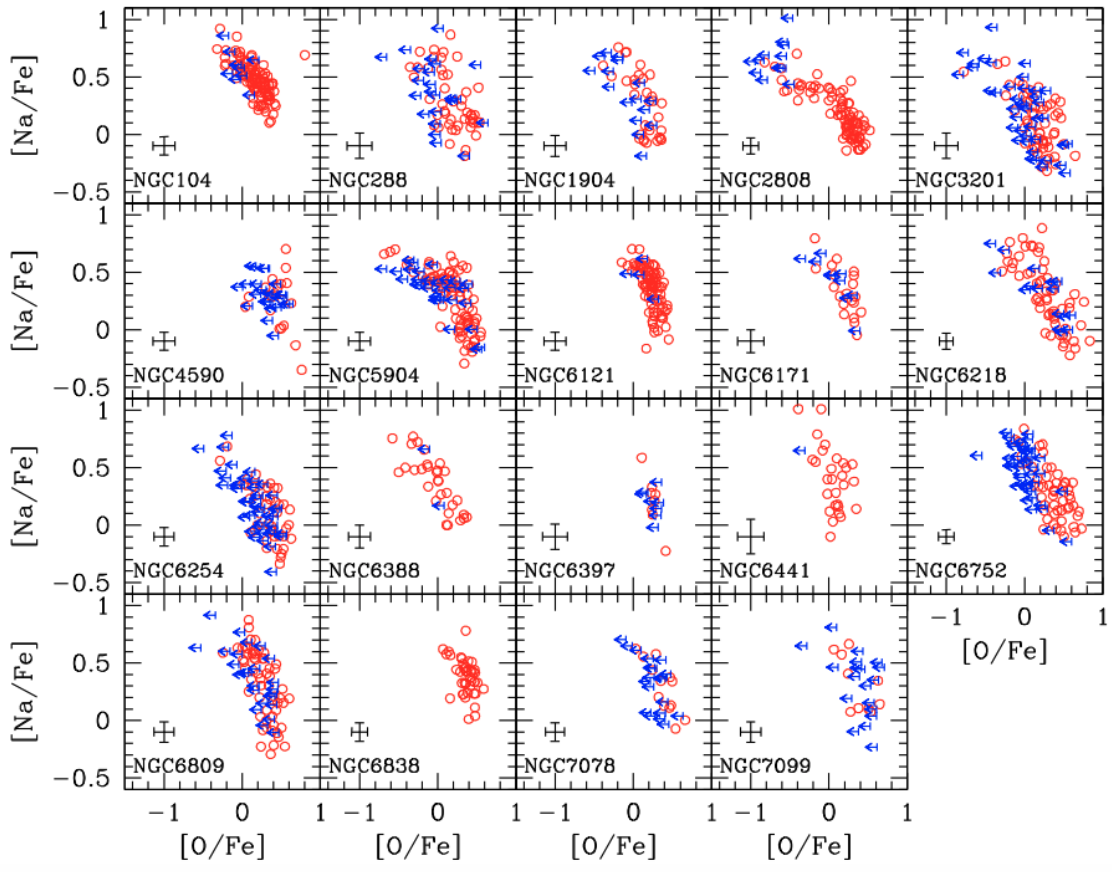

FIGURE 1.10: Na-O anticorrelation in 19 Galactic GCs as found by Carretta et al. (2009).

GC stars exhibit intrinsic star-to-star variations in their light-element content (see for instance figure 1.10 for the famous Na-O anticorrelation): while some GC stars have the same light-element abundances as field stars with similar metallicity (first population or generation, FP), others show enhanced He, N, Na, and Al along with depleted C, O, and Mg abundances (second population or generation, SP). Such chemical anomalies are not due to internal mixing processes but are intrinsic properties of the stars as they have been observed in stars in all evolutionary sequences (Cannon et al., 1998; Briley et al., 2004). The manifestation of light-element inhomogeneities is referred to as MPs (see Bastian & Lardo 2018;

Gratton et al. 2019 for a review of the subject). Light-element variations and their typical patterns appear to be linked to hot CNO/proton-capture thermonuclear reactions, which are expected to take place in relatively massive stars (e.g., Prantzos et al., 2007, 2017).

Light-element abundance variations can have an impact on stellar structures (as in the case of H) and atmospheres (as for Na, O, C, and N). They can therefore produce a broadening or splitting of different evolutionary sequences in color-magnitude-diagrams (CMDs) when appropriate filter combinations are used (especially with UV or near-UV filters Piotto et al., 2007; Sbordone et al., 2011; Dalessandro et al., 2011; Monelli et al., 2013; Piotto et al., 2015; Niederhofer et al., 2017; Cadelano et al., 2023).

It is well established that the MP phenomenon is (almost) ubiquitous among massive stellar clusters. It has been shown that nearly all massive ($> 10^4 M_\odot$; e.g., Dalessandro et al. 2014; Piotto et al. 2015; Milone et al. 2017; Bragaglia et al. 2017) and relatively old ($> 1.5 - 2$ Gyr; Martocchia et al. 2018a; Cadelano et al. 2022) GCs host MPs. In addition, MPs are observed in any environment: they are routinely found in the Magellanic Clouds' stellar clusters (Mucciarelli et al., 2009; Dalessandro et al., 2016), in GCs within dwarf galaxies such as Fornax (Larsen et al., 2012, 2018) and Sagittarius (e.g., Sills et al. 2019), and in the M31 GC system (Schiavon et al., 2013; Nardiello et al., 2018). There are also strong (though indirect) indications that stellar clusters in massive elliptical galaxies host MPs (e.g., Chung et al. 2011). Interestingly, stars characterized by enhanced N and depleted C are rarely found in the field and not present in OCs and dwarf galaxies (e.g., Martell et al., 2011; MacLean et al., 2015). This suggested that MPs in GCs arise due to processes unique to massive stellar systems and possibly linked to their formation.

MPs are, indeed, believed to have formed during the very early epochs of GC formation and evolution ($10 - 100$ Myr; see Martocchia et al. 2018b; Nardiello et al. 2015 and Saracino et al. 2020 for direct observational constraints). Over the years, many scenarios have been put forward to describe the sequence of physical events and mechanisms involved in their formation. We can schematically group them into two main categories. The first category of models envisions that MPs form during multiple (at least two) events of star formation and typically invoke self-enrichment processes, in which the SP forms out of the ejecta of relatively massive FP stars (e.g., Decressin et al., 2007; D'Ercole et al., 2008; de Mink et al., 2009; D'Antona et al., 2016). The second category groups models where MPs form simultaneously and SP stars accrete enriched gas during their pre-main sequence phases (e.g., Bastian et al. 2013; Gieles et al. 2018).

Independently of the specific differences, all models proposed so far have their own caveats and face serious problems in reproducing the variety of available observations. As a matter of fact, we still lack a comprehensive explanation of the physical processes at the basis of MP formation (e.g., see Bastian & Lardo 2018; Gratton et al. 2019).

Investigating the kinematical and structural properties of MPs can provide new insights into the early epochs of GC formation and evolution. Most formation models suggest that MPs form with different structural and kinematic properties. Differences between the FP and the SP kinematics can be either imprinted at the time of SP formation (see, e.g., Bekki 2010; Lacchin et al. 2022) or emerge during a cluster's evolution as a consequence of the initial differences between the FP and SP spatial distributions (see e.g., Tiongco et al. 2019; Vesperini et al. 2021; Sollima 2021). Although the primordial structural and kinematic differences between FP and SP stars are expected to be gradually erased during GC long-term

dynamical evolution (e.g., Vesperini et al. 2013; Hénault-Brunet et al. 2015; Tiongco et al. 2019; Vesperini et al. 2021; Sollima 2021), some clusters are expected to retain memory of these initial differences (see e.g., Dalessandro et al., 2019).

Spatial distributions alone can provide only a partial picture of the dynamical properties of MPs, and further key constraints on their formation are expected to be hidden in their kinematics. Because of the technical limitations in deriving kinematic information for large samples of resolved stars in dense environments, most of the information available so far has been obtained using *Hubble Space Telescope* (*HST*) proper motions (PMs) and *Multi-Unit Spectroscopic Explorer* (*MUSE*) line-of-sight[1] (LOS) velocities sampling relatively small portions of the cluster and focusing typically on the innermost regions. In a few particularly well-studied systems, MPs have been found to show different degrees of orbital anisotropy (e.g., Richer et al. 2013; Bellini et al. 2015; Libralato et al. 2023) and possibly different rotation amplitudes (e.g., Cordero et al. 2017; Kamann et al. 2020; Cordoni et al. 2020; Dalessandro et al. 2021a; Martens et al. 2023). In other cases, however, no significant differences were observed (see, e.g., Milone et al. 2018; Cordoni et al. 2020; Libralato et al. 2019; Szigeti et al. 2021a; Martens et al. 2023), thus not providing an exhaustive picture yet.

[1]Throughout the thesis we will not use the term radial velocity to identify the velocity component along the line-of-sight as derived from spectra. The reason is that we will typically deal with PMs or 3D kinematics. Hence with the radial velocity component, we define the projection of the PM vector (i.e., on the plane of the sky) along the line connecting the star's position to the system center. Using radial velocity for the velocity component along the line of sight would thus be misleading.

Chapter 2

Stellar kinematics as a tool to unveil cluster formation and evolution

> "The glory of battle, Koryk, dwells only in the bard's voice, in the teller's woven words. Glory belongs to ghosts and poets. What you hear and dream isn't the same as what you live - blur the distinction at your own peril, lad."
>
> The Complete Malazan Book of the Fallen, Steven Erikson

Internal cluster kinematics, in synergy with complementary data from photometry and spectroscopy, is a key tool to shed new light on the physical processes involved in cluster formation and evolution. The motion of stars in nascent star clusters is indeed inherited from the parent gas cloud, probing the initial conditions of cluster formation. On the longer time scales, stellar interactions dominate cluster evolution and their impact on internal kinematics was subject of detailed scrutiny for decades.

The *fil rougue* of this thesis is therefore the use of stellar kinematics to tackle the open questions on cluster formation and evolution. Exploiting stellar kinematics could provide us with a novel look to disentangle between different interpretations and push further our understanding of star clusters.

In this respect, the European Space Agency (ESA) mission *Gaia*[1] (Gaia Collaboration, 2016a) revolutionized the field. Thanks to exquisite astrometric precision, all-sky coverage, and multi-epoch observations all in a single spacecraft we can study the cluster internal kinematics from the very young clusters to the oldest stellar systems in the Galaxy with unprecedented details. Combining position, on-sky velocity, and parallax measurements, we can define cluster membership more firmly, allowing for decontamination in crowded environments. At the same time, *Gaia* could complement *HST* observations of the innermost regions of Galactic GCs, thus constraining their internal kinematics over the full cluster extension (something that would be hard with small-field instruments like *HST*).

This Chapter first provides an overview of the observational datasets and facilities used to study star clusters during my Ph.D. (in section 2.1). In particular, section 2.1.1 presents the *Gaia* mission along with selected science cases in which *Gaia* contributed, while sections 2.1.2

[1]The name *Gaia* stands for "Global Astrometric Interferometer for Astrophysics". The name reflected the optical technique originally planned for the spacecraft. Although optical interferometry was not used in the end, the name *Gaia* remained.

and 2.1.3 will then give a brief introduction to the *Hubble Space Telescope* and the *Multi Unit Spectroscopic Explorer* with a particular focus on the instruments and data products used in later chapters of this thesis. Finally, section 2.2 presents the simulation sets used during the three years of Ph.D. to interpret observations of internal stellar kinematics.

2.1 Observations of cluster internal kineamtics

2.1.1 The *Gaia* astrometric mission

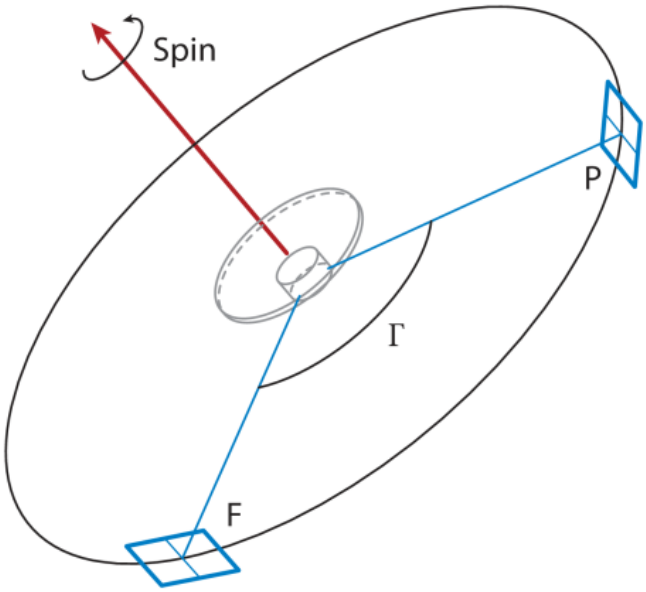

FIGURE 2.1: A sketch of the *Gaia* satellite (in light gray), with the spacecraft spin axis pointing away from the sun shield, and the lines of sight of the two telescopes, at right angles to the spin axis, separated by the basic angle Γ. The sky projections of the focal planes through both fields of view are indicated by P (for the preceding, i.e., the first charge-coupled device the source scans through according to the spacecraft spin direction) and F (standing for the following). Figure adapted from Brown (2021).

The spacecraft containing the *Gaia* satellite was launched on December 19, 2013, from Europe's Spaceport in French Guiana. The satellite then moved toward the L2 Lagrangian point of the Earth-Sun system. Gaia recently celebrated its 10th anniversary, more than doubling the initial mission timeline of five years.

Since 2013, *Gaia* performed repeated measurements of the positions of stars (but not only) in the sky with unprecedented precision, pushing forward the microarcsecond-astrometry era. On September 14, 2016, the first data release (DR1) was published (Gaia Collaboration, 2016b), which listed a "full astrometric solution" (i.e., PM, and parallax) for two million sources. Two years later (April 25, 2018) the DR2 was released (Gaia Collaboration, 2018) delivering PM measurements up to 100 times more accurate than DR1 down to $G \sim 20.5$ mag, with a profound impact on many fields in astronomy. Currently, we have DR3 data (Gaia Collaboration 2023a released on June 13, 2022, after an early data release on December 3, 2020, Gaia Collaboration 2021) providing, among others: *i)* photometry in the wide G band (covering the range 330−1050 nm) for about 1.806 billion sources, and broadband blue ($G_{\rm BP}$ in the range 330 − 680 nm) and red ($G_{\rm RP}$ in the range 640 − 1050 nm) filter magnitudes for a large subsample of sources (1.54 billion and 1.55 billion sources, respectively); *ii)* PM and parallax measurements for 1.46 billion sources; *iii)* astrophysical parameters (such as effective temperature, surface gravity, metallicity, reddening extinction in the G band, and distance)

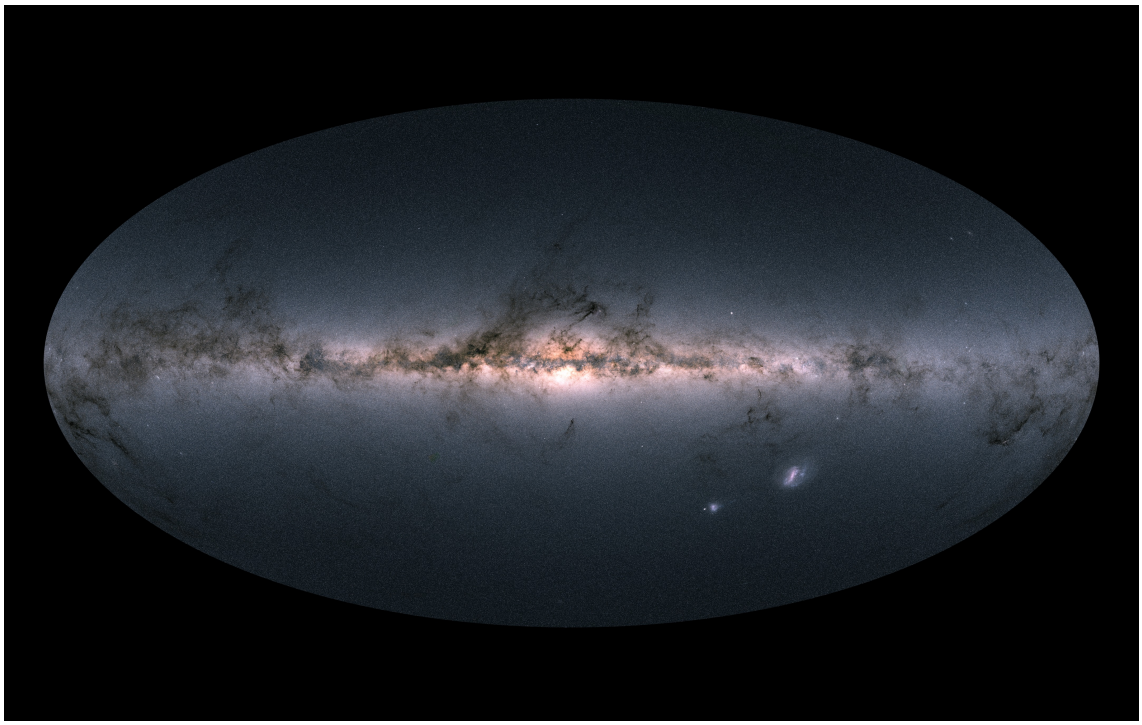

FIGURE 2.2: *Gaia*'s all-sky view of the Milky Way and neighboring galaxies, based on measurements of nearly 1.7 billion stars. The map shows the total brightness and color of stars observed by the ESA satellite in each portion of the sky between July 2014 and May 2016. Brighter regions indicate denser concentrations of stars, while darker ones correspond to regions where fewer bright stars are observed. Credits: ESA/Gaia/DPAC.

from BP/RP spectra for 1.59 billion sources and from RVS spectra for 5.5 million objects; *iv)* mean LOS velocities for 33 million stars and mean $G_{\rm RVS}$ magnitudes for 32 million objects with $G_{\rm RVS} \lesssim 14$ mag and effective temperatures in the range of 3100 to 14500 K; *v)* rotational velocities for 3.5 million sources with $G_{\rm RVS} \lesssim 12$ mag; and *vi)* variability analysis from multi-epoch photometry for 10.5 million sources, and much more. We refer the interested reader to the DR3 webpage on the *Gaia* website[2].

Figure 2.1 presents a sketch of the spacecraft featuring a three-meter-tall cylindrical structure, which hosts the science instruments, and a ten-meter-wide sun shield that keeps the main body in shade (see e.g., Gaia Collaboration, 2016a). The two telescope lines of sight separated by the basic angle $\Gamma = 106.5°$ are also shown (see figure 2.1). As the sources observed by Gaia drift across the focal plane, photoelectrons are accumulated into a single image of the source. The spacecraft then spins around the axis perpendicular to the sun shield, thus scanning along the great circle defined by the telescope's line of sight. The spacecraft completes a full revolution in about six hours. Finally, to cover the full sky the spin axis precesses around the direction of the Sun, maintaining a fixed angle of 45°. The precession takes about 63 days to complete. The combination of spinning and precession allows *Gaia* to cover the full sky in about $3 - 4$ months of continuous observation. Hence, every $3 - 4$ months each

[2]Available at `https://www.cosmos.esa.int/web/gaia/data-release-3`.

detectable source is observed at least twice: first by the preceding telescope and then from the following one (labeled as P and F respectively in figure 2.1).

It is possible to reconstruct the instantaneous celestial position of each source knowing the observation time together with spacecraft orientation and spin phase. Repeated measurements then yield the determination of the parallactic and proper motions. Indeed, each source observed by *Gaia* describes a track on the sky which is the combination of the intrinsic PM of the source (approximated as a straight line between consecutive observations) and the apparent parallax motion due to Earth's revolution around the Sun (see e.g., Penoyre et al. 2020). This is strictly true for single sources. Unresolved binaries present wobbles because of the intrinsic separation between the center of gravity (that follows the trajectory discussed above) and that of light (Penoyre et al., 2022a,b; Halbwachs et al., 2023). To ensure the best determination of such motions, the angular separations of the telescope lines of sight and the precession axis should be precisely known and stable through time (at a few microarcseconds). Also, repeated measurements over the years promised increasing precision and number of sources for which parallax and PM could be estimated over time (Brown, 2021).

The exquisite astrometric precision delivered by *Gaia* has revolutionized many fields in astronomy, including the establishment of the first optical celestial reference frame based solely on extragalactic sources. The improved reference frame has since been used to anchor other surveys. Also, every *Gaia* data release was made freely available to the astronomical community through the Gaia Archive[3] making *Gaia* an indispensable part of modern research in astronomy. In the following, we present a brief selection of science cases addressed using *Gaia* data.

Gaia in principle observes every source brighter than the survey limit ($G \sim 20.7$) and point-like (Gaia Collaboration, 2016a, see for instance figure 2.2 for the map of the Galaxy as traced by the stars observed by the *Gaia* satellite). Minor bodies in the Solar System would appear sufficiently point-like to be observed despite their high angular speed. Tanga & Mignard (2012) estimated that about 350,000 Solar System objects will be observed by Gaia, allowing for high-precision orbital classifications (Delbo' et al., 2012). So far, DR3 data provided a compilation of about 150 thousand Solar System objects, including asteroids and planetary satellites. It was also able to detect milliarcsecond-level wobbling of the asteroid photo centers (Tanga et al., 2023). In addition, *Gaia* DR3 featured, for the first time, the mean reflectance spectra of a selected sample of 60518 stellar system objects, primarily asteroids, observed between August 5, 2014, and May 28, 2017 (Gaia Collaboration, 2023b).

Through an analysis of the epoch astrometry, *Gaia* can detect planets. Indeed, the astrometric precision achieved by *Gaia* allows us to detect deviations from the simple single-track model due to planet-like companions. DR3 includes the first astrometric orbital solutions down to the planetary-mass regime (Holl et al., 2023).

On a Galactic scale, *Gaia* revealed disk disturbances due to close passages of the Sagittarius dwarf galaxy (Antoja et al., 2018) roughly 0.5 Gyr ago (Bland-Hawthorn et al., 2019), as well as the influence of the Galactic bar on the stellar disk population (Gaia Collaboration, 2023c). Also, *Gaia* is providing a more complete picture of the early evolution and assembly of the Milky Way (MW, Helmi, 2020).

Malhan et al. (2018); Ibata et al. (2019b) discovered several stellar streams crossing the Galactic halo by exploiting the full-sky coverage coupled with the excellent astrometry and

[3]Available at `https://gea.esac.esa.int/archive/`.

photometry by *Gaia*. Within this context, Ibata et al. (2019a) identified a tidal stream associated with ω-Centauri, supporting the claims that ω-Centauri is the remnant core of an accreted dwarf galaxy.

Besides stellar streams, *Gaia* was used to study the internal rotation of GCs (Bianchini et al., 2018) and their orbits within the Galactic halo, thereby probing the total MW mass (Vasiliev, 2019b). Also, the mean PM for several MW satellites was obtained, including the Magellanic Clouds. Vasiliev (2018) used red giants in the Large Magellanic Cloud (LMC) to derive projected kinematic maps, consisting of the mean PM and velocity dispersion out to 7 kpc from the LMC center.

Looking at the distant Universe, *Gaia* automatically observes galaxies that have bright cores as well as distant quasars that are point-like. Besides being the cornerstones of the celestial reference frame, active galactic nuclei (AGNs) offer a scientifically interesting sample. One of the novelties of *Gaia* DR3 is indeed the publication of the multiband light curves for about one million AGNs and the parameters characterizing their variability. In addition, more than 21000 were new identifications (Carnerero et al., 2023).

For further highlights on the latest Gaia science using DR3 data, we refer to the special issue published by the Astronomy and Astrophysics Journal[4].

The *Gaia* revolution on young star cluster science

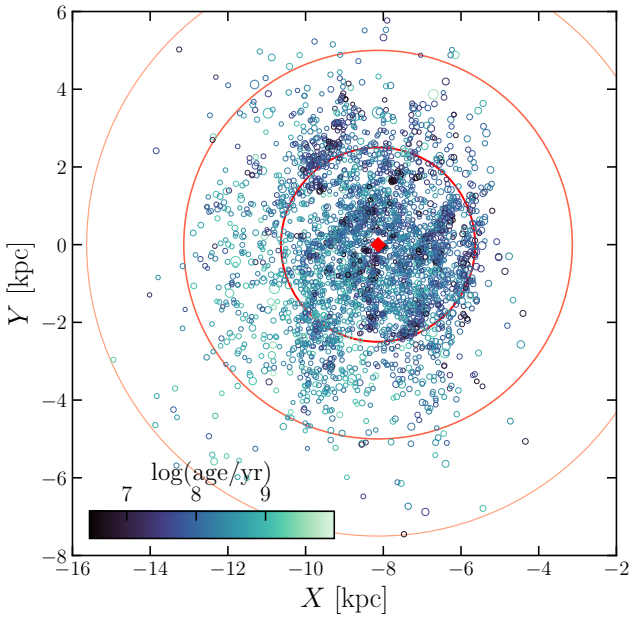

FIGURE 2.3: Spatial distribution of OCs in Galacto-centric coordinates. Star clusters are color-coded according to their age, while the size of the marker is proportional to the square root of the cluster mass (for visualization purposes only). The red diamond marks the Sun's position and red circles show progressively increasing heliocentric distances of 2.5 kpc, 5 kpc, and 7.5 kpc. Cluster data are from Hunt & Reffert (2023, high-quality cluster sample with reliable mass estimates).

Detecting Galactic OCs can be challenging due to their comparable density to field stars and the lack of gas. Before *Gaia*, many studies attempted to define a complete sample of open star clusters in the MW by using different astrometric datasets (e.g., Becker & Fenkart, 1971; Robichon et al., 1999; Dias et al., 2002; Alessi et al., 2003; Kharchenko et al., 2005a,b, 2012; Sampedro et al., 2017).

[4]Available at `https://www.aanda.org/component/toc/?task=topic&id=1641`.

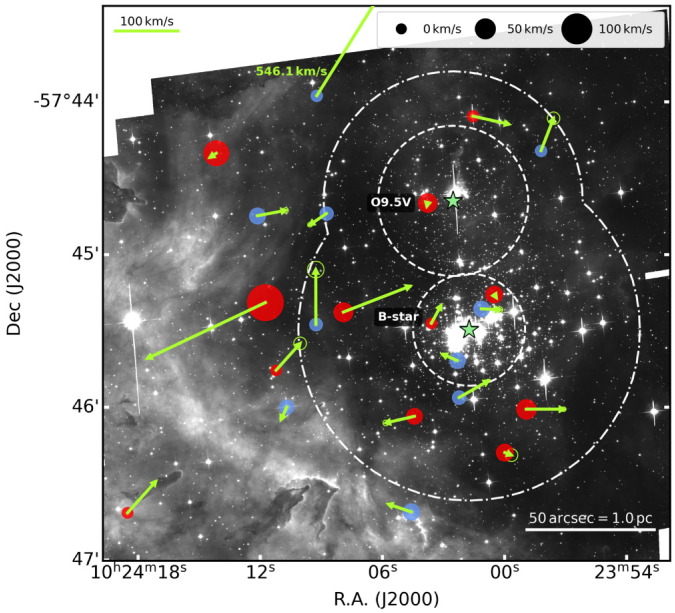

FIGURE 2.4: Stars with an absolute peculiar speed exceeding 30 km s^{-1} in the Westerlund 2 star cluster. The arrows show the PM vectors, while the circle size indicates the LOS velocity. Stars are shown as red and blue circles depending on whether they are moving away from us or toward us. The figure is reproduces from Zeidler et al. (2021).

In particular, Kharchenko et al. (2013, supplemented by Schmeja et al. 2014, and Scholz et al. 2015) compiled a catalog of 3061 OCs and 147 GCs. However, the existence of many OCs was questioned (see for example Kos et al., 2018). Many stellar over-densities are in fact not real clusters despite being located in the same region of the sky. *Gaia* data showed that putative member stars do not share a common motion through the MW (Cantat-Gaudin & Anders, 2020).

This highlights how the advent of *Gaia* completely revolutionized the field (see e.g., the recent review on the subject by Cantat-Gaudin 2022). Thanks to the five-dimensional (i.e., sky position, PM components, and parallax) information for billions of sources in our Galaxy (supplemented by LOS velocity for tens of millions Gaia Collaboration 2023a) we can search for OCs as overdense stellar groups in multi-dimensional space (i.e., groups that are at a similar distance from the Sun and are traveling together in the Galaxy). Furthermore, color-magnitude diagrams for putative cluster members from astrometric identifications can confirm that a group of stars is a true cluster. Many studies revisited the sample of Galactic OCs and the membership catalogs exploiting modern unsupervised machine learning algorithms (for example Castro-Ginard et al. 2018, 2019, 2020; Liu & Pang 2019; Cantat-Gaudin et al. 2019b, 2020; Cantat-Gaudin & Anders 2020; Jaehnig et al. 2021; Hunt & Reffert 2021 using DR2 data, and Castro-Ginard et al. 2022; Hunt & Reffert 2023 on DR3 data). Also, Hunt & Reffert (2021) tested different machine-learning algorithms for the detection of OCs in the Galaxy, finding that the more complete the catalog the less pure, and that post-processing analysis is needed. The current cluster census in our Galaxy counts about 7000 objects out of which $\sim$ 4000 are classified as true star cluster (according to Hunt & Reffert, 2023). Figure 2.3 shows the spatial distribution of known OCs projected on the Galactic plane. Substructures are directly visible from the OC distribution, especially if looking at the youngest ones, that are typically associated with Galactic spiral arms (e.g., Castro-Ginard et al., 2021).

Besides enlarging the cluster sample, *Gaia* enabled accurate characterization of known and newly discovered clusters, tremendously boosting research in the field. In particular, observations revealed significant structural and kinematical complexity in both star clusters and

larger young star associations. Indeed, recently formed systems show significant deviations from spherical symmetry (see e.g., Pang et al., 2021a, for a study of 13 OCs) which however were suggested to be imprinted at birth rather than resulting from internal processes (such as asymmetric expansion, e.g., Ward & Kruijssen 2018; Ward et al. 2020; Cantat-Gaudin 2022), Also, extended tidal-tail-like structures (e.g., Meingast & Alves, 2019; Röser et al., 2019; Meingast et al., 2021; Jerabkova et al., 2021), as well as complex clumpy distributions characterized by the presence of several coeval stellar subsystems (e.g., Kuhn et al., 2019a; Getman et al., 2019; Kuhn et al., 2020; Lim et al., 2020; Dalessandro et al., 2021b; Zeidler et al., 2021) were routinely discovered thanks for *Gaia* data. Finally, the identification of high-speed stars escaping clusters or star-forming regions (referred to as runaway stars) provides important clues on the efficiency of dynamical ejections and the initial conditions for cluster formation (see e.g., McBride & Kounkel, 2019; Schoettler et al., 2020; Zeidler et al., 2021). For example, figure 2.4 presents the distribution of high-speed stars found in the young massive cluster Westerlund 2 by Zeidler et al. (2021, using *Gaia* DR2 data).

Despite instrumental contributions to the field of star clusters, *Gaia* is still observing[5], and future data releases will provide us with more exciting data and science. Data release 4 is expected for mid-2026 and will be based on 5.5 years of observations. It will thus provide more precise astrometry, but more importantly, *Gaia* DR4 will release all the epoch data, meaning the astrometric, photometric, LOS velocity, and BP, RP, and RVS spectra time series for each source. Finally, a legacy data release (DR5) is envisioned not before the end of 2030.

Looking at the future, an infra-red astrometric mission is being proposed to ESA as the next astrometric mission to keep improving the existing astrometry and overcoming the limitations of *Gaia* in exploring dense and obscured regions of the Galaxy (Hobbs et al., 2021). *GaiaNIR*, if approved, will allow us to study the kinematics of stars within GMCs, where star clusters are formed, possibly providing us with further insights into this yet elusive process.

2.1.2 The Hubble Space Telescope

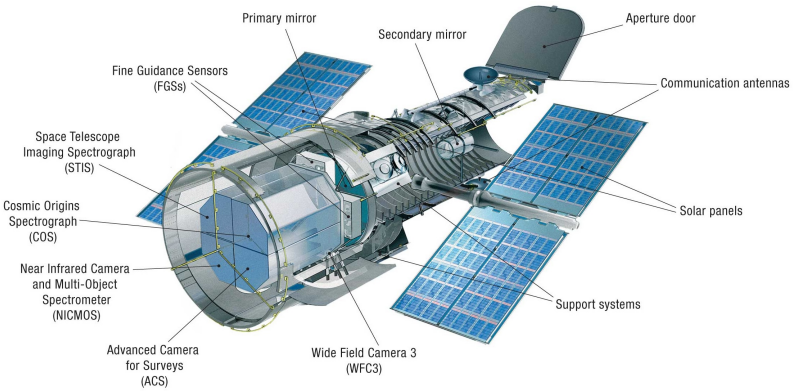

FIGURE 2.5: Diagram showing the locations of *Hubble Space Telescope*'s instruments inside the spacecraft. Credit:NASA, ESA.

NASA launched *HST* in April 1990 and since then it has been on a geocentric orbit about $537 - 541$ km in altitude and completing a full revolution around Earth every 95 minutes approximately. The telescope features a primary (2.4 m) and a secondary (30.5 cm) mirror (both coated with pure aluminum and magnesium fluoride layers) reflecting light into possibly five different science instruments: the Advanced Camera for Surveys (ACS), the Wide

[5]Although it will be soon shut down, early 2025, transitioning toward the end of life.

Field Camera 3 (WFC3), the Cosmic Origins Spectrograph (COS), the Space Telescope Imaging Spectrograph (STIS) and Fine Guidance Sensors (FGS). Figure 2.5 shows a sketch of the telescopes with the main components labeled.

The telescope was designed to observe in a wide range of wavelengths, from the near-IR (with NICMOS, decommissioned in 2008) to the optical and UV (with ACS and WFC3). In particular, in this thesis, I used data from the ACS (for the survey carried out by Sarajedini et al. 2007, see Chapter 7) and the WFC3 (used in synergy with ACS data to collect multi-epoch observations of the same sources and derive their sky velocities, see Bellini et al. 2017; Libralato et al. 2022 and Chapter 8). I will thus provide a brief overview of those instruments, while I refer the interested reader to the aforementioned papers for details on the observational setups and data reduction techniques.

The third generation instrument ACS (Sirianni et al., 2005) was installed in the Hubble Space Telescope on March 7, 2002 (during Servicing Mission 3B, SM3B). Its primary purpose was to increase *HST* imaging capabilities by a factor of 10, with a combination of detector area and quantum efficiency that surpassed previous instruments. ACS has three independent channels that provide wide field (ACS/WFC), high resolution[6] (ACS/HRC), and ultraviolet imaging respectively. In particular, the ACS/WFC employs a mosaic of two 4096×2048 CCDs attaining a spatial resolution of $\simeq 0.05$ arcsec/pixel, and resulting in a 202×202 arcsec^2 field of view. The camera is designed to observe from the near-IR to the UV using a broad assortment of filters.

The WFC3 is a fourth-generation imaging instrument. It was installed on the *HST* in May 2009 (during SM4) and became fully operational about one month later. The WFC3 features two independent channels, one sensitive at UV and optical wavelengths, approximately 200−1000 nm (the UVIS channel), and the other sensitive at near-IR wavelengths, approximately $800 - 1700$ nm (the IR channel). The UVIS channel mounts two 2051×4096 CCDs with a pixel scale of 0.04 arcsec/pixel and provides a 162×162 arcsec^2 rhomboidal FoV. On the other hand, the IR channel features a 136×123 arcsec^2 rectangular FoV sampled by a 1024×1024 pixel CCD, thus attaining a lower spatial resolution of 0.13 arcsec/pixel.

During the past 35 years of activity, thanks to its exquisite spatial resolution and wide filter selection, *HST* was instrumental in many science areas in astrophysics: from Solar system planet studies to the high-redshift Universe.

2.1.3 The Multi Unit Spectroscopic Explorer

MUSE (Bacon et al., 2010) is an Integral Field Spectrograph built for the Very Large Telescope (VLT) and commissioned by the European Southern Observatory. It has a modular structure composed of 24 integral-field units arranged in a near-contiguous field of view. Spectrally the instrument samples almost the full optical domain (in the wavelength range $465 - 930$ nm) with a mean resolution of 3000. *MUSE* could be supported by the VLT Adaptive Optics facility (Arsenault et al., 2008, via the GALACSI adaptive optics module, see Ströbele et al. 2012), offering both an adaptive-optics corrected field of view with 0.2 arcseconds sampling, and a 7.5×7.5 arcsec^2 FoV sampled at 0.025 arcsec/pixel (in the narrow field mode, NFM).

[6]Unavailable since January 2007 failure. Nonetheless, archival images prior to 2007 are still available for legacy science. They provide $\sim 0.028 \times 0.025$ arcsec^2/pixel spatial resolution observations in a 29×26 arcsec^2 field of view.

In the context of this thesis, *MUSE* data were used to complement *HST* observations of the very central regions of the GC 47 Tucanae (see Chapter 8). In particular, we used data from Kamann et al. (2018) collected using the wide field mode (WFM). In the WFM, the nominal spatial sampling of the sky is 0.2 arcsec/pixel. However, the actual spatial resolution is larger and wavelength dependent: the larger the wavelength the poorer the spatial resolution (for example, it is ~ 0.4 arcsec at 700 nm). The instrument FoV is $\simeq 1 \times 1$ arcmin covering the optical spectral range with variable spectral resolving power (ranging $1770 - 3590$ in the wavelength range $480 - 930$ nm). Concerning the specific observations used in Chapter 8, 47 Tucanae was observed with a mosaic of ten different pointings during seven epochs (to allow the detection of spectroscopic binaries through variable LOS velocity). Over the 6.4 hours of observations, 84558 spectra were collected for 19181 different stars (Kamann et al., 2018).

2.2 Numerical simulations of cluster internal dynamics

The modeling of stellar clusters through numerical simulations requires following the complex interplay of thermodynamic processes (such as energy and angular momentum transports through multiple distant stellar encounters, see section 1.3.2) with the physics of self-gravitating systems (see e.g., the recent review by Spurzem & Kamlah, 2023). In addition, the stochastic nature of star clusters having finite particle numbers (referred to as the "granularity" of the gravitational potential), the evolution of single and binary stars, and the role of external tidal forces (see section 1.3.4) should be included to perform realistic simulations. Opposite to collisionless systems, following the dynamical evolution of collisional ones (i.e., systems whose evolution is mainly driven by two-body interactions, see section 1.3.2) typically requires an energy accuracy of about $\Delta E/E < 10^{-5}$ per crossing time. Such high accuracy should be attained over very long integration times, usually of the order of $\gtrsim 10^3\, t_{\rm cr}$. At the same time, high central densities (e.g., those attained by GCs during their evolution) favor the formation of binaries and possibly direct stellar collisions.

During my Ph.D. I delved into two main aspects involving numerical simulations: *i)* the analysis of a set of Monte Carlo simulations (Della Croce et al., 2024c, presented in Chapter 7); *ii)* the comparison between observations and direct N-body simulations (e.g., Chapters 3, and 4, presented in Livernois et al. 2021). In the following, I shall thus briefly summarize the numerical methods and specifics of those simulations. We refer the reader to Spurzem & Kamlah (2023) for an interesting review of the developments of numerical methods for star clusters simulations, and on different numerical techniques and codes available.

The Monte Carlo simulations presented in Chapter 7 (see Bhat et al., 2024; Della Croce et al., 2024c) were performed with the MOCCA code (Giersz, 1998), which is a Henon-like Monte Carlo (Hénon, 1971a,b) code to simulate the long-term evolution of dense stellar systems. The method uses the constants of motion of a star in spherically symmetric potentials (i.e., energy and angular momentum) to quickly predict the star's orbit. Perturbations on the constants of motion due to multiple encounters are then evaluated for each star. The method was later extended to include binaries and stellar evolution (Stodolkiewicz, 1986). The MOCCA code features star-by-star modeling (much like N-body), where every star is a particle in the simulation. Comparison with direct N-body codes proved the reliability of MOCCA to simulate star cluster evolution (Giersz et al., 2013, 2015), and it has been since

used to perform a large number of studies (Hong et al., 2020; Leveque et al., 2021, 2022b, 2023). Despite the method limitations (i.e., smooth, strictly spherical potential, Spurzem & Kamlah 2023), Monte Carlo simulations can model the evolution of star clusters much faster than N-body ones, providing simulation sets from a grid of initial conditions and enabling comprehensive comparisons with observations.

Opposed to the Monte Carlo method, N-body simulations integrate the orbits of particles in time under their mutual gravitational interaction by directly solving the Poisson equation at the particle position. In N-body codes, force computation at each timestep is the most computationally expensive operation. Therefore, over the years, several algorithms, as well as special purpose chips (e.g., the `GRAPE` chips, Makino & Funato 1993; Makino et al. 1997; Makino & Taiji 1998; Makino et al. 2003), were developed to overcome this limitation and pave the way to one-million particle simulations of star clusters (e.g., Wang et al., 2016).

The most widely used direct N-body code in the field of stellar cluster simulations is `NBODY` developed by Sverre Aarseth (1963). For more than 50 years the code has been refined and improved and it is currently in its seventh version (i.e., `NBODY7`, Aarseth 2012, see Spurzem & Kamlah 2023 for a detailed presentation of the hardware and software developments over the years).

In Chapters 3, and 4 we used numerical simulations to interpret observations. In these studies (Della Croce et al., 2023, 2024b), we used the direct N-body simulations presented by Livernois et al. (2021), carried out with the GPU-accelerated version of the `NBODY6` code (Aarseth, 2003; Nitadori & Aarseth, 2012). The simulations were designed to model a star cluster with 10^5 particles spanning a wide range in stellar masses ($0.08 - 100$ $M_\odot$, sampled according to a Kroupa IMF), and orbiting within a Milky Way-like galaxy. Also, Livernois et al. (2021) explored the interplay between stellar interactions and both initial clumpy distributions and global stellar rotation as opposed to the monolithic, non-rotating case. Those simulations were thus well suited to provide further insights into the observed properties and evolution (see Della Croce et al., 2023, presented in Chapter 4), and into the evolution of out-of-equilibrium systems and possibly their observable properties (Della Croce et al., 2024b, further discussed in Chapter 3).

Part II

Formation and early evolution of star clusters

Chapter 3

Young star cluster kinematics

"Go on, go on and hurt the one that you love
Go on and make me the one that you want to hate
If it makes you feel better
Go on, go on and give me the best that you've got
Go on and make me the villain I'm not
If it makes you feel better"

Villan I'm not,
Three Days Grace

The response of star clusters to the gas removal and the subsequent expansion phase plays a critical role in the survival of bound stellar systems (see e.g., the discussion in section 1.2.2). Thanks to *Gaia* we are now probing expansion in several young star clusters and associations. In particular, Kuhn et al. (2019b) studied the kinematical properties of a sample of 28 young clusters (1 − 5 Myr) and associations by using *Gaia* DR2 PMs. According to those authors, observations are consistent with early cluster expansion driven by changes in the gravitational potential due to the dispersal of the molecular cloud. More recently, Guilherme-Garcia et al. (2023) investigated the kinematics of 1237 clusters using a technique that aims at reconstructing the underlying velocity field. They found 8 clusters that display rotation patterns (and an additional 9 candidates) and 14 clusters that show evidence of expansion in their velocity fields (and 15 candidates; Guilherme-Garcia et al., 2023). The vast majority of the expanding systems in their sample are younger than 100 Myr, with a peak around 10 Myr. While these studies provided important clues about the early evolution and survival of young clusters, the availability of more precise data from *Gaia* DR3 and the possibility to assess cluster membership more robustly would allow us to disentangle critical aspects related to their evolution.

In this Chapter, we present a comprehensive and systematic analysis of the kinematic properties of (virtually) all young stellar clusters ($t < 300$ Myr) identified so far in the MW (using the cluster catalog from Cantat-Gaudin & Anders, 2020; Cantat-Gaudin et al., 2020), with a particular focus on the early cluster expansion phase. Such a large sample provides an unprecedented opportunity to robustly constrain the timescale during which expansion has a prominent impact on the overall cluster kinematics. Also, it allows us to trace how expansion affects or is linked to the cluster properties and formation mechanisms.

The Chapter is organized as follows. In section 3.1 the cluster membership determinations and kinematic analyses are described. We present our results in section 3.2, and we compare them with numerical simulations in section 3.3. We assess the impact of different

age estimates on our results in section 3.4, and a detailed comparison with previous works is presented in section 3.5. Finally, conclusions are drawn in section 3.6.

The results presented in this Chapter are from Della Croce et al. (2024b, A&A, **683**, A10).

3.1 Data analysis

3.1.1 Revisiting cluster member catalogs

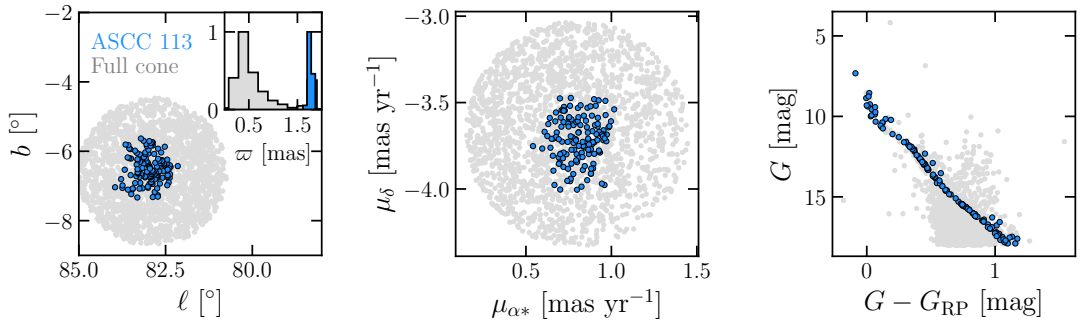

FIGURE 3.1: Astrometric and photometric properties of ASCC 113 members (shown in blue). In gray we show the properties of the initial sample of *Gaia* sources. The left panel shows the distributions in Galactic coordinates and parallax (top-right corner), the middle panel the PM distribution, and the right panel the CMD. The parallax distributions were scaled for visualization purposes only.

The present work makes use of the list of clusters identified by Cantat-Gaudin et al. (2020) using *Gaia* DR2 data. We focused on systems younger than $\leq$ 300 Myr (according to age estimates by Cantat-Gaudin et al., 2020) to investigate the evolution of star clusters in their very early stages. In this way, we selected 1179 clusters out of 2017 in the original catalog.

To take full advantage of the most recent and accurate *Gaia* DR3 data release for the definition of cluster member stars, we performed an independent membership analysis. For every cluster, we retrieved *Gaia* DR3 data for sources brighter than $G = 18$ and that have a five-parameter solution (i.e., with sky position, proper motions, and parallax measurements). In particular, every query was centered on the cluster's centroid (as reported by Cantat-Gaudin et al. 2020) and the search radius was defined as $R_{\rm search,\,sky} \equiv 2R_{95,\,\rm sky}$, where $R_{95,\,\rm sky}$ is the radius enclosing 95% of the member stars reported by Cantat-Gaudin et al. (2020).

For each cluster, we then selected stars according to their motion with respect to the cluster's bulk motion. Only sources within $R_{\rm search,\,PM} \equiv 2\,R_{95,\,\rm PM}$, with $R_{95,\,\rm PM}$ being a circle in PM space that encloses 95% of the members, were retained in the subsequent analysis. We did not apply any preliminary parallax selection. These selections allowed us to include all the previously listed members in our starting *Gaia* DR3 catalog.

We performed the clustering analysis in the five-dimensional space of Galactic coordinates, proper motions, and parallax (i.e., ℓ, b, $\mu_{\alpha*}$, μ_δ, and ϖ). Since we are dealing

with heterogeneous quantities, we preliminary scaled them all, so that the mean and standard deviation of their distributions are equal to zero and one, respectively. We used the `StandardScaler` provided by the Python library `sklearn`. We then performed an unsupervised clustering analysis on the scaled coordinates by means of the `HDBSCAN` (McInnes et al., 2017) algorithm.

Based on the results of several tests, we set the algorithm's parameters as follows:

$$\texttt{min\_cluster\_size} = \begin{cases} 20 & \text{for } N_{\rm CG20} < 100\,, \\ \frac{N_{\rm CG20}-100}{10} + 50 & \text{for } N_{\rm CG20} \geq 100\,, \end{cases} \tag{3.1}$$

and

$$\texttt{min\_samples} = \begin{cases} 5 & \text{for } N_{\rm CG20} < 100\,, \\ 10 & \text{for } N_{\rm CG20} \geq 100\,, \end{cases} \tag{3.2}$$

where $N_{\rm CG20}$ is the number of member stars reported by Cantat-Gaudin et al. (2020). These parameters appeared to be best suited for the unsupervised search for members in star clusters characterized by significantly different extensions ($R_{\rm search,\,sky}$), velocity distributions ($R_{\rm search,\,PM}$) and number of likely members ($N_{\rm CG20}$).

As a test case, in figure 3.1 we show the spatial, parallax, PM, and color-magnitude diagram (CMD) distributions for the selected members of ASCC 113 (whose kinematic properties are presented in figure 3.5). As expected, selected member stars are clustered in the five-dimensional astrometric space (i.e., ℓ; b; ϖ; $\mu_{\alpha*}$; μ_δ). Also, they exhibit a well-defined, cluster-like sequence in the CMD, thereby confirming the ability of our clustering analysis to recover stellar cluster members among field stars.

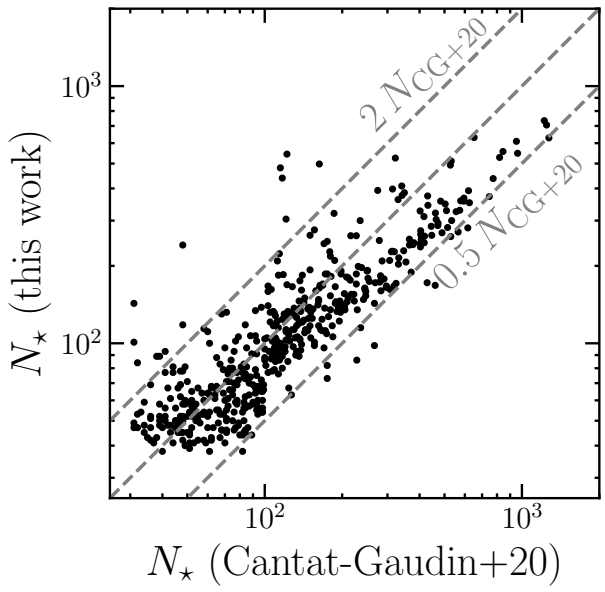

FIGURE 3.2: Comparison of member stars between this work and Cantat-Gaudin et al. (2020, $N_{\rm GC+20}$) for all the clusters included in the analysis. Diagonal lines show the one-to-one relation and the relations corresponding to half and twice the members (as also reported in the plot).

While running the procedure for all the clusters in the sample, we found that the algorithm performed poorly on clusters with only a few member stars ($N_{CG20} < 30$). This is probably due to the choice of `min_cluster_size`, which sets a lower limit to the number of member stars in our search for star clusters. However, since the kinematic analysis strongly benefits from the availability of relatively large samples of individual velocities, we decided to exclude these clusters from our analysis. In this way, we ended up with a final sample of 949 clusters for which the clustering analysis was performed.

figure 3.2 shows a direct comparison between the number of member stars obtained by using *Gaia* DR3 and that found by Cantat-Gaudin et al. (2020). While some differences are expected due to the different adopted clustering algorithms and *Gaia* data releases, figure 3.2 shows an overall agreement between the two compilations.

3.1.2 Measuring cluster expansion

First, we accounted for perspective effects induced by the cluster bulk motion following the equations reported by van Leeuwen (2009). To this aim, systemic LOS velocities from Tarricq et al. (2021) were used. Only 509 out of 949 clusters (see section 3.1.1) had reported LOS velocity and were thus retained in the subsequent analysis.

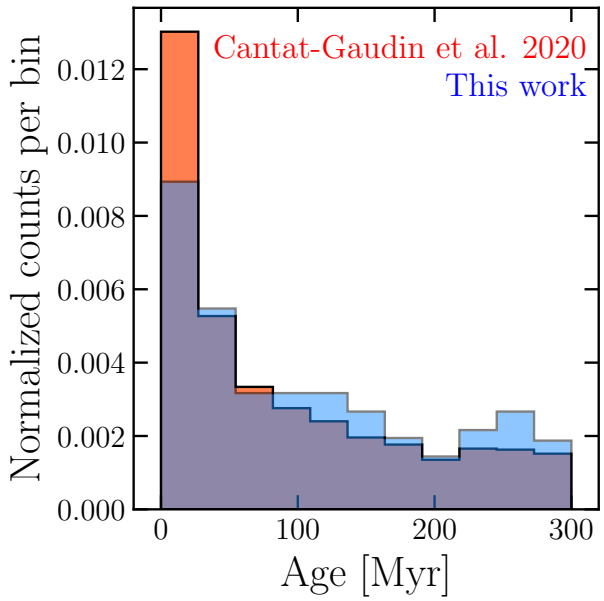

FIGURE 3.3: Age distributions for clusters in the starting catalog (in red, Cantat-Gaudin et al., 2020) and those retained in the kinematic analysis (in blue). Histograms were normalized such that their areas sum to unity.

In figure 3.3 we compare the age distributions within 300 Myr of the original catalog and the final sample of clusters. The distributions populate the investigated age range in a similar fashion and our final sample of 509 clusters is representative of the initial age distribution.

We then used stars with a membership probability larger than 70% based on the clustering analysis performed in this work (section 3.1.1). We also selected cluster members with `ruwe` ≤ 1.375, `astrometric_gof_al` ≤ 1, and `astrometric_excess_noise` ≤ 1 mas (if `astrometric_excess_noise_sig` > 2), thus excluding stars for which the standard five-parameter solution did not provide a reliable fit of the observed data (Lindegren et al., 2021a).

We inferred the mean radial velocity, $\langle v_{\rm R} \rangle$, and the radial velocity dispersion, $\sigma_{\rm R}$, in a fully Bayesian framework properly accounting for errors on individual velocities. We explored the parameters space employing a Markov chain Monte Carlo (MCMC) technique. In particular, we used the Python package `emcee`[1] (Foreman-Mackey et al., 2013), which provides a Python implementation of the affine-invariant MCMC sampler, enabling us to sample the posterior distribution. For each system, we assumed the likelihood (Pryor & Meylan, 1993)

$$\ln \mathcal{L} = -0.5 \sum_{\rm k} \left[\frac{(v_{\rm R,k} - \langle v_{\rm R} \rangle)^2}{e_{\rm R,k}^2 + \sigma_{\rm R}^2} + \ln(e_{\rm R,k}^2 + \sigma_{\rm R}^2) \right] , \tag{3.3}$$

with $v_{\rm R,k}$ and $e_{\rm R,k}$ being the radial velocity and the respective error of the k-th member. equation 3.3 assumes that the intrinsic distribution along the radial component of the velocity is a Gaussian with mean $\langle v_{\rm R} \rangle$ and velocity dispersion $\sigma_{\rm R}$. We used uniform priors within $[-10; +10]$ mas yr^{-1} and $[0.001; 15]$ mas yr^{-1} for $\langle v_{\rm R} \rangle$ and $\sigma_{\rm R}$, respectively. For each cluster, we initialized 50 walkers and ran the algorithm for 500 steps, which was found to be sufficient for both ensuring convergence (for which the first half of samples was discarded) and accounting for correlations between samples (typically on the order of 20). Median values and 16% and 84% quantiles (corresponding to the 1σ interval if the distributions were Gaussian) were then computed for each quantity directly from posterior samples. The kinematical analysis was performed by adopting the clusters' geometric center, defined as the median of the positions of member stars.

3.2 Results on the expansion of young star clusters

Figure 3.4 shows the ratio between the mean radial velocity and the radial velocity dispersion (hereafter $\langle v_{\rm R} \rangle / \sigma_{\rm R}$) as a function of clusters' ages from Cantat-Gaudin et al. (2020). This quantity provides an indication of the amplitude of the ordered to the disordered motion of stars along the radial component, thus directly tracing ongoing expansion or contraction. A positive value of $\langle v_{\rm R} \rangle / \sigma_{\rm R}$ implies expansion.

The first key result highlighted by figure 3.4 is that about 80% of clusters younger than $\sim$ 30 Myr show positive $\langle v_{\rm R} \rangle / \sigma_{\rm R}$ values. More in general, the total fraction of young ($<$ 30 Myr) systems having positive $\langle v_{\rm R} \rangle / \sigma_{\rm R}$ at the 3σ level is 43% (see table 3.2 for the fraction of expanding systems in different age bins). The distribution attains maximum values $\langle v_{\rm R} \rangle / \sigma_{\rm R} = 1.5 - 2$ (such clusters typically have $\langle v_{\rm R} \rangle \sim 2$ km s^{-1}) for clusters with age $\sim$ 10 Myr. Then it progressively decreases. For clusters older than $\sim$ 30 Myr, the distribution of $\langle v_{\rm R} \rangle / \sigma_{\rm R}$ flattens around 0 and it shows an intrinsic standard deviation of about 0.2 (corresponding to $\langle v_{\rm R} \rangle \lesssim 0.1$ km s^{-1}). Such a clear trend allows us to identify for the first time the timescale (of about 30 Myr) during which expansion plays a significant role in the overall cluster kinematics. We verified that these results do not change significantly if different age estimates were adopted (see section 3.4).

In the left panel of figure 3.4 clusters are color-coded according to the number of member stars. We note that the amplitude of the scatter around zero observed in systems older than 30 Myr strongly depends on the number of members identified. Results of numerical experiments of equilibrium stellar clusters (see section 3.3.2) suggest that the observed spread

[1]The library is available at `https://emcee.readthedocs.io/en/stable/`.

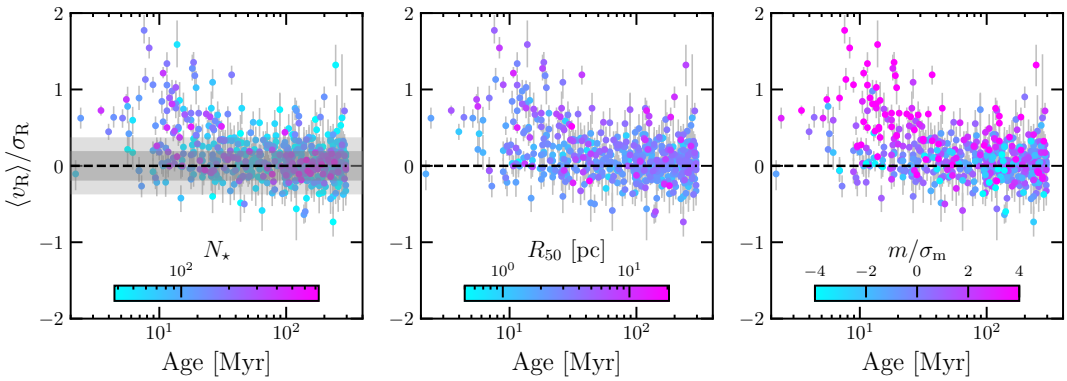

FIGURE 3.4: Ratio between the mean radial velocity and the radial velocity dispersion for clusters younger than 300 Myr (according to Cantat-Gaudin et al., 2020). Errors on the y-axes were obtained directly from the MCMC samples, and ages are from Cantat-Gaudin et al. (2020). In the left panel, clusters are color-coded according to the number of members. The standard deviation (and twice the value) of the $\langle v_R \rangle / \sigma_R$ ratio obtained from numerical realizations of equilibrium star clusters (see section 3.3.2) are shown as gray-shaded areas. Values obtained from numerical realizations were convolved with the median observational error to allow for a direct comparison with the underlying data. In the middle panel, colors depict R_{50}, whereas in the right panel, the color coding represents the ratio between the slope and the corresponding error from the linear regression of radial velocities as a function of cluster-centric distance.

around zero can be largely explained in terms of statistical fluctuations due to a low number of stars (gray shaded area in figure 3.4). This in turn confirms that the distribution observed for older clusters is consistent with what is expected for systems in equilibrium.

Most of the young (< 30 Myr) clusters with clear ongoing expansion are characterized by some of the largest values (up to ~ 10 pc) of R_{50} (figure 3.4, middle panel). We note that among the expanding systems, those with smaller R_{50} values preferentially attain smaller $\langle v_R \rangle / \sigma_R$ by up to a factor of 2. Finally, the old expanding clusters (> 30 Myr) typically have fewer members and greater extensions, suggesting that they might have been expanding for several tens of megayears.

Furthermore, we performed a linear fit to the distribution of v_R as a function of the cluster-centric distance for each cluster and we derived the angular coefficient m and its relative error σ_m. Interestingly, we found that the majority of the expanding clusters show a positive and significant ($m/\sigma_m \geq 3$) ranking in their v_R distributions as a function of their positions in the cluster (see the right panel of figure 3.4). These patterns could suggest that young expanding clusters are likely losing a fraction of their original mass as stars in the outskirts become unbound. However, we note in passing that this does not necessarily imply that all the expanding clusters will become unbound. In fact, stars in the external regions moving away from the cluster can produce a positive slope even if the inner parts are not expanding.

Finally, we present the kinematic properties of a few prototypical systems in figure 3.5. We selected two young (< 30 Myr) clusters, namely NGC 6193 and NGC 4103, and two older systems, LP 2219 and NGC 3114. Within each group, we picked one system showing significant evidence of expansion (NGC 6193 and LP 2219), whereas the other one is compatible with equilibrium (NGC 4103 and NGC 3114). Relevant cluster properties are reported in table 3.1 for reference.

TABLE 3.1: Main properties of the four clusters whose kinematic features are shown in figure 3.1.

Cluster name	$\langle v_R \rangle / \sigma_R$	$N_\star$	Age [Myr]	R_{50} [pc]
NGC 6193	$0.62^{+0.12}_{-0.13}$	93	5	$2.0^{+0.1}_{-0.2}$
NGC 4103	$-0.04^{+0.08}_{-0.08}$	148	21	$1.7^{+0.2}_{-0.1}$
LP 2219	$0.56^{+0.10}_{-0.11}$	128	126	$6.8^{+0.3}_{-0.5}$
NGC 3114	$0.08^{+0.05}_{-0.05}$	501	145	$4.5^{+0.2}_{-0.1}$

Notes. From left to right: cluster name, the ratio between the mean radial velocity and the radial velocity dispersion, number of members, cluster age (according to Cantat-Gaudin et al., 2020), and radius enclosing half of the members. Errors on $\langle v_R \rangle / \sigma_R$ are directly obtained from the MCMC sampling of the posterior distribution, whereas errors on R_{50} are obtained by bootstrap resampling the radial distribution of stellar members. The values reported correspond to the 16th and 84th percentiles of the distributions (i.e., corresponding to the 1σ value if the distributions were Gaussian).

In particular, the left panels of figure 3.5 show the spatial distribution of members used to compute $\langle v_R \rangle / \sigma_R$ (see figure 3.4), as well as the velocity vectors on the plane of the sky. Arrow lengths are proportional to their total speeds whereas the color coding traces the amplitude of the radial velocity component (figure 3.5). Right panels, on the other hand, show the distribution of individual velocities as a function of the cluster-centric distance. The linear regression used to obtain the m/σ_m parameter (see figure 3.4) is also shown and the value of the slope is reported. To ease the comparison, spatial coordinates are scaled to R_{50} for each cluster, and their velocities are shown in the same velocity scale.

Expanding clusters (NGC 6193 and LP 2219) show a preferential alignment of velocity vectors along the positive (i.e., pointing outward) radial direction, as highlighted by the color coding (figure 3.5). This feature is particularly evident in the external regions. A clear trend is also observed in v_R versus R distribution, and it is reflected in the positive value of the slope from the linear regression (as already pointed out in figure 3.4).

Non-expanding clusters (NGC 4103 and NGC 3114), on the other hand, present radial velocities that are scattered around zero, without any preferential alignment along the radial direction or significant radial trend. All these features are consistent with the systems being in equilibrium.

Lastly, we looked for any dependence of the expansion properties on the cluster masses. In particular, we crossmatched our cluster catalog with the recent compilation of cluster masses provided by (Almeida et al., 2023). We found 227 clusters in common. For those clusters, we

show $\langle v_R \rangle / \sigma_R$ as a function of cluster age, color-coded according to the mass reported by Almeida et al. (2023, see figure 3.6 in this work). Qualitatively, expansion affects clusters of any mass, from about 10^2 $M_\odot$ to a few times 10^3 $M_\odot$. To elaborate more on this point, we split the population of clusters younger than 30 Myr (45 clusters) into two subsamples: expanding (27 clusters, about 60% of the sample) and non-expanding clusters (18 out of 45 systems, i.e., 40%). For the purpose of this analysis, we classified a cluster to be expanding if the expansion signal is significant at the 1σ level. The only purpose here is to obtain two almost equally populated samples of clusters. We then compared the mass distribution of the two subpopulations with each other and with the full sample of young clusters. A Kolmogorov-Smirnov test shows that there is no significant statistical difference between the three populations. Although based on a few dozen clusters, this result suggests that the physical processes driving the expansion of star clusters in their early stages of formation and evolution are effective irrespective of the cluster mass.

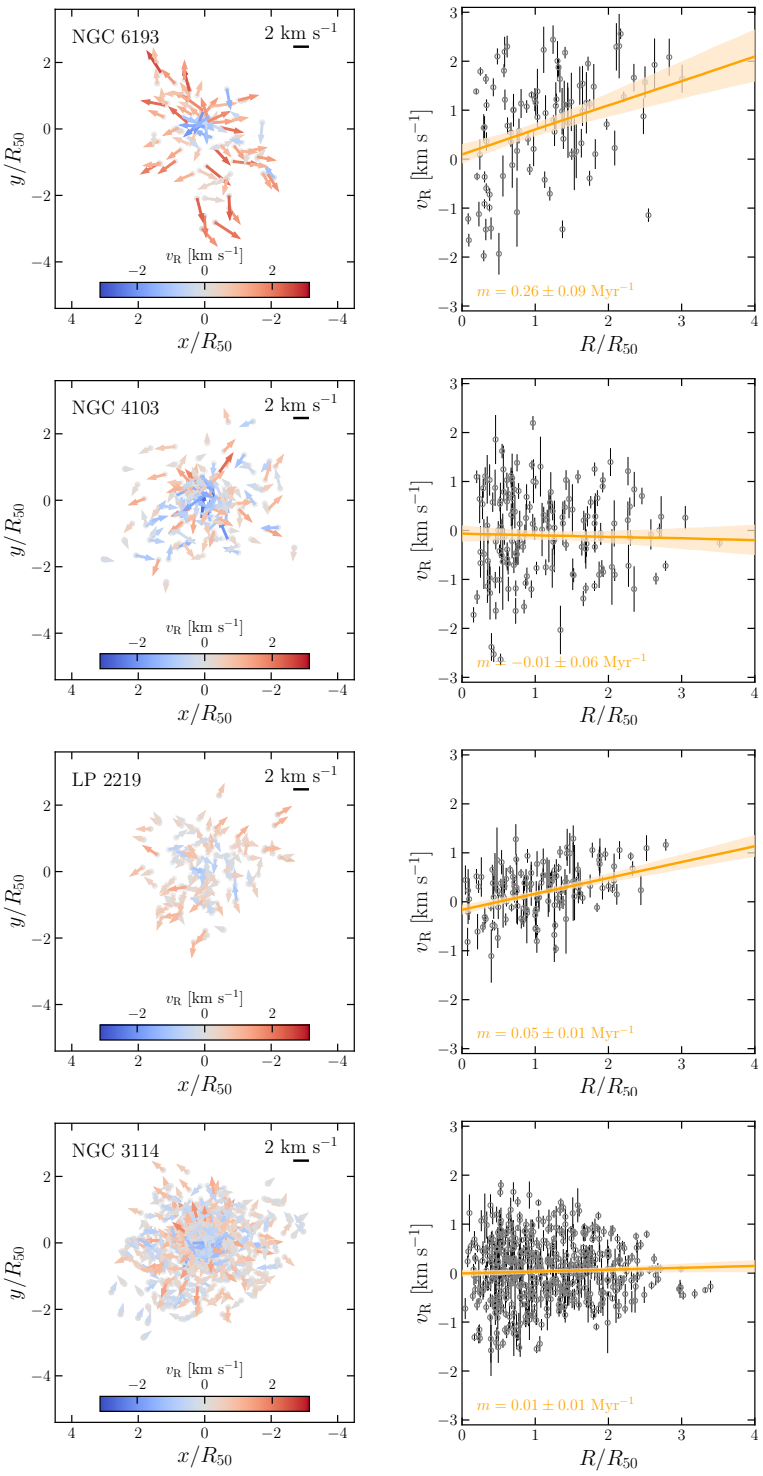

FIGURE 3.5: Kinematic properties of NGC 6139, NGC 4103, LP 2219, and NGC 3114 (from top to bottom). The left panels show the spatial distribution of members in Cartesian coordinates normalized to the radius enclosing half of the members, with arrows showing the velocity vectors on the plane of the sky. The arrow lengths are proportional to the speed on the plane of the sky (velocity scale reported in the top-right corners), while their colors map the radial component (v_R) of the velocity. Positive values point outward. The right panels show the distribution of members in the $v_R - R$ plane. The linear regressions of velocities as a function of the cluster-centric distances are shown (orange lines), as are the posterior values on the slopes (at the bottom).

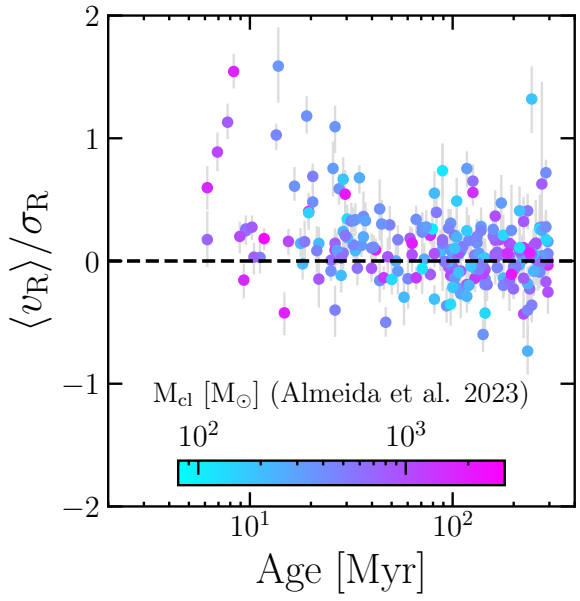

FIGURE 3.6: Distribution of $\langle v_R \rangle / \sigma_R$ as a function of the age for the 227 clusters in common with Almeida et al. (2023). The color coding depicts the cluster mass, M_{cl}.

3.3 Comparison with numerical simulations

3.3.1 *N*-body simulations of cluster formation

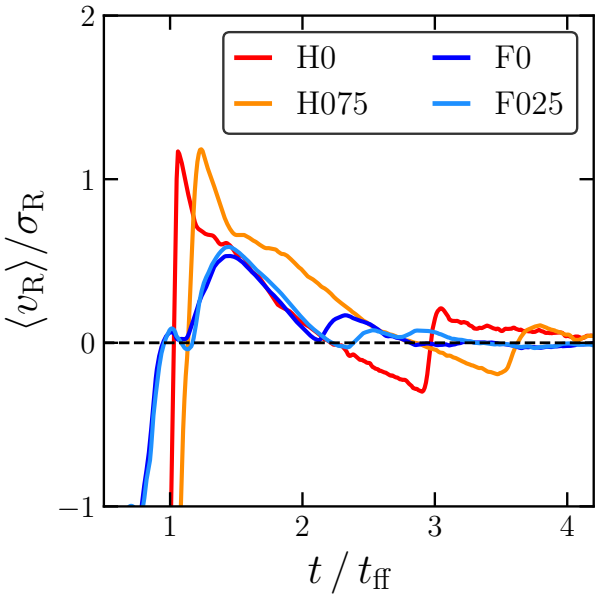

FIGURE 3.7: Time evolution of the ratio between the mean radial velocity and the radial velocity dispersions for a selection of models from Livernois et al. (2021) for all stars within the tidal radius.

In this section, we present a brief analysis of a few *N*-body simulations of young star clusters undergoing the violent relaxation phase and evolving toward their final virial equilibrium

state. The goal here is to illustrate the time evolution of their global expansion pattern and establish a general connection with the observational results presented in the previous sections. The simulations considered here are part of the suite discussed in detail in Livernois et al. (2021) who explored the early evolution of systems starting with the homogeneous or fractal spatial distribution and investigated the role of initial rotation on the cluster's early evolutionary phases. Here we focus on four models: two models with homogeneous initial spatial distributions, one without and one with rotation (hereafter referred to as H0 and H075, respectively; see Livernois et al., 2021, for further details about the initial conditions) and two models with an initial fractal spatial distribution without and with the initial rotation (hereafter F0 and F025). figure 3.7 shows the time evolution of $\langle v_{\rm R} \rangle / \sigma_{\rm R}$ for the selected models as obtained by using all stars in the system within the tidal radius. All models show an initial contracting phase followed by significant expansion. The initially homogeneous models display more rapid and extreme collapse and expansion phases than the initially fractal models as the clumps within these models merge and interact with other clumps before arriving at the center of the system Although these specific models do not reach the extreme values of $\langle v_{\rm R} \rangle / \sigma_{\rm R}$ found in our study (figure 3.4), the range of expansion values found in these simulations spans those attained by most of the observed clusters, thus suggesting that violent relaxation can play a key role in triggering and driving early cluster expansion. We emphasize that the idealized models presented here are included just to illustrate the general kinematic behavior during these early evolutionary phases and they are not meant to provide a detailed fit to the observational data. Different initial conditions and more realistic simulations including additional processes such as gas expulsion and mass loss due to stellar evolution might be necessary to reach the most extreme values found in the observational sample and to constrain the range of timescales of the early expansion, of the settling to the final equilibrium as well as the timescale associated with the possible cluster's dissolution. We note also that the theoretical lines shown in figure 3.7 represent the evolutionary path of the $\langle v_{\rm R} \rangle / \sigma_{\rm R}$ ratio of clusters surviving the early evolutionary phases. We point out that it is likely that not all the clusters with age < 30 Myr in the observational sample will follow this path as some of them will continue expanding and will eventually dissolve.

3.3.2 Distribution of $\langle v_{\rm R} \rangle / \sigma_{\rm R}$ for star clusters in equilibrium

The results presented in figure 3.4 suggest that, for $t > 30$ Myr, the distribution of the $\langle v_{\rm R} \rangle / \sigma_{\rm R}$ is compatible with what is expected for clusters in equilibrium and that the broadening of the distribution might be mostly driven by statistical fluctuations.

To check whether this is indeed the case, we created 100 random realizations of a population of clusters. Each population contains the same number of clusters as in our observed sample and in each realization the clusters have the same number of stars as in the observed sample. Positions and velocity of stars in each cluster follow those of a King model with central dimensionless potential $W_0 = 5$ (but the results do not have any significant dependence on the particular model adopted). For each realization, we then calculated the dispersion in the distribution of the values of $\langle v_{\rm R} \rangle / \sigma_{\rm R}$ of the clusters in the sample. The average value of the dispersion found in the 100 realizations is equal to about 0.11 and is shown as a gray-shaded area in figure 3.4. The comparison demonstrates that 1) the spread observed for older systems can be largely accounted for by statistical fluctuations and 2) equilibrium models

cannot account for large positive $\langle v_R \rangle / \sigma_R$ (i.e., expansion) observed in clusters with $t < 30$ Myr and that those systems are therefore out of equilibrium.

We note, however, that the observed spread is larger (about a factor of 2) than that derived from the simulations. While these residuals might suggest that some of the clusters older than $\sim$ 30 Myr are still oscillating around equilibrium configurations, it is important to emphasize that in the analysis of the $\langle v_R \rangle / \sigma_R$ from the numerical realizations of cluster populations, not all the possible effects that can determine the spread of this quantity are included. They do not account, for example, for a number of possible uncertainties associated with the observational data such as the uncertainties induced by wrong LOS systemic velocities (mainly due to low-number statistics). Further investigation is needed to properly study this issue.

3.4 Testing the impact of different age estimates

The reference age compilation adopted in this analysis is the one by Cantat-Gaudin et al. (2020). Here we test the robustness of our results against different compilations of clusters ages from literature. In particular, we used cluster ages obtained by Kharchenko et al. (2013), Bossini et al. (2019), and Dias et al. (2021) determined ages for several star clusters in our Galaxy through isochrone fitting. We note that Kharchenko et al. (2013) exploited pre-main-sequence stars as a further age indicator to obtain more reliable ages in the young end. Hunt & Reffert (2023), performed an all-sky search for OCs and they provided ages for every cluster in their sample obtained by means of a convolutional neural network. We crossmatched the sample of 509 clusters adopted in this study with these catalogs.

Figure 3.8 shows the distribution of $\langle v_R \rangle / \sigma_R$ as a function of age (as in figure 3.4) for the clusters in common with the four compilations. Also, in table 3.2 we report the fractions (as well as the total numbers) of clusters exhibiting evidence (at the 3σ level) of expansion in different age bins. Although different catalogs span different age ranges for the same clusters, the trend of expanding clusters for ages below $\simeq$ 30 Myr is clearly visible in all the catalogs. This test demonstrates that the results presented in the manuscript are robust against different age estimates, also in terms of timescale during which expansion has an important role in cluster kinematics.

3.5 Comparison with previous works

Kuhn et al. (2019b) investigated the expansion properties of twenty-eight stellar clusters and associations, concluding that at least 75% of clusters in their sample are expanding. Among the clusters in common, we find a significant expansion for NGC 1893, NGC 2244, and NGC 2362 and a mild expansion for IC 348 and NGC 6231, consistent with the results by Kuhn et al. (2019b) for these systems.

Recently, Guilherme-Garcia et al. (2023) investigated the internal kinematics of many OCs. In particular, they identified expansion in 14 clusters with 15 more candidates. Among the 14 expanding clusters, 5 were not included in our study, namely Alessi 13, Aveni Hunter 1, Collinder 132 (as they have fewer than 30 members in our catalog; see section 3.1.1), Ruprecht 98, and Stock 1 (as they are older than 300 Myr according to Cantat-Gaudin et al. 2020). For all the others, we confirm their state of significant expansion, with the only exception of

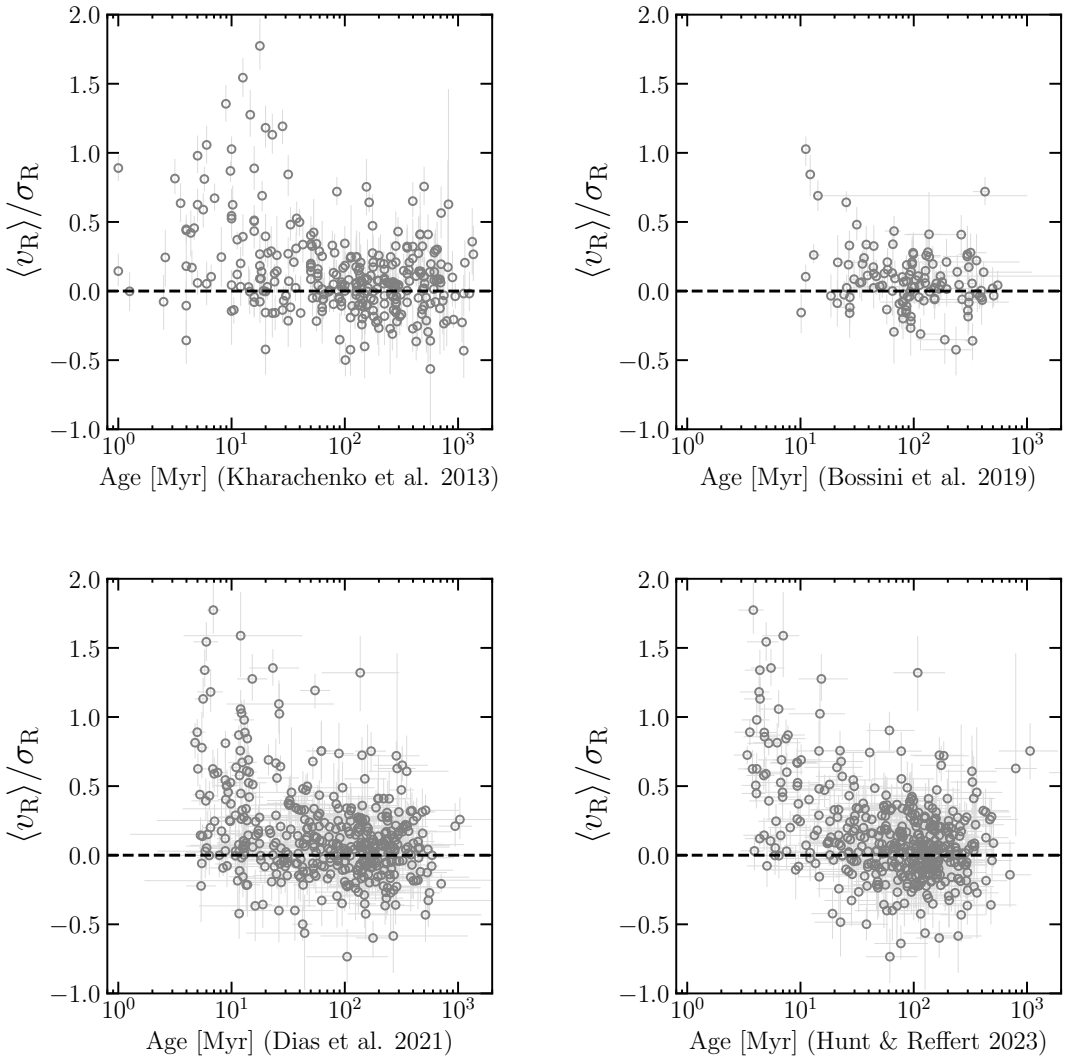

FIGURE 3.8: Mean radial velocity to radial velocity dispersion ratio as a function of cluster age for different age estimates (from left to right): Kharchenko et al. (2013), Bossini et al. (2019), Dias et al. (2021), and Hunt & Reffert (2023). Errors on the y-axis are obtained from the MCMC sampling of the posterior, while those on the x-axis (if present) are age errors provided by the different catalogs. The zero-level expansion is marked by the dark dashed line.

BH 164, for which we derived $\langle v_R \rangle / \sigma_R \simeq +0.13^{+0.10}_{-0.11}$. Among the 15 candidates, according to our analysis we confirm that IC 1805 ($\langle v_R \rangle / \sigma_R \simeq +1.77^{+0.20}_{-0.17}$), Roslund 2 ($\langle v_R \rangle / \sigma_R \simeq +1.06^{+0.14}_{-0.14}$), Trumpler 16 ($\langle v_R \rangle / \sigma_R \simeq +0.81^{+0.15}_{-0.10}$), and vdBergh 92 ($\langle v_R \rangle / \sigma_R \simeq +1.13^{+0.15}_{-0.14}$) are expanding, whereas ASCC 127 ($\langle v_R \rangle / \sigma_R \simeq -0.02^{+0.15}_{-0.13}$), and BH 99 ($\langle v_R \rangle / \sigma_R \simeq -0.075^{+0.081}_{-0.080}$) are not. In addition to differences in specific systems, we note that in our analysis we found a significantly larger sample of expanding clusters than Guilherme-Garcia et al. (2023). This is probably due to different approaches and membership probabilities that are based on *Gaia* DR3 data (section 3.1.1) in our case and DR2 in the case of

TABLE 3.2: Fraction of expanding clusters.

Ref. ages compilation	≤ 10 Myr	$(10; 30]$ Myr	$(30; 50]$ Myr	> 50 Myr
Kharchenko et al. (2013)	17/32 ($\simeq$53%)	13/44 ($\simeq$30%)	4/14 ($\simeq$29%)	9/219 ($\simeq$4%)
Bossini et al. (2019)	–	6/18 ($\simeq$33%)	1/12 ($\simeq$8%)	2/93 ($\simeq$2%)
Cantat-Gaudin et al. (2020)	15/28 ($\simeq$54%)	43/108 ($\simeq$40%)	5/53 ($\simeq$9%)	14/320 ($\simeq$4%)
Dias et al. (2021)	21/41 ($\simeq$51%)	28/83 ($\simeq$34%)	4/43 ($\simeq$9%)	12/226 ($\simeq$5%)
Hunt & Reffert (2023)	34/51 ($\simeq$67%)	15/57 ($\simeq$26%)	1/39 ($\simeq$3%)	11/302 ($\simeq$4%)

Notes. The fraction and the absolute number of clusters that show significant expansion (at the 3σ level). Values are reported in four age bins, namely ≤ 10 Myr, between $10-30$ Myr, between $30-50$ Myr, and > 50 Myr, according to five different age compilations (left column). The only exception is the catalog of Bossini et al. (2019) for which we did not have any cluster younger than 10 Myr in common.

Guilherme-Garcia et al. (2023).

Besides dedicated studies (such as Kuhn et al., 2019b; Guilherme-Garcia et al., 2023), evidence of expansion was found in several works. For instance, Bravi et al. (2018) investigated the kinematical properties of four young ($\gtrsim 30$ Myr) OCs, namely IC 2602, IC 2391, IC 4665, and NGC 2547. They found that all the clusters but IC 4665 (for which they only put an upper limit) are super virial, concluding that this is consistent with the residual gas expulsion scenario. Clusters indeed expand eventually returning to an equilibrium state after unbound stars are dispersed. This process might take several tens of system crossing times (Baumgardt & Kroupa, 2007). Consistently, we found that all these four clusters show slow expansion speeds (typically $\langle v_{\rm R} \rangle / \sigma_{\rm R} \lesssim 0.3 \pm 0.1$), suggesting they might be close to equilibrium.

Lim et al. (2020) studied the star-forming region W4, where the cluster IC 1805 is located. They found that the cluster is composed of an isotropic core and an external region showing clear evidence of expansion. These features suggest that the cluster is experiencing expansion after an early, initial collapsing phase (Lim et al., 2020). We also found a strong indication of expansion in IC 1805, although we did not find evidence for a central isotropic core in the cluster.

The cluster NGC 2244 lies at the center of the Rosette Nebula. The region shows a complex interplay between stellar and gas kinematics and feedback-driven star formation in sub-structured environments. Both rotation and expansion were found in NGC 2244 (Lim et al., 2021). In our study we also found NGC 2244 to be significantly expanding ($\langle v_{\rm R} \rangle / \sigma_{\rm R} \simeq +0.98^{+0.14}_{-0.13}$).

Pang et al. (2021b) investigated the connection between the cluster's internal kinematics and their morphology. They found younger clusters to exhibit filament-like substructures while older ones show tidal-tail features. The majority of the systems are inferred gravitationally unbound and expanding (Pang et al., 2021b). In the present study, mild expansion has been directly detected in NGC 2422, NGC 2451a, NGC 2451b, and NGC 2232. On the other hand, neither expansion nor contraction has been found in NGC 2516, which is suggested to be in a super virial state (Pang et al., 2021b). Investigating internal kinematic patterns, or

dependences on cluster morphology for each cluster is beyond the scope of this work. We defer this topic to a follow-up study.

In summary, the excellent agreement with previous, detailed studies that focused on a handful of systems suggests that our results are solid and that we are effectively probing the expansion of young stellar clusters.

3.6 Summary and conclusions

We performed a comprehensive analysis of the internal kinematics of young star clusters ($t < 300$ Myr) in the MW with the aim of reconstructing the key properties and possible physical mechanisms shaping the early cluster expansion. We emphasize that this analysis is based on a sample that is 20 times larger and spans a cluster age range 60 times larger than previous analyses (see, e.g., Kuhn et al., 2019b), thus enabling for the first time the possibility of constraining the timescale during which expansion has a dominant impact on cluster kinematics and the fraction of stellar systems significantly affected by the expansion.

Our analysis reveals a clear trend in which the fraction of expanding clusters increases for younger clusters (see table 3.2): a significant fraction of clusters younger than ∼30 Myr are characterized by a significant expansion, reaching values as large as $\langle v_{\rm R} \rangle / \sigma_{\rm R} = 1.5 - 2$. On the contrary, older clusters (t > 30 Myr) are mostly consistent with what is expected for systems in equilibrium. While it would be tempting to interpret the $\langle v_{\rm R} \rangle / \sigma_{\rm R}$ distribution as a function of time as an evolutionary sequence, we stress here that it represents an instantaneous picture of the current properties of stellar clusters and not a time evolution pattern. The results presented in this work would not significantly change if different catalogs of cluster ages were adopted.

A general comparison of the evolution of $\langle v_{\rm R} \rangle / \sigma_{\rm R}$ in N-body simulations following the violent relaxation and early dynamics of star clusters reveals $\langle v_{\rm R} \rangle / \sigma_{\rm R}$ values that span those found in most of the observed clusters. More realistic simulations that include additional processes (such as gas expulsion and mass loss due to stellar evolution) and explore a broader range of initial conditions will be required to explain the most extreme cases of expanding systems ($\langle v_{\rm R} \rangle / \sigma_{\rm R} > 1.5 - 2$) sampled by our observational analysis and for a more detailed and quantitative comparison of the observed kinematic patterns and the timescales associated with the early evolution. Finally, we note that extremely young clusters (with ages of less than a few megayears) not included in our sample would be necessary to probe the kinematic patterns associated with the systems' very early dynamics. The lack of these systems is likely a selection effect, as they are probably embedded clusters that are harder to observe with *Gaia*. In this respect, future data from infrared surveys would provide relevant insights into the embedded cluster population (see for example the VISIONS survey; Meingast et al., 2023) and allow us to build a more complete dynamical picture of the evolution of these systems.

Chapter 4

LISCA II: a hierarchical structure in the Perseus complex

> " 'I wish it need not have happened in my time,' said Frodo. 'So do I,' said Gandalf, 'and so do all who live to see such times. But that is not for them to decide. All we have to decide is what to do with the time that is given to us.' "
>
> The Lord of the Rings,
> J.R.R. Tolkien

The study presented in the previous Chapter showed that young ($\lesssim$ 30 Myr) star clusters can exhibit significant expansion. Older systems likely survived this stage and potentially lost a fraction of their mass. However, we treated star clusters as isolated entities, while there is increasing evidence that star clusters do not evolve in isolation but are often characterized by a complex and clumpy structure (Kuhn et al., 2019b, 2020; Getman et al., 2019; Lim et al., 2020; Zeidler et al., 2021). While some of these systems will dissolve, some may evolve into massive and long-lived clusters.

Interestingly in this context, Dalessandro et al. (2021b) have found that the well-known clusters h and χ Persei are in an association of clusters embedded in a wide stellar halo of similar age. This structure, named LISCA I (where LISCA stands for "Lively Infancy of Star Clusters and Associations"), provided the first detailed observational picture of an ongoing massive cluster hierarchical assembly (see section 1.2.5). This is the first time such a formation mechanism has been identified in the MW, thus having important implications for our understanding of the environmental conditions (both locally and in the distant Universe) necessary to form massive stellar clusters.

In this Chapter, we present a detailed photometric and kinematic study of a region in the Galactic Perseus complex including the clusters NGC 663 and NGC 654, that appears to be analogous to LISCA I. The data set adopted is presented in section 4.1. Sections 4.2 and 4.3 describe the physical properties of the area under study, its structure, and kinematics, respectively. Section 4.4 presents the physical properties of star clusters belonging to the system. In Section 4.5 we discuss the total system's mass. A comparison with a set of N-body simulations is described in section 4.6. The main conclusions are drawn in section 4.7.

The results presented in this Chapter are from Della Croce et al. (2023, A&A, **674**, A93).

4.1 Preliminary data analysis

4.1.1 The starting catalogs

From the Gaia Archive[1] we retrieved DR3 data for sources distributed within a large area on the sky (5° in radius) arbitrarily centered on the position of NGC 654 and having a five-parameter astrometric solution (i.e., sources with sky position, PM, and parallax measurements) and $G < 19.5$ mag. This catalog comprised 4.5 million sources.

We supplemented this data set with high-resolution optical and near-infrared spectra obtained with the HARPS-N (Cosentino et al., 2014) and GIANO-B (Oliva et al., 2012; Tozzi et al., 2016) spectrographs at the TNG as part of the SPA - Stellar Population Astrophysics: the detailed, age-resolved chemistry of the Milky Way disk Large Program (Program ID A37TAC13, PI: L. Origlia). LOS velocities were obtained for all the observed stars, while detailed chemical abundances for the subsample of red supergiants were computed by Fanelli et al. (2022).

4.1.2 Searching for star clusters in the region

As any coherent stellar structure in the considered area should appear as an overdensity in the multi-dimensional phase-space of positions and velocities, we performed a clustering analysis on the whole catalog by means of the Hierarchical Density-Based Spatial Clustering of Application with Noise (`HDBSCAN`) algorithm (McInnes et al., 2017). For each star we used as inputs the Galactic coordinates, parallax, and PM components $(\ell, b, \varpi, \mu_{\alpha*}, \mu_\delta)$ (after proper rescaling, see discussion in Chapter 3), and we set the `HDBSCAN` parameters as `min_cluster_size` = 40 and `min_samples` = 30. The parameter `min_cluster_size` sets a lower limit to the number of objects an overdensity should have to be identified as a cluster (hence we could not identify clusters with fewer than 40 members), while `min_samples` represents the number of sources used in determining the nearest neighbor distance for each source. Hence, increasing `min_samples` increases the mutual reachability distance among sources, and only the densest areas survive as clusters[2]. Furthermore, `HDBSCAN` assigns a cluster membership probability to each star based on its distance from the neighboring stars. The closer the star is to the other cluster members, the higher the membership probability, and vice versa.

We identified 131 clustered systems within the full 5° field of view. To exclude spurious detections and select only systems that can be classified as clusters to a high significance level, we followed the post-processing approach described by Hunt & Reffert (2021), which uses the nearest-neighbors distance as a proxy for the local density. Only structures with a median value of the nearest-neighbors distance smaller than that of field stars at a 3σ level according to a Mann-Whitney statistics (Mann & Whitney, 1947) were flagged as true stellar clusters. Out of 131 putative clusters, 54 systems fulfilled these criteria and were retained for the subsequent analysis. Recent OCs catalogs (e.g., Cantat-Gaudin & Anders, 2020; Cantat-Gaudin et al., 2020; Castro-Ginard et al., 2022) list 45 clusters in the region

[1] `https://gea.esac.esa.int/archive/`.

[2] We refer to the online documentation (`https://hdbscan.readthedocs.io/en/latest/index.html`) for further details.

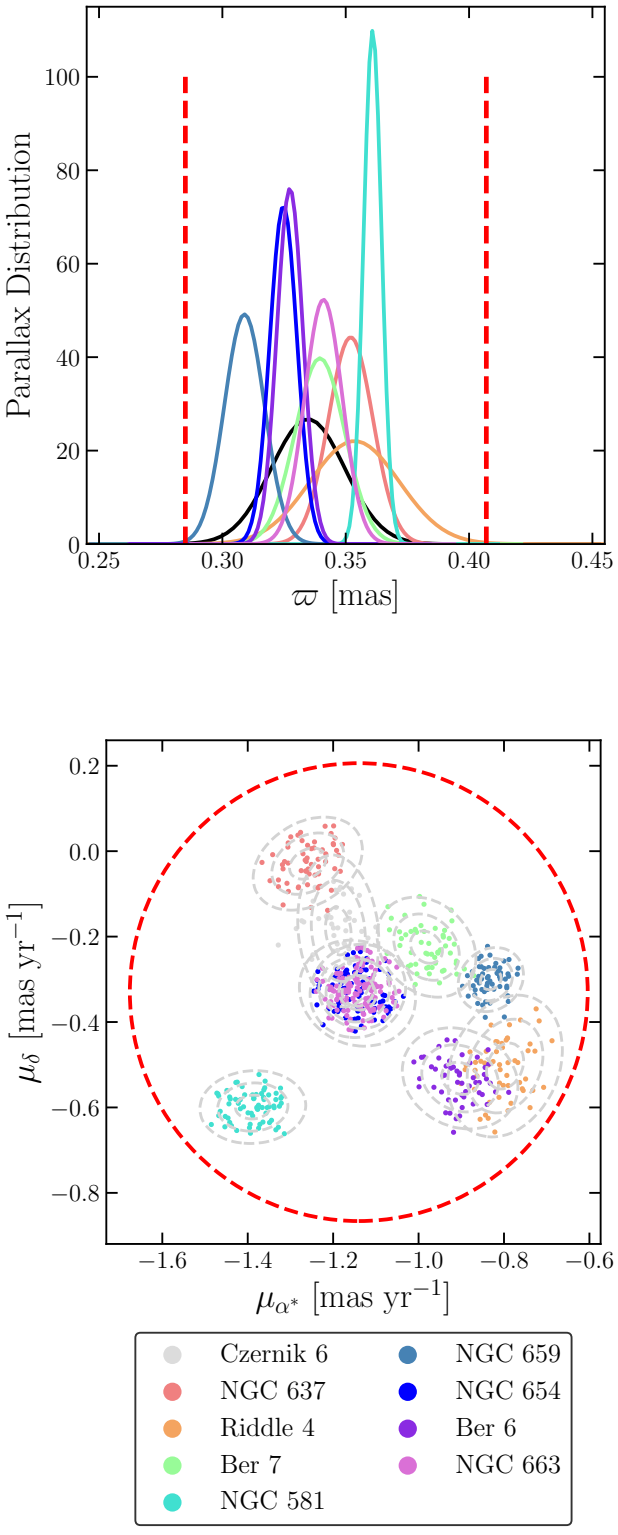

FIGURE 4.1: Inferred distributions in parallax (top panel) and PM (bottom panel) from likely ($>$ 90%) cluster members. Different stellar clusters are in different colors. Dashed gray lines in the bottom panel are iso-probability contours at the 1, 2, and 3σ levels. The red dashed circle and vertical lines represent the range in PM and parallax inside which stars were selected.

with more than 40 members (which is our threshold for identification). Interestingly, we recovered all the known clusters but two (hence 11 unknown structures were identified by this study), namely UBC 186 and UPK 265. We verified that UPK 265 could have been recovered

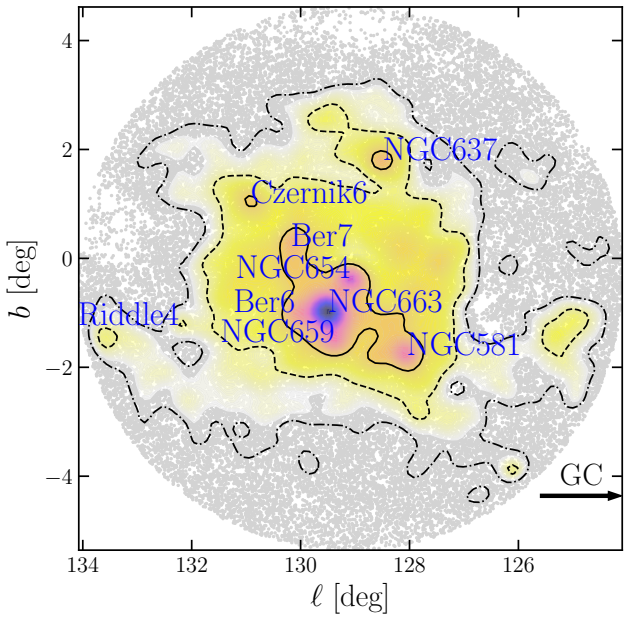

FIGURE 4.2: Spatial distribution in Galactic coordinates of stars selected in PM and parallax. Star cluster names are shown in blue, while black lines are iso-density contours enclosing 11.8% (solid), 39.3% (dashed), and 67.5% (dash-dotted) of the normalized star density distribution. The black arrow shows the direction of the Galactic center (GC).

by slightly changing the input parameters we set for the clustering analysis; however, it would have been excluded by the preliminary parallax selection (according to its value reported by Cantat-Gaudin et al., 2020) described below. The case of UBC 186 is more interesting. A careful investigation of its members reveals significant overlap with NGC 581 (128 out of 131 of NGC 581 members are in common with UBC 186; Cantat-Gaudin et al., 2020). Our analysis was able to properly identify both NGC 581 and another nearby structure that was labeled as UBC 186 by Cantat-Gaudin et al. (2020). However, the latter was flagged as a false detection by the adopted post-processing routine. It is important to note here, however, that the analysis and the results presented in this Chapter do not depend on the inclusion or exclusion of any specific substructure or cluster.

Starting from the sample of 54 structures, we performed a preliminary selection to identify clusters sharing 3D position and 2D velocity with NGC 654 ($\varpi = 0.31 \pm 0.05$ mas, $\mu_{\alpha*} = -1.1 \pm 0.1$ mas yr^{-1} and $\mu_\delta = -0.3 \pm 0.1$ mas yr^{-1}, obtained by Cantat-Gaudin et al., 2020, using Gaia DR2 data), retaining only those with distance $D = 2.8 - 3.2$ kpc and co-moving within about 5.5 km s^{-1} (corresponding to 0.38 mas yr^{-1} at 3 kpc), according to their median parallax and PM estimated from Gaia DR3 data. Nine clusters (comprising NGC 654 itself) were selected in this way. We note in passing that none of the 11 previously unknown structures fulfilled these criteria.

Finally, we determined physically motivated selections in parallax and PM with the aim of selecting all the sources in the field of view sharing 3D position and 2D velocity with the nine clusters. Specifically, we inferred the intrinsic cluster distributions in parallax and PM (by using only stars with membership probability higher than 90%) by means of a Gaussian mixture modeling technique (the Extreme Deconvolution[3] package developed by Bovy et al., 2011), thereby properly accounting for errors and correlation between measurements. In

[3] https://github.com/jobovy/extreme-deconvolution

figure 4.1 we show the distributions inferred in this way in the parallax (top panel) and PM components (bottom panel).

We thus retained all the sources in the Gaia catalog with proper motions and parallaxes compatible, within 3σ, to the cluster distribution. Selected stars share similar distances, $\varpi \in [0.285;\ 0.407]$ mas, which corresponds to $D \in [2.46;\ 3.51]$ kpc, and co-move within 0.536 mas yr^{-1} (about 7.5 km s^{-1}). In figure 4.2 we show the 2D density map of the region along with iso-density contours. The iso-density curves highlight the presence of small-scale clumpy structures corresponding to the identified stellar clusters (labeled in blue) as well as a lower-density diffuse halo extending for at least 3° from NGC 663 and NGC 654 and co-moving with the clusters.

4.1.3 Completeness of the Gaia catalog

The estimate of the Gaia catalog completeness is certainly a challenge due to, for instance, a composite data reduction pipeline and a complex satellite scanning law. Moreover, it does not depend only on the telescope properties themselves, but also on the physical properties of the observed regions such as crowding and extinction. This issue was first tackled by Everall et al. (2021, for the DR2,) and Everall & Boubert (2022, for the EDR3,) who directly modeled Gaia's reduction pipeline and scanning law. More recently, Cantat-Gaudin et al. (2023) adopted an empirical approach to estimate the photometric completeness in the G band by comparing the Gaia catalog with the Dark Energy Camera Plane Survey (Schlafly et al., 2018; Saydjari et al., 2023).

For the purpose of this study, we need to assess the probability that a source is included in the catalog with magnitude G measure and a five-parameter solution. The resulting joint probability is

$$p(5\,\mathrm{params}\ \cdot\ G) = p(G) \times p(5\,\mathrm{params}\,|\,G)\,. \tag{4.1}$$

We retrieved the first term on the right-hand side from the completeness maps of Cantat-Gaudin et al. (2023), whereas the $p(5\,\mathrm{params}\,|\,G)$ term in equation 4.1 was estimated from the number count ratios between sources with the five-parameter solution (k) compared to the total number of sources (n) for a given sky patch and magnitude bin

$$p(5\,\mathrm{params}\,|\,G) = \frac{k+1}{n+2}\,, \tag{4.2}$$

following the documentation of the GaiaUnlimited project.[4] We computed equation 4.2 for a regular spatial grid in a region of 10° around NGC 654 assuming a spatial bin size of $\Delta\delta = 0.2°$ (thus it follows $\Delta\alpha = \Delta\delta\ \cos\delta_{\mathrm{NGC654}} \simeq 0.42°$ in order to obtain a square grid) and for magnitude bins of $\Delta G = 0.2$ mag down to $G \leq 19.5$ mag.

In figure 4.3 we show as examples the 2D $p(5\mathrm{params}\,|\,G)$ maps computed for $G = 18.5$ mag (left panel) and $G = 19.5$ mag (right panel).

Figure 4.3 shows that selecting sources with the five-parameter solution has a prominent impact on the final completeness. Indeed, $p(5\mathrm{params}\,|\,G)$ significantly drops for $G > 18.5$ mag, while $p(G)$ remains almost equal to 1 down to $G = 19.5$ mag. Hence, in the following

[4] See, e.g., https://gaiaunlimited.readthedocs.io/en/latest/dr3-rvs.html

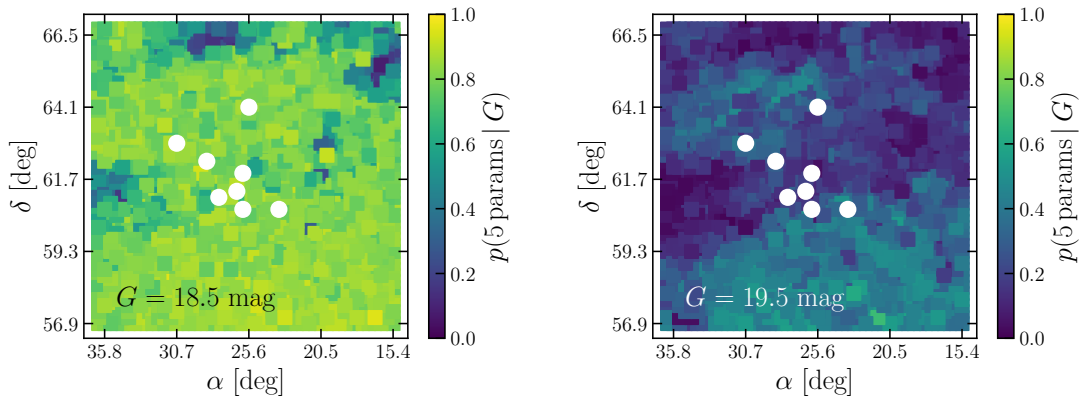

FIGURE 4.3: Catalog completeness in the five-parameter solution estimated from star count ratios ($p(5\text{params}|G)$ term in equation 4.2) for $G = 18.5$ mag (left panel) and $G = 19.5$ mag (right panel). White points give the positions of star clusters.

we assumed $p(G) = 1$, and thus simplifying equations 4.1 and 4.2 into

$$p(5\text{params} \cdot G) \simeq \frac{k+1}{n+2} \quad \forall\, G < 19.5\,\text{mag}\,. \tag{4.3}$$

In the subsequent analyses we correct stellar counts for incompleteness according to equation 4.3.

4.2 Physical properties of the observed area

In section 4.1.2 we identified a region encompassing nine star clusters embedded in a low-density and diffuse stellar halo (see figure 4.2) lying within strict ranges in 2D velocity, position, and parallax by construction. In this section we characterize the physical properties of the area based on the Gaia photometry and the spectroscopic data.

4.2.1 Differential reddening

Available Galactic extinction maps (e.g., Schlegel et al. 1998 and recalculations from Schlafly & Finkbeiner 2011) report a quite significant and strongly variable (E(B−V)$\sim 0.5-3.5$ mag) extinction along the LOS for the region under investigation. Here we provide an independent estimate of the differential reddening based on a suitable color-color diagram and following the approach adopted by Dalessandro et al. (2018b). In particular, combining the Gaia G band with the r, i, z photometric bands from the Panoramic Survey Telescope and Rapid Response System (Pan-STARRS data release 2, Chambers et al., 2016), we constructed the $(G-r)$ versus $(i-z)$ color-color diagram. This diagram turned out to be the most suitable choice as the evolutionary sequences run almost orthogonally to the reddening vector in these colors.

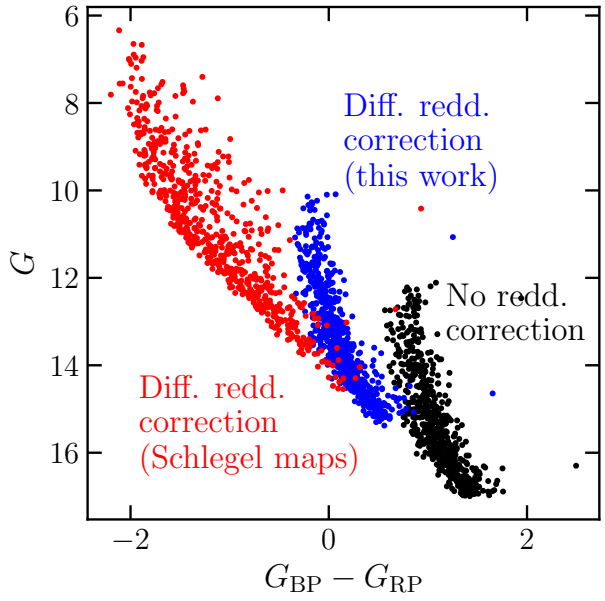

FIGURE 4.4: Color-magnitude diagram for NGC 663 members. In black the observed photometry, while in red and blue are shown the distributions of stars after correcting for differential reddening. For the former Galactic extinction maps by Schlegel et al. (1998); Schlafly & Finkbeiner (2011) are used, and for the latter the reddening corrections estimated in this work.

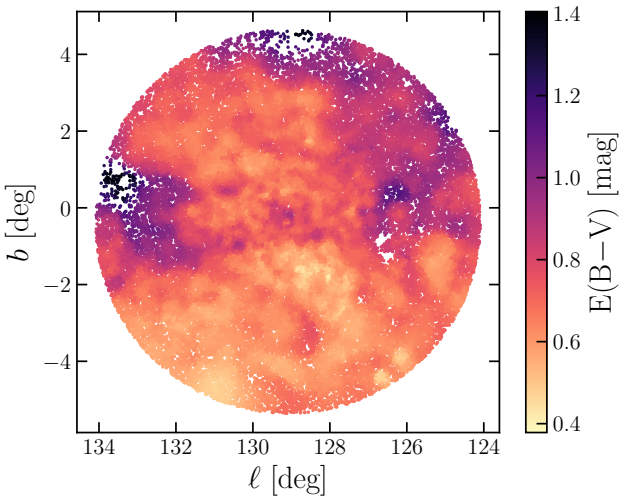

FIGURE 4.5: Two-dimensional reddening map in Galactic coordinates. The extinction was computed star by star from color-color diagrams (see text for further details). White areas correspond to regions devoid of stars.

We derived differential extinction star by star by minimizing differences along the reddening vector with respect to a reference system. As a reference, we chose the median color-color distribution of likely main sequence stars ($G > 12$ mag or $G_{BP}-G_{RP} < 0.5$ mag) belonging to the cluster NGC 581. NGC 581 stars are distributed on average at bluer colors than other stars in the field, thus suggesting they are located in a region with relatively small extinction (color excess for these stars was derived from Schlegel et al. 1998; Schlafly & Finkbeiner 2011: $E(B-V)_{NGC581} \simeq 0.54$ mag). Afterward, for each star, we obtained the median colors of the closest 50 likely main sequence ($G > 12$ mag or $G_{BP}-G_{RP} < 0.5$ mag) neighbor stars, and we determined the distance of this median value to the reference point along the reddening vector (using coefficients from Cardelli et al., 1989). The extinction value corresponding to the derived distance is then assigned to the specific star. To all the

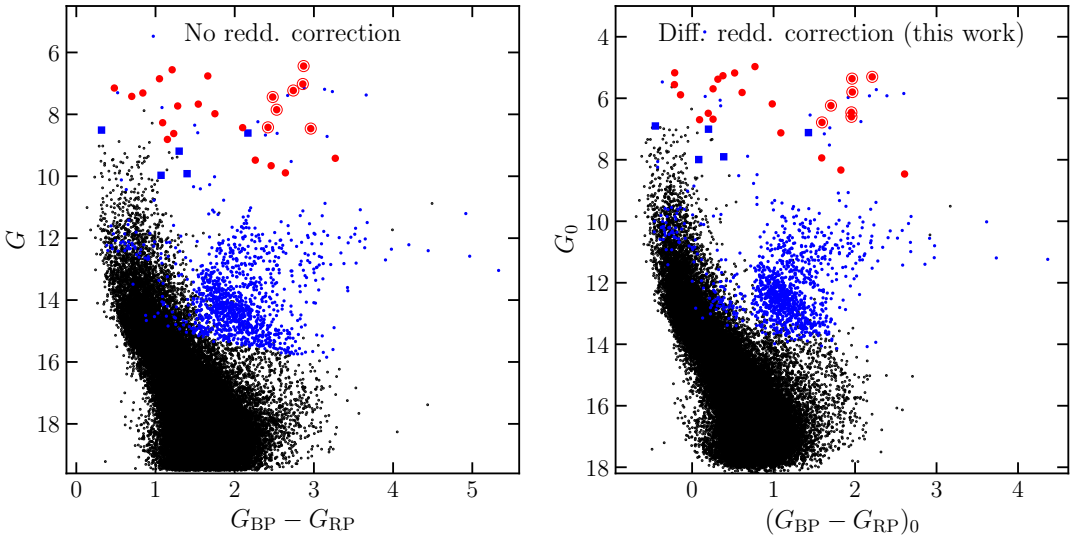

FIGURE 4.6: Observed (left panel) and differential reddening corrected (right panel) CMD for the full catalog. In blue we show stars with LOS velocity measurements from Gaia DR3 (big squares for stars considered in the LOS analysis), whereas in red are stars targeted by high-resolution spectroscopy. The subsample with chemical abundances is circled in red.

sources that do not fulfill the criteria of being likely main sequence stars and to those that do not have a counterpart in the PanSTARRS catalog, we assign the median reddening of the closest 50 neighbors.

As a representative example, we show in figure 4.4 the observed CMD of NGC 663 members as well as those obtained using extinction values from Schlafly & Finkbeiner (2011) (in red) and obtained in this work (in blue). The differential reddening corrections derived in this work nicely squeeze the sequence in the CMD compared to the observed one, and thus confirm the robustness of our estimates. On the contrary, those from Schlafly & Finkbeiner (2011) significantly spread the sequence and move stars at nonphysical colors, reaching $(G_{BP} - G_{RP})_0 = -2$ mag, thus suggesting that the adopted values for the E(B−V) variations are likely overestimated.

Finally, in figure 4.5 we show the resulting reddening map, as derived in this work, in which each star in the catalog is color-coded according to the inferred extinction. We note here that while differential reddening might play a role in shaping specific features of the iso-density contours shown in figure 2 (i.e., missing sources due to locally higher extinction artificially produces underdense regions), it is unlikely that it impacts the overall observed density gradient across the field of view as low-extinction regions, such as $b \lesssim -3°$ (see figure 4.5), still result as underdense compared to the diffuse halo. In figure 4.6 we show the observed (left panel) and differential reddening corrected (right panel) CMDs of the full catalog for comparison.

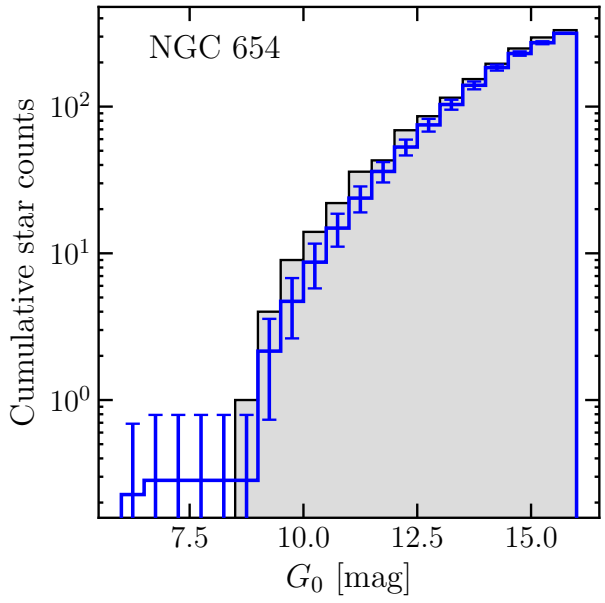

FIGURE 4.7: Cumulative luminosity function for the stellar cluster NGC 654 (gray histogram), along with the normalized histogram of a 32 Myr old synthetic population computed with the PARSEC model (blue histogram). The error bars show the standard deviation of the model's count fluctuations due to several extractions (see text for further details). Bins are 0.5 mag wide.

4.2.2 Cluster and halo ages

Determining the ages of young (< 100 Myr) sparsely populated star clusters is certainly a challenge. At these ages, the color-magnitude distribution of turn-off stars is strongly affected by stellar rotation (Li et al., 2019b). Moreover, the low number of stars and short evolutionary timescales of massive stars (> 10 $M_\odot$) might hamper a detailed estimate of the bright and blue main sequence termination, which in turn would bias the age inferred by standard methods such as isochrone fitting. Notwithstanding these limitations, here we attempt to tackle this issue by adopting a specific approach that is only marginally sensitive to stellar rotation and minimizes the impact of low-number statistics. In particular, we used a set of synthetic simple stellar populations obtained from the PARSEC database (Bressan et al., 2012) with $[\mathrm{Fe/H}] \simeq (-0.30 \pm 0.01)$ dex (corresponding to the mean metallicity of the area Fanelli et al., 2022) and sampling the age range 1−100 Myr with a regular step of 1 Myr. We compared them with the observed cumulative luminosity functions (CLFs) in the G band, after correcting for differential reddening[5] and completeness, as described in section 4.1.3.

In order to account for number fluctuations, we randomly picked several times ($\simeq$100) a (virtually) independent sample of N stars from each synthetic population. The number of extracted stars N was set to be the number of objects in the synthetic population with $G_0 > 6$ mag after applying a normalization to the luminosity function in the range $12.5 < G_0 < 16$ mag (at least 2 mag fainter than the main sequence termination for populations younger than 100 Myr at a distance of about 3 kpc). For each extraction, we then constructed the CLF, and we determined the median CLF of all the extractions (as well as its corresponding 68% credible region). The median CLF obtained for different ages was then compared to the

[5]We use the subscript "0" for reddening-corrected magnitudes and not for absolute ones, i.e., they are not corrected for dimming due to the distance.

observed one (see, e.g., figure 4.7) and the best fit was defined as the one that minimizes the χ^2 statistics. Comparison with the CLF was carried out up to $G = 18$ mag (corresponding to about $G_0 \simeq 16$ mag), below which the catalog's completeness drops (see figure 4.3).

Furthermore, when comparing the synthetic CLF to the observed one, we looked for supergiant stars in the range $G_0 < 8$ mag and $(G_{BP}-G_{RP})_0 > 0.2$ mag. If present, these stars provide strong constraints on the age, and hence we limited the analysis only to those ages that are able to explain the presence of evolved stars at the observed magnitudes. This allowed us to inform the fitting procedure about the likely young age of the system, even in the absence of bright, blue main sequence stars. We note that with this procedure we assigned a narrower uniform prior to the cluster's age. If red supergiants were not present we did not apply any selection on the age.

Color-magnitude diagrams for each cluster are shown in figure 4.8 along with best-fit isochrones. The nine clusters have ages in a narrow range of $14-44$ Myr. The only exception is Berkeley 6, for which we derived an age of 95^{+4}_{-15} Myr. We also found a slight mismatch between isochrones and data, especially visible in the clusters Riddle 4 and NGC 654. This discrepancy likely results from local underestimations of the differential reddening, which in turn biases the age inference toward older ages. We checked that the mismatch is not due to a broad range of effective temperatures, which would affect the adopted reddening coefficients (see e.g., Danielski et al., 2018). This is particularly relevant though, for very young stars ($\lesssim 10$ Myr), see discussion in Chapter 5. Nevertheless, typical errors in age estimates are about $10-15$ Myr (figure 4.8). They account only for uncertainties arising from the fitting procedure, although errors in the differential reddening, distance, and incorrect membership assignment might also be important sources of uncertainties. However, we note that we are mainly interested in constraining relative ages rather than absolute ones.

A comparison with ages from the literature shows qualitatively overall agreement as they are in the range $15-38$ Myr for the clusters under study (Cantat-Gaudin et al., 2020). The only exception is Berkeley 6 for which Cantat-Gaudin et al. (2020) report an age of about 200 Myr, consistent with the system being older than other clusters.

Finally, the same analysis was carried out for the stellar halo (i.e., all the stars that did not belong to any cluster according to the membership probabilities assigned by the clustering algorithm), finding that its age ($\sim 16^{+1}_{-1}$ Myr) is consistent with the ages of the clusters embedded within it.

4.2.3 Line-of-sight velocity distribution and iron content

We investigated the LOS velocity and the metallicity distributions in the region using the TNG-GIARPS spectroscopic catalog presented in section 4.1.1 (shown in red in figure 4.6), and we compared them with those expected for the surrounding Galactic field obtained from the Besançon MW model (Robin et al., 2003) after applying the same parallax and PM selections. We computed LOS velocities for 24 stars, five of which are cluster members, while the remaining 19 belong to the halo. Among them, chemical abundances are available for the seven red supergiants (double red circles in figure 4.6), one of which belongs to NGC 581.

We also note that, while Gaia DR3 (Gaia Collaboration et al., 2023) provides LOS velocity for 1164 selected stars, their color-magnitude distribution (shown in figure 4.6) suggests they are mostly field interlopers. Nevertheless, some bright stars that are likely members of the system have LOS measurements from Gaia. We therefore selected those stars

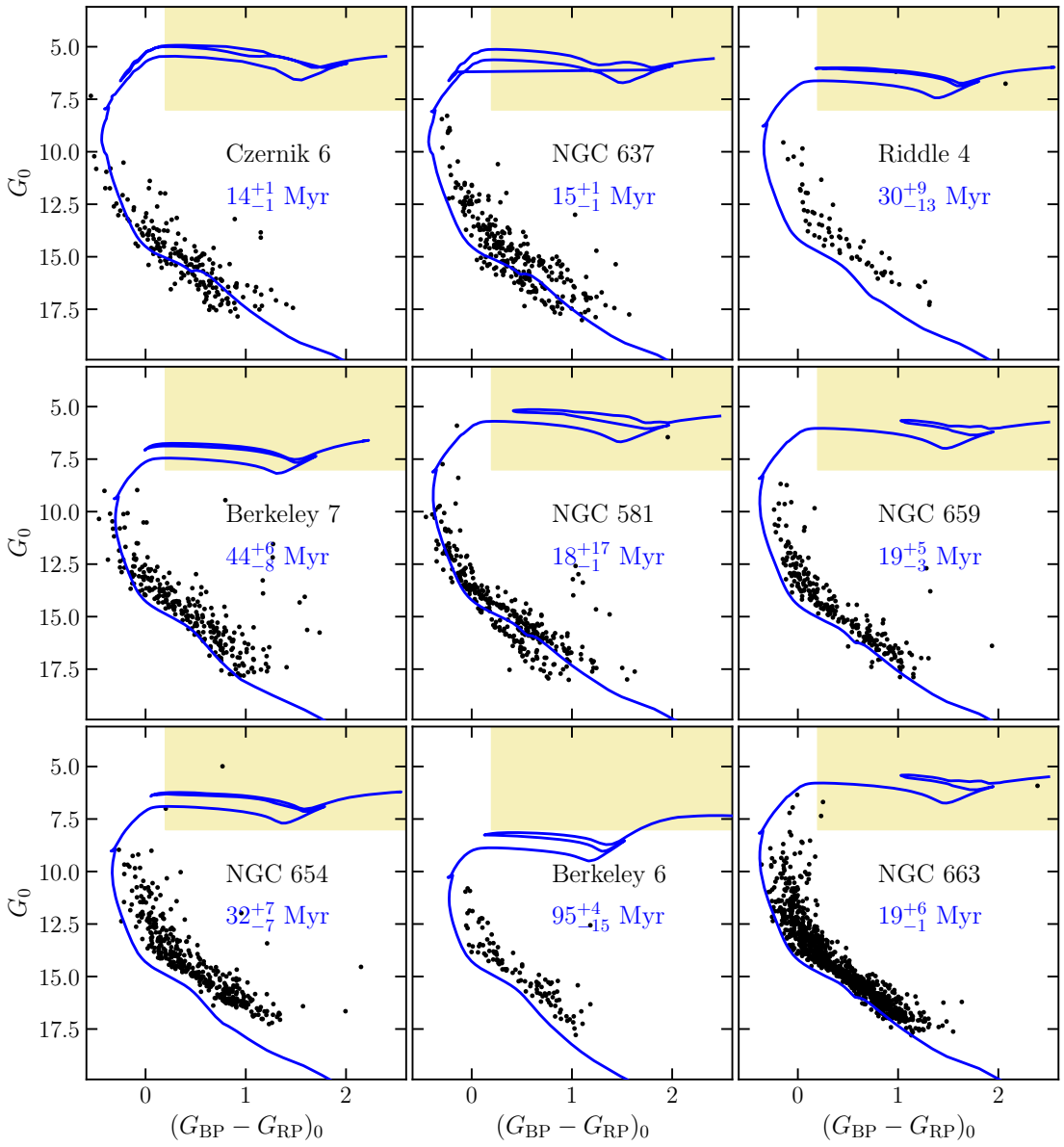

FIGURE 4.8: Color-magnitude diagrams of cluster members (black dots) corrected for differential reddening. For each cluster, the best-fit isochrone is shown in blue and the median age along with the 68% credible interval is also reported. The shaded areas show the region inside which stars are flagged as supergiants.

with $G_0 < 8$ mag (removing objects belonging to the older disk population) and with `rv_expected_sig_to_noise` > 5 and `rv_renormalised_gof` < 2 (thus selecting sources with reliable LOS velocity; see Katz et al., 2019). Out of the 1164 stars, only 4 fulfilled these criteria and were thus included in the catalog (shown as larger blue squares in figure 4.6).

In figure 4.9 we show the distributions in LOS velocity (left panel, constructed with 24 stars from the high-resolution spectroscopic catalog plus 4 stars from Gaia DR3) and in

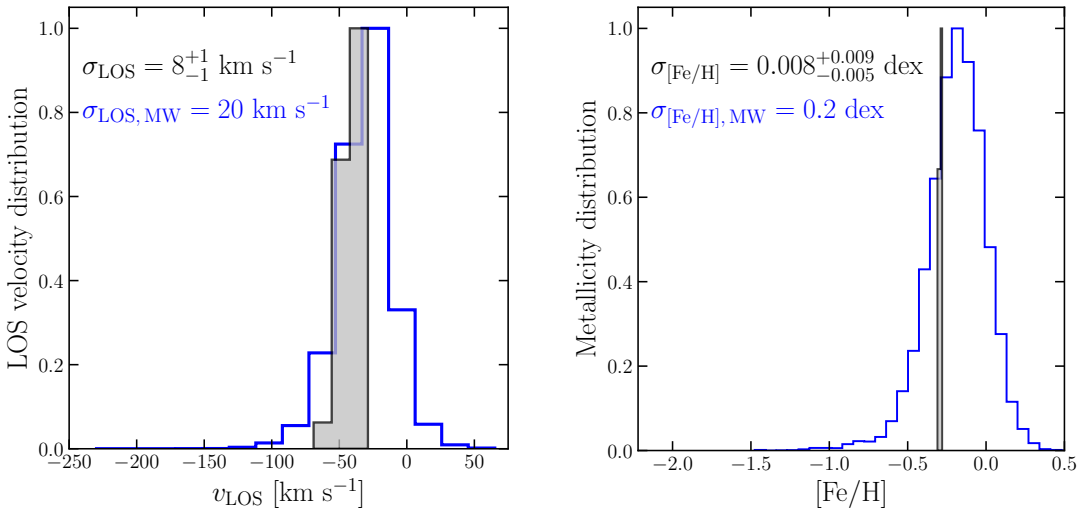

FIGURE 4.9: LOS velocity (left panel) and iron-over-hydrogen abundance (right panel) distributions for members of the selected structure (gray histogram) and for a MW model (blue histogram). The intrinsic dispersions are also shown in the top left corners. All the distributions are scaled by a constant factor for visualization purposes only.

[Fe/H] abundance (right panel, for the seven red supergiants), superimposed to the distributions of the surrounding Galactic field. The intrinsic widths of the observed distributions were inferred by means of a maximum likelihood approach (accounting for individual errors on measurements), and in figure 4.9 we report their median values along with the 68% credible intervals. In particular, we obtained a LOS velocity dispersion $\sigma_{\rm LOS} = 8^{+1}_{-1}$ km s^{-1} (to be compared with $\sigma_{\rm LOS,MW} = 20$ km s^{-1}) and a mean velocity $\langle v_{\rm LOS} \rangle = -41^{+2}_{-2}$ km s^{-1}, whereas for the metallicity we obtained a dispersion $\sigma_{\rm [Fe/H]} = 0.008^{+0.009}_{-0.005}$ dex (opposed to $\sigma_{\rm [Fe/H]} = 0.2$ dex for the Galactic field) and a mean metallicity $\langle {\rm [Fe/H]} \rangle = -0.30^{+0.01}_{-0.01}$ dex.

Interestingly, the observed distributions of the stars in the region are significantly narrower than those expected for a randomly selected group of co-moving Galactic stars, thus strengthening the evidence of kinematic coherence and suggesting a significant chemical homogeneity. In addition, the consistency in both LOS velocity and chemical content between cluster and halo stars further validates the assumption of a physical and coherent structure embedding the star clusters.

The literature data on the bulk clusters' LOS velocity support the kinematic coherence of all clusters but one. The LOS velocity reported for Berkeley 6 ($v_{\rm LOS} \simeq -89 \pm 52$ km s^{-1}, Tarricq et al., 2021) is significantly lower than the system's bulk velocity. However, we note that this value is still compatible within the huge uncertainty as only two stars were used for its estimate. Moreover, Spina et al. (2021) measured the iron content for one member of Berkeley 6 to be around [Fe/H] ~ -0.179 dex, significantly higher than [Fe/H] $\simeq -0.3$ dex, although we note again that chemical abundances were derived for only one cluster member whose membership probability is $< 30\%$ (Spina et al., 2021). Therefore, better constraints on the stellar membership, age, and 3D velocity are needed before drawing any conclusions about the role of Berkeley 6 in the system.

4.3 Structural and kinematic properties of the diffuse stellar halo

4.3.1 Density distribution

We constructed the number density profile of the diffuse stellar halo. We took as the system's center the center of mass of stars with $m \geq 2\,\mathrm{M}_{\odot}$. First, celestial coordinates were converted into local Cartesian ones, assuming the centroid of the system as an initial guess for the system's center. After that, the center of mass was computed in Cartesian coordinates and it was converted back into celestial coordinates, obtaining $(\alpha_{\mathrm{CM}}; \delta_{\mathrm{CM}}) = (26.4559°; 61.7865°)$.

We binned stars radially with respect to this center and we set the width of each radial annulus to contain 2500 sources each. Radial shells were then split into four angular sectors where the density was computed simply as the ratio of the number of stars to the sector's area. The final shell density and error were the mean and standard deviation of the four measurements, respectively. Finally, we also accounted for Poissonian error in each bin by summing in quadrature to the standard deviation a term $1/\sqrt{N_{\mathrm{shell}}}$, with N_{shell} being the number of stars within the shell.

In figure 4.10 we show the number density profile for sources out to 8° from the system's center of mass and with $G \leq 18$ mag. When studying the density distribution, we temporarily extended the catalog up to 8° from the system's center in order to assess the background density, while the selection in G was a good compromise between the catalog's completeness and statistics. Interestingly, the observed density resembled a cluster-like profile over about a factor of 10 in density. At about $R \gtrsim 6°$, the density profile flattens, and we estimated the background density as the weighted mean of bins at distances larger than 6° from the adopted center, obtaining $\Sigma_{\mathrm{background}} \simeq 1.5 \times 10^{-5}$ arcsec^{-2}, which was then subtracted from the observed profile.

Finally, we fitted the density distribution within 5° using the King (King, 1962) and Plummer (Plummer, 1911) models, which are typically adopted to reproduce stellar cluster density profiles. All the free parameters were constrained assuming a χ^2 likelihood and uniform priors (in logarithm), and exploring the parameter space with a MCMC technique using the Python package `emcee` (Foreman-Mackey et al., 2013).

In figure 4.10 we therefore show the density profile (before the background subtraction in gray, and after in black) along with the best-fit models and the associated errors. Both models provided a nice description of the data.

4.3.2 Kinematic properties

We investigated the kinematic properties of the stellar halo by further selecting stars fulfilling the following astrometric quality selection criteria (Lindegren et al., 2021b): `ruwe` ≤ 1.4, `astrometric_gof_al` ≤ 1 and `astrometric_excess_noise` ≤ 1 mas (if `astrometric_excess_noise_sig` > 2), thus excluding those sources for which the standard five-parameter solution does not provide a reliable fit of the observed data.

First, we accounted for perspective effects induced by the system's bulk motion (van Leeuwen, 2009) on the $\mu_{\alpha*}$ and μ_{δ} components; we thus corrected the velocities for each star assuming a bulk average motion of $(\langle\mu_{\alpha*}\rangle; \langle\mu_{\delta}\rangle) = (-1.14; -0.33)$ mas yr^{-1} (estimated using Gaia data for sources with reliable astrometry) and the mean LOS velocity obtained from

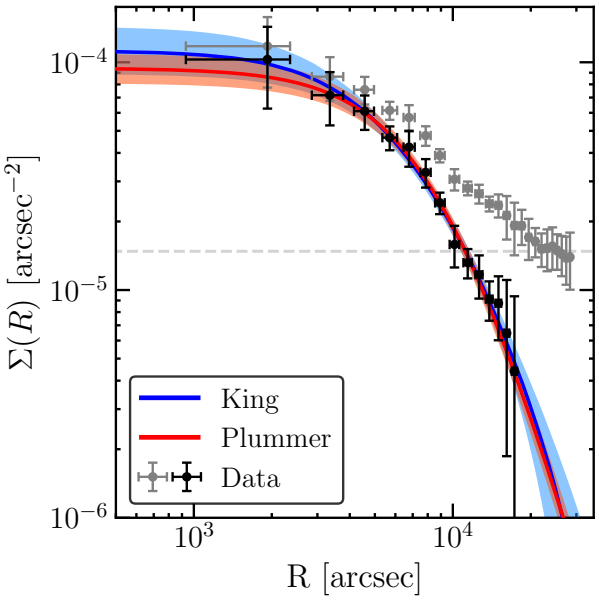

FIGURE 4.10: Stellar number density profile of an 8° region around the system's center of mass and considering stars brighter than $G = 18$ mag. The observed profile is shown in gray, while the intrinsic profile (after background subtraction) is shown in black. The Plummer model (in red) and the King model (in blue) are also shown, along with the corresponding 68% credible regions constructed from the posterior samples.

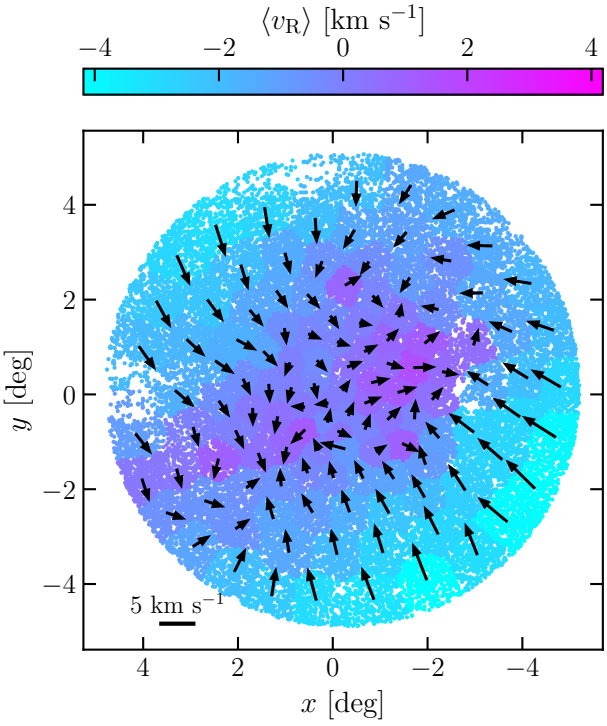

FIGURE 4.11: Two-dimensional distribution of stars in local Cartesian coordinates $(x; y)$. Stars are color-coded according to the inferred mean radial component of the velocity in their Voronoi bin, while black arrows show the mean velocity vector in each bin. Radial velocity is defined as positive if pointing away from the center, thus $\langle v_R \rangle > 0$ means expansion and $\langle v_R \rangle < 0$ means contraction. The velocity scale is shown in the bottom left corner.

the spectroscopic catalog supplemented with Gaia DR3 data (see section 4.2.3). Owing to the large area of the sky covered by our data, the magnitude of the perspective correction resulted as non-negligible, reaching up to 0.2 mas yr^{-1} (about 2.8 km s^{-1}) at 5° from the center, and hence caution must be taken when interpreting results at such large angular scales.

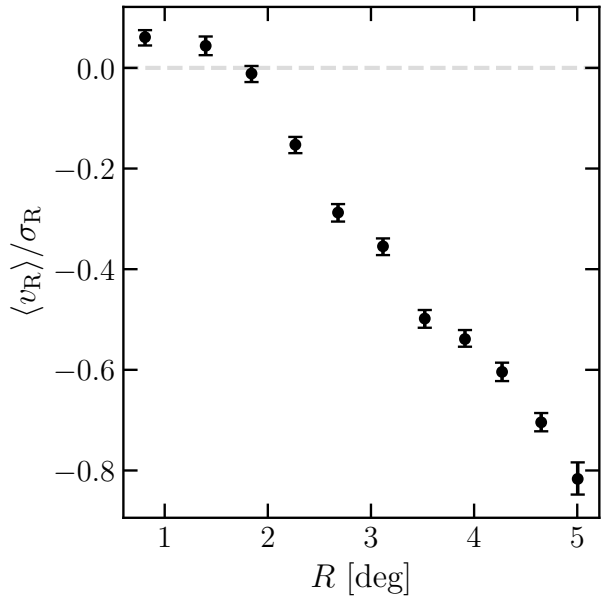

FIGURE 4.12: Radial profile of the ratio of the radial mean velocity to the radial velocity dispersion computed in spherical shells. Black dots show the median values, while quoted errors are the 16th and 84th percentiles of the distributions. The dashed horizontal line shows the zero expansion–contraction level.

Looking at the distribution of velocities on the plane of the sky may offer a first glimpse of the dynamic state of the system. We thus performed a centroidal Voronoi tessellation (Cappellari & Copin, 2003), exploiting the density profile shown in figure 4.10, such that each bin contains about the same number of stars.

Radial velocities in each bin were inferred by means of an MCMC exploration assuming as likelihood (see, e.g., Pryor & Meylan, 1993; Raso et al., 2020)

$$\ln \mathcal{L} = -\frac{1}{2} \sum_i \left[\frac{(v_{\mathrm{R,i}} - \langle v_\mathrm{R} \rangle)^2}{\sigma_\mathrm{R}^2 + e_{\mathrm{R,i}}^2} + \ln(\sigma_\mathrm{R}^2 + e_{\mathrm{R,i}}^2) + \frac{(v_{\mathrm{T,i}} - \langle v_\mathrm{T} \rangle)^2}{\sigma_\mathrm{T}^2 + e_{\mathrm{T,i}}^2} + \ln(\sigma_\mathrm{T}^2 + e_{\mathrm{T,i}}^2) \right], \tag{4.4}$$

where $v_{\mathrm{X,i}}$ and $e_{\mathrm{X,i}}$ with $\mathrm{X} \in \{\mathrm{R}, \mathrm{T}\}$ are the radial (R) and tangential (T) components of the velocity and error for the i-th star, respectively. Furthermore, we assumed uniform priors in the logarithms of the velocity dispersion (σ_R and σ_T) and uniform priors in the mean velocities ($\langle v_\mathrm{R} \rangle$ and $\langle v_\mathrm{T} \rangle$). In figure 4.11 we show the mean velocity vectors for each tile, and we color-coded stars in each Voronoi bin according to the mean radial velocity inferred in the bin. The directions of the arrows clearly show a contraction of the external regions (reaching speeds up to $\sim 4 - 5$ km s^{-1}), also confirmed by the color distribution of stars in figure 4.11. Interestingly, in the central regions ($\mathrm{R} < 1 - 2°$), a mild expansion on the order of $\simeq 1$ km s^{-1} is observed, mainly visible in the purplish bins.

The same pattern emerges when computing the mean radial velocity $\langle v_\mathrm{R} \rangle$ in spherical shells (see equation 4.4), as shown in figure 4.12. In particular, the innermost 2° show a flat slightly positive profile ($\langle v_\mathrm{R} \rangle / \sigma_\mathrm{R} > 0$) indicating central expansion, although the radial motion is highly dominated by random motion ($\langle v_\mathrm{R} \rangle / \sigma_\mathrm{R} < 0.1$). However, moving toward

larger radii, the contraction ($\langle v_{\rm R} \rangle / \sigma_{\rm R} < 0$) becomes increasingly more prominent and the radial motion more ordered. The robustness of the contraction pattern (figures 4.11 and 4.12) was tested against the assumption of a particular bulk LOS velocity when accounting for perspective expansion (since we had only a few measurements). We considered the worst-case scenario in which stars followed the LOS velocity distribution expected for the MW field stars in the region ($\langle v_{\rm LOS} \rangle \simeq -35$ km s^{-1} and $\sigma_{\rm LOS,MW} \simeq 20$ km s^{-1}, see figure 4.9).

The transverse motions were then corrected by randomly assigning to each star a LOS velocity extracted from the MW-like distribution. We iterated this procedure 100 times finding that the velocity pattern observed was weakly affected by our mean bulk motion assumption and the contraction showed in figure 4.12 was always recovered.

4.3.3 Multi-mass structural and kinematic analyses

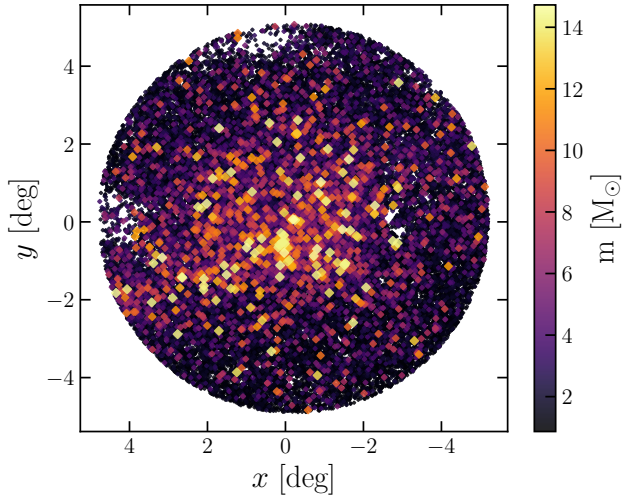

FIGURE 4.13: Spatial distribution of stars color-coded by mass. Masses were obtained by mass-absolute magnitude relation (see text for further details).

The presence of a mass spectrum has a non-negligible role in the dynamics of both young and old stellar systems. Old stellar clusters are indeed known to naturally develop mass segregation due to two-body interactions that cause significant kinetic energy exchange among stars and cause massive stars to sink toward the cluster's center (Binney & Tremaine, 2008a). However, evidence of mass segregation has also been found in younger Galactic clusters (e.g., Hillenbrand & Hartmann, 1998; Gouliermis et al., 2004; Stolte et al., 2006; Evans & Oh, 2022), thus possibly implying a connection with the early stages of cluster formation (McMillan et al., 2007; Allison et al., 2009; Livernois et al., 2021). In addition, numerical simulations showed that during the violent relaxation phase, young stellar systems can start developing a dependence of the kinematical properties (rotation, velocity dispersion) on the stellar mass (see, e.g., Livernois et al., 2021). The investigation of possible mass-dependent dynamical properties is therefore crucial to shed further light on the dynamics of young stellar systems.

We estimated stellar masses using theoretical M$-$G$_0$ relation for zero age main sequence stars. This relation was obtained from the PARSEC models for a population of 14 Myr in age (the youngest age we estimate) with [Fe/H] $= -0.3$ dex. Stellar masses were therefore derived by interpolation of this relation, and in figure 4.13 we show the spatial distribution of stars color-coded by their mass.

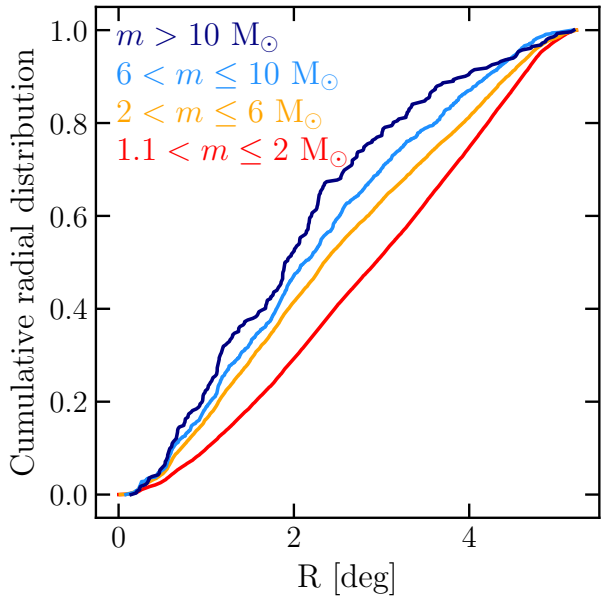

FIGURE 4.14: Cumulative radial profiles constructed in four different mass bins from stars with masses between 1.1−2 M$_\odot$ (in red) up to stars more massive than 10 M$_\odot$ (in dark blue). Stellar counts were corrected for incompleteness star by star.

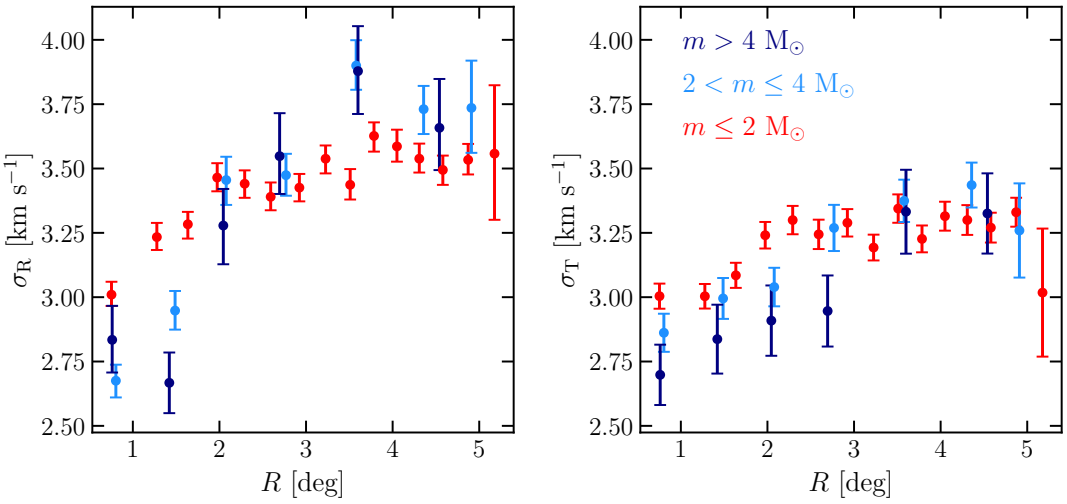

FIGURE 4.15: Velocity dispersion profiles in the radial (left panel) and tangential (right panel) components, in three different mass bins depicted with different colors: red for the least massive bin and dark blue for the most massive.

figure 4.13 indicates that massive stars (lighter symbols) are more centrally concentrated than lower mass ones (darker symbols). We thus quantitatively investigated this feature by looking at the cumulative profiles in different mass bins, after correcting for completeness (see figure 4.3) by assigning to each star a weight =1/completeness. We limited the analysis to stars more massive than 1.1 M$_\odot$ to avoid very low completeness values. figure 4.14 shows that the massive stars exhibited a more centrally concentrated spatial distribution than the lower

mass ones. In addition, a Kolmogorov-Smirnov test confirmed the statistical significance of this result ($p < 0.003$) for every combination of mass bins. In section 7.3.2 we show the completeness distributions for each mass bin.

Finally, we looked for evidence of a dependence of the kinematic properties on the stellar masses. In figure 4.15 we show the velocity dispersion profiles constructed for different mass bins, specifically for stars with mass $m \leq 2$ M$_\odot$ (red symbols), 2 M$_\odot$ $< m \leq 4$ M$_\odot$ (light blue symbols) and $m > 4$ M$_\odot$ (dark blue symbols).

Our analysis reveals mild evidence of a dependence of the velocity dispersion on the stellar mass within about 2° from the center in both the radial and tangential components: more massive stars show a slightly smaller velocity dispersion. At radii $R > 2{-}3°$ the velocity dispersion profiles become indistinguishable and no signs of equipartition are found. The trend is consistent with that expected for a stellar system that has started to evolve toward energy equipartition during its early evolutionary phases and is in general agreement with the trends found in the simulations presented in Livernois et al. (2021). We discuss this point further in section 4.6.

Finally, we observed an increase in the velocity dispersion moving away from the center in every mass bin (variations up to $\sim$ 0.6 km s^{-1}, see figure 4.15). Several effects might be at play in driving such a pattern, for instance deviation from spherical symmetry (see, e.g., the color-coded map in figure 4.11, whose expansion pattern was clearly nonspherical), a nonconstant mean velocity within bins (as noted by Da Rio et al., 2017), and possibly the presence of residual field interlopers.

We also observed a clear dependence of the radial velocity component on the stellar mass. In particular, stars more massive than about $\gtrsim 2$ M$_\odot$ exhibit a higher positive mean radial velocity (up to about 1 km s^{-1}) than lower mass stars within the innermost 3° (see figure 4.16), while at larger radii massive stars contract toward the center ($\langle v_R \rangle < 0$) with a similar slope to lower mass stars, albeit with a higher normalization.

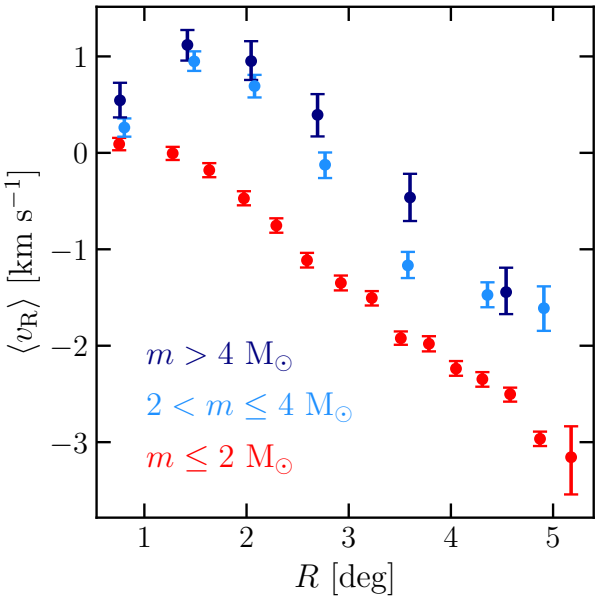

FIGURE 4.16: Mean radial velocity profiles for stars in three different mass bins: $m \leq 2$ M$_\odot$ (red symbols), $2 < m \leq 4$ M$_\odot$ (light blue symbols), and $m > 4$ M$_\odot$ (dark blue symbols). Positive values of $\langle v_R \rangle$ should be interpreted as expansion and negative values as contraction.

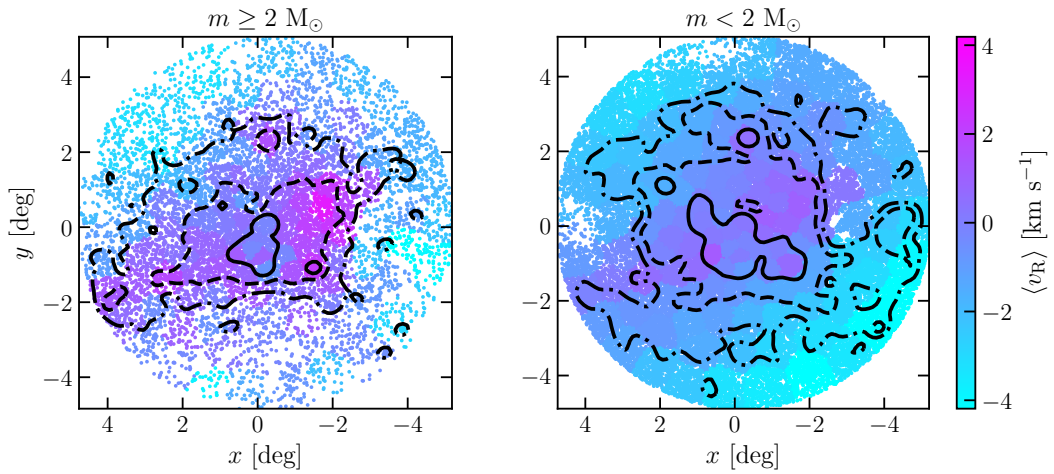

FIGURE 4.17: Two-dimensional maps of mean radial velocity for high-mass stars ($m \geq 2\,M_\odot$, left panel) and low-mass stars (right panel). Stars belonging to the same Voronoi bin are color-coded according to the mean radial velocity, while black lines are iso-density contours of the respective populations enclosing about 12% (solid line), 39% (dashed line), and 67% (dash-dotted line) of the underlying density distribution.

We thus further investigated this feature in the 2D plane using the Voronoi tessellation, giving particular attention to non-spherically symmetric features and putative links with the spatial distribution of stars. In figure 4.17 we show 2D maps of mean radial velocity for stars with mass above (left panel) and below (right panel) 2 M$_\odot$. Expansion ($\langle v_R \rangle > 0$) is depicted in purple, contraction ($\langle v_R \rangle < 0$) is depicted in blue, and black lines highlight iso-probability contours of the density distribution of the respective populations.

Interestingly, a clear connection between expansion and density comes up when looking at massive stars (left panel of figure 4.17), suggesting that higher-density regions expand faster than lower ones, whereas no clear connection is found for the low-mass population (right panel). In addition, we found consistent features to what is observed in figure 4.16: massive stars expand faster than lower mass ones, which in turn had higher contraction speeds in the outskirts.

The spectro-photometric (i.e., age and metallicity), structural (i.e., density profiles and mass segregation), and kinematic (i.e., contraction and equipartition) evidence collected so far suggests that the stars selected within a few degrees of NGC 654 are not just a group of co-moving stars; rather, the nine identified clusters and the extended low-density halo surrounding them are part of a common, substructured, and still-forming massive stellar system. Following the definition introduced in Dalessandro et al. (2021b), we named it LISCA II.

4.4 Star cluster properties

In this section, we present the structural and kinematic properties of the nine star clusters composing LISCA II.

First, we constructed the number density radial profiles for all the clusters (following the same approach described in section 4.3) with respect to their center of mass, and we fitted them with the Plummer (Plummer, 1911) and King (King, 1962) models. figure 4.18 shows the observed profiles and the models, normalized to the clusters' central densities and observed projected half-mass radii ($R_{\rm hm}$) enabling a quantitative comparison among different clusters. The quantity $R_{\rm hm}$ is defined as the projected radius that encloses half of the total cluster's mass directly obtained from the radial distribution of member stars.

Every star cluster exhibits a cluster-like profile that, within the errors, is equally well modeled by both the Plummer and King models, with the only exception of NGC 581 (see figure 4.18), which exhibits a sharper truncation not captured by the Plummer model.

In addition, we present the kinematic properties of star clusters: figure 4.19 shows the inferred 1D velocity dispersion, which is defined as

$$\sigma_{\mu} \equiv \sqrt{\frac{\sigma_{\rm R}^2 + \sigma_{\rm T}^2}{2}}\,, \tag{4.5}$$

with $\sigma_{\rm R}$ and $\sigma_{\rm T}$ being the projected radial and tangential components of the velocity dispersion inferred assuming the likelihood in equation 4.4 and sampling the parameter space with an MCMC technique.

For two clusters, namely Riddle 4 and Berkeley 6, we could not compute reliable kinematic profiles since few stars (51 and 84 respectively) fulfilled the astrometric quality selections presented in section 4.3.

All the other clusters exhibit rather flat dispersion profiles that can be hardly explained by equilibrium models, for instance those adopted to fit the stellar density distributions. Several effects might be at play in producing the observed flat dispersion profiles, such as contaminants from the stellar halo and dynamical heating due to tidal interactions with other clusters and substructures possibly taking place during the system's early evolution. We discuss dynamical heating in more detail in section 4.6.

To estimate the total mass of each cluster we followed the same approach described in Dalessandro et al. (2021b), and we normalized a Kroupa (2001) and a Salpeter (1955) initial mass function (IMF) in the range $m > 4$ M$_\odot$, such that the number of member stars matched the number predicted by direct integration of the IMF

$$N_{\star\,\rm observed} = \int_{m_{\rm min}}^{m_{\rm max}} IMF(m)\, dm\,, \tag{4.6}$$

with $m_{\rm min} = 4$ M$_\odot$ and $m_{\rm max} = 11 - 14$ M$_\odot$ for every cluster but Berkeley 6, whose maximum stellar mass is approximately 7 M$_\odot$ according to its inferred age. Once the normalization was obtained, we computed the total visible mass by integrating the IMF in the range $m_{\rm min} - m_{\rm max} = 0.09 - 14.73$ M$_\odot$

$$M_{\rm tot} = \int_{m_{\rm min}}^{m_{\rm max}} IMF(m)\, m\, dm\,, \tag{4.7}$$

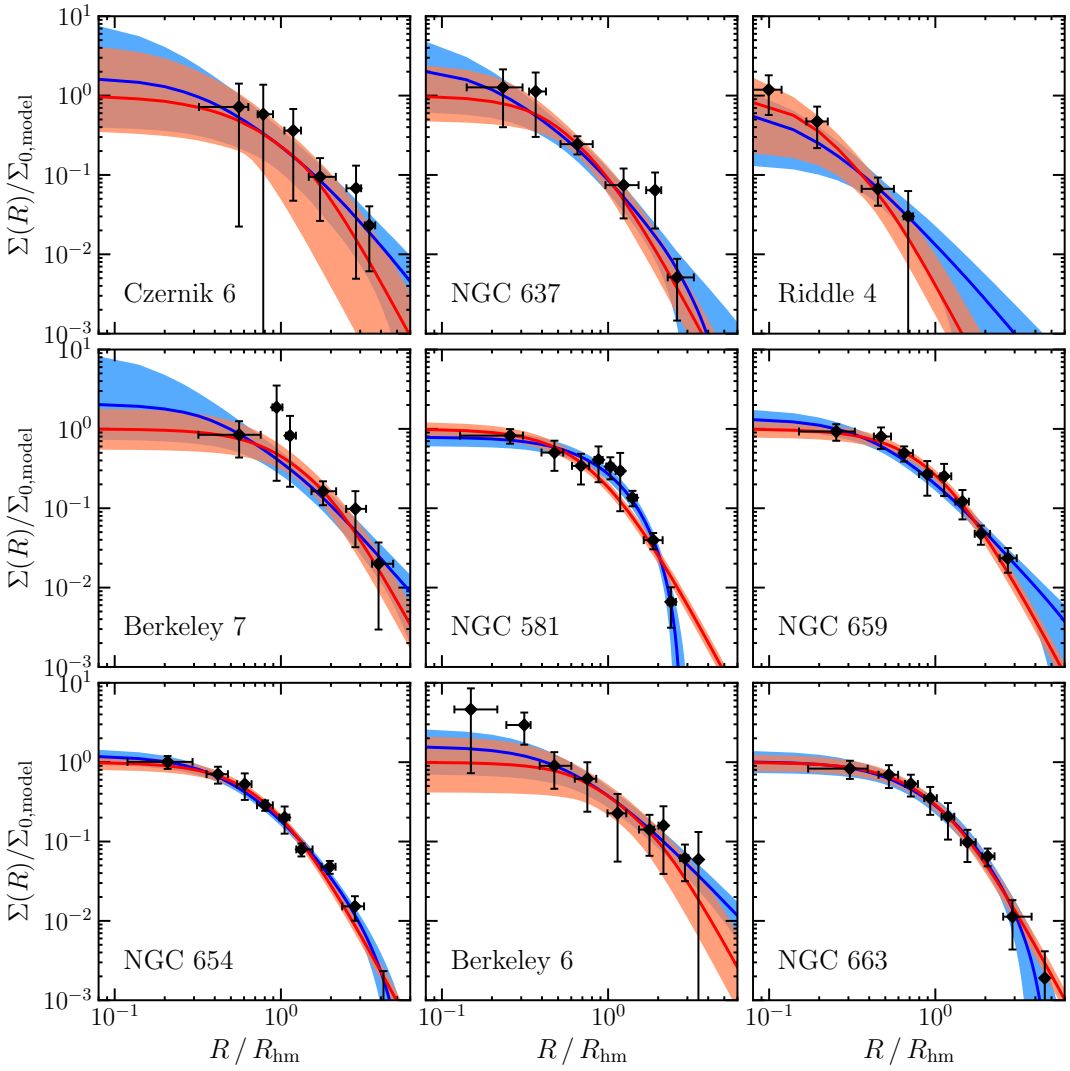

FIGURE 4.18: Number density profiles (black symbols) for the nine star clusters. Also shown are the model predictions for the Plummer (red) and King (blue) models. Shaded areas represent the 68% credible regions. All the profiles, both observed and models, were scaled to the central density predicted by the Plummer model $\Sigma_{0,\mathrm{model}}$ and to the observed projected half-mass radius R_{hm}.

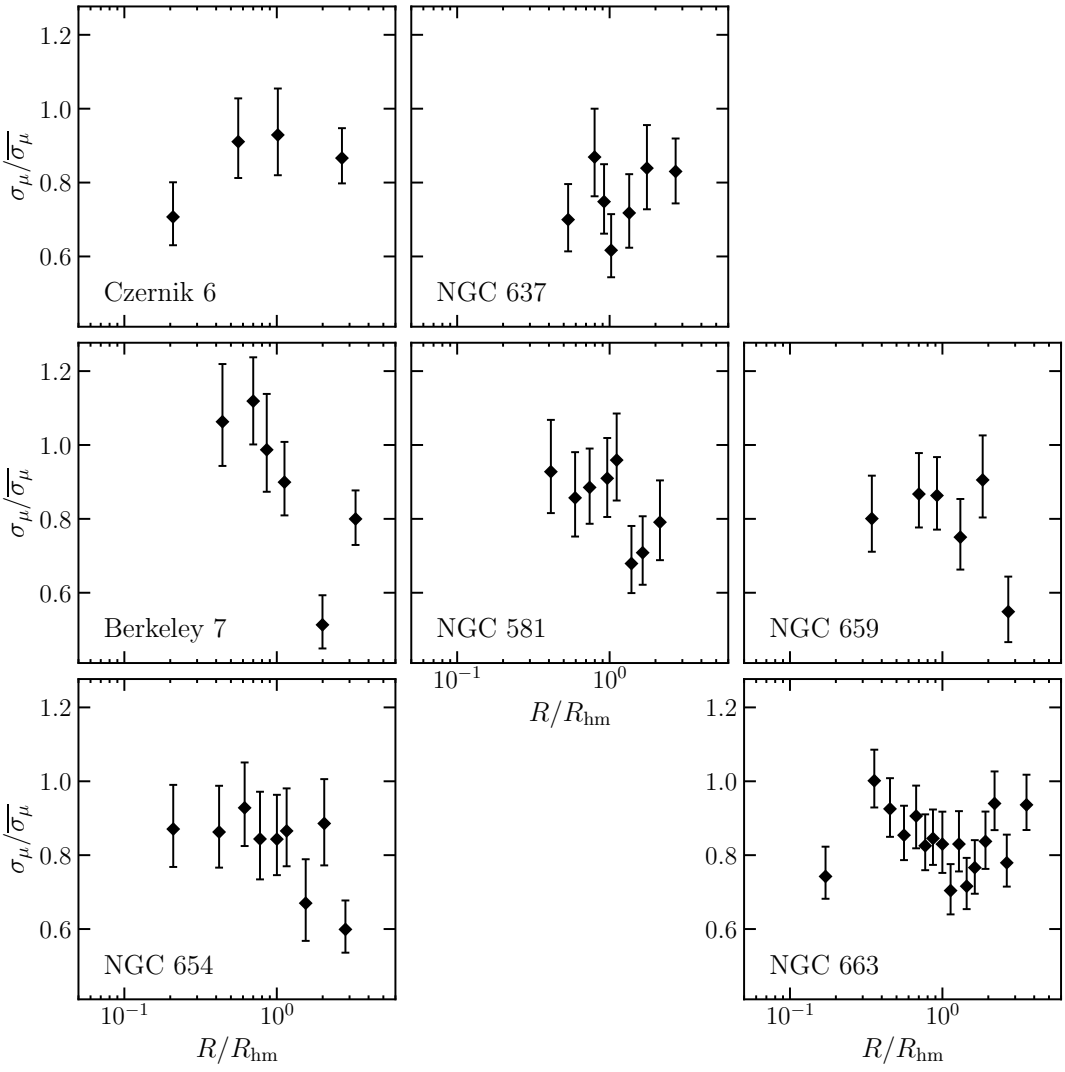

FIGURE 4.19: One-dimensional velocity dispersion profiles for seven out of nine star clusters. Velocity dispersion was normalized to the same quantity computed for all the cluster's members ($\overline{\sigma_\mu}$, i.e., without binning the stars), while projected distances from the cluster center of mass were normalized to the observed half-mass radius.

TABLE 4.1: Star cluster properties obtained in this study.

Name	$\alpha_{\rm CM}$ [°]	$\delta_{\rm CM}$ [°]	$\langle\varpi\rangle$ [mas]	$\langle\mu_{\alpha*}\rangle$ [mas yr^{-1}]	$\langle\mu_{\delta}\rangle$ [mas yr^{-1}]	a [pc]	$R_{\rm c}$ [pc]	$\rm M_{tot,\,Kroupa}$ [10^2 $\rm M_\odot$]	$\rm M_{tot,\,Salpeter}$ [10^2 $\rm M_\odot$]	$N_{\rm member}$
Czernik 6	30.5313	62.8293	0.335±0.015	-1.19 ± 0.03	-0.19 ± 0.06	$7.4^{+5.3}_{-5.1}$	$2.8^{+4.0}_{-1.6}$	4.9	7.7	191
NGC 637	25.8828	64.1880	0.352±0.009	-1.26 ± 0.04	-0.03 ± 0.04	$5.7^{+2.2}_{-1.9}$	$1.9^{+2.7}_{-0.9}$	10.1	15.9	291
Riddle 4	32.0533	60.3979	0.354±0.018	-0.80 ± 0.04	-0.50 ± 0.06	$2.2^{+1.9}_{-0.7}$	$1.4^{+2.3}_{-0.5}$	4.9	7.7	67
Berkeley 7	28.5599	62.2259	0.340±0.010	-0.98 ± 0.04	-0.22 ± 0.04	$5.8^{+0.6}_{-0.6}$	$4.0^{+1.5}_{-1.1}$	8.9	14.1	272
NGC 581	23.3985	60.7205	0.361±0.004	-1.39 ± 0.04	-0.60 ± 0.03	$3.5^{+0.3}_{-0.3}$	$4.4^{+1.6}_{-1.1}$	14.6	23.0	319
NGC 659	26.1205	60.6937	0.309±0.008	-0.83 ± 0.03	-0.30 ± 0.03	$3.2^{+0.3}_{-0.3}$	$1.4^{+0.5}_{-0.3}$	11.5	18.1	240
NGC 654	26.0235	61.8833	0.325±0.006	-1.14 ± 0.05	-0.33 ± 0.04	$2.3^{+0.2}_{-0.2}$	$1.2^{+0.2}_{-0.2}$	20.8	32.8	421
Berkeley 6	27.7991	61.0746	0.327±0.005	-0.90 ± 0.05	-0.53 ± 0.04	$3.1^{+1.8}_{-1.1}$	$1.3^{+0.9}_{-0.3}$	4.3	6.6	107
NGC 663	26.5625	61.1930	0.341±0.008	-1.14 ± 0.04	-0.33 ± 0.04	$5.8^{+0.6}_{-0.6}$	$4.0^{+1.5}_{-1.1}$	55.8	88.0	1079

Notes. Cluster name; center of mass coordinates obtained from stars with mass $m > 2\,M_\odot$; mean cluster parallax; mean proper motions; Plummer scale length; King core radius; total system mass obtained assuming either a Kroupa or a Salpeter IMF; total number of Gaia sources flagged as cluster members.

respectively the minimum and maximum stellar mass for a 14 Myr-old simple stellar population with [Fe/H] $= -0.3$ dex (Bressan et al., 2012). The derived cluster masses are in the range $\simeq 0.5 - 5.6 \times 10^3$ M$_\odot$ ($\simeq 0.7 - 8.8 \times 10^3$ M$_\odot$) according to a Kroupa (Salpeter) IMF.

The main kinematic and structural properties of the clusters are summarized in Table 4.1. Specifically, for each cluster we included the coordinates of the center of mass (for stars more massive than 2 M$_\odot$), the mean parallax and PM (of the distributions shown in figure 4.1) along with errors, the Plummer scale length and the King core radius (obtained from the models shown in figure 4.18 and converted to parsec using the mean parallax also reported in Table 4.1), the total masses inferred by assuming either a Kroupa or a Salpeter IMF, and finally the total number of member stars for each cluster.

4.5 Total system mass

The total mass of LISCA II was estimated by using equation 4.7 and roughly the same approach as for the single clusters. However, in this case, we had to assume a radial extension of the system within which to integrate the stellar masses. To this end we used the Jacobi radius (R_J; see, e.g., Binney & Tremaine, 2008a) as a first-order physically plausible radial extension of the system. The radius R_J is simply defined as

$$R_\mathrm{J} = R_0 \left(\frac{M_\mathrm{LISCAII}}{3 M_\mathrm{MW}(< R_0)} \right)^{1/3} , \tag{4.8}$$

with $R_0 \simeq 10.2$ kpc and $M_\mathrm{MW}(< R_0) = 10.98^{+0.12}_{-0.10} \times 10^{10}$ M$_\odot$ being the galactocentric distance of the system and the MW mass enclosed within that radius, respectively (Cautun et al., 2020), and M_LISCAII is the total system mass. Starting from equation 4.8, we estimated both R_J and the mass of the system by using an iterative procedure until final convergence was reached. Depending on the assumed IMF we obtain

$$\begin{aligned} R_{\mathrm{J,\,Kroupa}} &= 1.07\,^\circ \simeq 55\,\mathrm{pc}\,, \\ R_{\mathrm{J,\,Salpeter}} &= 1.35\,^\circ \simeq 70\,\mathrm{pc}\,, \end{aligned} \tag{4.9}$$

with the corresponding enclosed ($< 2\,R_\mathrm{J}$) masses being

$$\begin{aligned} M_{\mathrm{LISCAII,\,Kroupa}} &= 6.4 \times 10^4 M_\odot\,, \\ M_{\mathrm{LISCAII,\,Salpeter}} &= 1.2 \times 10^5 M_\odot\,. \end{aligned} \tag{4.10}$$

It is important to note here that in this case R_J is only meant to provide a general indication of the spatial scale related to the strength of the tidal field at the location of LISCA II. In the complex case of a clumpy system far from a spherical configuration in dynamical equilibrium like that of LISCA II, the detailed implications of the effects of the tidal field truncation for this system would require a tailored set of simulations. We also note that the kinematical properties revealed by our analysis (section 4.3) indicate that in this system all the stars, including those beyond the present estimate of R_J, are strongly contracting toward the center of the system, which is just the opposite of what is expected for stars escaping the system.

4.6 Comparison with N-body simulations of early cluster evolution

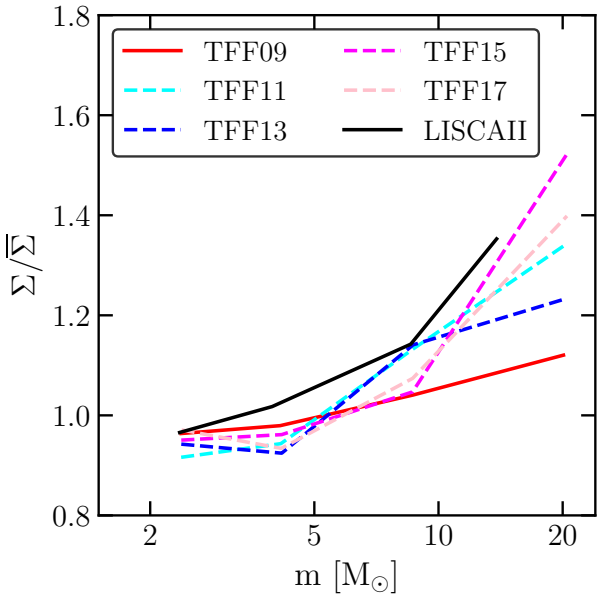

FIGURE 4.20: Local number density of stars as a function of stellar mass (see section 4.6.1). The local density is normalized by the median local surface density of the entire cluster. The increase in local density with stellar mass indicates mass segregation on local scales across all clusters shown.

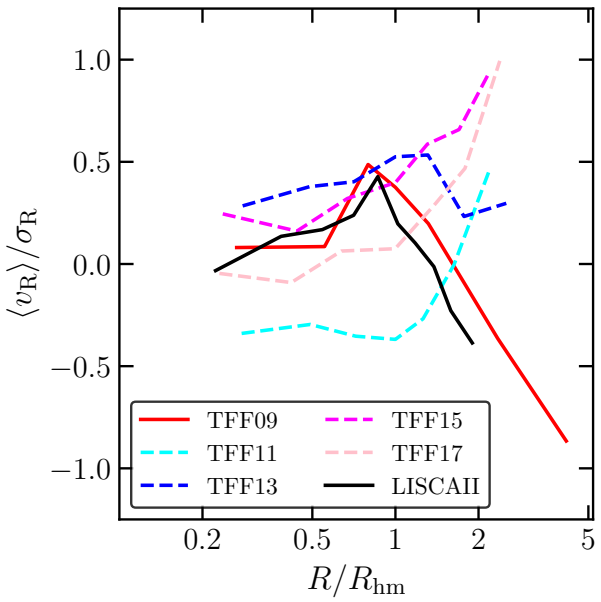

FIGURE 4.21: Projected radial velocity profiles for each snapshot of the N-body simulation and the LISCA II system. The projected radius is normalized to the projected half-mass radius of the system in each snapshot, and the radial velocity is normalized to the radial velocity dispersion of all stars in the system.

In this section we present an analysis of the dynamical properties of one of the N-body models studied in Livernois et al. (2021). The simulations of Livernois et al. (2021) explored the early evolution and violent relaxation phases of young rotating star clusters and followed their evolution from a hierarchical structure to a final monolithic equilibrium configuration.

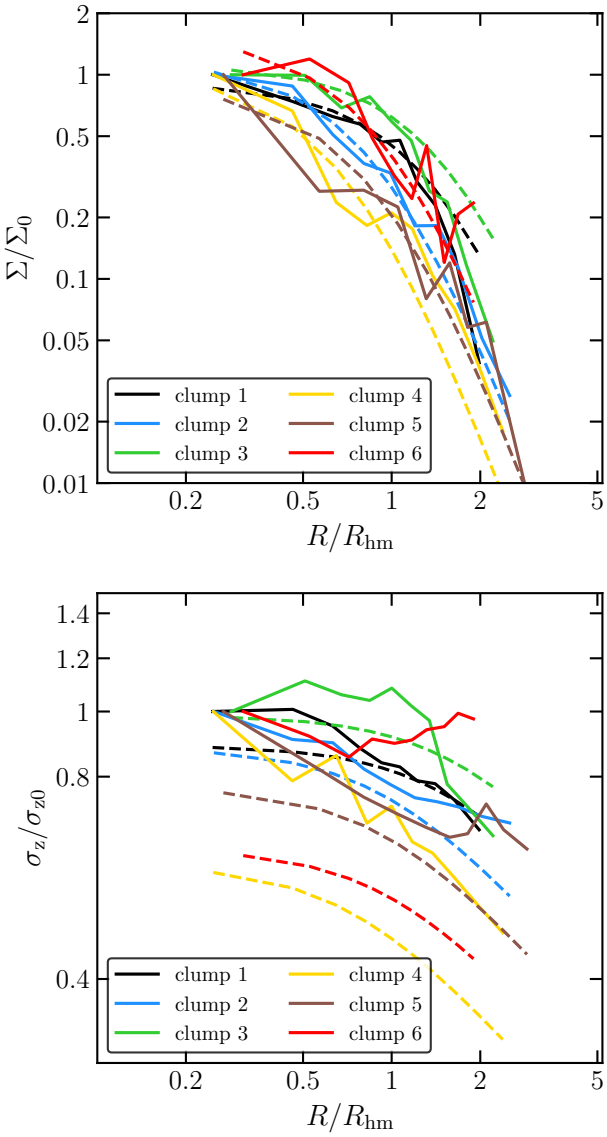

FIGURE 4.22: Surface density profiles (top) and 1D velocity dispersion profiles (bottom) for the TFF09 snapshot. The best-fit Plummer model for each clump is also shown (dashed lines). The best-fit Plummer model is determined by fitting the surface density profile within one projected half-mass radius. The surface density and 1D velocity dispersion are both normalized to the corresponding values in the innermost radial bin of each clump.

We note that our goal here is not to build a detailed model of the LISCA II system, but rather to gather further insight into our observational analysis. Hence, here we just provide a theoretical example of the general dynamical properties expected in a hierarchical stellar cluster undergoing its early evolutionary phases. The model we analyzed is the F025 one of Livernois et al. (2021). The model is fully described in Livernois et al. (2021), but we summarize its main features for the purposes of this study. The model starts with 10^5 stars with mass range $0.08 - 100$ $M_\odot$, initially following a fractal distribution with a fractal dimension equal to 2.6; the system is initially dynamically cold and undergoes the collapse and subsequent structural oscillations typical of the violent relaxation phase. As a reference timescale for the presentation of our results, we adopt the system free-fall timescale, $t_{\rm ff}$, which corresponds approximately to the timescale needed for the system to reach its maximum contraction during its initial collapse. Assuming an initial mass of $5 \times 10^4 - 10^5$ $M_\odot$ and an

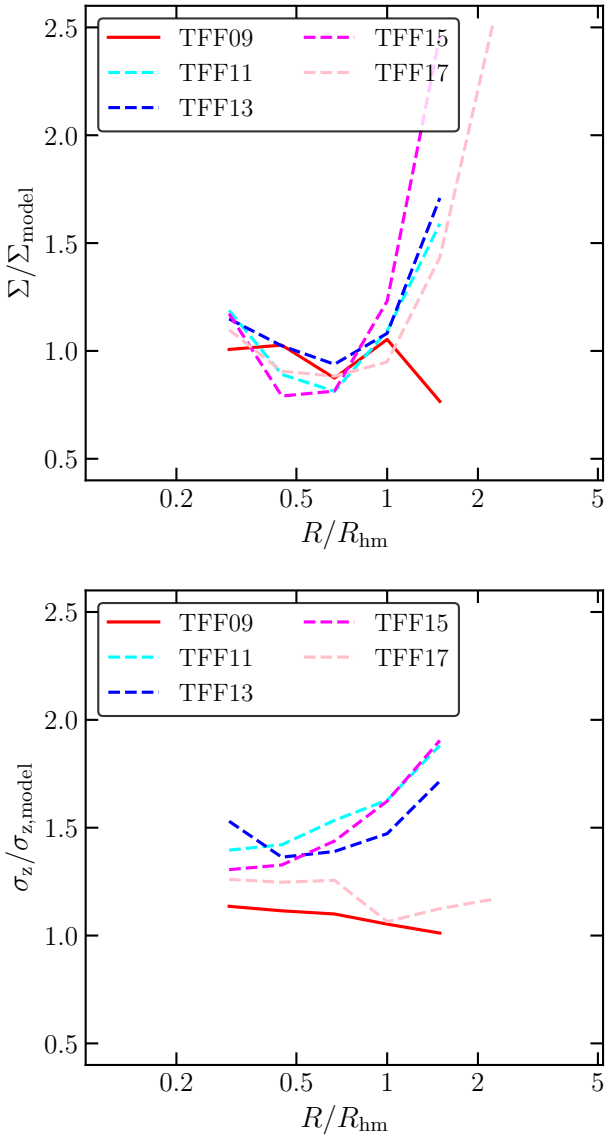

FIGURE 4.23: Radial profiles of the ratio of the clump radial profiles to the best-fit Plummer models for surface density (top) and 1D velocity dispersion (bottom). This ratio is averaged over the three largest clumps within each snapshot.

initial radius of $\sim 50-60$ pc, the $t_{\rm ff}$ would roughly correspond to $20-35$ Myr. To capture the model at multiple evolutionary stages, we focus our attention on the snapshots at the following values of $t/t_{\rm ff}$: 0.9 (denoted TFF09), 1.1 (TFF11), 1.3 (TFF13), 1.5 (TFF15), and 1.7 (TFF17).

4.6.1 Mass segregation and bulk internal motion

We start our analysis with the study of mass segregation in the N-body model and the LISCA II system. Here we focus on an analysis specifically aimed at detecting mass segregation on a local scale, which might provide further insight into the dynamics of systems characterized by the presence of clumps and substructures like those studied here. To quantify the level of mass segregation, we first calculate the local surface number density for each star using the distance of the sixth nearest star of any mass (Casertano & Hut, 1985); the median local

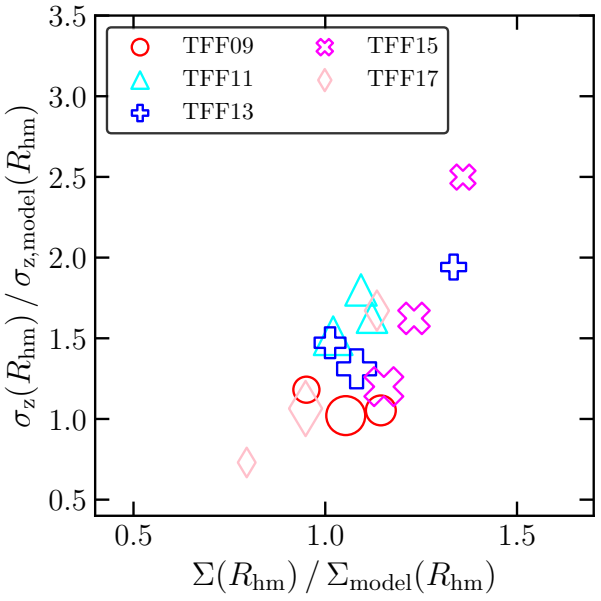

FIGURE 4.24: One-dimensional velocity dispersion vs. projected surface density for the three largest clumps in each snapshot (see legend), each calculated at one projected half-mass radius. The 1D velocity dispersion and the projected surface density are both normalized by the value expected from the Plummer model best fitting the surface density profile. Point sizes are proportional to the total mass of each clump.

surface density of different mass bins, normalized by the median local surface density of the entire cluster, is plotted against the median stellar mass of each bin in figure 4.20. All snapshots show clear evidence of a local surface density increasing with the stellar mass, implying the presence of local-scale mass segregation, where massive stars are migrating toward the centers of the subclusters they are members of. A similar trend is also present in LISCA II, which shows significant local-scale mass segregation, complementing the global-scale mass segregation found in figure 4.14. This trend appears to evolve with time in the model snapshots; the two latest snapshots have the strongest trend of local-scale mass segregation.

Focusing on the bulk internal motion of the system, we analyzed the radial velocity profile of the simulation data as a comparison to figure 4.12. In figure 4.21, we plot the radial velocity profile normalized by the velocity dispersion of the cluster, including only stars with $m > 2M_\odot$. As the cluster evolves, we see the different regions of the cluster transition between expansion and contraction. The TFF09 snapshot is characterized by a trend similar to that found in LISCA II: an expansion of the inner regions and a strong contraction in the outer regions.

4.6.2 Dynamics of subclusters

For insight into the possible dynamical evolution of the subclusters within LISCA II, we analyzed the dynamical properties of selected clumps from our N-body models. For each snapshot in the N-body data, we selected a few clumps in spherical 3D regions and determined their centers as the location of the maximum local density. These clumps are in dynamically active environments, and no clustering metrics were found to be appropriate across all snapshots for clump identification.

We start by showing in figure 4.22 the surface density profile (top panel) and LOS velocity dispersion profile (bottom panel) for the clumps selected in the TFF09 snapshot. We fit a Plummer model based on the surface density profile and enclosed mass within one projected

half-mass radius, and overplot the best-fit model lines. All clumps show radial variation of the surface density profiles following the general shape of the Plummer model; on the other hand, the velocity dispersion profiles are flatter and more elevated than is expected from the best-fit Plummer models. This is the manifestation of the tidal heating in the cluster environment and is similar to what is seen in figure 4.19.

We repeated the above analysis for all of our snapshots, and plot in figure 4.23 the average ratio of the surface density (top panel) and LOS velocity dispersion (bottom panel) to the best-fit Plummer models across the three biggest clumps in each snapshot. The surface density fits well out to approximately one projected half-mass radius, outside of which the clumps generally have a higher density than the best-fit Plummer model; these deviations from the best-fit Plummer model can be attributed to the high density of the surrounding environment and the perturbations due to interactions in the cluster environment. The effects of these perturbations are clearly visible in the LOS velocity dispersion profiles of all the snapshots analyzed. All the velocity dispersion profiles deviate from the profiles expected from the best-fit Plummer models across all radii with a dependence on the projected radius that varies in different snapshots.

Finally, we summarized the relation between structural and kinematic perturbations by plotting, in figure 4.24, the ratio of density and LOS velocity dispersion to the corresponding values of these quantities from the best-fit Plummer models at $R_{\rm h}$ for the three biggest clumps in each snapshot. This plot clearly shows that the fingerprints of the highly active environment, where each clump is undergoing rapid interactions, mergers, and fragmentations, are more evident in the kinematic properties, as illustrated by the larger deviations of the velocity dispersion from the expected equilibrium values.

4.7 Summary and conclusions

The unprecedented quality of the Gaia DR3 data (Gaia Collaboration et al., 2023), supplemented by high-resolution spectra (Fanelli et al., 2022) obtained as part of the SPA-TNG large program, allowed us to identify the LISCA II system in the Perseus complex.

The spectro-photometric, structural, and kinematical properties of this system are in generally good agreement with those theoretically expected from the early dynamical evolution of a massive molecular cloud that experienced violent relaxation and is now in the process of hierarchically assembling its stellar constituents and evolving toward a monolithic structure. In particular, the observed evidence of mass segregation on a local and global scale, the mass-dependent kinematic properties, and out-of-equilibrium internal kinematics of individual subclusters, as well as the observation of a dominant contraction pattern toward the system center mainly driven by the external regions of LISCA II and of a milder central expansion, are compatible with what is expected in the early evolutionary phases of stellar systems assembling as a coherent massive structure by N-body models. The properties of these hierarchical stellar systems are shaped by a combination of large-scale variations of the system's potential and smaller scale interactions of individual subclusters and clumps.

Although more detailed models and additional data would be necessary to further explore the possible fate of this system, the evidence collected suggests that LISCA II is a good candidate to evolve into a young massive ($10^4 - 10^5$ $M_\odot$) star cluster on a timescale of ~ 100

Myr, corresponding to a few free-fall times. These results make LISCA II the second structure, the first being LISCA I (Dalessandro et al., 2021b), ever found in the MW in the process of hierarchically assembling in a massive stellar cluster. LISCA II is located at only $\sim 6°$ from LISCA I, with which it shares similar chemical composition ([Fe/H]$= -0.30$ dex), age ($t \sim 20$Myr), and overall mass.

In conclusion, the present analysis has provided a comprehensive characterization of the process of cluster assembly with a level of detail that cannot be achieved in external galaxies or at high redshift (where the progenitors of the oldest clusters formed), thus showing that probing cluster formation in local environments can help shed light on the physical processes involved in massive cluster formation and their role in determining the cluster's dynamical properties. Moreover, we further showed that hierarchical cluster assembly is a viable process, even in low-density environments such as the MW (former observational evidence was mainly in high-density environments, e.g., Bastian et al., 2011; Chandar et al., 2011), and a statistical assessment of its effectiveness on Galactic scales is the subject of an ongoing study. It is interesting to note in this respect that the possible observed internal age spreads of the stellar populations belonging to LISCA I and II ($\sim$ 10 Myr) nicely fit the observed trend (Parmentier et al., 2014) between the cluster formation environment stellar density and final cluster age internal variations, which possibly results from the different duration of the star formation processes and the link between their efficiency and the systems' free-fall time. This further strengthens the idea that clusters with different present-day properties likely underwent similar formation processes.

Chapter 5

Tracing the W3/W4/W5 and Perseus complex dynamical evolution with star clusters

> "- In my village no one is a stranger - and this is what civilization has turned its back on. One day, Munug, I will make a world of villages, and the age of cities will be over. And slavery will be dead, and there shall be no chains - tell your god. Tonight, I am his knight. - [...]. The old man smiled. - He knows. -"
>
> The Complete Malazan Book of the Fallen, Steven Erikson

As shown by Dalessandro et al. (2021b), and Della Croce et al. (2023, see results presented in Chapter 4), the Perseus complex offers the ideal laboratory for studying cluster formation. Besides the LISCA systems (located in the Per OB1 and Cassiopeia OB8 large associations), the complex hosts an actively star-forming region, known as the W3/W4/W5 complex (hereafter W345). W345, located on the Galactic plane, is a well-studied massive star-forming region, containing two giant H II regions (W4 and W5), a massive molecular ridge with active formation (W3), and several embedded star clusters (e.g., Carpenter et al., 2000; Koenig et al., 2008; Román-Zúñiga et al., 2015; Jose et al., 2016; Sung et al., 2017).

In this Chapter, we present a study that aims to characterize the Preseus region using its star clusters rather than individual stars, thereby complementing previous studies. We first searched for star clusters in the W345 region (in section 5.1), and we studied their structural and kinematical properties (section 5.2). Moving to progressively larger scales, we studied the properties of the W345 complex in section 5.3. Finally, section 5.4 traces the evolution of the Perseus complex using 6D phase-space information of star clusters within it. Conclusions are drawn in section 5.5, and additional material is presented in section 5.6.

The results presented here are part of the recent work: Della Croce et al., submitted to A&A.

5.1 Identifing star clusters in the W345 region

To study the stellar population of the W345 complex we preliminary retrieved from the *Gaia* archive[1] sources with Galactic coordinates $\ell \in [133.5°; 138.5°]$, and $b \in [-0.3°; 2°]$. The

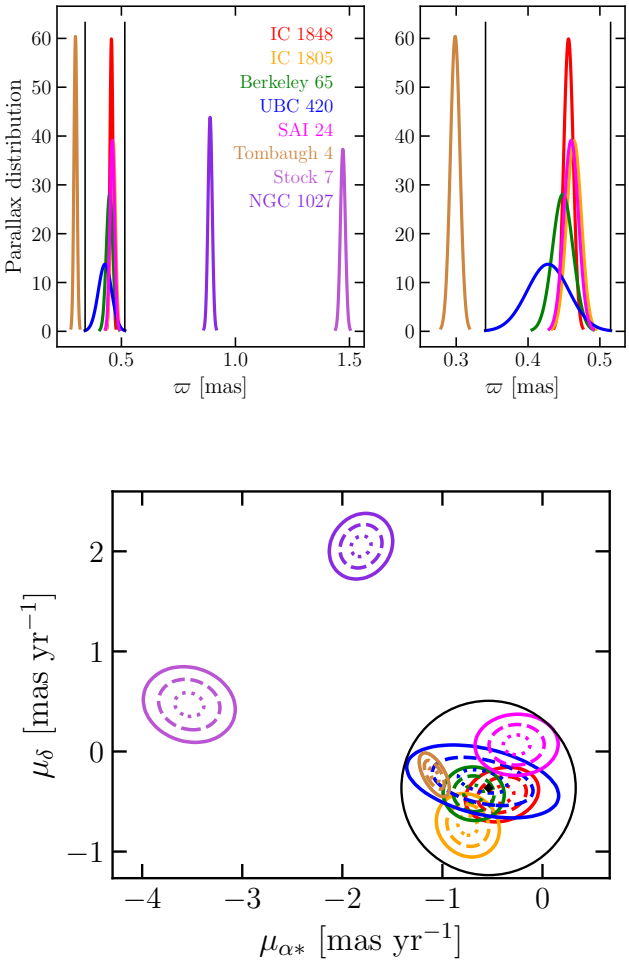

FIGURE 5.1: Intrinsic, i.e. deconvolved, parallax (top panel), and PM (bottom panel) distributions for the eight clusters in the region defined by the preliminary Galactic coordinates ranges. Cluster names are reported in the top left panel. Black lines show the parallax and PM ranges adopted for selecting *Gaia* sources. The top right panel shows a narrower parallax range centered around the W345 star clusters to visualize the cluster parallax distributions better. Finally, in the bottom panel, different contours represent the 1σ (dotted lines), 2σ (dashed lines), and 3σ (solid lines) regions for each cluster. Also, correlations among $\mu_{\alpha*}$ and μ_δ are visible.

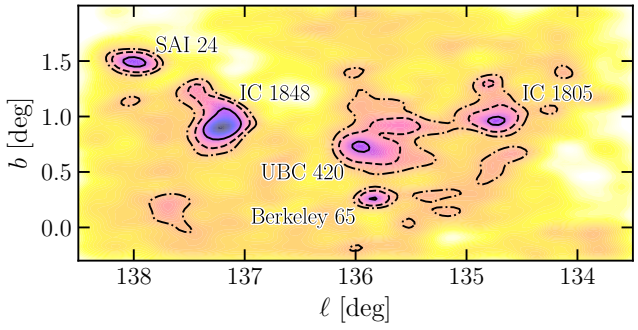

FIGURE 5.2: Two-dimensional density map in Galactic coordinates of *Gaia* sources after the parallax and PM selections. Darker colors for denser regions. Iso-density contours at 0.5σ (solid), 1σ (dashed), and 1.5σ (dash-dotted) are shown in black. The cluster positions and names are marked.

[1] https://gea.esac.esa.int/archive/

ranges are defined such that they enclose the W345 complex as traced by the gas distribution at NIR wavelengths (e.g., from the allWISE survey, Wright et al., 2010). We further selected sources with G magnitude brighter than 18 (i.e., `phot_g_mean_mag` < 18) and having parallax and PM measurements (i.e., `astrometric_params_solved` $= 31$). We did not apply any prior cut in parallax or PM to avoid possible selection biases in tracing the stellar content (and thus cluster population) of the complex. Instead, we performed data-driven selections as explained in the following (see also Della Croce et al., 2023).

We performed an unsupervised clustering analysis on the whole catalog using the `HDBSCAN`[2] algorithm (McInnes et al., 2017) to identify overdensities in the five-dimensional space of Galactic coordinates (ℓ, b), PM $(\mu_{\alpha*}, \mu_\delta)$, and parallax (ϖ). After several tests, we adopted as input parameters `min_cluster_size` $= 50$ and `min_sampels` $= 30$. Twelve overdensities were thus identified as star cluster candidates in the region, but four of them were then flagged as false detections by the post-processing routine. We refer the interested reader to Hunt & Reffert (2021) for the details of the post-processing routine. Briefly, the nearest-neighbor distance among candidate members and field stars is used as a proxy for local density contrast. Only structures significantly denser than nearby Galactic field stars are considered as true stellar clusters. The eight clusters identified in our analysis are all known in literature (e.g., Cantat-Gaudin et al., 2020; Hunt & Reffert, 2023). Namely, they are IC 1848, IC 1805, Berkeley 65, UBC 420, SAI 24, Tombaugh 4, Stock 7, and NGC 1027. We note that one additional cluster (with a reported number of members greater than 50) is known in the region: UBC 1242 (Castro-Ginard et al., 2022; Hunt & Reffert, 2023). Our analysis recovered the cluster but was later rejected as a false positive from the post-processing routine, probably due to the small density contrast with respect to the surrounding field stars.

We then studied the parallax and PM distributions for the eight clusters identified. The observed parallax and PM distributions were deconvolved using Gaussian modeling and properly accounting for errors and correlations between measurements, thereby obtaining their intrinsic distributions. In particular, for each star i we defined the covariance matrix

$$\Sigma_i = \begin{pmatrix} \delta\mu_{\alpha*}^2 & \rho_{\mu_{\alpha*}\mu_\delta}\delta\mu_{\alpha*}\delta\mu_\delta & \rho_{\mu_{\alpha*}\varpi}\delta\mu_{\alpha*}\delta\varpi \\ \rho_{\mu_{\alpha*}\mu_\delta}\delta\mu_{\alpha*}\delta\mu_\delta & \delta\mu_\delta^2 & \rho_{\mu_\delta\varpi}\delta\mu_\delta\delta\varpi \\ \rho_{\mu_{\alpha*}\varpi}\delta\mu_{\alpha*}\delta\varpi & \rho_{\mu_\delta\varpi}\delta\mu_\delta\delta\varpi & \delta\varpi^2 \end{pmatrix}_i , \tag{5.1}$$

where $\delta\mu_{\alpha*}$, $\delta\mu_\delta$, and $\delta\varpi$ are the individual errors, and ρ_{ab} is the correlation coefficient among the a and b quantities. Using the Extreme Deconvolution package[3] by Bovy et al. (2011), we obtained the best fit mean PM components $(\langle\mu_{\alpha*}\rangle, \langle\mu_\delta\rangle)$ and parallax $(\langle\varpi\rangle)$, along with the corresponding dispersions around the mean values, namely $\sigma_{\mu_{\alpha*}}$, σ_{μ_δ}, σ_ϖ. We ran this analysis on likely cluster member stars adopting a membership threshold, as defined by the clustering algorithm, of 90%) and selecting stars with reliable astrometry (Lindegren et al., 2021a): `ruwe` < 1.4, $\delta\varpi/\varpi < 0.2$, and `astrometric_excess_noise` smaller than the 95th percentile (applied only to stars with `astrometric_excess_noise_sig` > 2). We tested different membership thresholds (down to 70%), finding compatible results, within the errors.

[2] https://hdbscan.readthedocs.io/en/latest/index.html
[3] https://github.com/jobovy/extreme-deconvolution

Figure 5.1 shows the parallax and PM intrinsic distributions. Some clusters are grouped in both spaces, including the young clusters typically associated with the W345 complex, such as IC 1848, and IC 1805. Therefore, to identify the stars belonging to W345 in the *Gaia* catalog, we exploited the intrinsic distributions of those clusters showing similar (within 3σ) parallax and PMs. In particular, five out of eight clusters presented compatible distributions in both spaces: IC 1848, IC 1805, Berkeley 65, UBC 420, and SAI 24. We then defined the sources belonging to the W345 region by selecting stars with parallax and PM within 3σ from the mean value of any of the five clusters. For the parallax, this translates into sources with $\varpi \in [0.341; 0.515]$ mas. In the PM space, sources within 0.87 mas yr^{-1} from $(\langle\mu_{\alpha*}\rangle, \langle\mu_\delta\rangle) = (-0.539; -0.364)$ mas yr^{-1} were selected. The PM reference point was obtained as the average of the five mean cluster motions. Such ranges are also depicted in figure 5.1. These data-driven selections in parallax and PM allowed us to adopt some physically motivated ranges for the region under investigation, avoiding any a priori selection. The final catalog counts 8869 sources.

In table 5.1 we list the mean cluster properties. We find a good agreement ($< 2\sigma$) with Hunt & Reffert (2023) for IC 1848, IC 1805, and Berkeley 65 and an excellent ($< 1\sigma$) agreement with Cantat-Gaudin & Anders (2020) for UBC 420, which is not included in the "bona fide" cluster sample by Hunt & Reffert (2023).

Table 5.1: Mean properties of clusters in the W345 complex

Cluster	(α, δ)	$\langle\mu_{\alpha*}\rangle$	$\sigma_{\mu_{\alpha*}}$	$\langle\mu_\delta\rangle$	σ_{μ_δ}	$\langle\varpi\rangle$	σ_ϖ	$\rho_{\mu_{\alpha*}\mu_\delta}$	$\rho_{\mu_{\alpha*}\varpi}$	$\rho_{\mu_\delta\varpi}$
	[degree]	[mas yr^{-1}]		[mas yr^{-1}]		[mas]				
IC 1848	(42.851, 60.438)	-0.40	0.12	-0.43	0.09	0.456	0.007	0.19	0.43	0.12
IC 1805	(38.198, 61.510)	-0.75	0.11	-0.74	0.11	0.464	0.010	-0.13	-0.32	-0.09
Berkeley 65	(39.766, 60.408)	-0.69	0.10	-0.42	0.09	0.448	0.014	-0.03	-0.60	-0.19
UBC 420	(40.174, 60.864)	-0.60	0.25	-0.30	0.12	0.428	0.029	-0.39	-0.16	0.09
SAI 24	(44.732, 60.578)	-0.26	0.14	0.07	0.10	0.460	0.010	0.02	0.42	0.30

Notes. Cluster name, center celestial coordinates, mean PM along the right ascension and declination coordinates, mean parallax, along with the corresponding intrinsic distribution widths. The last three columns list the correlation coefficients.

Finally, figure 5.2 shows a 2D density map of the region. Clusters clearly appear as overdensities and are clustered in three main regions corresponding to W4 (e.g., Lim et al., 2020), W5-E (e.g., Karr & Martin, 2003), and W5-W (e.g., Morgan et al., 2004). The W3 region is indeed deeply embedded in the gas and hardly probed by *Gaia* (see e.g., Román-Zúñiga et al., 2015).

5.2 Properties of star clusters in the W3/W4/W5 region

5.2.1 Structure

We constructed projected number counts density profiles for each cluster using stars with membership above 70% [4]. The density was obtained in spherically symmetric and evenly-populated bins centered on the median cluster positions (see table 5.1). In each radial bin, the density was computed as the average of the values obtained in four angular sectors and the standard deviation of these different measurements (summed in quadrature with Poissonian error) was adopted as the error.

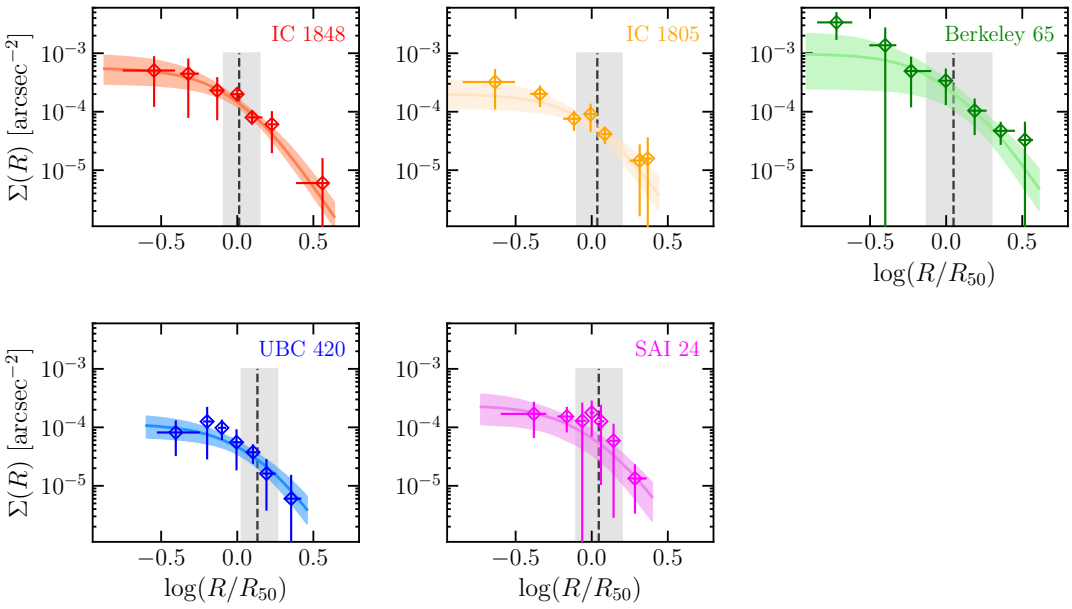

FIGURE 5.3: Projected number density profiles for the five clusters analyzed in this study. Distances from the center were normalized to $r_{\rm h}$. Errors in each evenly-populated bin were computed as the standard deviation of density measurements in different angular sectors (concerning the y axis) and as the quantiles of the radial distribution within the bin (for the x axis). The solid lines show the median Plummer model fit of the profile, whereas the shaded areas show the 68% (i.e., 1σ) confidence interval. Finally, the dashed black lines (the gray shaded areas) show the median Plummer scale radius (68% confidence interval) from the marginalized posterior distributions.

Figure 5.3 shows the cluster number density profiles obtained this way. We then fitted the observed density profiles with Plummer (1911) models (see figure 5.3). The best-fit models were obtained through a Markov chain Monte Carlo (MCMC) exploration of the parameter space, using the `emcee`[5] Python package (Foreman-Mackey et al., 2013). In general, Plummer models reproduce the observed density profiles fairly well. Indeed, the Plummer

[4] For SAI 24 we adopted instead a membership threshold of 75% as a lower threshold would also include small clumps of spatially detached stars, possibly biasing the calculation of the cluster density structure.

[5] The package is publicly available at `https://emcee.readthedocs.io/en/stable/`.

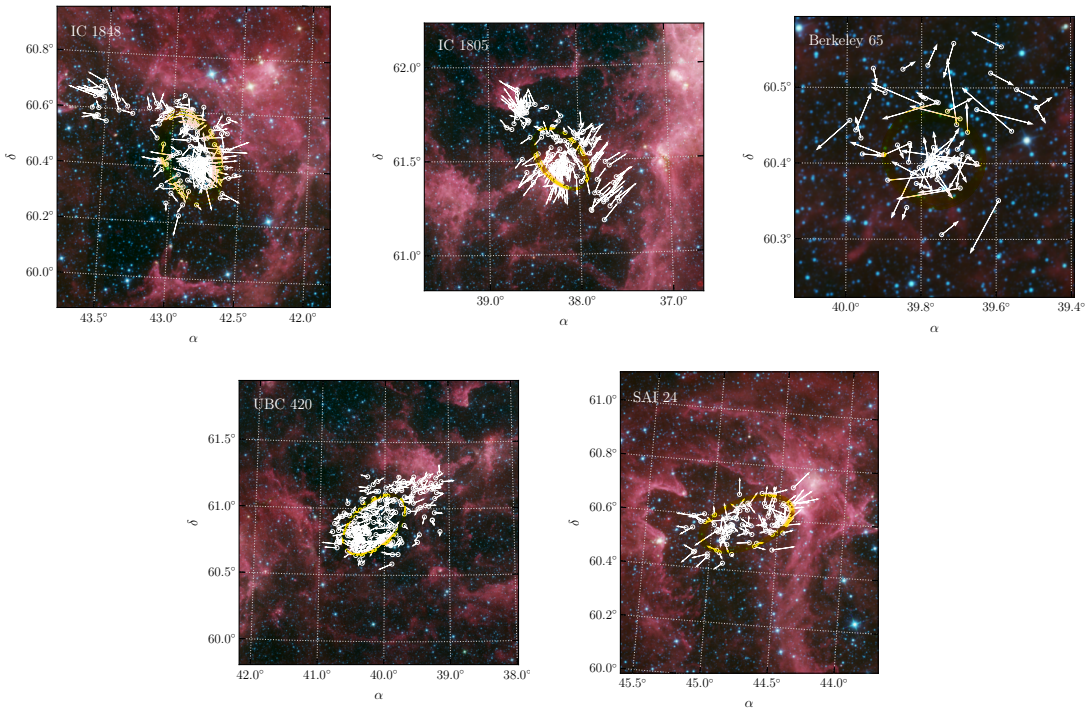

FIGURE 5.4: On-sky spatial distribution of cluster members. For each cluster star, PM vectors are shown on top of the RGB image of the region from the allWISE survey. We mapped the W3 band in red, W2 in green, and W1 in blue. The W3 filter mainly traces small grain dust and polycyclic aromatic hydrocarbon emissions, whereas the W1 and W2 filters are dominated by young stars (Wright et al., 2010). The best-fit ellipses of the spatial distributions are shown in gold.

radii ($R_{\rm Plummer}$, inferred from the density profile fitting) and the 2D radii enclosing half of the members ($r_{\rm h}$, directly computed from the cluster member spatial distributions) agree in general within less than 1σ (see figure 5.3, and the values reported in table 5.2).

We further characterized the morphological properties of each cluster by determining the axis ratio (q) and the position angle (PA) defined respectively as the ratio between the minor and major axes and the angle between the semi-major axis and the positive x direction. We thus constructed the so-called shape tensor (Zemp et al., 2011), which is defined by the following equation:

$$S_{\rm ij} \equiv \frac{\sum_{\rm k=1}^{\rm k=N} (R_{\rm k})_{\rm i} (R_{\rm k})_{\rm j}}{N}\,, \tag{5.2}$$

where $R_{\rm k}$ is the projected distance from the cluster center of the k-th star, within the i-th and j-th elements of the shape tensor grid, and N is the total number of cluster member stars. The shape tensor was computed starting from a spherical grid, whose nodes are the stellar radial distribution's 10th, 50th, and 90th percentiles. We adopted an iterative procedure for each bin during which the shape tensor is initially constructed from spherical distances. After that, with $(w_0; w_1)$ being the eigenvalues (with $w_0 > w_1$) and $(\boldsymbol{v}_0; \boldsymbol{v}_1)$ the respective

TABLE 5.2: Structural, photometric, and kinematic properties of clusters in the W345 complex

Cluster	$R_{\rm Plummer}$ [arcsec]	$r_{\rm h}$ [arcsec]	q	PA [deg]	age [Myr]	$\langle v_{\rm R}\rangle/\sigma_{\rm R}$
IC 1848	377^{+132}_{-77}	367^{+12}_{-10}	$0.59^{+0.02}_{-0.03}$	73^{+2}_{-2}	5^{+1}_{-1}	$0.64^{+0.08}_{-0.09}$
IC 1805	579^{+264}_{-158}	531^{+8}_{-9}	$0.59^{+0.04}_{-0.07}$	51^{+4}_{-4}	5^{+1}_{-1}	$1.01^{+0.10}_{-0.08}$
Berkeley 65	151^{+137}_{-51}	133^{+17}_{-2}	$0.85^{+0.05}_{-0.06}$	26^{+49}_{-12}	33^{+2}_{-2}	$0.06^{+0.13}_{-0.13}$
UBC 420	972^{+355}_{-208}	722^{+27}_{-13}	$0.58^{+0.02}_{-0.04}$	137^{+1}_{-2}	8^{+1}_{-1}	$0.05^{+0.07}_{-0.07}$
SAI 24	401^{+169}_{-117}	363^{+5}_{-8}	$0.49^{+0.01}_{-0.02}$	159^{+2}_{-2}	5^{+1}_{-1}	$0.83^{+0.12}_{-0.12}$

Notes. Cluster name, Plummer scale radius, median cluster-centric distance, axis ratio, position angle, age, and the ratio between mean velocity and velocity dispersion. Errors on $r_{\rm h}$, q, and PA were computed through 1000 bootstrap extractions of the 90% of the sample. We stress that such analysis accounts only for fluctuations due to small statistics or outliers. Values obtained through a proper exploration and sampling of the parameter space, as the one performed for $R_{\rm Plummer}$, are thus more realistic.

eigenvectors of the shape tensor, it follows (Zemp et al., 2011) that

$$q = \frac{w_1}{w_0} \quad \text{and} \quad \text{PA} = \arctan\frac{v_{0,\rm y}}{v_{0,\rm x}}\,. \tag{5.3}$$

The particle coordinates were then rotated by the angle $-$PA, and distances to the center were defined by means of the circularized distance

$$R_{\rm ell} \equiv \sqrt{x'^2 + \frac{y'^2}{\epsilon^2}}\,, \tag{5.4}$$

where $(x';y')$ are the rotated, locally Cartesian coordinates of the stars. Finally, stars were binned in the new coordinate system according to the initial grid, and the shape tensor was computed using $R_{\rm ell}$ instead of R. Such a procedure was then iterated until a relative precision of 10% on the axis ratio was reached. Best-fit q and PA values and relative errors were obtained by means of a bootstrapping analysis. In detail, the shape tensor was computed 1000 times for each cluster by randomly selecting a subsample including only 90% of the stars at each time. The values corresponding to the 50th percentile of the distributions of all the q and PA values were then adopted as the best fits, while the errors correspond to the 16th and 84th percentiles.

Figure 5.4 presents the spatial distribution of cluster members with best-fit ellipses on top of false RGB images of the gas emission in the region. The possible link between elongation and internal kinematics is discussed in section 5.2.3, while the values are reported in table 5.2. Generally, all clusters in our analysis are pretty elongated, with the youngest clusters representing the most extreme cases.

5.2.2 Differential reddening and cluster ages

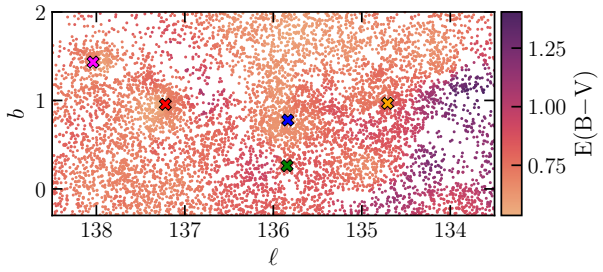

FIGURE 5.5: Spatial distribution in Galactic coordinates of *Gaia* DR3 sources, selected according to section 5.1. Each star is color-coded according to its reddening value. Crosses show the centers of the five stellar clusters analyzed in this work (SAI 24 in purple, IC 1848 in red, Berkeley 65 in green, UBC 420 in blue, and IC 1805 in yellow).

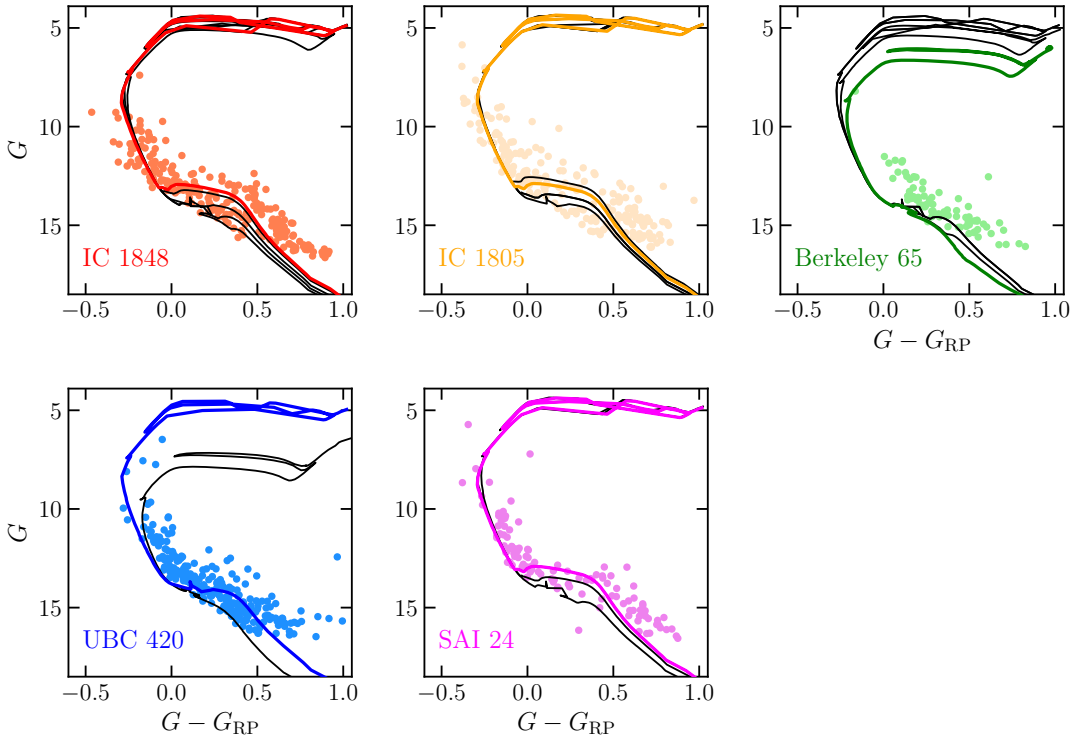

FIGURE 5.6: Color magnitude diagrams in the *Gaia* filters for cluster members. The best-fit isochrones from differential-reddening-corrected, *G*-band luminosity function fits are shown using the same color palette as cluster members. In black are multiple isochrones from literature works: Cantat-Gaudin et al. (2019b); Dias et al. (2021); Hunt & Reffert (2023); Cavallo et al. (2024).

We constrained cluster ages by fitting the cumulative luminosity function in the differential reddening corrected *G* band as previously done in Della Croce et al. (2023, see Chapter 4). Differential reddening was computed using the same approach described in the same Chapter. Briefly, *Gaia* DR3 sources selected according to section 5.1 were cross-matched with panSTARRS DR1 exploiting the matching tables provided by the *Gaia* Data Processing and

Analysis Consortium. We thus retrieved g, r, i, z, and y-band photometry for the 98% of the stars selected in *Gaia*. We then used the color-color ($G - r$, $i - z$) diagram to assign star-by-star relative reddening values. In particular, for each star, we computed the distance along the reddening vector from the median colors of the closest 50 neighbors (to minimize fluctuations) and a reference point (see Della Croce et al., 2023, for further technical details). We used IC 1848 member stars as a reference, as previous studies (e.g., Cantat-Gaudin & Anders, 2020; Hunt & Reffert, 2023; Cavallo et al., 2024) roughly agree on the extinction value of this system, of about $A_V = 1.86$ mag. On the contrary, either large discrepancies or much larger extinction values are reported for other clusters, such as Berkeley 65 or IC 1805. Figure 5.5 shows the resulting two-dimensional reddening map of the region: as expected, sparser areas are characterized by higher extinction values, suggesting that lower-density regions correspond to areas of significant photometric incompleteness. Indeed, these under-sampled regions trace the spatial distribution of the W3, W4, and W5 GMCs (Koenig et al., 2008; Megeath et al., 2008).

Given the large *Gaia* photometric bands (Jordi et al., 2010), extinction coefficients also depend on the star's effective temperature. We accounted for such an effect following Danielski et al. (2018) and using extinction temperature-dependent coefficients tailored to *Gaia* DR3[6]. We note that such relations were calibrated for an effective temperature ($T_{\rm eff}$) range of $3500 - 10000$ K (Gaia Collaboration et al., 2018), however for clusters as young as 5 Myr we sample stars as hot as $T_{\rm eff} = 30000$ K. Nonetheless, we adopted such relations for all the stars, although they were extrapolated for the hottest stars in the sample. Figure 5.6 shows the differential reddening corrected color-magnitude diagrams along with the best-fit isochrones as obtained from the G luminosity function analysis. Our analysis shows that the clusters in the W345 region are almost coeval with Berkeley 65 being the older one, with an age of 33^{+2}_{-2} Myr. Table 5.2 reports the inferred ages, which are in good agreement with the literature estimates, confirming that IC 1805, IC 1848, and SAI 24 are the youngest clusters in the region (with an age of about 5 Myr). We note however, that for UBC 420 we infer an age of 8^{+1}_{-1} Myr significantly younger than the reported age of $\sim$ 65 Myr by Cantat-Gaudin et al. (2019b). The reason for the discrepancy may reside in the different member compilations. Indeed, no UBC 420 members with $G < 9$ mag are present in the catalog by Cantat-Gaudin et al. (2019b), possibly leading to the inference of an older age.

5.2.3 Kinematics

In this section, we present the analysis of the internal dynamical properties of the five stellar clusters. Their kinematics can in principle give us insights into several physical processes: from the interplay between gas and stellar dynamics, the role of massive star feedback in both sweeping out the left-over gas and triggering star formation, up to cluster-cluster interactions.

In figure 5.4 we show the spatial distribution of likely member stars on top of a false-color RGB image using allWISE photometry (Wright et al., 2010). Figure 5.4 shows that some clusters in the sample, namely IC 1848, IC 1805, UBC 420, and SAI 24 are still partially embedded in the gas (at least in projection), whereas Berkeley 65 does not show any clear evidence of surrounding gas. This is consistent with the picture of it being older (see figure 5.6), and

[6] See the online documentation `https://www.cosmos.esa.int/web/gaia/edr3-extinction-law`.

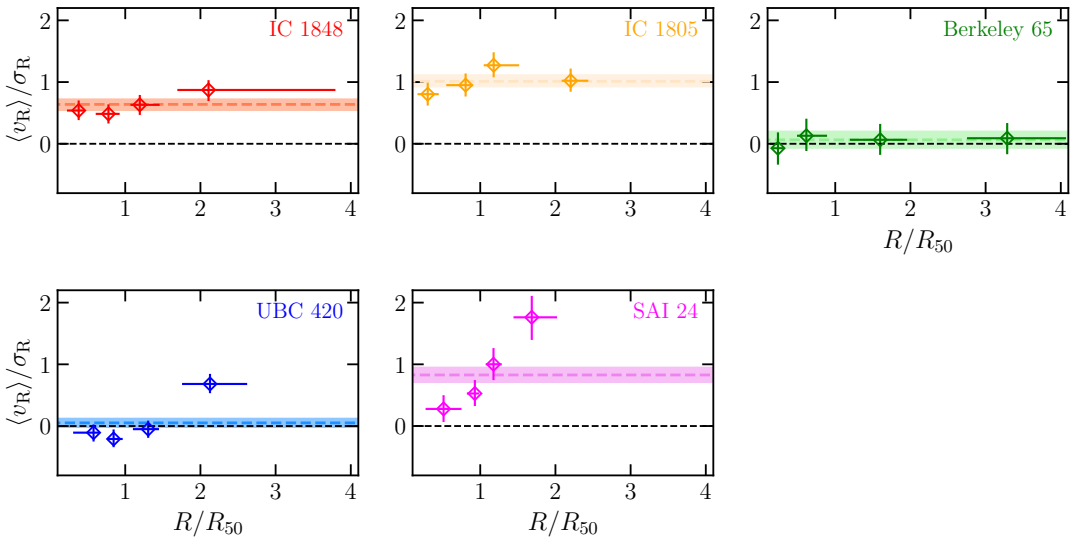

FIGURE 5.7: Mean radial velocity to the radial velocity dispersion ratio profiles. Cluster-centric distances were normalized to R_{50}. The integrated values using all the cluster members are shown as horizontal lines (along with errors depicted as shaded areas). A black dashed line marks the zero expansion (contraction) level.

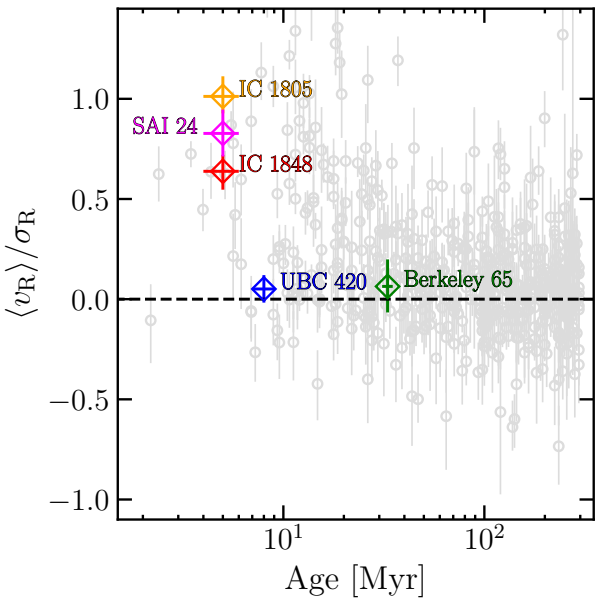

FIGURE 5.8: The ratio between the radial mean velocity and velocity dispersion as a function of the cluster age. Underlying data are from Della Croce et al. (2024b). Different colors highlight the position and results for the clusters analyzed in this work.

having completely removed its primordial gas. Figure 5.4 also shows the projected velocity vectors for member stars: at least three clusters exhibit clear expansion features i.e., IC 1848, IC 1805, and SAI 24, with IC 1805 standing out for amplitude and coherence. Consistently, previous studies reported evidence for expansion for these systems (e.g., Lim et al., 2020).

Several processes can cause clusters to expand, such as left-over gas removal and violent relaxation processes (Elmegreen, 1983; Mathieu, 1983; Kroupa et al., 2001; Goodwin & Bastian, 2006; Pelupessy & Portegies Zwart, 2012; Dinnbier & Kroupa, 2020a,b; Dinnbier et al., 2022; Farias & Tan, 2023; Della Croce et al., 2024b), tidal forces from nearby clouds (Elmegreen & Hunter, 2010; Kruijssen et al., 2011), up to sub-cluster mergers (Wright et al., 2019, and references therein). Interestingly, Lim et al. (2020) studied the internal kinematics of IC 1805 and found that the cluster is composed of an isotropic core (defined as the region within the half-mass radius) and an external expanding halo. By investigating the distribution of individual radial velocities we found that while a fraction of stars are symmetrically distributed around zero within $0.7\ r_{\rm h}$ (about the half-mass radius reported by Lim et al. 2020), there is an excess of stars departing from the cluster center with increasing speed, hence driving the expansion signal also within $r_{\rm h}$ (see e.g. figure 5.7). Furthermore, most cluster members are enclosed within the tidal radius (roughly corresponding to $2.25\ r_{\rm h}$ according to the estimate by Lim et al. 2020) and there is no significant evidence of extra-tidal features. This suggests that internal processes are likely responsible for the observed expansion rather than Galactic tidal forces (as already suggested by Lim et al., 2020).

Expansion can also shape the cluster distribution if stars depart faster in a direction than its orthogonal one, a process usually referred to as asymmetric expansion (see e.g., Wright et al., 2019). In figure 5.4 we show the ellipses describing the cluster shapes. The PA and q defining these ellipses were obtained as described in section 5.2.1 (values are reported in table 5.2). All clusters exhibit significant deviation from spherical symmetry and complex structures (as routinely found in many star-forming regions, see e.g. Cartwright & Whitworth 2004; Gutermuth et al. 2008). We thus studied the distribution of individual radial velocities ($v_{\rm R}$, i.e., the proper motion vector projected along the radial direction from the cluster center) as a function of elliptical radii $R_{\rm ell} \equiv \sqrt{x'^2 + y'^2/q^2}$ (where x' and y' are projected Cartesian coordinates rotated according to PA), or distance along the semi-major axis (a). In the case of expansion-driven elongations, we would expect tighter correlations between $v_{\rm R}$ and $R_{\rm ell}$ (or a) than with circular radii. However, we did not find significant differences for all the clusters investigated except possibly for IC 1848. This suggests that the cluster's internal kinematics does not drive the present-day cluster morphologies. In contrast, it is likely inherited either from processes that occurred earlier (possibly tidal interactions or mergers) or from the parent gas structure.

Finally, we delved into the expansion features shown by the clusters. In particular, we used the ratio between the mean radial velocity and radial velocity dispersion, $\langle v_{\rm R} \rangle / \sigma_{\rm R}$, as defined in Della Croce et al. (2024b, see table 5.2 for the results). This integrated quantity provides a direct indication of the expansion ($\langle v_{\rm R} \rangle / \sigma_{\rm R} > 0$), contraction ($\langle v_{\rm R} \rangle / \sigma_{\rm R} < 0$), or equilibrium ($\langle v_{\rm R} \rangle / \sigma_{\rm R} = 0$) state of the system. Also, it allows meaningful comparison between different clusters as opposed to absolute quantities like $\langle v_{\rm R} \rangle$ (see Della Croce et al., 2024b). For the five clusters included in this study, we also computed radial profiles of $\langle v_{\rm R} \rangle / \sigma_{\rm R}$, presented in figure 5.7, which give us a more complete picture of the cluster's internal kinematics. Radial trends are observed in IC 1848, IC 1805, and SAI 24, reaching values as high as $\langle v_{\rm R} \rangle / \sigma_{\rm R} \simeq 1 - 2$ (see figure 5.7). On the other hand, distributions consistent with equilibrium are found in Berkeley 65, and UBC 420. There are a few more additional interesting points highlighted in figure 5.7: Berkeley 65 shows a flat $\langle v_{\rm R} \rangle / \sigma_{\rm R}$ profile centered around 0 over a large radial extension ($> 3 r_{\rm h}$). On the other hand, the external stars

of UBC 420 are departing from the cluster bulk members. This is particularly evident in the north-east side of the cluster (see figure 5.4) possibly suggesting that these stars are currently being stripped from the cluster.

Lastly, we present the expansion properties of clusters in the W345 complex within the larger picture of the expansion of young Galactic clusters (Della Croce et al., 2024b, see Chapter 3). In Figure 5.8 we show $\langle v_R \rangle / \sigma_R$ as a function of the cluster ages for all the systems studied in Della Croce et al. (2024b, Chapter 3) along with the five clusters analyzed in this Chapter. The W345 complex clusters perfectly fit in the general emerging picture in which young ($\lesssim 30$ Myr) stellar systems are preferentially expanding, while older ones are roughly compatible with equilibrium configurations. We also note that except for IC 1848, IC 1805, and SAI 24, other clusters were not included in our previous study due to missing LOS velocity in Tarricq et al. (2021) catalog. Here we adopted the mean LOS velocity of -39 km s^{-1}(obtained from high-resolution spectra by Fanelli et al., 2022). Nonetheless, we checked that perspective effect corrections (van Leeuwen, 2009) are typically negligible ($< 1\%$) for these clusters.

5.3 Young stars in the W3/W4/W5 region: their link with star clusters

On a larger scale, the Perseus complex is an extended region of recent star formation located towards the Galactic anti-center, which hosts several star clusters and associations. In particular, some of these clusters were found to be organized in larger hierarchical agglomerates that we named LISCA I (Dalessandro et al., 2021b), and LISCA II (Della Croce et al., 2023). These are likely the fossils of the star formation within a large gas cloud a few tens of million years ago, and the possible progenitor of massive (a few $10^5 M_\odot$) stellar systems forming hierarchically.

5.3.1 The YSO population

Young stellar objects (YSOs) trace the most recent star-formation sites, typically younger than a few million years. They thus are used to trace star formation in giant molecular clouds and to constrain the role played by massive stars in either halting or promoting star formation (see Massey et al., 1995; Koenig et al., 2008; Megeath et al., 2008; Niwa et al., 2009; Morgan et al., 2009; Chauhan et al., 2011a,b, for a compilation of studies on the W345 complex). Many studies looked for YSOs in regions of recent star formation, primarily exploiting color-color selections for their identification (e.g., Allen et al., 2004; Whitney et al., 2004; Koenig et al., 2008; Snider et al., 2009; Cutri et al., 2013, 2021; Yadav et al., 2016; Jose et al., 2016; Panwar et al., 2017, 2019). YSOs indeed exhibit infra-red (IR) emission excess due to infalling, and illuminated material in their early stages and disk emission later on, historically referred to as Class I and Class II, respectively, and classified according to their near IR (NIR) spectral energy distribution slope (Adams et al., 1987; Whitney et al., 2003a,b). Also, young stars are prominent X-ray emitters due to magnetic reconnection flares at the stellar surface (see e.g., Güdel & Telleschi, 2007), hence X-ray observations could be used to complement infrared catalogs of YSOs (Hofner et al., 2002; Feigelson & Townsley, 2008; Rauw & Nazé, 2016; Townsley et al., 2019).

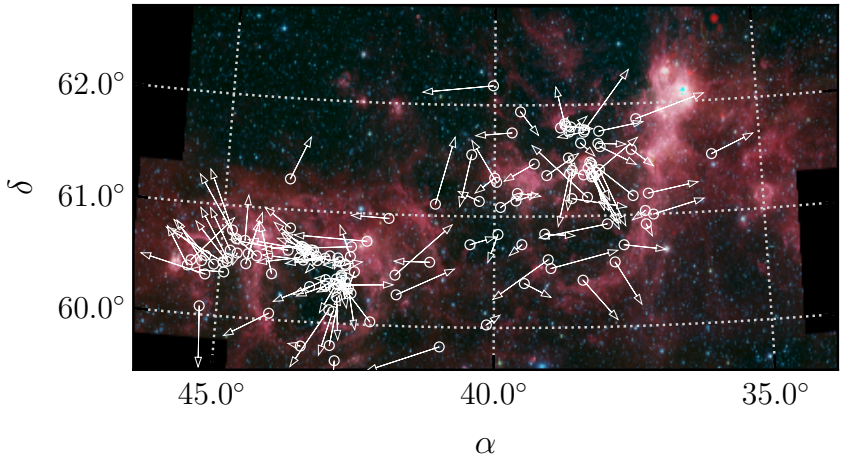

FIGURE 5.9: Spatial distribution of the *Gaia* YSO sample, with PMs depicted with arrows. PMs were referred to the clusters mean motion in the regions (see section 5.1). The background image is the composite RGB image of the W345 complex using data from the allWISE survey.

Koenig et al. (2008) studied the star-formation history of the W345 region, by using YSOs identified through the Spitzer space telescope. Furthermore, Panwar et al. (2017, 2019) characterized the low-mass YSO population around IC 1805 through a multi-wavelength approach from the NIR to the X-rays. In particular, Panwar et al. (2019) supplemented the YSO catalog with *WISE* data. They used the YSO catalog by Cutri et al. (2013, 2021) from the allWISE program.

While these studies deeply characterized the YSO spatial distribution and its link with the gas, YSO kinematics in the region remains largely unexplored. We thus aim to study their kinematics in the context of the W345 complex. To do so, we cross-matched the catalogs by Koenig et al. (2008); Cutri et al. (2013, 2021); Panwar et al. (2019) with *Gaia* data. We selected Class I and Class II sources from Koenig et al. (2008), and non-extended, non-variable sources from Cutri et al. (2013, 2021), with confusion flags "000" and with photometric quality flags not worse than "B" in each band. The starting YSO catalog comprised 4096 sources almost half of which were from Koenig et al. (2008). The catalog was then crossmatched with *Gaia* DR3 sources selected in section 5.1, obtaining a final catalog of 178 (about 4.4% of the starting one, out of which 129 had good astrometry according to *Gaia* quality flags, see section 5.1) sources. We will refer to this catalog as the *Gaia* YSO. In figure 5.9 we show the spatial distribution of *Gaia* YSOs with PM vectors shown as arrows. We note that: *i)* YSOs are spatially concentrated either at the edges of the gas distribution or at young star cluster locations (e.g., SAI 24, IC 1848, IC 1805, see section 5.2.2); *ii)* YSOs trace the expansion observed in IC 1805, and IC 1848 (see section 5.2.3); *iii)* in the W5-E region (around $\alpha \simeq 45°$, see Karr & Martin 2003), YSOs are coherently moving northward. Given their position on the north side of the W5-E HII region, their motion may be inherited from the parent gas. This analysis further confirms that YSO kinematics is a powerful tool for tracing young cluster formation.

5.3.2 Bright-rimmed cloud ionizing sources

TABLE 5.3: Properties of the ionizing sources in the W345 complex

SIMBAD identifier	*Gaia* DR3 `source_id`	region	BRCs	cluster	membership
BD 60 502 / HD 15558	465528726379402112	W4	5,7,8,9	-	-
BD 60 504 / HD 15570	465527523789596160	W4	5,6,7,8,9	-	-
BD 60 507 / HD 15629	465535048571192704	W4	5,7,8,9	IC 1805	100%
HD 17505	-	W5-West	10,11	-	-
BD 60 586	464697873547937664	W5-West	12	IC 1848	65%
BD 59 578 / HD 18326	466127062559750528	W5-East	13,14	SAI 24	100%
V 1018 Cas	463122720055223168	W5-East	pillars	SAI 24	72%

Notes. Star name (multiple identifiers are listed if present). Unique *Gaia* DR3 `source_id`, crossmatched from the SIMBAD database (for all but HD 17505 which is not in *Gaia* although present in the HIPPARCOS catalog). Region of the W345 complex where the star belongs. BRCs (or pillars) the source is likely ionizing and triggering star formation (from Morgan et al. 2004). The cluster and the corresponding membership probability each source was assigned to, if any. We used the nomenclature introduced by Karr & Martin (2003) for the W5 region.

HII regions expanding in the surrounding gas might trigger star formation, forming the so-called bright-rimmed clouds (BRCs, Bertoldi, 1989; Bertoldi & McKee, 1990; Lefloch & Lazareff, 1994, 1995). The bubble expansion drives shock in the surrounding medium possibly resulting in gravitationally unstable and triggering star formation (Thompson et al., 2004). The study of BRCs and whether they are in fact star-forming or not (Sugitani et al., 1991; Sugitani & Ogura, 1994) can thus provide valuable insights into the role of massive star feedback. In addition, identifying the feedback source is crucial to understanding how star formation proceeded.

In this section, we aim to tag candidate ionizing sources to known star clusters and investigate their kinematics within the cluster. Firstly, we further confirm using *Gaia* DR3 parallaxes that the three regions (W3, W4, and W5) lie at the same distance from the Sun, hence their vicinity is not a projection effect, as already suggested by Xu et al. (2006); Hachisuka et al. (2006); Megeath et al. (2008).

We collected candidate ionizing sources from Morgan et al. (2004); Deharveng et al. (2012), and used the SIMBAD database to retrieve their *Gaia* DR3 `source_id` if present (see table 5.3). This allowed us to look for each source in our cluster member catalogs. We found that at least one source for each region belonged to the central cluster. BD 60 507 is one of the candidate ionizing sources in W4, possibly triggering star formation in the BRCs 5, 7, 8, and 9 (Morgan et al., 2004). It belongs to the star cluster IC 1805 with a high membership probability (see table 5.3). From *Gaia* data, we found that the star is close to the cluster center (about $0.5r_{\rm h}$) and it is moving at about 0.1 mas yr^{-1} (i.e., roughly 0.95 km s^{-1}at 2 kpc) relative to the mean cluster motion. Moreover, the star has radial velocity spectrometer spectra, resulting in a fast rotator with `vbroad` $= 180 \pm 48$ km s^{-1}.

The candidate ionizing source for BRC 12 in the W5-West region is BD 60 586 (Morgan et al., 2004). This star was assigned to IC 1848 (with a membership of 65%). It is located at about $3.6r_{\rm h}$ but it was not used in the IC 1848 kinematic characterization as it has `ruwe` $= 2.74$, suggesting that single-star track did not provide a good fit to the observed astrometry. Nonetheless, the generalized stellar parameterizer from photometry (GSP-Phot) provides $T_{\rm eff} = 21635^{+139}_{-235}$ K.

Concerning the W5-East region, BD 59 578 (also known as HD 18326) is widely referred to as the main ionizing source in the region (Chauhan et al., 2011a). According to our catalog, it belongs to SAI 24, being located $\sim 0.55r_{\rm h}$ away from the cluster center, with a relative speed of 0.166 mas yr^{-1} (i.e, 1.57 km s^{-1}at 2 kpc). Besides, Deharveng et al. (2012) suggested V 1018 Cas as an additional ionizing source in W5-East for the observed pillars. The source belongs to SAI 24 although with lower membership, 72%. It lies at about $2r_{\rm h}$ with a relative speed of 0.41 mas yr^{-1} ($\sim$ 4 km s^{-1}at 2 kpc). According to the GSP-Phot, it has $T_{\rm eff} = 25709^{+561}_{-246}$ K.

Interestingly, none of the cross-matched sources was found to depart at a high relative speed from the cluster regardless of their cluster-centric distance and the expanding nature of the clusters (see section 5.2.3). This further suggests that those massive stars constitute the core of the clusters.

5.4 The kinematics of the Perseus complex

Román-Zúñiga et al. (2019) studied the internal dynamics of the Perseus complex using a sample of young stars and *Gaia* DR2 data. The authors found a Hubble-like expansion flow in the region, with an estimated rate of 15 km s^{-1} kpc^{-1}. As possible explanations, the authors suggested that the observed expansion could be due to supernova explosions in the region, interactions with the spiral arm, or the result of a large unbound stellar association that is expanding (Román-Zúñiga et al., 2019). Here we further investigate the dynamics of the complex using its star clusters. There are two main advantages in using star clusters: *i)* the LOS component of the velocity is more widely accessible compared to individual stars, especially when dealing with luminous hot ones observed through *Gaia* RVS (Katz et al., 2023); *ii)* average position and velocity are more precise and reliable as averaged among several member stars.

5.4.1 3D cluster positions and velocities

We constructed a catalog of star clusters in the Perseus complex by gathering clusters in the W345 region (see section 5.2), in LISCA I (Dalessandro et al., 2021b), and LISCA II (Della Croce et al., 2023). Cluster member catalogs were either presented in section 5.1 (for W345) or in Dalessandro et al. (2021b) and Della Croce et al. (2023). We obtained mean sky positions, PM components, and distances for all clusters directly from their members (defined by the membership threshold $> 90\%$). Also, we adopted homogeneous astrometric selections (see section 5.1) and analysis. Cluster on-sky coordinates (α_0, δ_0) were obtained by averaging the positions of cluster members. To derive mean PM and distances for each cluster, we sampled

TABLE 5.4: Six-dimensional coordinates of the Perseus complex star clusters analyzed in this work

Cluster	α_0 [°]	δ_0 [°]	$\langle d \rangle$ [pc]	$\langle \mu_{\alpha*} \rangle$ [mas yr^{-1}]	$\langle \mu_\delta \rangle$ [mas yr^{-1}]	$v_{\rm LOS}$ [km s^{-1}]	$N_{\rm LOS}$	source
Berkeley 65	39.769	60.403	2013^{+19}_{-18}	$-0.688^{+0.014}_{-0.014}$	$-0.423^{+0.013}_{-0.014}$	-60.4 ± 7.0	1	(1)
IC 1805	38.198	61.469	1982^{+10}_{-9}	$-0.741^{+0.015}_{-0.015}$	$-0.735^{+0.015}_{-0.015}$	-43.8 ± 3.0	18	(0)
IC 1848	42.816	60.412	2004^{+9}_{-9}	$-0.405^{+0.015}_{-0.014}$	$-0.431^{+0.011}_{-0.011}$	-37.0 ± 3.3	16	(0)
SAI 24	44.732	60.577	1989^{+10}_{-9}	$-0.257^{+0.018}_{-0.019}$	$0.068^{+0.012}_{-0.012}$	-48.5 ± 5.4	7	(1)
UBC 420	40.172	60.862	2106^{+7}_{-7}	$-0.599^{+0.017}_{-0.017}$	$-0.298^{+0.008}_{-0.008}$	–	–	–
NGC 884	35.513	57.148	2220^{+15}_{-12}	$-0.620^{+0.011}_{-0.010}$	$-1.153^{+0.013}_{-0.014}$	-33.7 ± 4.0	5	(0)
NGC 869	34.736	57.130	2217^{+12}_{-11}	$-0.651^{+0.010}_{-0.009}$	$-1.161^{+0.011}_{-0.012}$	-67.6 ± 10.4	6	(1)
NGC 957	38.348	57.559	2155^{+19}_{-20}	$-0.303^{+0.016}_{-0.014}$	$-1.132^{+0.012}_{-0.012}$	-37.5 ± 5.5	2	(1)
Basel 10	34.879	58.291	2002^{+19}_{-19}	$-0.422^{+0.014}_{-0.015}$	$-0.839^{+0.012}_{-0.013}$	–	–	–
NGC 654	26.004	61.883	2699^{+20}_{-19}	$-1.140^{+0.007}_{-0.006}$	$-0.336^{+0.006}_{-0.007}$	-20.6 ± 8.1	3	(1)
NGC 663	26.574	61.195	2610^{+13}_{-11}	$-1.140^{+0.004}_{-0.004}$	$-0.326^{+0.004}_{-0.004}$	-24.9 ± 15.8	3	(1)
NGC 659	26.108	60.677	2843^{+23}_{-26}	$-0.831^{+0.004}_{-0.004}$	$-0.301^{+0.005}_{-0.004}$	-48.2 ± 13.0	2	(1)
NGC 581	23.339	60.664	2468^{+17}_{-15}	$-1.387^{+0.006}_{-0.006}$	$-0.597^{+0.005}_{-0.005}$	-38.1 ± 4.4	2	(1)
Berkeley 6	27.801	61.059	2702^{+31}_{-27}	$-0.900^{+0.009}_{-0.009}$	$-0.527^{+0.009}_{-0.009}$	-88.9 ± 5.9	2	(1)
Berkeley 7	28.545	62.367	2597^{+27}_{-29}	$-0.980^{+0.006}_{-0.006}$	$-0.220^{+0.007}_{-0.007}$	-48.4 ± 5.1	1	(0)
Czernik 6	30.539	62.839	2653^{+29}_{-30}	$-1.184^{+0.008}_{-0.007}$	$-0.186^{+0.011}_{-0.013}$	-56.26 ± 0.03	1	(0)
Riddle 4	31.868	60.258	2588^{+26}_{-29}	$-0.808^{+0.009}_{-0.010}$	$-0.503^{+0.011}_{-0.012}$	-25.3 ± 20.3	3	(1)
NGC 637	25.775	64.041	2524^{+18}_{-17}	$-1.259^{+0.006}_{-0.007}$	$-0.027^{+0.006}_{-0.006}$	–	–	–

Notes. Cluster name, center equatorial coordinates, distance from the Sun, PM components, LOS velocity, number of stars used in $v_{\rm LOS}$ calculation, and source catalog for the LOS velocity: (0) for Tarricq et al. (2021), and (1) for Hunt & Reffert (2023).

the posterior distribution

$$\ln p(\langle \boldsymbol{x} \rangle | \boldsymbol{x}_i) = -\frac{1}{2} \sum_{i=1}^{N} \left((\langle \boldsymbol{x} \rangle - \boldsymbol{x}_i) \cdot \Sigma_{\rm conv,i} \cdot (\langle \boldsymbol{x} \rangle - \boldsymbol{x}_i)^{\rm T} + \ln |\Sigma_{\rm conv,i}| \right) . \tag{5.5}$$

In equation 5.5, $\langle \boldsymbol{x} \rangle \equiv (\langle \mu_{\alpha*} \rangle, \langle \mu_\delta \rangle, 1/\langle d \rangle)$ is the array of mean quantities (with the distance in kpc), and $\boldsymbol{x}_i \equiv (\mu_{\alpha*,i}, \mu_{\delta,i}, \varpi_i)$ is the array of observables for the i-th member star. Also, the covariance matrix $\Sigma_{\rm conv,i} \equiv \Sigma_{\rm i} + \Sigma_{\rm model}$ with $\Sigma_{\rm i}$ defined in equation 5.6 (to account for the non-negligible correlations in the *Gaia* astrometric solution), and

$$\Sigma_{\rm model} = \begin{pmatrix} \sigma^2_{\mu_{\alpha*}} & \rho_{\rm PM}\sigma_{\mu_{\alpha*}}\sigma_{\mu_\delta} & 0 \\ \rho_{\rm PM}\sigma_{\mu_{\alpha*}}\sigma_{\mu_\delta} & \sigma^2_{\mu_\delta} & 0 \\ 0 & 0 & 0 \end{pmatrix} , \tag{5.6}$$

where $\sigma_{\mu_{\alpha*}}$, σ_{μ_δ}, $\rho_{\rm PM}$ are the PM dispersions and correlation coefficients. Using equation 5.5 we can sample the joint posterior distribution in the mean PM components, velocity dispersions, correlation, and cluster distance. We note however that the distance term in equation 5.5 assumes cluster member stars to lie at the same distance (thereby neglecting the cluster depth) and parallax measurements for nearby stars to be independent (although see Vasiliev 2019c) as discussed by Cantat-Gaudin et al. (2018). Nonetheless, here we account for the correlation between PM and parallax as discussed in section 5.1. We sample the joint posterior distribution (assuming uniform priors for the parameters) with an MCMC approach using the `emcee` package by Foreman-Mackey et al. (2013). Before sampling the posterior distribution, we accounted for the *Gaia* DR3 parallax bias following the prescription by Lindegren et al. (2021c).

Concerning the LOS velocity ($v_{\rm LOS}$) component, we merged multiple catalogs. We adopted the LOS velocity from the catalog with the largest number of member stars with LOS measurement between Tarricq et al. (2021) and Hunt & Reffert (2023), to have a more robust estimate of the mean LOS velocity. If a cluster had no measurements in these two catalogs, we searched for LOS velocity measurements in Tsantaki et al. (2022). The only exception to this general approach is the case of SAI 24. For this cluster, Tarricq et al. (2021) measured $v_{\rm LOS} = +52 \pm 22$ km s^{-1}(using 8 stars), whereas Hunt & Reffert (2023) found $v_{\rm LOS} = -48 \pm 5$ km s^{-1}(using 7 stars). The two measurements are highly discrepant (3.7σ), possibly due to different membership compilations. However, the measurement from Hunt & Reffert (2023) is closer to the mean LOS velocity of the W345 complex (around -40 km s^{-1}, Fanelli et al. 2022) it belongs to. We thus adopted the value by Hunt & Reffert (2023). We note that SAI 24 is not included in the Tsantaki et al. (2022) catalog. Furthermore, the clusters UBC 420, Basel 10, and NGC 637 had no LOS velocity measurements in any catalog, whereas Berkeley 6 has a significantly lower $v_{\rm LOS}$ in all the catalogs (has already pointed out in Della Croce et al., 2023).

Table 5.4 presents the six-dimensional phase-space information for the Perseus complex star clusters. The values reported for the distance and mean PM components represent the median value of the marginalized one-dimensional distribution, along with the 16th and 84th percentiles quoted as errors. Our results are generally consistent with those reported by the

recent compilation of Hunt & Reffert (2023), although we find systematically lower values ($\lesssim$ 50 pc) for the cluster distances. We verified that the results presented in the following sections do not change if we adopted Hunt & Reffert (2023) catalog for the cluster data.

5.4.2 The projected kinematics

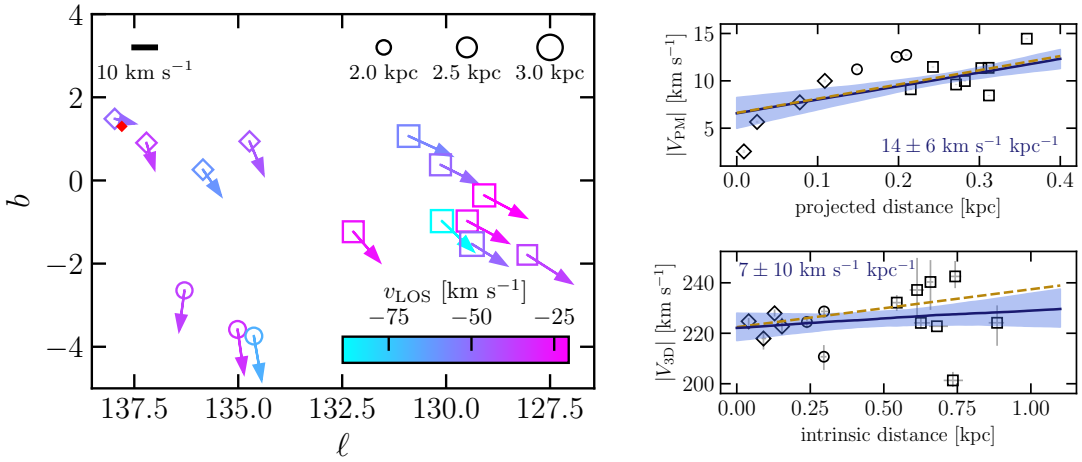

FIGURE 5.10: Projected kinematic properties for the Perseus star clusters. Left panel: spatial distribution of the Perseus complex star clusters. Arrows show the PM vectors, converted in km s^{-1}according to the cluster distance (mapped into the size of markers, the smaller, the closest, see the distance coding the top-right corner of the plot). The color coding shows v_{LOS}. All data are reported in table 5.4. The red diamond shows the claimed expansion origin according to the study of Román-Zúñiga et al. (2019). Right panels: distance-absolute velocity plots for the projected quantities (top sub-panel) and 3D quantities (i.e., accounting for the position in the Galaxy and v_{LOS} velocity, bottom sub-panel), and assuming that the Sun lies at a distance of 8.178 kpc (GRAVITY Collaboration et al., 2019) from the Galactic center, 20.8 pc above the disk (Bennett & Bovy, 2021) and that it is orbiting in the Galaxy at $(V_X, V_Y, V_Z) = (11.1, 248.5, 7.25)$ km s^{-1}(Schönrich et al., 2010; Reid & Brunthaler, 2020). In the top sub-panel, on-sky distances are from the expansion center suggested by Román-Zúñiga et al. (2019). Velocities and distances were converted in physical units assuming the distance of IC 1805 (see table 5.4). In the sub-bottom panel, 3D distances are relative to IC 1805. Errors are computed by the propagation of distance and v_{LOS} errors (reported in table 5.4). Both sub-panels show the linear regression obtained from cluster data (in blue) and the one by Román-Zúñiga et al. (2019, in brown). The best-fit angular coefficient obtained in this work is also reported. Finally, the shaded areas represent the 68% credible interval, corresponding to 1σ if the distribution were Gaussian.

In this Section, we present the projected kinematics of the Perseus complex as seen from a star cluster perspective. Figure 5.10 shows the absolute, on-sky velocities for the star clusters in the Perseus complex. LISCA II clusters are located in $\ell = 128 - 132$ degree, LISCA I lies

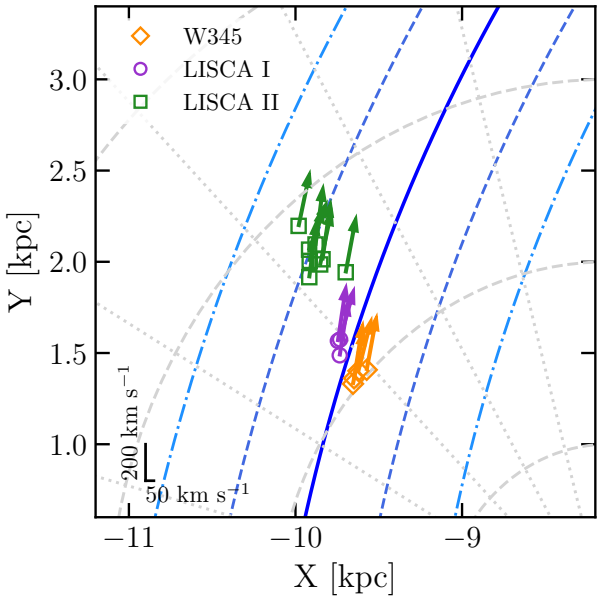

FIGURE 5.11: XY projection of the star cluster Galactocentric positions, while arrows show the V_X, V_Y velocities (with velocity scale reported in the bottom-left corner). Galactocentric coordinates were obtained by direct de-projection of the 6D coordinates listed in table 5.4. Each cluster is color-coded according to the structure it belongs, namely orange diamonds for W345 , purple circles for LISCA I , and green squares for LISCA II . The blue lines show the Perseus spiral arm model (solid) by Reid et al. (2019), with one time (dashed) and twice (dash-dotted) the arm width. The background grid is a Heliocentric polar grid with the dashed gray lines showing distances from 1 to 4 kpc, and the dotted ones sampling the angular direction every 15 degrees.

eastern at $b < -2°$, while in the region $b = 0 - 2$ degrees is W345 . Román-Zúñiga et al. (2019) found a Hubble-like expansion pattern for the region using individual stars. The projected star cluster kinematics qualitatively fits into this picture: looking at the distribution of on-sky absolute PMs as a function of the projected distance we nicely recover the trend reported by Román-Zúñiga et al. (2019), finding a similar amplitude (see the top-right panel in figure 5.10). However, considering the 3D cluster positions and velocities in the Galaxy, this large-scale motion is not observed. By a similar analysis indeed, we found no net trend with the intrinsic distance (see the bottom-right panel of figure 5.10). This may be because the Perseus complex spans more than 1 kpc along the LOS, hence when looking at the PM only we are projecting an almost 1.2 kpc-deep on a 10°-wide region (about 350 pc at 2 kpcs, see left panel of figure 5.10).

Given the available 6D data for clusters in the sample (table 5.4), we thus investigated their dynamics in a broader, Galactic framework. Figure 5.11 presents the top-down view of the Galactic disk for the Perseus region. Star cluster positions and in-plane velocities are shown color-coded according to the structure they belong to, along with the Perseus spiral-arm model from Reid et al. (2019). Interestingly, star clusters appear to be moving almost parallel to the arm. This, together with the figure 5.10 discussion, argues in favor of the Hubble-like expansion flow reported by Román-Zúñiga et al. (2019) likely being a projection effect arising from different orbital velocities at slightly different Galactocentric distances. In this scenario, the Perseus complex kinematics is governed by the Galactic potential, possibly perturbed by the Perseus spiral arm, rather than internal dynamical processes.

5.4.3 Orbits in an axisymmetric potential

We tested the hypothesis that the star clusters in the Perseus complex are not dispersing but rather orbiting in the Galaxy at slightly different Galactocentric distances and speeds, by directly integrating their orbits. Starting from the 6D projected data (see table 5.4), we obtained Galactocentric coordinates and velocity components assuming that the Sun lies at a distance of 8.178 kpc (GRAVITY Collaboration et al., 2019) from the Galactic center, 20.8 pc above the disk (Bennett & Bovy, 2021) and that it is orbiting in the Galaxy at $(V_X, V_Y, V_Z) = (11.1, 248.5, 7.25)$ km s^{-1}(Schönrich et al., 2010; Reid & Brunthaler, 2020). Also, since we are measuring cluster mean positions (i.e., mean celestial coordinates and distances), and velocities (i.e., PMs and v_{LOS}), literature catalogs provide errors in these quantities (Tarricq et al., 2021; Hunt & Reffert, 2023, see table 5.4). We thus accounted for distance and v_{LOS} errors (typically the primary uncertainty sources) by sampling their distributions 500 times and obtaining Galactocentric coordinates for all the extractions.

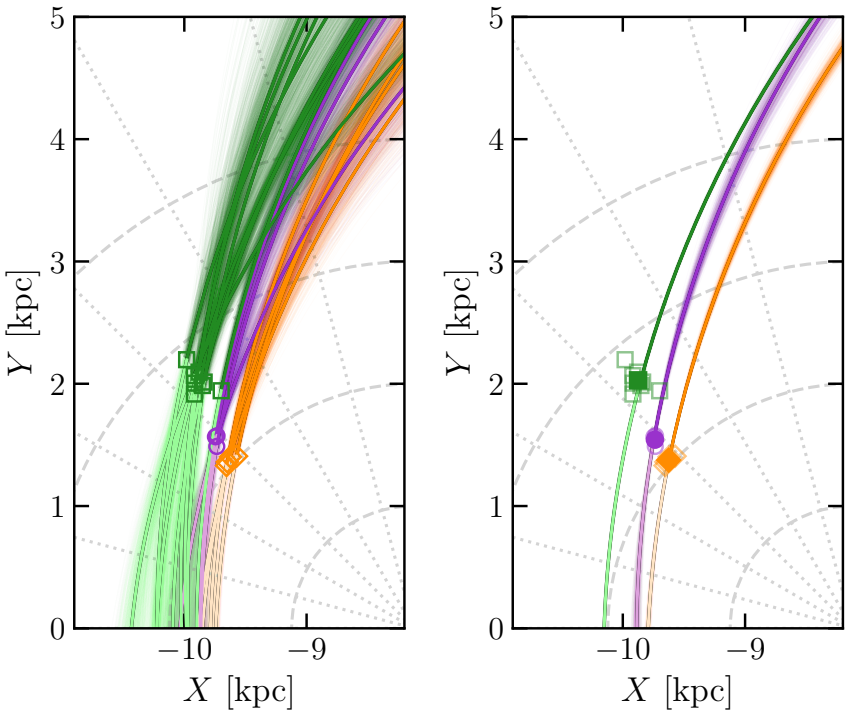

FIGURE 5.12: XY projection for individual cluster orbits (left panel) and stellar cluster aggregates (right panel). Darker lines trace the orbits forward in time, whereas lighter ones are backward. Thin lines show orbit integrations from multiple initial condition extractions. Solid thick lines show median orbits. Present-day cluster positions are also marked: orange diamonds for W345 , purple circles for LISCA I , and green squares for LISCA II clusters.

Orbits were integrated in the axisymmetric McMillan (2017) potential using the Action-based Galaxy Modelling Architecture (`AGAMA` [7]) library (Vasiliev, 2019a) for 200 Myr. Besides, to constrain the formation scenario and the initial size of the Perseus complex we performed a backward orbit integration by flipping the velocity vectors for each cluster. In the framework

[7] Publicy available at `https://github.com/GalacticDynamics-Oxford/Agama`.

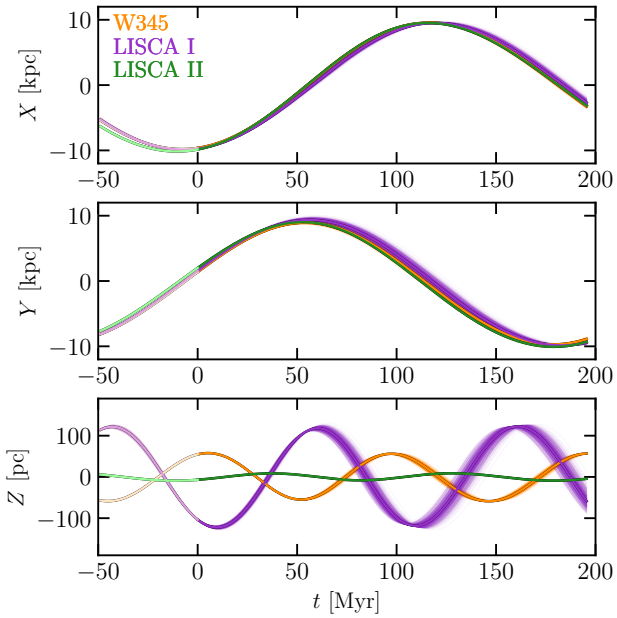

FIGURE 5.13: Galactocentric coordinates time evolution for the star cluster aggregates. Darker lines are the forward in time (i.e., $t > 0$) integrations while lighter ones are backward (i.e., $t < 0$). The present-day positions are at $t = 0$. Initial conditions were sampled 500 times to account for errors in the mean distance and $v_{\rm LOS}$, and are shown by thin lines. The thicker solid lines are the median (of those multiple extractions) orbits.

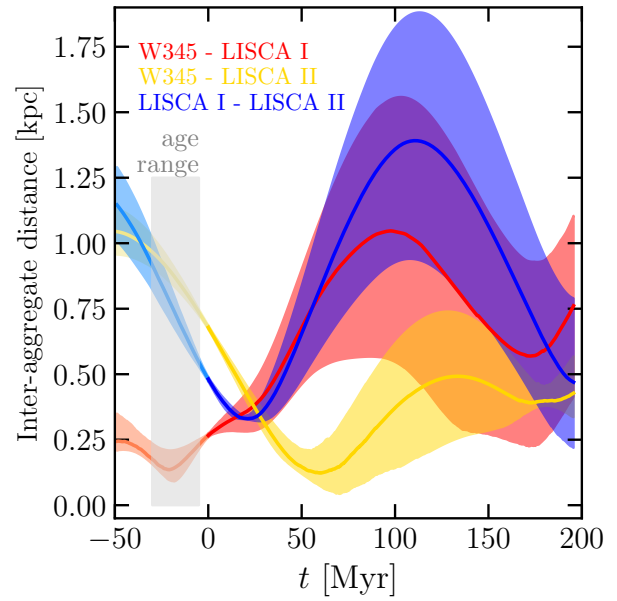

FIGURE 5.14: Time evolution of all combinations of inter-aggregate 3D distances. Darker colors trace the forward ($t > 0$) integration while lighter colors are the backward integration. Median distances are shown as solid lines, with shaded areas being the 16th (lower distance) and 84th (upper distance) percentiles of the 3D-distance distributions from multiple initial-condition extractions. The vertical gray area delimits the stellar age ranges, from 5 Myr (for W345 complex star clusters) to about 30 Myr for LISCA II (see Della Croce et al., 2023).

of the canonical set of angle-action coordinates (Binney & Tremaine, 2008b), this transformation allows us to follow the same orbit (as the action integrals are unchanged) but in the opposite direction along the angle space. Backward orbits were integrated for 50 Myr which is generally larger than the stellar ages in the region (Della Croce et al., 2023; Hunt & Reffert, 2023; Cavallo et al., 2024). In figure 5.12 we show the top-down view of the Galactic plane with individual cluster orbits both forward and backward in time. Also, in section 5.6.1 we present and discuss the time evolution of Galactocentric coordinates for every cluster. There are a few interesting points to highlight from figure 5.12: *i)* LISCA I clusters move slightly

outward in the Galactic plane, and toward LISCA II ; *ii)* two clusters, namely Berkeley 65 and NGC 869, depart the most from the other neighbor clusters (LISCA II and LISCA I clusters respectively). This is likely due to the difference in their $v_{\rm LOS}$ to the other clusters (see table 5.4); *iii)* going back in time in the cluster orbit reconstruction, LISCA I appears to converge toward the W345 complex.

Finally, we note that accounting for distance and $v_{\rm LOS}$ errors is key in constraining the origin and evolution of star cluster systems. Although on Galactic scales the orbits are well constrained (see figure 5.18) when looking at their distribution on cluster scales (or inter-cluster distance scales) errors on the initial conditions are far from negligible. This may also account for the apparent separation of LISCA II star clusters into two branches.

While individual star cluster orbits could give us insights into their evolution and origin, they may suffer of strong assumptions and shortcomings, particularly in the context of the Perseus complex. Star clusters in LISCA I and LISCA II are not isolated (Dalessandro et al., 2021b; Della Croce et al., 2024b). On the contrary, clusters are likely interacting with each other and they are also embedded in a more diffuse stellar halo. Therefore their present-day properties (mainly in terms of velocity distributions) may be strongly affected by their mutual interaction with other clusters. We thus decided to study the Persues complex at large using larger structures, such as the LISCA systems and clusters in the W345 region. We shall refer to these structures as cluster aggregates. Such an approach has multiple advantages. Firstly, it allows us to trace the Perseus complex evolution on finer scales. Secondly, we are not considering star clusters as isolated entities, but rather as part of larger complexes (as suggested by previous studies, e.g., Dalessandro et al. 2021b, and Della Croce et al. 2023). We stress here, though, that despite the evidence of W345 complex star clusters being co-moving and co-spatial, treating them as a single aggregate does not imply any physical connection as for the LISCAs.

We obtained mean Galactocentric positions and velocities for the cluster aggregates by averaging the individual cluster quantities. In particular, we followed Sivia & Skilling (2006) to estimate mean values and standard errors while taking into account heterogeneous errors. Finally, figure 5.12 (right panel) presents the cluster aggregate orbits projected on the XY plane. As anticipated, the use of cluster aggregates provides a clearer picture: LISCA I is currently in the process of drifting away from the W345 complex toward LISCA II , while LISCA II and W345 seems to evolve in parallel. Furthermore, in figure 5.13 we present the evolution of XYZ coordinates with time. Interestingly, the three structures evolve similarly in the plane for almost a full orbital period (of about $250 - 260$ Myr) while experiencing different oscillation amplitude up and down the plane, with LISCA I showing the largest amplitude, up to 100 pc.

Lastly, to quantitatively constrain the evolution and formation of the Perseus complex, we traced the 3D inter-aggregate distances with time (figure 5.14). At each time step, distances between the three cluster aggregates were computed for each orbit from the pool of initial conditions, and the median distance, along with the 16th and 84th percentiles, were obtained. We conclude that: *i)* LISCA I is currently moving away from W345 , reaching a distance of about 1.1 kpc in 100 Myr, before approaching it again; *ii)* at the same time, LISCA I and LISCA II are getting closer, reaching minimum distance in about $30 - 40$ Myr *iii)* despite their appearance in the XY plane, LISCA II and W345 are in fact approaching each other. In about 60 Myr they reach a distance of a few hundred parsecs, before slowly departing; *iv)*

concerning the backward integration, we can trace the formation condition of the Perseus complex. LISCA I and the W345 region were at their minimum distance about 25 Myr ago of just a few hundred parsecs, while LISCA II formed further away, between $0.6 - 1$ kpc; *v)* we do not observe a Hubble-like expansion of the region. According to the rate reported by Román-Zúñiga et al. (2019), in 150 Myr the region should reach a size of about 5 kpc, inconsistent with figure 5.14.

5.4.4 Orbits in a spiral-perturbed potential

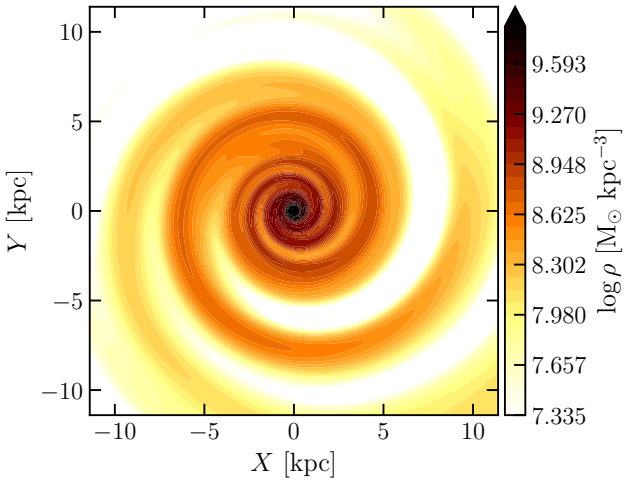

FIGURE 5.15: Density map on the XY Galactic plane (i.e., computed at $Z = 0$) for a spiral perturbation with $f = 0.3$ (used as a reference model). The Sun is located at $X = -8.178$ kpc and $Y = 0$.

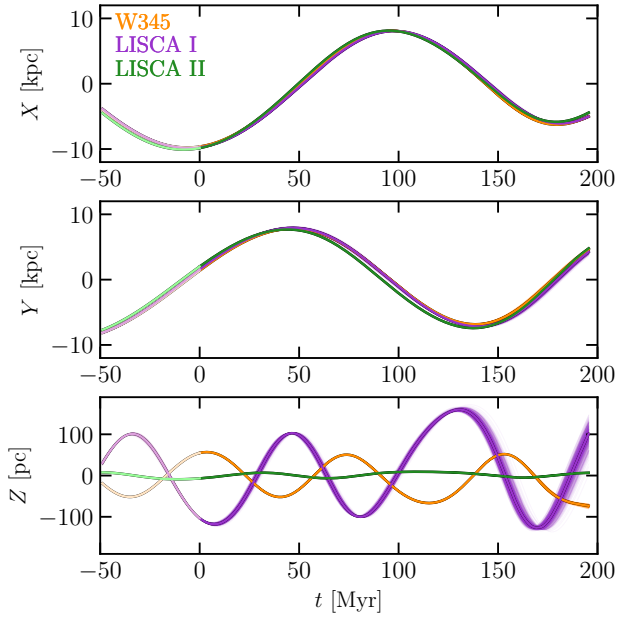

FIGURE 5.16: The same as figure 5.13 but for a spiral-perturbed potential with $f = 0.3$.

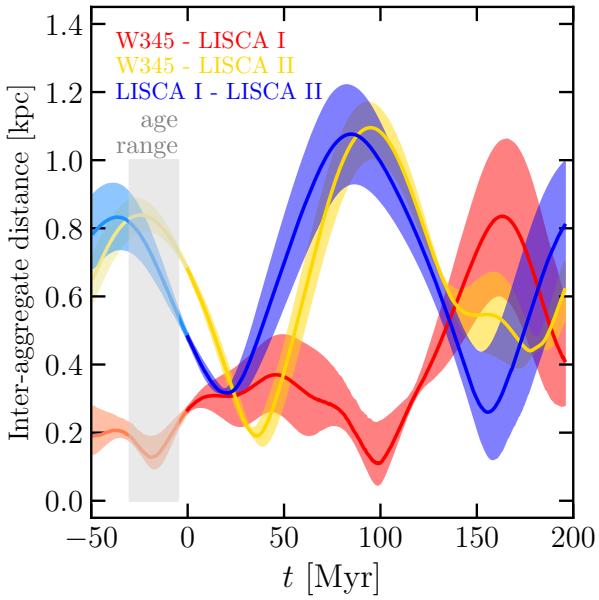

FIGURE 5.17: The same as figure 5.14 but for a spiral-perturbed potential with $f = 0.3$.

Figure 5.11 shows that Perseus star clusters lie on the spiral arm (Reid et al., 2019). Spiral structures (see Lin & Shu, 1964; Shu, 2016; Sellwood & Carlberg, 1984, for different formation theories) are believed to play an important role in gathering gas, triggering star formation, and perturbing stellar orbits thanks to the locally deeper potential well (Baba et al., 2016; Tchernyshyov et al., 2018). In addition, Román-Zúñiga et al. (2019) suggested that the apparent expansion of the Perseus complex could be due to spiral arm interaction. We thus built a Galactic potential toy model in which we consider spiral arm perturbations to assess their effect on the cluster orbits.

We started from the spiral arm model provided by Reid et al. (2019). The authors modeled the spiral arm shape as

$$\ln(R/R_{\rm kink}) = -(\theta - \theta_{\rm kink}) \tan\psi \,, \tag{5.7}$$

where $R_{\rm kink}$, and $\theta_{\rm kink}$ are characteristic Galactocentric radius (on the plane) and azimuth respectively, and ψ is the pitch angle. Also, they allowed the arm to abruptly change the pitch angle at $\theta_{\rm kink}$ and considered a distance-dependent arm width (see figure 5.11). Finally, Reid et al. (2019) concluded that the young-star distribution is consistent with a five-arm model including the Scutum, the Sagittarius-Carina, the Local, the Perseus, and the Outer spiral arm. We thus used the potential formulation derived by Cox & Gómez (2002) for the density in equation 5.7, assuming each arm is a single spiral, and considered them as perturbations of the underlying axisymmetric potential (McMillan, 2017). Such an approach has some assumptions and limitations that we discuss here. *i)* The potential model (Cox & Gómez, 2002) does not allow for a change in the pitch angle, we thus assumed the average value for ψ. In particular, for the Perseus arm, we assumed $\psi = 9.5°$; *ii)* the amplitude of the density variations (f) with respect to the underlying potential is largely unconstrained by observations. This is a rather key parameter as increasing f enhances density perturbations. Levine et al. (2006) found that the density ratio between arm and inter-arm region using HI

observations is about ~ 3. Assuming that the stellar distribution presents the same ratio, we can translate it into f, finding that $f_{\rm HI} = 0.53 - 0.66$. However, this assumption is most likely wrong as the arm-to-inter-arm ratio for the gas is expected to be larger than the stellar one. Indeed, the gas gathers in the overdensities (i.e., the spiral arm) thereby being converted into stars. On the other hand, stars formed in the arms can drift away populating the interarm region. Therefore, $f_{\rm HI}$ represents an upper limit; *iii)* recent studies found that spiral arm pattern speed decreases with Galactocentric radius (Naoz & Shaviv, 2007; Castro-Ginard et al., 2021). Our spiral arm model does not allow for different pattern speeds as orbits are integrated into the non-inertial, co-rotating frame. Since we are mainly interested in the role of the Perseus arm we decided to adopt the pattern speed $\Omega_{\rm p} = 17.82 \pm 2.98$ km s^{-1} kpc^{-1} derived for the Perseus arm by Castro-Ginard et al. (2021) from the youngest open-cluster sample (that supposedly better traces the spiral structures in which they formed); *iv)* our potential model does not include the bar which was shown to have a prominent impact on the Galactic stellar kinematics (e.g., Kawata et al., 2021; Drimmel et al., 2023). Orbits were integrated for at most 200 Myr, during which clusters orbit at about 10 kpc from the Galactic center. Hence the role of the bar could be treated as a second-order effect compared to the local spiral arm potential perturbations. We nevertheless present in section 5.6.2 the orbits for a Galactic potential which includes the bar; *v)* spiral arms unrealistically extend to the Galactic center, well beyond the data coverage (Reid et al., 2019). However, as discussed above, we are mainly interested in the local effects on the Perseus complex. Despite the aforementioned caveats, figure 5.15 shows the density map projected on the Galactic plane for the perturbed McMillan (2017) potential with $f = 0.3$. Qualitatively, the density potential model closely resembles the spiral arm structure presented by Reid et al. (2019, see their figures 1, 10). We explored several f finding qualitatively similar results, and we present them in section 5.6.3.

Having built the Galactic potential, we computed the cluster aggregate orbits to study the evolution of the Perseus complex in the presence of spiral-arm perturbation. Figure 5.16 presents the evolution of Galactocentric coordinates with time. We broadly found that the Perseus spiral arm pulls star clusters towards higher-density regions during their orbit. Since the star clusters in the Perseus complex are within the spiral arm, the stronger gravitational force may keep the star clusters closer for large times when compared to the axisymmetric case. Figure 5.17 shows the inter-aggregate distance evolution for the perturbed ($f = 0.3$) potential. Opposed to the axisymmetric case (figure 5.14), their relative distances oscillate between about $0.25 - 1$ kpc for more than 200 Myr. However, star clusters may escape the spiral arm due to either differences in the orbital frequency and pattern speed or net relative inclination of the velocity vector to the arm pitch angle. In these cases, the Perseus spiral arm (or other nearby arms) drags the star clusters, profoundly changing the orbit. Such orbit perturbations are largely dependent on the value of f (see for instance figure 5.26). Finally, integrating the orbits backward in time[8] in the presence of spiral arm perturbations produces similar results with the interesting trend of decreasing the distance of LISCA II about 30 Myr ago with increasing f down to $500 - 750$ pc (see section 5.6.3). This suggests that in the presence of stronger perturbations the size of the Perseus complex at the formation of its

[8]To integrate orbits backward also the potential should evolve accordingly. Therefore, the pattern speed sign was changed. We verified that the integrator adopted conserves the Jacobi integral, with a typical relative precision of a few 10^{-8} for the investigated temporal range.

major stellar associations would be smaller.

We conclude that spiral arms play a role in shaping the cluster orbits and in the evolution of the Perseus complex. Also, different values of f do not qualitatively change the evolution on short time scales $\lesssim 100$ Myr.

5.5 Summary and conclusions

We studied the properties of the W345 region by using its cluster population and in the context of the more extended Perseus Complex. We identified five clusters in the W345 region, namely IC 1805, IC 1848, Berkeley 65, UBC 420, and SAI 24, all previously known in the literature and sharing similar 3D velocities and positions. All the clusters exhibit well-defined density structures as shown by comparing the observed density profiles with theoretical models. Also, they present significant deviations from spherical symmetry. We found no evidence of a link between clusters' morphological properties and asymmetric expansion thus suggesting the present-day spatial distribution is likely inherited from earlier processes or star formation. On the internal kinematics side, the three youngest (IC 1805, IC 1848, and SAI 24) clusters show prominent expansion, consistent with the picture that young star clusters are more likely to expand (Della Croce et al., 2024b). Also, a clear trend of $\langle v_{\rm R} \rangle / \sigma_{\rm R}$ with the distance from the center is observed within individual clusters suggesting that expansion dominates cluster dynamics in the outskirts.

The W345 region was targeted by many studies that characterized the YSO population and spatial distribution. We complemented these studies by investigating the YSO kinematics within the region. YSOs were found to trace young star clusters' expansion and, most probably, the parent gas bulk motion. Finally, we characterized the candidate ionizing sources in H II regions finding that at least one for each H II region was assigned as a high-probable ($\geq 65\%$) cluster member.

Lastly, we further zoomed out to study the Perseus complex kinematics using its star clusters. Six-dimensional phase space data were obtained from the latest *Gaia* compilation coupled with large spectroscopic surveys (mainly for the LOS velocity component). Star clusters trace the expansion rate reported by Román-Zúñiga et al. (2019) when looking at on-sky coordinates. However, we found that such expansion is likely a projection effect due to different orbital velocities at slightly different Galactocentric distances. Integrating the orbits of the three major structures in the complex (i.e., LISCA I , LISCA II , and W345), we traced their relative distance with time, concluding that: *i)* LISCA I is drifting away from W345, reaching a distance of about 1.1 kpc in 100 Myr, before approaching it again; *ii)* at the same time, LISCA I and LISCA II are getting closer, reaching their minimum relative distance in about $30 - 40$ Myr; *iii)* LISCA II and W345 are approaching each other: in about 60 Myr they reach a distance of a few hundred parsecs, before slowly departing; *iv)* we do not observe the Hubble-like expansion of the region suggested by Román-Zúñiga et al. (2019). According to their reported rate, in 150 Myr the region should reach a size of about 5 kpc, inconsistent with their orbit in the Galaxy. In addition, backward orbit integration provides us with insights into the formation conditions of the Perseus complex: LISCA I and the W345 region were at their minimum distance about 25 Myr ago of just a few hundred parsecs, while LISCA II formed further away, between $0.6 - 1$ kpc.

We also tested the role of spiral-arm perturbations in the orbit evolution since the Perseus complex spatially coincides with the Perseus spiral arm (see e.g., Reid et al., 2019). The spiral arm perturbs the cluster orbits by dragging them toward higher-density regions, thus possibly keeping clusters closer for longer times when compared to the axisymmetric case. We found this result to be fairly robust on short time scales ($\lesssim$ 100 Myr) to varying density perturbation strength.

In summary, we presented a detailed characterization of the Perseus complex, starting from the clusters in the W345 region up to its kinematics on large scales by progressively zooming out. Particular attention was paid to complementing the numerous previous literature studies with kinematic data from *Gaia* DR3. We showed indeed that kinematics (supplemented by photometric and spectroscopic data) is key to understanding the formation and evolution of large stellar complexes from cluster scales to Galactic ones.

5.6 Supplementary material

5.6.1 Perseus star cluster orbits in an axisymmetric potential

This section presents the individual cluster orbits integrated within the axisymmetric McMillan (2017) potential. The evolution of each cluster was followed for 200 Myr forward in time and 50 Myr backward. Figures 5.18, and 5.19 show the XYZ Galacto-centric coordinates as a function of time for all 15 clusters.

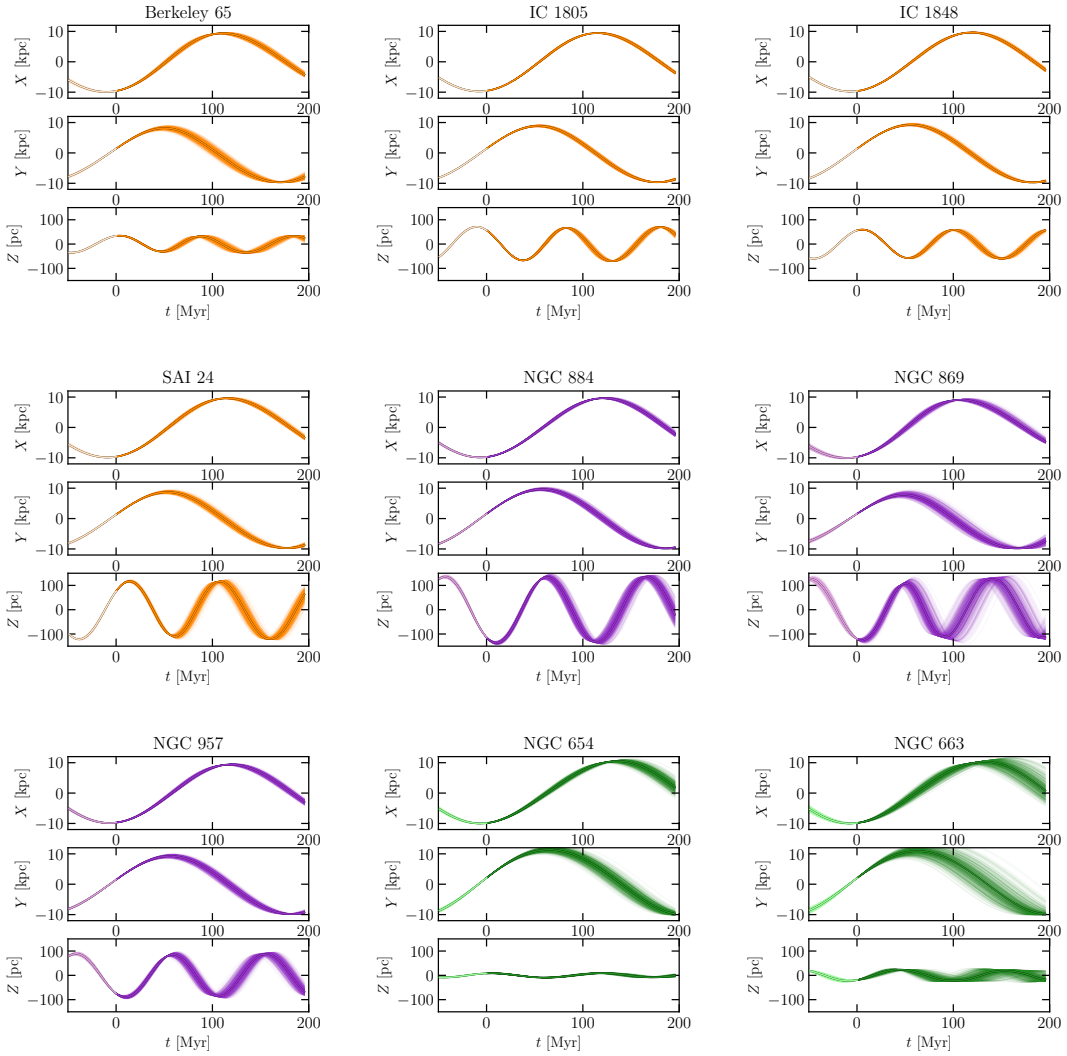

FIGURE 5.18: Temporal evolution of XYZ Galactocentric coordinates for the 15 star clusters in the Perseus complex. Temporal evolution for 500 orbit integrations is shown with background thin lines. Initial conditions were extracted according to the distance and $v_{\rm LOS}$ error distributions. Thicker foreground lines depict the median over multiple integrations. Cluster orbits are color-coded according to the larger cluster agglomerate to which they belong: orange for W345 complex, purple for LISCA I , and green for LISCA II .

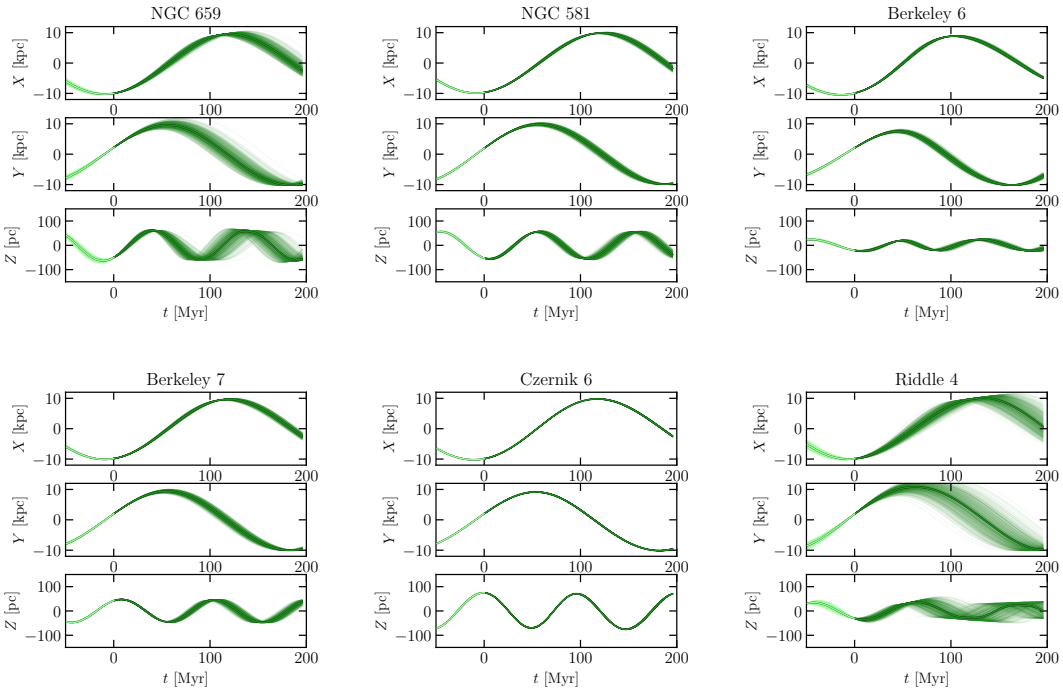

FIGURE 5.19: Figure 5.18 continues.

5.6.2 Testing the impact of the Galactic bar

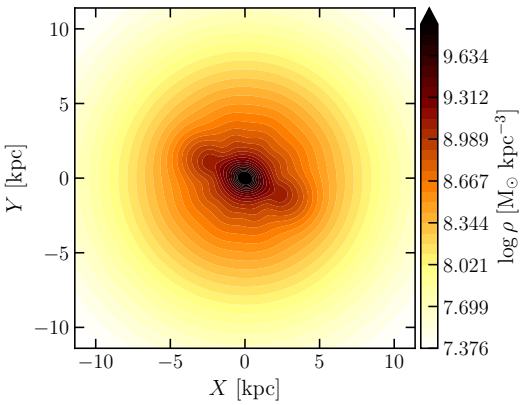

FIGURE 5.20: Density map on the XY Galactic plane (i.e., computed at $Z = 0$) for a Galactic potential which includes a titled, rotating bar.

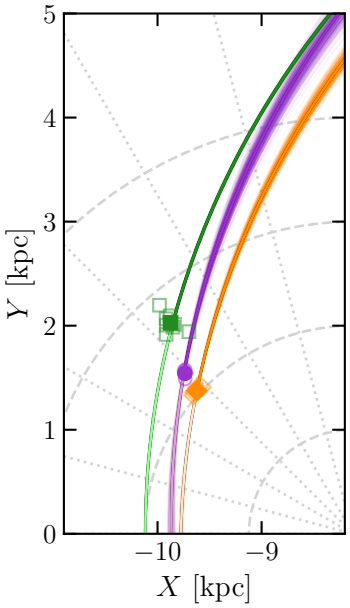

FIGURE 5.21: Orbits for the three stellar aggregates studied in this work on the Galactic plane. Orbits were computed within the potential model including the Galactic bar.

In this Section, we present the impact of the Galactic bar on the cluster aggregate orbits. In particular, we constructed the bar potential as defined in Sormani et al. (2022). Briefly, the authors provided analytic formulae to match the N-body models by Portail et al. (2017). Such numerical models were in turn constrained to match the red clump stars density from a combination of infrared surveys, and the stellar kinematics in the bulge and the bar regions (Portail et al., 2017). The analytical model includes three components: an X-shaped, a long, and a short bar (Sormani et al., 2022). The model was implemented within the `AGAMA` library[9]

[9]See the `Python` example scripts in the documentation: `https://github.com/GalacticDynamics-Oxford/Agama/tree/master/py`.

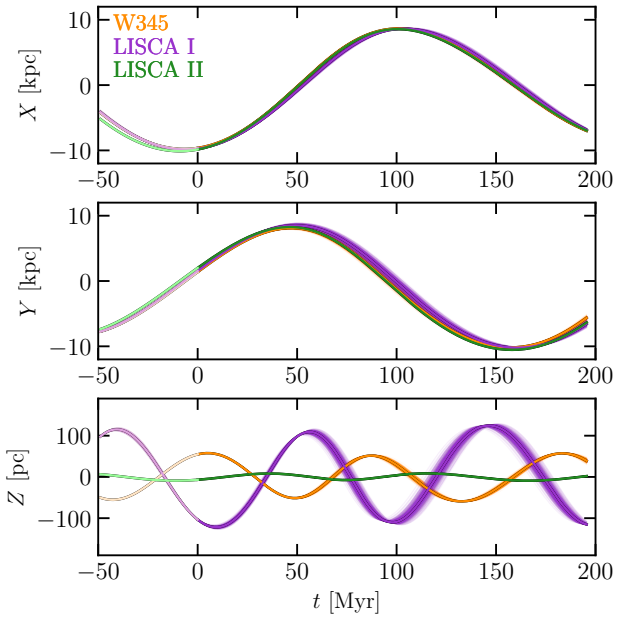

FIGURE 5.22: Galactocentric coordinates time evolution for the three stellar aggregates studied in this work. Orbits were computed within the potential model including the Galactic bar. Thin lines show different integrations from error distribution sampling of the initial conditions, while thicker ones are the median position at any given time.

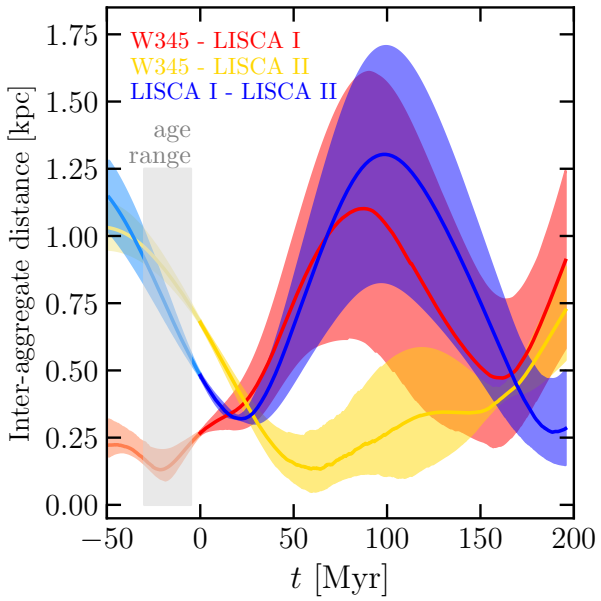

FIGURE 5.23: 3D inter-cluster aggregate distance as a function of time. Orbits were computed in the Galactic potential which includes the bar.

and considered as a perturbation of the McMillan (2017) potential (as done for the spiral arms, see Section 5.4.4). Figure 5.20 shows the 3D density computed on the Galactic plane ($Z = 0$) constructed for such MW potential. The bar is roughly confined in the central 5 kpc, although resonances can strongly perturb orbits well outside that region. We assumed a tilt angle of $-25°$ to the positive direction of the X axis.

To quantitatively assess the impact of the Galactic bar, we then performed the same analysis as Section 5.4.3 but for the MW potential model with the bar. For the purposes of orbit integration, we assumed $\Omega_{\mathrm{p,\,bar}} = 37.5$ km s^{-1} kpc^{-1} (Sormani et al., 2022). Figures 5.21

and 5.22 present the orbits in the MW model with the bar. In particular, figure 5.21 shows the orbits projected onto the Galactic plane, while in figure 5.22 the time evolution (both forward and backward) of the Galactocentric coordinates are shown. Finally, the impact of the bar on the 3D relative distances of the aggregates is presented in figure 5.23. As expected, the results are remarkably similar to those obtained in the purely axisymmetric case (see figure 5.14), thus confirming that the Galactic bar has a negligible effect on the Perseus cluster orbits compared to the local spiral arm structure.

5.6.3 Exploring different f values

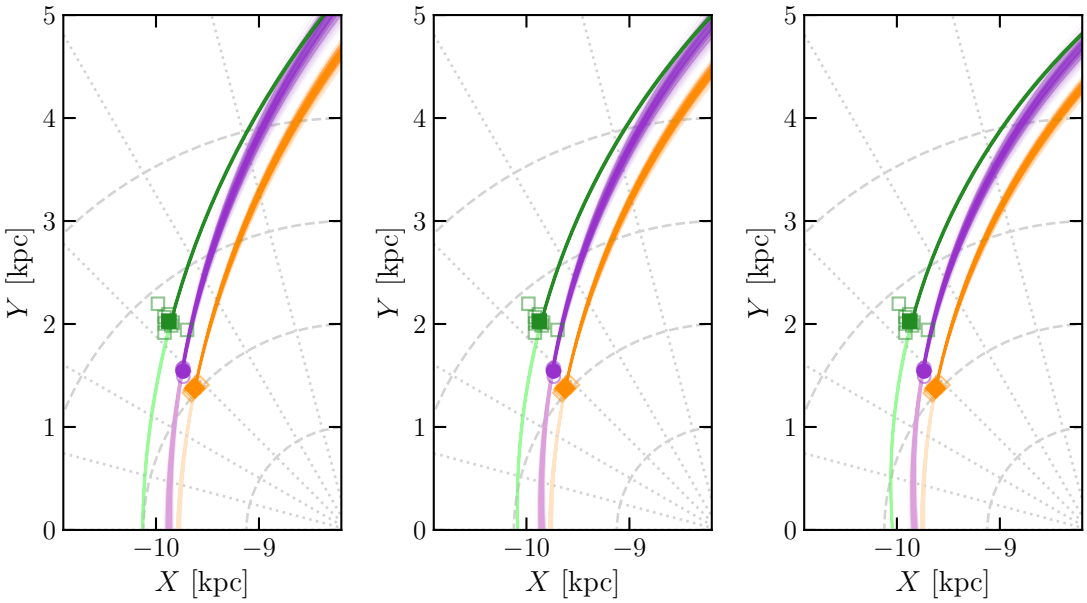

FIGURE 5.24: Stellar aggregate orbits on the Galactic plane for three values of f. From left to right $f = 0.1, 0.3, 0.5$, resulting in stronger density and potential perturbations. Different curves are orbits for different initial conditions extracted according to observed error distributions. W345 , LISCA I , and LISCA II orbits are in orange, purple, and green respectively. Present-day positions are also shown with filled symbols.

In this section, we show the cluster aggregates orbits for different non-axisymmetric potentials. Among the different integrations only f was changed exploring $f = 0.1, 0.3, 0.5$. Figure 5.25 presents the XY projections of the aggregate orbits on the Galactic plane (f is increasing rightward). Similarly, figure 5.25 presents the evolution with time of the XYZ coordinates for the three cluster aggregates. As could be seen, the stronger the density perturbation (i.e., increasing f) the more bend the orbits, which tend to follow the spiral structure. Finally, the implications of stronger spiral perturbations on the inter-aggregate distances are shown in figure 5.26.

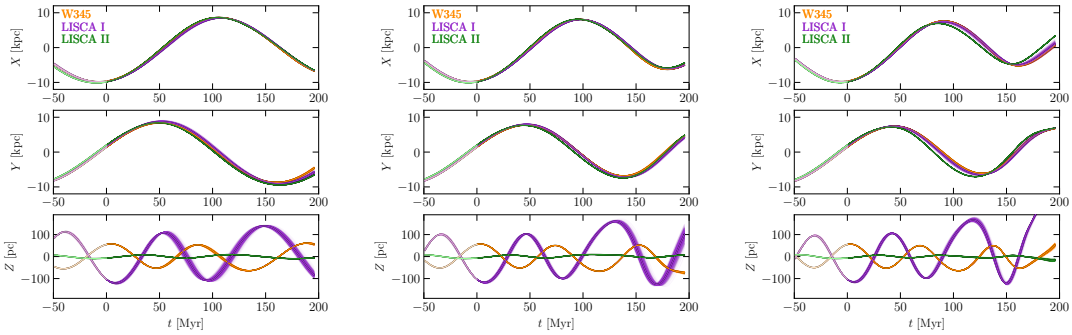

FIGURE 5.25: Temporal evolution of Galactocentric coordinates for the three cluster aggregates integrated in different spirally-perturbed potential: from left to right $f = 0.1,\ 0.3,\ 0.5$. Darker colors show the forward integration for about 200 Myr, whereas lighter ones show the backward integration. Different colors depict different aggregates: the W345 complex in orange, LISCA I in purple, LISCA II in green.

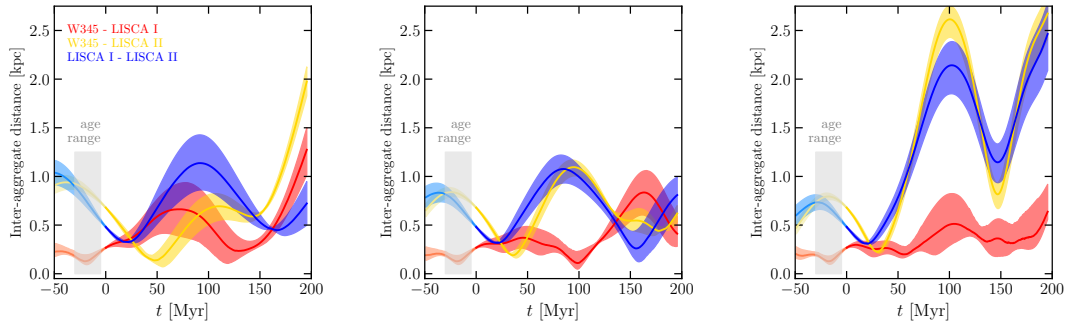

FIGURE 5.26: Inter-aggregate distances evolution for different spirally-perturbed potentials. From left to right $f = 0.1,\ 0.3,\ 0.5$. Mind the different scales on the y-axis. The gray shaded areas mark the cluster ages range, from $5 - 30$ Myr.

Chapter 6

Multiple population kinematics in Galactic GCs: a window on the complex processes of massive cluster formation

> "Far above the Ephel Duath in the West the night-sky was still dim and pale. There, peering among the cloud-wrack above a dark tor high up in the mountains, Sam saw a white star twinkle for a while. The beauty of it smote his heart, as he looked up out of the forsaken land, and hope returned to him. For like a shaft, clear and cold, the thought pierced him that in the end the Shadow was only a small and passing thing: there was light and high beauty for ever beyond its reach."
>
> The Lord of the Rings,
> J.R.R. Tolkien

As discussed in section 1.4, there is still no consensus on the origin of multiple stellar populations in GCs. However, recent observations opened the window to studying their internal kinematics, an almost uncharted territory (see e.g., Libralato et al., 2023). To move a step forward in our understanding of MP kinematic properties and their possible implications on GC formation, it is thus fundamental to perform a systematic and homogeneous study of clusters sampling a wide range of dynamical ages. At the same time, studying the clusters' outer regions, which are expected to retain some memory of the primordial structural and kinematic differences for longer timescales, is critical. As a first step in this direction, we performed for the first time a self-consistent study of the 3D kinematics of MPs in a representative sample of Galactic GCs for which it is virtually possible to sample their entire radial extension. This study has the additional advantage of overcoming the typical limitations connected with projection effects, which typically arise when LOS or PMs are used independently, possibly hampering the detection of the actual differences between the MP kinematic properties (see, e.g., the discussion concerning these issues in Tiongco et al. 2019).

This Chapter is structured as follows. In section 6.1 we describe the kinematic analysis along the three velocity components. In section 6.2 we present the main observational results along with a detailed comparison to dynamical simulations, and in section 6.3 we compare

them with the literature. In section 6.4 we summarize our findings and discuss their possible implications in the context of massive clusters formation and early evolution. Finally, additional material and analyses are presented in section 6.5.

The results presented in this Chapter are a selection from Dalessandro, Cadelano, **Della Croce**, et al. (2024, A&A, **691**, A94).

6.1 Kinematic analysis of internal rotation differences

The kinematic analysis presented in this Chapter targets 16 Galactic GCs. The selected clusters are representative of the overall Galactic GC population spanning a wide range of central densities and concentrations, different stages of dynamical evolution, and different environmental conditions. The details of the datasets, the membership selections, and MP classifications are presented in section 6.5.1.

For each cluster in the sample we first analyzed the kinematic properties in terms of velocity dispersion and rotation profiles for the LOS and plane-of-the-sky components separately (section 6.1.1); then, for the fraction of stars for which all velocity components are available, we performed a full 3D study (section 6.1.2). We adopted the cluster centers reported by Goldsbury et al. (2010). All velocities were corrected for perspective effects induced by the clusters' systemic motions by using the equations reported in van Leeuwen (2009) and following the approach already adopted in Dalessandro et al. (2021b) and Della Croce et al. (2023).

6.1.1 1D velocity dispersion and rotation profiles

To characterize the kinematic properties of the clusters in the sample and of their subpopulations, we adopted the Bayesian approach described in Cordero et al. (2017, see also Dalessandro et al. 2018c) , which is based on the use of a discrete fitting technique to compare simple kinematic models (including a radial dependence of the rotational amplitude and velocity dispersion of the cluster) with individual radial velocities. We stress that this is a purely kinematic approach aimed at searching for relative differences among different clusters and sub-populations, and it is not aimed at providing a self-consistent dynamical description of each system.

The likelihood function for the radial velocities of individual stars depends on our assumptions about the formal descriptions of the rotation and velocity dispersion radial variations. For the velocity dispersion profile we assumed the functional form of the Plummer model (Plummer, 1911), which is simply defined by its central velocity dispersion σ_0 and its scale radius a:

$$\sigma^2(R) = \frac{\sigma_0^2}{\sqrt{1 + R^2/a^2}} \,, \tag{6.1}$$

where R is the projected distance from the center of the cluster. We adopted the same formal description for all velocity components. For the rotation curve, we assumed cylindrical rotation and adopted the functional form expected for stellar systems undergoing violent relaxation during their early phases of evolution (Lynden-Bell, 1967):

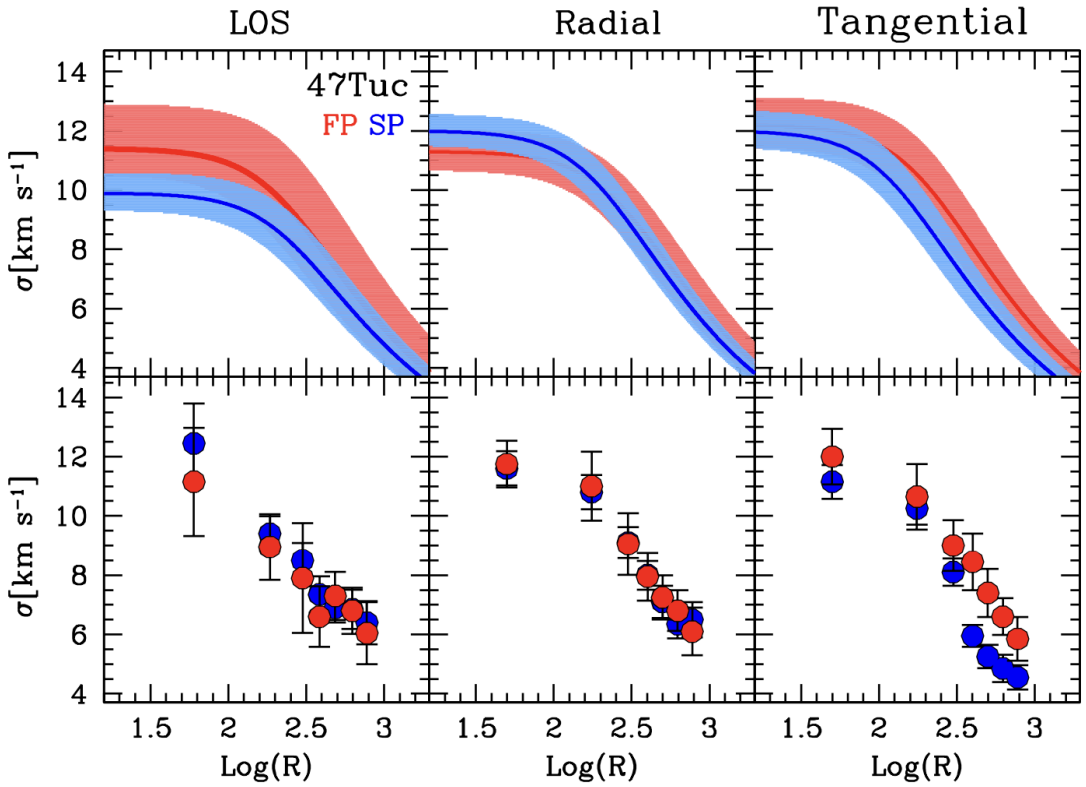

FIGURE 6.1: Velocity dispersion profiles of MPs in 47 Tucanae. *Bottom panels:* observed velocity dispersion profiles along the LOS, radial, and tangential velocity components by using a maximum-likelihood approach on binned data. *Upper panels:* Best-fit velocity dispersion profiles as obtained using the Bayesian analysis on discrete velocities described in section 6.1.1.

$$V_{\rm rot}\sin i(X_{\rm PA_0}) = \frac{2A_{\rm rot}}{R_{\rm peak}}\frac{X_{\rm PA_0}}{1+(X_{\rm PA_0}/R_{\rm peak})^2}, \tag{6.2}$$

$$v_{\rm T} = \frac{2V_{\rm peak}}{R_{\rm peak}}\frac{R}{1+(R/R_{\rm peak})^2}, \tag{6.3}$$

for the LOS (equation 6.2) and tangential (equation 6.3) velocity components, respectively. In equation 6.2, $V_{\rm rot}\sin i$ represents the projection of the rotational amplitude along the LOS velocity component at a projected distance $X_{\rm PA_0}$ from the rotation axis. $A_{\rm rot}$ is the peak rotational amplitude occurring at the projected distance $R_{\rm peak}$ from the cluster center. We defined the rotation axis PA as increasing anti-clockwise in the plane of the sky from the north (PA= 0°) to the east (PA= 90°). Since the inclination of the rotation axis is unknown, $V_{\rm rot}\sin i$ represents a lower limit to the actual rotational amplitude. As an extreme case, if the rotation axis is aligned with the LOS, the rotation would be in the plane of the sky. In equation 6.3, $V_{\rm peak}$ represents the maximum (in an absolute sense) of the mean motion in the tangential component.

The fit of the kinematic quantities was performed by using the `emcee` (Foreman-Mackey

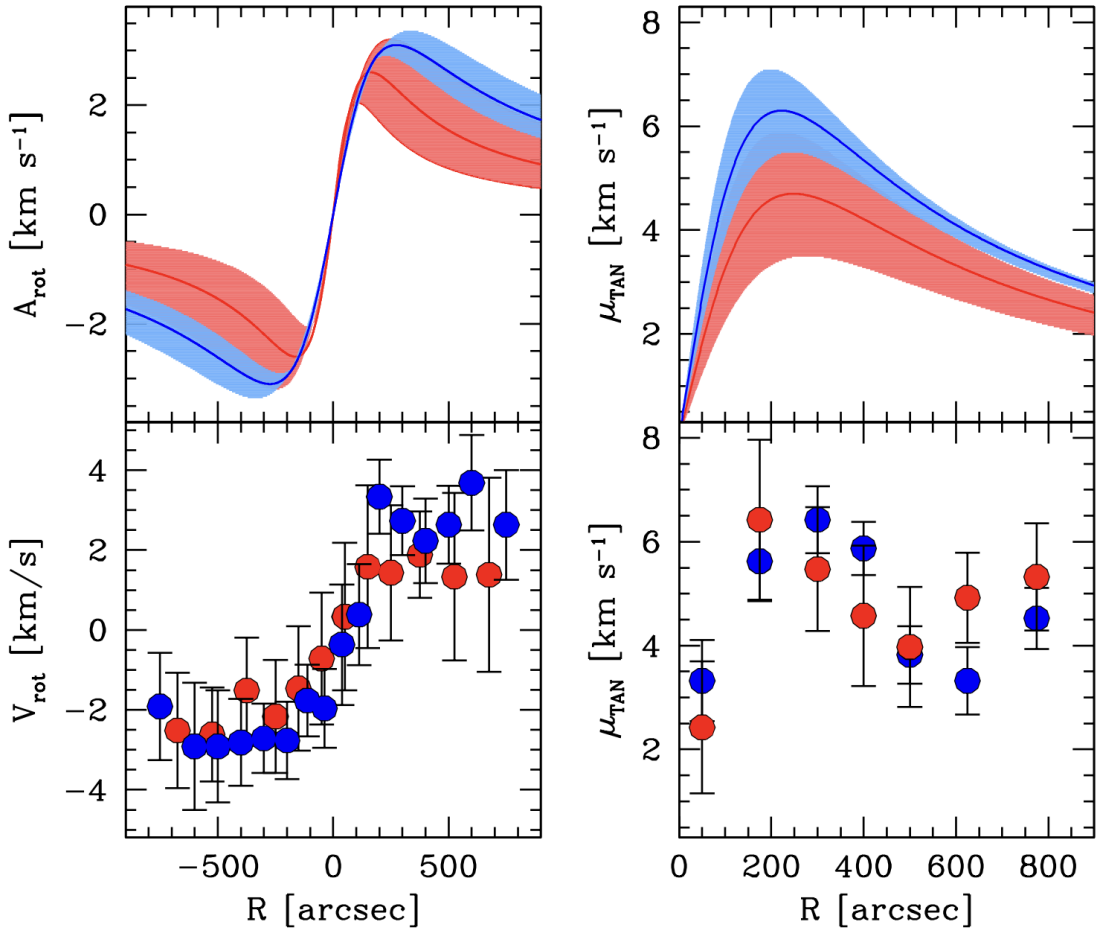

FIGURE 6.2: Same as figure 6.1, but for rotation profiles along the LOS (left panel) and tangential (right panel) components for MPs in 47 Tuc.

et al. 2013) implementation of the MCMC sampler, which provides the posterior probability distribution function for σ_0, a, $A_{\rm rot,}$ and PA_0. For each quantity, the 50th, 16th, and 84th percentiles of the PDF distributions were adopted as the best-fit values and relative errors, respectively. We assumed a Gaussian likelihood and flat priors on each of the investigated parameters within a reasonably wide range of values. It is important to note that in general, since the analysis is based on the conditional probability of a velocity measurement given the position of a star, our fitting procedure is not biased by the spatial sampling of the stars in the different clusters and subsamples. However, the kinematic properties are better constrained in regions that are better sampled (i.e., more stars with available kinematic information).

As a sanity check and comparison, we also derived the velocity dispersion and rotation profiles by splitting the surveyed areas in a set of concentric annuli, whose width was chosen as a compromise between a good radial sampling and a statistically significant number of stars. In this case, the analysis was limited radially within a maximum distance from the center of the clusters to guarantee a symmetric coverage of the field of view. The adopted limiting distance varies from one cluster to the other depending on the photometric and kinematic dataset field-of-view limits (section 6.5.1). While this approach requires the splitting of the

sample in concentric radial bins, whose number and width are at least partially arbitrary and can potentially have an impact on the final results, it has the advantage of avoiding any assumption on the model description of the velocity dispersion and rotation profiles.

In each radial bin, the velocity dispersion was computed by following the maximum-likelihood approach described by Pryor & Meylan (1993). The method is based on the assumption that the probability of finding a star with a velocity of v_i and error e_i at a projected distance from the cluster center R_i can be approximated as

$$p(v_i, e_i, R_i) = \frac{1}{2\pi\sqrt{\sigma^2 + e_i^2}} \exp -\frac{1}{2}\frac{(v_i - v_0)^2}{\sigma^2 + e_i^2}, \tag{6.4}$$

where v_0 and σ are the systemic velocity and the intrinsic dispersion profile of the cluster along the three components (i.e., LOS, R, and T) at a cluster-centric distance R_i, respectively.

As for the rotation along the LOS component, we used the method fully described in Bellazzini et al. (2012) and already adopted by Ferraro et al. (2018b); Lanzoni et al. (2018a); Dalessandro et al. (2021a); Leanza et al. (2022). In brief, we considered a line passing through the cluster center with the position angle varying from $-90°$ to $90°$ in steps of $10°$. For each value of PA, such a line splits the observed sample in two. If the cluster is rotating along the LOS, we expect to find a value of PA that maximizes the difference between the median LOS velocities of the two sub-samples, since one component is mostly approaching and the other is receding with respect to the observer. Moving PA from this value has the effect of gradually decreasing the difference in the median LOS velocity. Hence, the appearance of a coherent sinusoidal behavior as a function of PA is a signature of rotation, and its best-fit sine function provides an estimate of the rotation amplitude ($A_{\rm rot}$) and the position angle of the cluster rotation axis ($\rm PA_0$). For the plane-of-the-sky rotation, we used the variation of the mean values within each radial bin of the tangential velocity component with respect to the systematic motion.

Examples of the results obtained with both the Bayesian and maximum-likelihood analyses are shown in figures 6.1 and 6.2 for the MPs of the GC 47 Tuc. For all clusters in the sample, we find a good agreement between the discrete and binned analysis; however, in the following we adopt the best-fit results (and errors) obtained with the Bayesian approach. table 6.3 reports the best-fit values and relative errors for the most relevant quantities along both the LOS and plane of the sky for both the FP and SP.

6.1.2 Full 3D kinematic analysis

To perform a full 3D analysis, we used the kinematic sample of member stars with both LOS velocities and *Gaia* PMs after quality selection (see section 6.5.1). We also limited the analysis to the same radial extension adopted for the binned maximum-likelihood analysis (section 6.1.1).

We followed the approach described in Sollima et al. (2019), which has the advantage of constraining a cluster full-rotation pattern by estimating the inclination angle of the rotation axis (i) with respect to the LOS, the position angle of the rotation axis (θ_0), and the rotation velocity amplitude (A), by means of a model-independent analysis. In a real cluster, the angular velocity is expected to be a function of the distance from the rotation axis (see, e.g., equations 6.2-6.3). To account for such a dependence in a rigorous way, a rotating model

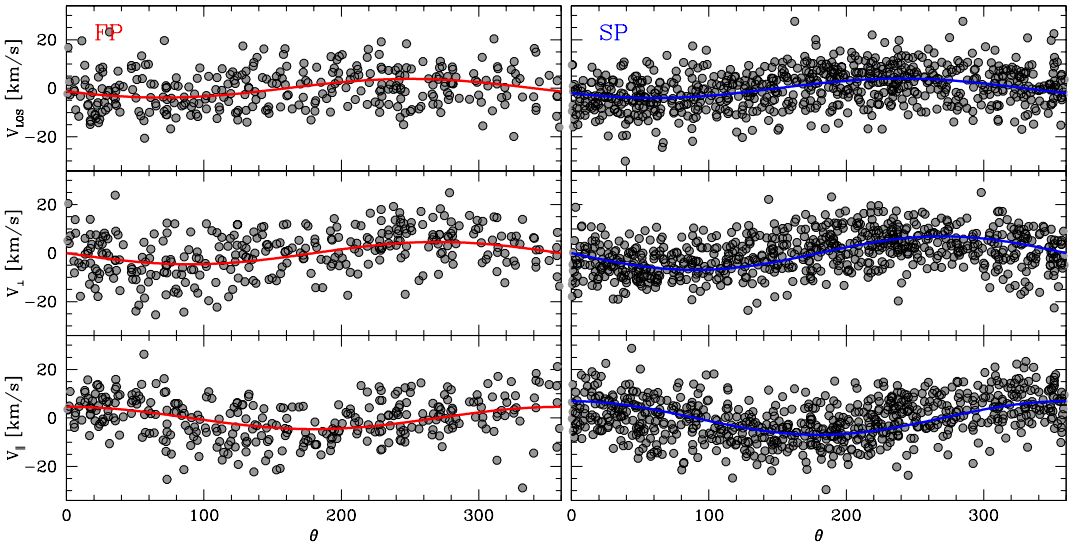

FIGURE 6.3: Distribution of the three velocity components as a function of the position angle for MPs in 47 Tuc. Left and right panels refer to the FP and SP subpopulations, respectively. The solid lines show the best-fitting trend in all panels.

should be fit to the data. However, to perform a model-independent analysis, we considered an average projected rotation velocity with amplitude A_{3D}, which has been assumed to be independent of the distance from the cluster center. While of course this represents a crude approximation of the rotation patterns expected in GCs and provides a rough average of the actual rotation amplitude, it is important to stress that it does not introduce any bias in the estimation of θ_0 and i.

A_{3D}, i, and θ_0 were derived by solving the equations describing the rotation projection along the LOS (V_{LOS}) and those perpendicular ($V_\perp$) and parallel ($V_\parallel$) to the rotation axes (see equation 2 in Sollima et al. 2019). While the velocity component perpendicular to the rotation axis has a dependence on stellar positions within the cluster along the LOS, we neglected it in our analysis. In fact, we note that the dependence on the stellar distance along the LOS does not affect the mean trend of the perpendicular velocity component, but it can only introduce an additional spread on its distribution. We assumed that i varies in the range $0° < i < 90°$ with respect to the LOS and the position angle in the $0° < \theta_0 < 360°$ range. θ_0 grows counterclockwise from north to east, and A_{3D} is positive for clockwise rotation in the plane of the sky. Following the approach already adopted for the 1D analysis, we derived the best-fit rotation amplitudes, position and inclination angles, and relative errors by maximizing the likelihood function reported in equation 3 of Sollima et al. (2019) using the MCMC algorithm `emcee`. Best-fit results are reported in table 6.3. Figure 6.3 shows the result of the best-fit analysis along the three velocity components for the FP and SP subpopulations of 47 Tuc.

6.2 Results

To obtain quantitative and homogeneous estimates of the possible kinematic differences among MPs, to follow their evolution, and eventually to compare the results obtained for all GCs in the sample with theoretical models and dynamical simulations, we introduced a few simple parameters described in detail in the following. These parameters are meant to incorporate, in a meaningful way, all the main relevant physical quantities at play in a single value. The general approach of our analysis is not to focus on the detection of specific and particularly significant kinematic differences of specific targets, but rather to compare the general kinematic behaviors described by MPs in all targets in the sample in the most effective way.

A description about the approach adopted to quantify the possible impact of the intrinsically limited statistical kinematic samples and of their incompleteness on the final results is discussed in section 6.5.3. Here, we briefly stress that the main effects are not on the derived best-fit values, but rather on their uncertainties. While the main focus of the following sections is the MP kinematics, we also analyzed the entire sample of stars with kinematic information (hereafter labeled TOT) for comparison with previous works, and we present the main results in section 6.5.4.

6.2.1 Observational evidence of internal rotation differences

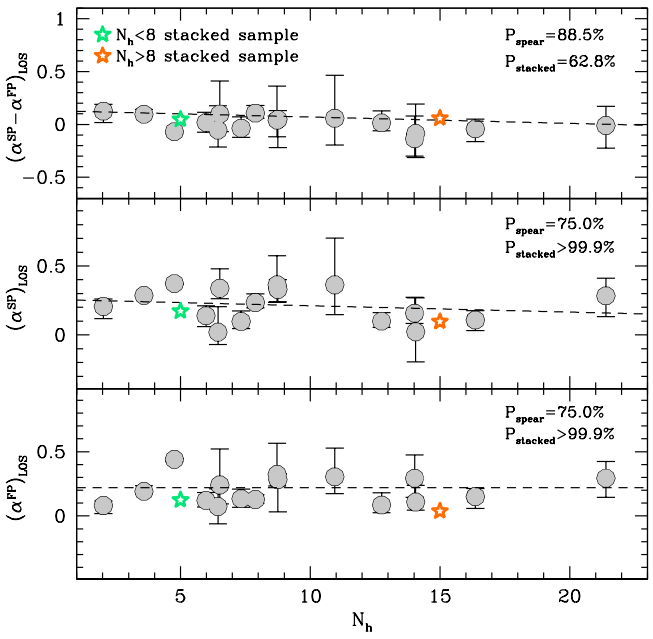

FIGURE 6.4: Bottom and middle panels show the distribution of the $(\alpha)_{\rm LOS}$ parameter for the FP and SP as a function of the dynamical age $n_{\rm h}$ for all clusters in the sample (gray circles). The upper panel shows the distribution of the rotation differences $(\alpha^{\rm SP} - \alpha^{\rm SP})_{\rm LOS}$. The dashed lines represent the linear best-fit to the GC distribution. In all panels, the star symbols refer to the results obtained for the stacked analysis on the dynamically young (green) and old (orange) samples. The size of the star matches the amplitude of the errorbars.

To measure the rotation differences between the SP and FP subpopulations for all clusters in the sample for both the LOS and tangential velocity components, we introduced a parameter, hereafter referred to as α. It is defined as the area subtended by the ratio between the best-fit rotation velocity profile and the best-fit velocity dispersion profile for each subpopulation in a cluster (section 6.1.1) after rescaling the cluster-centric distance to the value of the peak (R_α) of such a distribution:

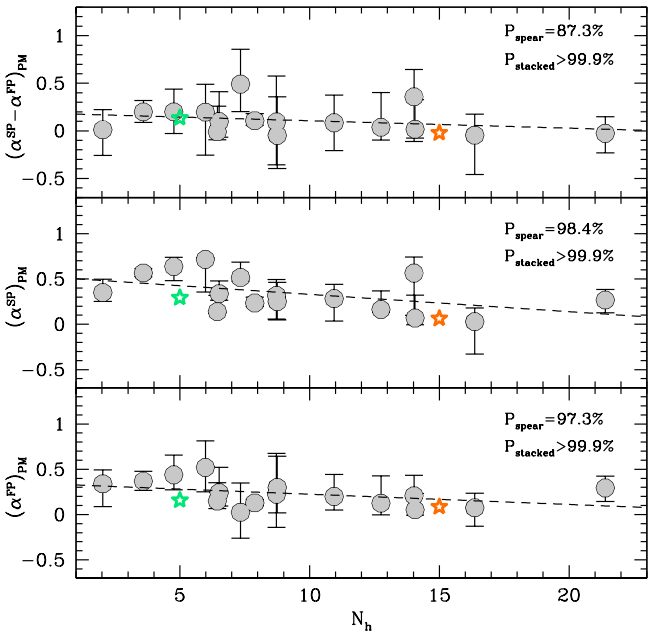

FIGURE 6.5: Same as in figure 6.4, but for $(\alpha)_{PM}$.

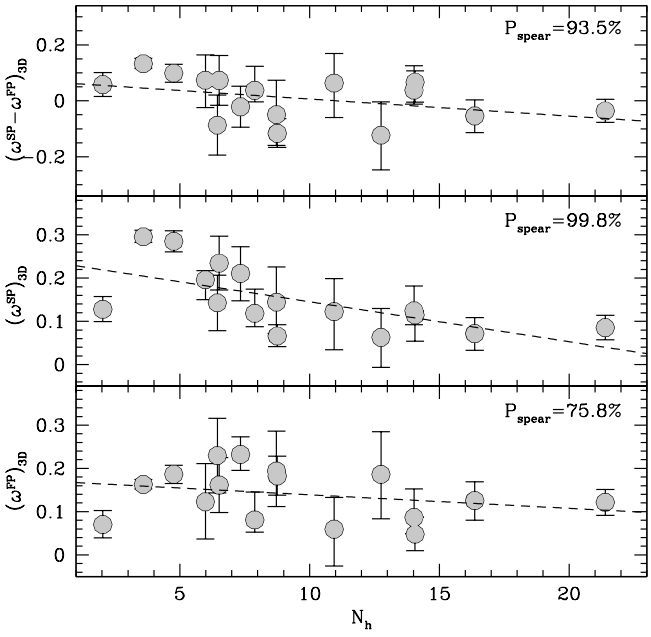

FIGURE 6.6: As in figures 6.4 and 6.5, but now for the ω_{3D} parameter.

$$\alpha^X = \int_0^1 V_{\rm rot}(\xi)/\sigma(\xi) d\xi, \tag{6.5}$$

where $V_{\rm rot}$ and σ can either refer to the LOS or the tangential velocity components, ξ is the cluster-centric distance normalized to the R_α, and the index X refers to the different subpopulations (i.e., FP or SP).

This parameter has the advantage of providing a robust measure of the relative strength

of the rotation signal over the disordered motion at any radial range without making any assumption about the underlying star or mass distribution. By construction α depends on the considered cluster-centric distance and therefore a meaningful cluster-to-cluster comparison requires that the parameter is measured over equivalent radial portions in every system. As shown in a number of numerical studies (see, e.g., Hénault-Brunet et al. 2015; Tiongco et al. 2019), dynamical evolution is expected to smooth out primordial kinematic and structural differences in the innermost regions first and then in the cluster's outskirts. Therefore, capturing rotation differences between MPs requires a compromise between probing a fairly wide radial coverage in order to trace regions where kinematic differences should be present for a longer time and sampling distances from the cluster center where rotation is more prominent. With this in mind, we decided to measure α within R_{α}. We also verified that the adoption of different radial selections does not have a significant impact on the overall relative distribution of α values. Errors on α were obtained by propagating the posterior probability distributions obtained from the MCMC analysis for the best-fit rotation and velocity dispersion profiles' derivation (see section 6.1.1). Differences between SP and FP kinematic patterns are constrained simply by $(\alpha^{\rm SP} - \alpha^{\rm FP})$. With such a definition, a more rapidly rotating SP yields positive values of $(\alpha^{\rm SP} - \alpha^{\rm FP})$.

Along similar lines, we defined a parameter to describe the 3D rotation:

$$\omega^{X}_{3D} = (A_{\rm 3D}/\sigma^{\rm 3D}_{0})/(R_{\rm m}/R_{\rm hl}), \tag{6.6}$$

where $\sigma^{\rm 3D}_{0}$ represents the 3D central velocity dispersion and it is defined as the quadratic average of the σ_0 values obtained for the three velocity components (i.e., LOS, R, and T - section 6.1.1); $R_{\rm m}$ is the average cluster-centric distance of stars for which we have tridimensional velocity measures, and $R_{\rm hl}$ is the system half-light radius (from Harris 1996). Here, $R_{\rm hl}$ is adopted as a meaningful radial normalization factor to secure a direct comparison among different GCs attaining significantly different projected radial extensions. In the assumption of a pure solid-body rotation, $\omega_{\rm 3D}$ would represent the best-fit angular rotation. As for the 1D analysis, the introduction of $\omega_{\rm 3D}$ is primarily meant to provide a direct and reliable characterization of the 3D rotation based only on quantities that are directly derived from the observations. Differences in the 3D rotation of SP and FP are given by $(\omega^{\rm SP}_{\rm 3D} - \omega^{\rm FP}_{\rm 3D})$, which yields positive values for a more rapidly rotating SP.

Several works have shown that the rotation strength observed in GCs is primarily shaped by their dynamical age, with dynamically young systems typically showing the larger degree of rotation (e.g., Fabricius et al. 2014; Bianchini et al. 2018; Kamann et al. 2018; Sollima et al. 2019). We used $n_{\rm h} = t_{\rm age}/t_{\rm rh}$ as a proxy of the clusters' dynamical ages. We adopted the half-mass relaxation time ($t_{\rm rh}$) values reported by Harris (1996) and ages derived by Dotter et al. (2010) for all clusters except for NGC 1904, for which we used the age inferred by Dalessandro et al. (2013).

In figure 6.15, we show the distribution of the α values (along both the LOS and tangential velocity components) and of $\omega_{\rm 3D}$ as a function of $n_{\rm h}$ for the TOT population. In general, we find a very good agreement with previous analyses (e.g., Bianchini et al. 2018; Kamann et al. 2018; Baumgardt et al. 2019; Sollima et al. 2019) in terms of correlation between cluster rotation strength and dynamical age, thus further strengthening the idea that the present-day cluster rotation is the relic of that imprinted at the epoch of cluster formation, and that it has since progressively dissipated via two-body relaxation (Einsel & Spurzem, 1999; Hong

et al., 2013; Tiongco et al., 2017; Livernois et al., 2022; Kamlah et al., 2022). Interestingly, such an agreement also provides an independent assessment of the reliability of the adopted kinematic parameters.

In figures 6.4, 6.5, and 6.6, we show the distributions of α (for both the LOS and PM components) and of ω_{3D} as a function of n_h for both SP and FP stars (bottom and middle panels). Interestingly, a number of common patterns can be highlighted in the three figures. First, we note that in a large fraction of clusters (up to $\sim 50\%$) both FP and SP show evidence of non-negligible rotation. Second, both subpopulations show evidence of anticorrelation with n_h in all three analyzed velocity components, with dynamically young clusters being characterized by a larger rotation strength. This behavior turns out to be more prominent when the PM and 3D analyses are considered. This is somehow expected as PMs are less affected than the LOS velocities by the smoothing introduced by the superposition of stars located at different cluster-centric distances and attaining different rotation velocities. In addition, the 3D analysis accounts for any rotation axis inclination and projection effects. Finally, we observe that for all velocity components, in dynamically young clusters the SP is characterized by larger α and ω_{3D} values (i.e., more rapid rotation) than that observed for the FP at similar n_h, and it shows a more rapid decline than the FP as a function of n_h. In fact, a Spearman correlation test gives a probability P_{spear} larger than $\sim 99\%$ of correlations between $(\alpha^{SP})_{PM}$ or ω^{SP}_{3D} and n_h, while probabilities are smaller when either the LOS component or the FP is considered. We note here that by using the approach described in Curran (2015) we have verified that the results of the Spearman rank correlation tests performed in our analysis and reported in the following are robust against possible outliers and errors associated with the adopted kinematic parameters.

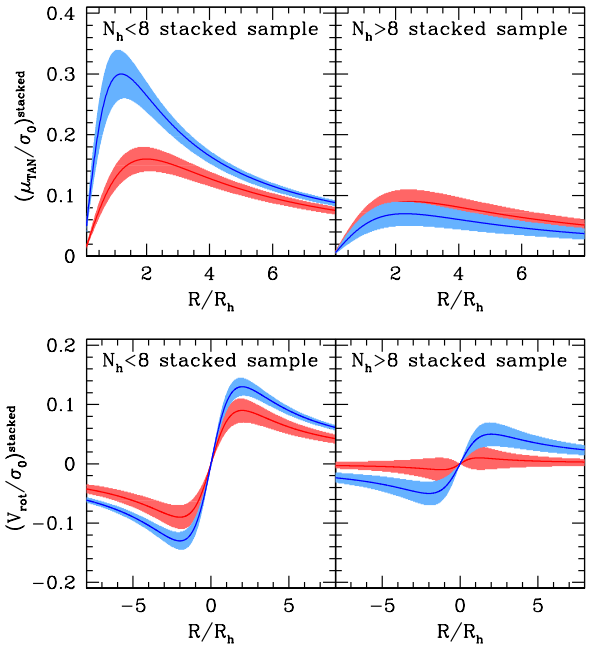

FIGURE 6.7: Best-fit results of kinematic analysis of dynamically young ($n_h < 8$) and old ($n_h > 8$) stacked samples. FP is in red and SP in blue. The lower panels refer to the LOS rotation, while the upper row shows the results for the tangential velocity component.

To better highlight such a differential behavior, the upper panels of figures 6.4, 6.5, and 6.6 show the difference between the rotation strength of the SP and FP as given by $(\alpha^{SP}-\alpha^{FP})$ and $(\omega^{SP}_{3D}-\omega^{FP}_{3D})$. Admittedly, neither $(\alpha^{SP}-\alpha^{FP})$ nor $(\omega^{SP}_{3D}-\omega^{FP}_{3D})$ show striking

variations in the dynamical age range sampled by the target clusters ($2 < n_{\rm h} < 25$). In fact, Spearman rank correlation tests give probabilities of correlation of $P_{\rm spear} \sim 90\%$ ($\sim 95\%$ in the 3D case). Interestingly, however, a negative trend between the rotation strength differences and $n_{\rm h}$ is consistently observed in all velocity components. In fact, both ($\alpha^{\rm SP} - \alpha^{\rm FP}$) and ($\omega_{\rm 3D}^{\rm SP} - \omega_{\rm 3D}^{\rm FP}$) show positive values for dynamically young GCs, and then they progressively approach zero for dynamically older clusters, meaning that FP and SP rotate at the same velocity. The good agreement between the results obtained in the three analyses definitely supports the fact that there is a real correlation between the SP and FP rotation strength differences and $n_{\rm h}$, and that SP generally shows a more rapid rotation than the FP at dynamically young ages. These results represent the first observational evidence of the link between MP rotation patterns and clusters' long-term dynamical evolution.

We do not find any significant difference between the MP rotation axis orientation for the LOS and 3D analyses. In fact, the mean difference between the best-fit $\rm PA_0$ values of the SP and FP is $-2^\circ \pm 19^\circ$, and those between θ_0 and i are $4^\circ \pm 24^\circ$ and $2^\circ \pm 12^\circ$, respectively.

As an additional way to analyze the data and search for possible trends, we divided the clusters in two subgroups according to their dynamical ages. In particular, we defined a group of clusters with $n_{\rm h} < 8$ and a complementary one ($n_{\rm h} > 8$) including all the remaining GCs. In this way, the two subgroups turn out to be populated by the same number of systems. Within each subgroup and subpopulation, we then stacked all the available kinematic information after normalizing the cluster-centric distances to the cluster's $R_{\rm hl}$ (from Harris 1996), the velocities to the central velocity dispersion in a given velocity component (as obtained by the analysis described in section 6.1), and rotating all clusters to have the same $\rm PA_0$ (section 6.1.1). In this way, we were able to jointly compare the behavior of MPs for multiple clusters at once, thus increasing the number of stars that can be used to study the kinematics of each subpopulation and narrowing down the uncertainties on the derived kinematic parameters. The kinematics of MPs in the two stacked samples was then analyzed following the same approach described in section 6.1 and previously adopted for single GCs. Figure 6.7 shows the results of the kinematic analysis for the two stacked samples for both the LOS and tangential components (lower and upper panels, respectively). In both cases, a significant difference between the FP and SP rotation profiles is observed for the dynamically young ($n_{\rm h} < 8$) stacked sample, while they almost disappear for the dynamically old GCs. We then derived the same kinematic parameters described by equation 6.5for a direct comparison with single GCs. Results are shown in figures 6.4 and 6.5 by the two star symbols. Both in the LOS and tangential components and for each subpopulation, results are fully consistent with the general trend described by single clusters. Interestingly, the reduced uncertainties strengthen the significance of the observed differences discussed above. In particular, the stacked analysis shows that the observed trends between $\alpha^{\rm FP}$, $\alpha^{\rm SP}$, and $n_{\rm h}$ along both the LOS and tangential components are significant at a large confidence level ($P_{\rm stacked} > 5\sigma$). Also, while the ($\alpha^{\rm SP} - \alpha^{\rm FP}$) difference between dynamically young and old clusters is only marginally significant along the LOS component, it turns out to be significant at an$\sim 6\sigma$ level for the tangential component. Unfortunately, we could not apply the 3D rotation analysis (section 6.1.2) to the stacked samples as it is not possible to report all clusters to the same values of θ_0 and i.

6.2.2 Exploring the link between MP ellipticity and rotation

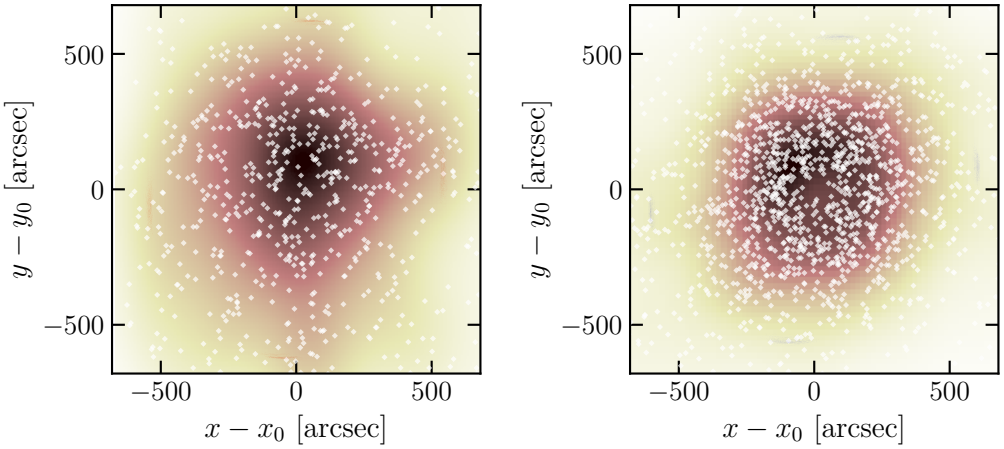

FIGURE 6.8: 2D density maps of stars selected in the GC 47 Tuc for kinematic analysis. FPs are shown in the left panel, while SPs in the right panel. Overplotted to the density distributions are the best-fit ellipses.

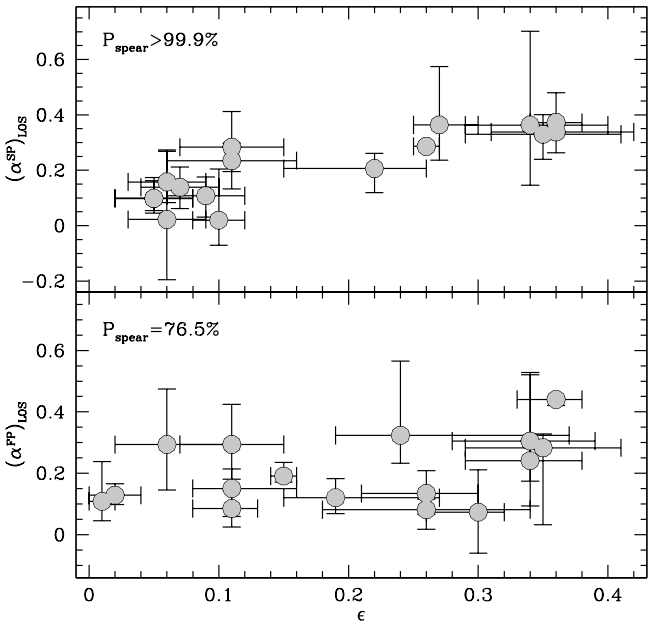

FIGURE 6.9: Distributions of $(\alpha)_{\rm LOS}$ parameter for FP and SP (lower and upper panel respectively) as a function of the best-fit ellipticity values for the two subpopulations.

In general, a rotating system is also expected to be flattened in the direction perpendicular to the rotation axis (Chandrasekhar, 1969). Under the assumption that GCs can be described by the same dynamical model, such as an isotropic oblate rotator (e.g., Varri & Bertin 2012), stronger rotation would be expected in more flattened systems. However, various effects can dilute a possible correlation, the most important ones being anisotropies, inclination effects,

or tidal forces from the MW (see van den Bergh 2008 for an estimate of the impact of the latter). Nevertheless, Fabricius et al. (2014) and Kamann et al. (2018) were able to reveal a correlation between cluster rotation and ellipticity in a sample of Galactic GCs (see also Lanzoni et al. 2018a; Dalessandro et al. 2021a and Leanza et al. 2023 for similar analyses on specific clusters).

Following on from those results, we searched for any link between MP rotation and ellipticity for all clusters in our sample. The results of such a comparison for population TOT are reported in section 6.5.4. We inferred the ellipticity (defined as $\epsilon \equiv 1 - q$, see equation 5.3) of FP and SP stars by following the procedure presented in section 5.2.1. As an example, figure 6.8 shows the result of the analysis for the MPs in 47 Tuc, while table 6.3 reports the best-fit values for each GC and subpopulation.

We compared the ellipticity estimates with the $(\alpha)_{\rm LOS}$ MP values in figure 6.9. Both populations show a positive correlation between $(\alpha)_{\rm LOS}$ and ϵ, with Spearman rank correlation probabilities $P_{\rm spear} \sim 80\%$ and $P_{\rm spear} > 99.9\%$ for the FP and SP, respectively, which is in good agreement with previous results by Fabricius et al. (2014) and Kamann et al. (2018). In detail, the FP shows a pretty flat distribution of $(\alpha^{\rm FP})_{\rm LOS}$ up to ellipticity values of $\epsilon \sim 0.2$. Then, $(\alpha^{\rm FP})_{\rm LOS}$ starts to increase almost linearly with ϵ. As discussed in section 6.2.1, the SP tends to show larger values of rotation than the FP. Likely driven by such a stronger rotation, in the upper panel of figure 6.9, we observe that $(\alpha^{\rm SP})_{\rm LOS}$ follows a nicely linear correlation with ϵ for the entire range of ellipticity values sampled by the target GCs.

Following the analysis by Fabricius et al. (2014) and Kamann et al. (2018), we computed the differences between the PA values for the 2D stellar spatial distribution and the best-fit rotation axis position angles ($\rm PA_0$). Interestingly, while the distribution of the difference is pretty scattered, we find that the average value for the systems in our sample is $\sim 85°$, thus implying that the stellar density distribution is on average flattened in the direction perpendicular to the rotation axis. This behavior is in general agreement with what is expected for a rotating system, and it is qualitatively consistent with what was predicted, for example, by the models introduced by Varri & Bertin (2012) and previously found in other observational studies (e.g., Bianchini et al. 2013; Bellini et al. 2017; Dalessandro et al. 2021a; Leanza et al. 2022).

6.2.3 Numerical simulations of rotating MP clusters

To conclude the discussion about the rotational properties of MPs in our target GCs, we briefly present the results of a set of N-body simulations aimed at exploring the evolution of rotating MP clusters. A full discussion and detailed description of the results of these simulations will be presented in White et al. (in prep.). Here, we only report the evolutionary path followed by the α parameter to trace the strength of rotation of FP and SP stars and their difference. In our simulations, we only focused on the long-term dynamics driven by the effects of two-body relaxation for star clusters evolving in the external tidal field of their host galaxy. Each system starts with 10^5 stars with masses between 0.1 and 1 $M_\odot$ distributed according to a Kroupa (2001) stellar initial mass function. Our systems start with an equal number of FP and SP stars; following the general properties emerging from a few studies of the formation of SP stars in rotating clusters (see, e.g., Bekki 2010, 2011; Lacchin et al. 2022), the SP is initially more centrally concentrated and more rapidly rotating than the FP. The two populations rotate around a common axis. To explore the interplay between internal

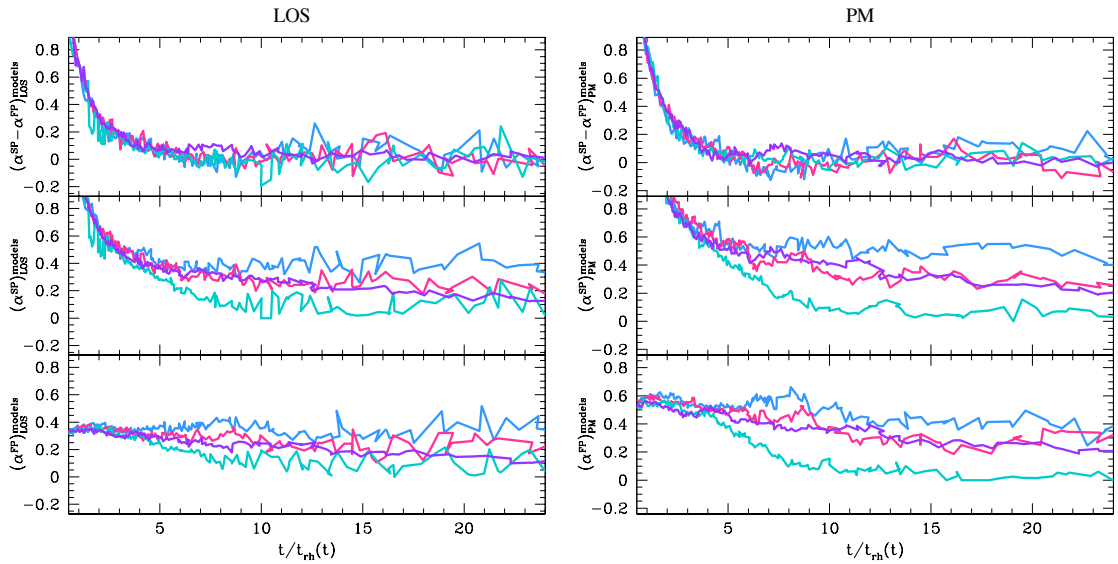

FIGURE 6.10: Time evolution of rotational parameters $\alpha^{\rm FP}$, $\alpha^{\rm SP}$, and their differences (see section 6.2.1) for the simulations described in section 6.2.3. The blue line corresponds to the model with $\delta = 0°$; the pink, cyan, and purple correspond to $\delta = 45°, 90°$, and $180°$, respectively.

dynamics and the effects due to the external tidal field, we explored models with different angles δ between the internal rotation axis and the rotation axis of the cluster orbital motion around the center of the host galaxy. In particular, we explored systems with values of δ equal to 0°, 45°, 90°, and 180°. The simulations were run with the `NBODY6++GPU` code (Wang et al., 2015). In figure 6.10, we show the time (normalized to $t_{\rm rh}$) evolution of $\alpha^{\rm FP}$, $\alpha^{\rm SP}$, and $(\alpha^{\rm SP} - \alpha^{\rm FP})$ for these models using rotational velocity profiles calculated for both the LOS (left panel) and the tangential component (right panel). For these plots we adopt an ideal LOS perpendicular to the cluster angular momentum or parallel to it. We emphasize that these simulations are not aimed at a detailed comparison with observations, but they serve as a guide to illustrate the extent of the effects of dynamical processes on the initial differences between the rotational kinematics of the FP and SP populations. We also reiterate that our simulations are focussed on the effects of two-body relaxation and do not include early dynamical phases such as those during which a star cluster responds to the mass loss due to stellar evolution, which can have an effect on the subpopulations' dynamical differences (see, e.g., Vesperini et al. 2021; Sollima 2021).

By construction, the α values derived for the SP are significantly larger (by about a factor of 2-3) than those of the FP. The results of our simulations show that the effects of two-body relaxation lead to a rapid and significant reduction of the initial difference between the FP and the SP rotation in the first $2 - 4\ t_{\rm rh}$ reaching values of $(\alpha^{\rm SP} - \alpha^{\rm FP})$ similar to those found in our observational analysis. Then, at later dynamical ages, $(\alpha^{\rm SP} - \alpha^{\rm FP})$ keeps decreasing at a slower pace, and it progressively approaches values close to zero around ten relaxation times, at which point FP and SP stars rotate at the same velocity. We note that, as already discussed in section 6.2.1 and in agreement with what was found in the observations, the rotation strength for both the FP and SP along with their difference is stronger when a PM-like projection is considered (figure 6.10). The behavior described by the simulations

is generally in good agreement with the observed trends (figures 6.4, 6.5, and 6.6). Such an agreement strongly suggests that both the rotational differences and the mild trend between the rotation strength and the dynamical age revealed by our observational analysis are consistent with those expected for the long-term dynamical evolution of GCs born with an SP initially rotating more rapidly than the FP.

6.3 Comparison with the literature

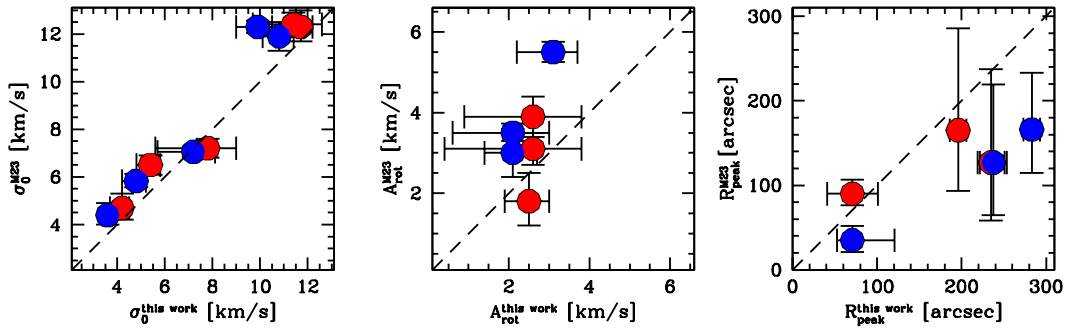

FIGURE 6.11: Comparison between best-fit σ_0, $A_{\rm rot}$, and $R_{\rm peak}$ values obtained for MPs in the present work and by Martens et al. (2023). Blue dots refer to SP and red ones to FP results.

In section 6.5.4, we report on a quantitative comparison between the results obtained in the present work and those available in the literature for the TOT population in each cluster. Here, we detail the comparison with previous works focusing on the kinematics of MPs. We stress that the full 3D kinematic analysis presented is the first ever obtained for MPs. Hence, in the following, our comparison is limited to studies considering a single velocity component.

Our sample has six GCs in common with the recent analysis by Martens et al. (2023) based on *MUSE* LOS velocities. The authors were able to find MP best-fit solutions for both the velocity dispersion and rotation profiles for three of them (namely 47 Tuc, NGC 5904, and NGC 6093), while for NGC 3201 and NGC 6254 they report only conservative upper limits for the MP rotation amplitudes, and for NGC 1904 they provide information only for the TOT population. Figure 6.11 shows the distributions of the differences in terms of σ_0 (which is defined as $\sigma_{\rm max}$ in Martens et al. 2023), $A_{\rm rot}$ ($v_{\rm max}$ in Martens et al. 2023), and $R_{\rm peak}$ for the FP and SP subpopulations. A good agreement is observed both for the MP central velocity dispersion values (left panel of figure 6.11) and the rotation amplitude (middle panel), with the most discrepant value being that corresponding to the rotation of the SP in 47 Tuc. Within the errors, there is also a reasonable match between the values of $R_{\rm peak}$. We note, however, that while the sample is certainly small, the estimates of $R_{\rm peak}$ by Martens et al. (2023) tend to be slightly smaller than those derived in this work. This might be somehow linked to the smaller radial coverage of the Martens et al. (2023) analysis. In fact, all values derived by Martens et al. (2023) for the clusters in common are located well outside the *MUSE* field of view, and therefore they might be only partially constrained by their analysis.

Table 6.1: MP kinematic parameters describing the radial anisotropy and rotation along the LOS, PM, and 3D components.

Cluster	$\alpha_{\rm LOS}$	$\alpha_{\rm PM}$	$\omega_{\rm 3D}$	POP
NGC 104 (47 Tuc)	$0.19^{+0.04}_{-0.02}$	$0.37^{+0.11}_{-0.10}$	$0.16^{+0.02}_{-0.02}$	FP
	$0.29^{+0.01}_{-0.01}$	$0.57^{+0.05}_{-0.04}$	$0.30^{+0.02}_{-0.02}$	SP
NGC 288	$0.12^{+0.06}_{-0.05}$	$0.52^{+0.30}_{-0.27}$	$0.12^{+0.09}_{-0.09}$	FP
	$0.14^{+0.07}_{-0.08}$	$0.72^{+0.02}_{-0.36}$	$0.20^{+0.02}_{-0.05}$	SP
NGC 1261	$0.32^{+0.24}_{-0.09}$	$0.22^{+0.45}_{-0.36}$	$0.19^{+0.09}_{-0.08}$	FP
	$0.36^{+0.21}_{-0.13}$	$0.32^{+0.18}_{-0.26}$	$0.14^{+0.08}_{-0.07}$	SP
NGC 1904 (M 79)	$0.29^{+0.18}_{-0.15}$	$0.21^{+0.22}_{-0.02}$	$0.08^{+0.06}_{-0.04}$	FP
	$0.16^{+0.12}_{-0.07}$	$0.57^{+0.18}_{-0.47}$	$0.12^{+0.06}_{-0.03}$	SP
NGC 3201	$0.07^{+0.14}_{-0.13}$	$0.15^{+0.20}_{-0.08}$	$0.23^{+0.08}_{-0.08}$	FP
	$0.02^{+0.18}_{-0.09}$	$0.14^{+0.18}_{-0.02}$	$0.14^{+0.06}_{-0.06}$	SP
NGC 5272 (M 3)	$0.08^{+0.03}_{-0.06}$	$0.34^{+0.15}_{-0.25}$	$0.07^{+0.03}_{-0.03}$	FP
	$0.21^{+0.05}_{-0.09}$	$0.35^{+0.14}_{-0.10}$	$0.13^{+0.03}_{-0.03}$	SP
NGC 5904 (M 5)	$0.44^{+0.01}_{-0.02}$	$0.44^{+0.22}_{-0.16}$	$0.19^{+0.02}_{-0.02}$	FP
	$0.37^{+0.01}_{-0.01}$	$0.64^{+0.10}_{-0.15}$	$0.29^{+0.02}_{-0.02}$	SP
NGC 5927	$0.11^{+0.13}_{-0.06}$	$0.05^{+0.18}_{-0.06}$	$0.05^{+0.04}_{-0.04}$	FP
	$0.02^{+0.24}_{-0.22}$	$0.07^{+0.25}_{-0.07}$	$0.11^{+0.01}_{-0.06}$	SP
NGC 5986	$0.28^{+0.04}_{-0.25}$	$0.30^{+0.34}_{-0.28}$	$0.18^{+0.05}_{-0.04}$	FP
	$0.33^{+0.07}_{-0.09}$	$0.25^{+0.21}_{-0.20}$	$0.07^{+0.3}_{-0.03}$	SP
NGC 6093 (M 80)	$0.29^{+0.13}_{-0.15}$	$0.29^{+0.13}_{-0.15}$	$0.12^{+0.03}_{-0.03}$	FP
	$0.28^{+0.13}_{-0.15}$	$0.27^{+0.12}_{-0.14}$	$0.09^{+0.03}_{-0.03}$	SP
NGC 6171 (M 107)	$0.09^{+0.10}_{-0.06}$	$0.13^{+0.30}_{-0.13}$	$0.19^{+0.10}_{-0.10}$	FP
	$0.10^{+0.06}_{-0.04}$	$0.16^{+0.20}_{-0.03}$	$0.06^{+0.07}_{-0.07}$	SP
NGC 6205 (M 13)	$0.24^{+0.28}_{-0.15}$	$0.24^{+0.28}_{-0.15}$	$0.16^{+0.06}_{-0.06}$	FP
	$0.34^{+0.14}_{-0.07}$	$0.34^{+0.14}_{-0.07}$	$0.24^{+0.06}_{-0.06}$	SP
NGC 6362	$0.13^{+0.04}_{-0.03}$	$0.13^{+0.04}_{-0.03}$	$0.08^{+0.06}_{-0.03}$	FP
	$0.24^{+0.06}_{-0.04}$	$0.24^{+0.06}_{-0.04}$	$0.12^{+0.06}_{-0.03}$	SP
NGC 6254 (M 10)	$0.15^{+0.06}_{-0.09}$	$0.07^{+0.16}_{-0.20}$	$0.13^{+0.04}_{-0.05}$	FP
	$0.11^{+0.07}_{-0.08}$	$0.03^{+0.15}_{-0.36}$	$0.07^{+0.04}_{-0.04}$	SP
NGC 6496	$0.30^{+0.22}_{-0.13}$	$0.20^{+0.24}_{-0.15}$	$0.06^{+0.07}_{-0.09}$	FP
	$0.36^{+0.34}_{-0.22}$	$0.28^{+0.16}_{-0.25}$	$0.12^{+0.08}_{-0.09}$	SP
NGC 6723	$0.13^{+0.07}_{-0.07}$	$0.03^{+0.32}_{-0.29}$	$0.23^{+0.04}_{-0.04}$	FP
	$0.10^{+0.08}_{-0.05}$	$0.52^{+0.17}_{-0.04}$	$0.21^{+0.06}_{-0.06}$	SP

The sample analyzed in this work also counts four GCs in common with Cordoni et al. (2020), namely 47 Tuc, NGC 288, NGC 5904, and NGC 6254. Our results are in agreement with theirs in that 47 Tuc and NGC 5904 are the systems showing the larger rotation among the clusters in common. However, at odds with their results, we also find that in both GCs the SP show a larger rotation (as inferred both by $A_{\rm rot}$ and α values) than the FP. Also, within the uncertainties, we do not find evidence of any significant misalignment of the FP and SP rotation curves for these systems, nor in terms of position angles and inclination, as constrained by both the LOS and the full 3D analysis. Finally, our analysis is in good agreement with the results presented by Cordero et al. (2017) for the MP rotation patterns of M 13.

6.4 Summary and conclusions

We present the first self-consistent 3D kinematic analysis of MPs for a sample of Galactic GCs. The study targets 16 systems spanning a broad range of dynamical ages ($2 < n_{\rm h} < 25$) and is based on a large and mostly homogeneous observational dataset securing several hundreds of accurate LOS velocities and PMs for each cluster and sampling virtually their entire extension.

Our study is mainly focused on the analysis of the MP rotation along the three velocity components. The adopted approach is aimed at providing new insights into the long-term evolution of the kinematic properties of MPs (and their differences) for the entire sample of GCs and for the entire dynamical age covered by our analysis instead of focusing on the kinematic differences in specific clusters. To this aim, starting from the observed velocity distributions we defined a few key quantities to quantitatively and homogeneously compare the results obtained for all the observed GCs.

Our analysis provides the first observational determination of the dynamical path followed by MP kinematic properties during their long-term evolution. The main observational results we find can be schematically summarized as follows.

- ✧ We observe evidence of differential rotation between MPs with the SP preferentially rotating more rapidly than the FP. This result is consistent (although with different amplitudes) along both the LOS and tangential velocity components, as well as in the full 3D analysis. In all GCs in our sample, we find that the rotation position and inclination angles are consistent within the uncertainties between FP and SP.

- ✧ The strength of the rotation signal of both FP and SP subpopulations nicely correlate with the ellipticity values derived for the two subpopulations. In addition, we find that the rotation axis position angle is typically perpendicular to the ellipses' major axis.

- ✧ The difference in the rotation strength between MPs is mildly anticorrelated with the cluster dynamical age. In particular, differences are larger for dynamically young clusters, and they become progressively indistinguishable as dynamical evolution proceeds.

The combination of these results with the analysis of the MP radial distributions of a representative sample of GCs carried out by Dalessandro et al. (2019), provides a full picture

of the present-day kinematic and structural properties of MPs in GCs and of their evolution. The comparison with dynamical models following the long-term evolution of MPs in GCs suggests that these properties, and their evolution with dynamical age, are generally in good agreement with those expected in clusters forming with an SP subsystem that is initially more centrally concentrated and more rapidly rotating than the FP (see e.g., D'Ercole et al. 2008; Bekki 2010; Calura et al. 2019; Lacchin et al. 2022). In turn, this could suggest (see, e.g., Hénault-Brunet et al. 2015 and discussion in Martens et al. 2023) that GCs experienced multiple events of star formation during their early phases of evolution, with the rotation properties being the more stringent discriminating factors. In fact, according to multi-epoch formation models, the SP is expected to form a low-mass, more centrally concentrated and more rapidly rotating stellar subsystem than the FP. In such a configuration, dissipative accretion processes of material ejected by FP stars and angular momentum conservation in subsystems with different initial concentrations can produce a larger initial rotation of the SP subsystem (Bekki, 2011; Hénault-Brunet et al., 2015; Tiongco et al., 2017). Interestingly, it has been shown (e.g., Bekki 2011) that even if only a very small fraction of the kinetic energy of the FP is in the form of bulk rotation energy, SP stars can acquire a much stronger rotation than what remains in the FP.

It is important to note that, as shown here and in a number of previous studies, early and long-term evolution can significantly reduce the initial differences between the FP and SP rotational velocities making them virtually indistinguishable in dynamical old systems. The combination of these physical effects with the observational uncertainties arising from the limited available stellar samples, partial cluster coverage, and possible biases introduced by the different rotation inclination angles, can make it extremely difficult to capture present-day kinematic differences between MPs, in particular in the LOS velocity component. As a consequence, it is important to use caution in drawing conclusions about the physical mechanisms at the basis of GC formation and early evolution based on the present-day kinematic and structural properties of individual systems or small samples.

The results presented in this Chapter demonstrate that significant advances in our understanding of cluster formation and early evolution are only possible through a multifaceted and multi-diagnostic approach and by combining state-of-the-art observations and simulations.

A homogeneous dataset obtained by combining multi-object spectrographs and *Gaia*, along with an increased cluster sample size, represents a promising next step. This dataset would be particularly sensitive to larger cluster-centric distances in GCs, while integral field unit spectrographs and *HST* more efficiently sample the clusters' innermost regions, (see e.g., Martens et al. 2023; Libralato et al. 2023). Such a strategy could potentially enable the exploration of additional physical ingredients at play.

6.5 Supplementary material

6.5.1 Sample definition and observational datasets

The analysis presented in this Chapter targets 16 Galactic GCs. In detail, the sample includes all clusters analyzed by Ferraro et al. (2018b) and Lanzoni et al. (2018a,b) in the context of the ESO/VLT Multi Instrument Kinematic Survey of Galactic GCs (MIKiS), except NGC 362 as

TABLE 6.2: Properties of the 16 GCs analyzed in the present work.

Cluster	D [kpc]	r_h [arcsec]	$\log(t_{\rm rh}/{\rm yr})$	age [Gyr]	$N_{\rm LOS}$	$N_{\rm PM}$
NGC 104 (47 Tuc)	4.5	190.2	9.55	12.75	1190	2427
NGC 288	8.9	133.8	9.32	12.50	293	519
NGC 1261	16.3	40.8	9.12	11.50	99	291
NGC 1904 (M 79)	12.9	39.0	8.95	12.50	214	415
NGC 3201	4.9	186.0	9.27	12.00	415	664
NGC 5272 (M 3)	10.2	138.6	9.79	12.50	370	900
NGC 5904 (M 5)	7.5	106.2	9.41	12.25	480	787
NGC 5927	7.7	66.0	8.94	12.25	137	619
NGC 5986	10.4	58.8	9.18	13.25	160	633
NGC 6093 (M 80)	10.0	36.6	8.80	13.50	433	668
NGC 6205 (M 13)	7.1	101.4	9.30	13.00	313	1201
NGC 6362	7.6	123.0	9.20	12.50	489	713
NGC 6171 (M 107)	6.9	103.8	9.00	12.75	184	379
NGC 6254 (M 10)	4.4	117.0	8.90	13.00	296	589
NGC 6496	11.3	61.2	9.04	12.00	92	174
NGC 6723	8.7	91.8	9.24	12.75	251	515

Notes. Distances are from Baumgardt et al. (2019), structural parameters from Harris (1996), and ages from the compilation by Dotter et al. (2010), with the exception of NGC 1904 for which we used the age derivation by Dalessandro et al. (2013). $N_{\rm LOS}$ and $N_{\rm PM}$ represent the number of LOS velocities and PMs used for the kinematic analysis.

it lacks near-UV photometric data needed for the study of MPs (see section 6.5.1 for details). We added NGC 104 (47 Tuc) to the target list as it is a massive, relatively close, and well-studied GC, which can be useful for comparative analysis. We also included NGC 6362, for which we secured a large kinematic dataset in Dalessandro et al. (2018c, 2021a), NGC 6089 (M 80) and NGC 6205 (M 13), as they have been found to show interesting kinematic properties in a previous analysis by Cordero et al. (2017) and Kamann et al. (2020). table 6.2 summarizes some useful properties of the targets, such as distances, structural properties, age, relaxation times, and kinematic sample sizes. The selected clusters are representative of the overall Galactic GC population as they properly encompass the cluster's dynamically-sensitive parameter space, spanning a wide range of central densities and concentrations, different stages of dynamical evolution, and different environmental conditions. They are also more massive than $M > 10^4\ M_\odot$ and relatively close to the Earth (within $\sim$ 16 kpc), thus providing data with good signal-to-noise ratios (S/Ns) for a large sample of stars.

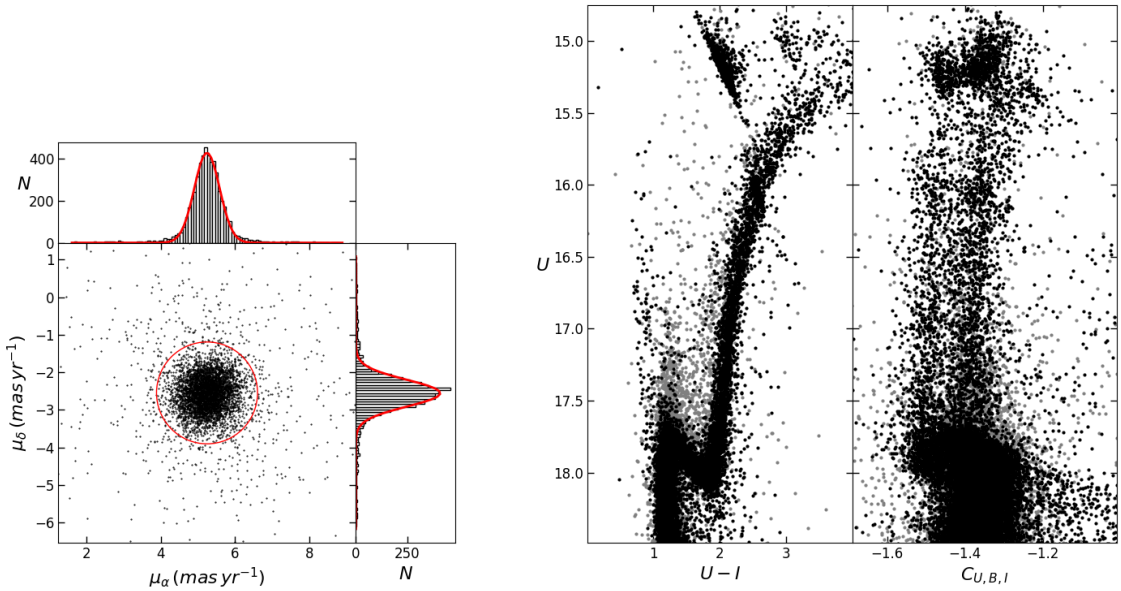

FIGURE 6.12: Selection of likely cluster member stars for the GC 47 Tuc. On the left, the vector-point diagram obtained using *Gaia* DR3 PMs is shown along with the distribution of stars along the $\mu_{*\alpha}$ and μ_δ velocity components. The red circle represents the 2σ selection described in section 6.5.1. The panel on the right shows the (U, U-I) and (U, $C_{U,B,I}$) CMDs for 47 Tuc obtained using ground-based photometric catalogs published by Stetson et al. (2019). Likely member stars based on the PM selection shown in the left panel are highlighted in black, while likely field interlopers are shown in gray.

Kinematic database

The analysis performed in this work is based on two main kinematic datasets securing LOS velocities and PMs for hundreds (or thousands in a few cases - table 6.2) of red giant branch stars (RGBs) in each GC. For 12 out of 16 GCs, most of the adopted LOS velocities were obtained using ESO/VLT *KMOS* and *FLAMES* data acquired as part of the MIKiS survey. We refer the reader to Ferraro et al. (2018b) for details on the overall observational strategy and data analysis. MIKiS LOS velocities were then complemented by those from the publicly available catalog of Baumgardt et al. (2019) to improve the sampling of the external regions of the target clusters. All LOS velocities used for 47 Tuc come from the Baumgardt et al. (2019) catalog. For NGC 6362, M 80, and M 13, the LOS velocities were obtained using *MUSE* and *FLAMES* data (Cordero et al., 2017; Dalessandro et al., 2018c, 2021a; Kamann et al., 2020).

For each of the investigated GCs, astrometric information, namely absolute PMs ($\mu_{*\alpha}$, μ_δ) and relative errors, were retrieved from the ESA/*Gaia* DR3 (Gaia Collaboration et al., 2023) archive out to the clusters' tidal radius. Only stars with `ruwe` < 1.3[1] were then used for the kinematic analysis.

[1] `ruwe` is the *Gaia* renormalized unit weight error and provides a measure of the quality of the astrometric observation's fit.

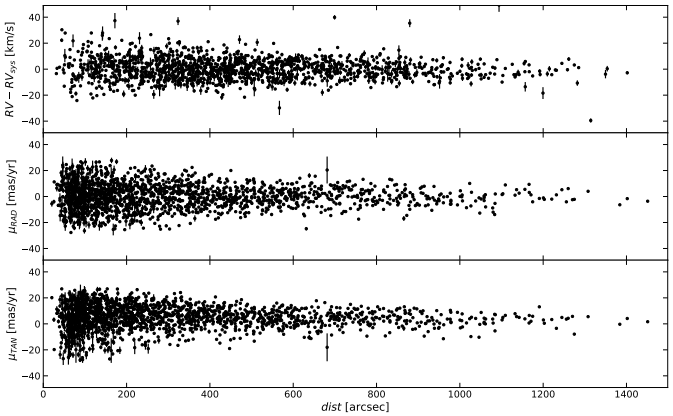

FIGURE 6.13: LOS, radial, and tangential velocity distributions of likely member stars of the GC 47 Tuc as a function of the cluster-centric distance. All velocities are shown with respect to the cluster systemic velocity along the corresponding component.

Photometric dataset, membership selection, and differential reddening correction

We used the wide-field catalogs published by Stetson et al. (2019) including the U, B, V, R, and I bands to identify MPs in the target GCs (see section 6.5.1). While these data are seeing-limited and can suffer from incompleteness in the crowded central regions, they have similar spatial resolution to the kinematic LOS velocities dataset. In addition, they are typically not affected by saturation problems, and therefore they maximize the number of bright stars in common with the kinematic samples. The photometric catalogs were cross-matched with the kinematic ones based on their absolute coordinates (α, δ) and using the cross-correlation tool `CataXcorr`[2]. For each cluster in the sample, the final catalog includes all stars in common between *Gaia* and the photometric catalogs. A fraction (typically larger than $\sim 60\%$ along the RGB) of these stars also have LOS velocities and is therefore suited to a full 3D analysis (see table 6.2).

To separate likely cluster members from field interlopers, we selected stars whose PMs are within 2σ of the cluster systemic velocity (adopted from Vasiliev & Baumgardt 2021), where σ is the standard deviation of the observed ($\mu_{*\alpha}$, μ_δ) distribution of RGB stars. We verified that, for the clusters in our sample, reasonable variations of the adopted cluster membership selection criteria do not have a significant impact on the main results of the kinematic analysis. As an example, figure 6.12 shows the PM distribution of 47 Tuc stars along with the (U, U-I) and (U, $C_{U,B,I}$ – where $C_{U,B,I} = (U - B) - (B - I)$; Monelli et al. 2013) CMDs for both selected cluster stars and field interlopers. Figure 6.13 shows the distributions of the velocities along the LOS, the PM radial (R), and PM tangential (T) components as a function of the cluster-centric distance for likely member RGB stars of the same cluster. It is worth mentioning here that the kinematic catalogs obtained from the MIKiS survey already rely on the cluster membership selection performed by Ferraro et al. (2018b) and Lanzoni et al. (2018a,b), which is based on both the LOS velocity and [Fe/H] distributions (we refer the reader to those papers for further details).

Available magnitudes were then corrected for differential reddening by using the approach described in Dalessandro et al. (2018a, see also Cadelano et al. 2020). In short, differential reddening was estimated by using likely member stars selected in a magnitude range

[2] `CataXcorr` is a code aimed at cross-correlating catalogs and finding geometrical transformation solutions - `http://davide2.bo.astro.it/~paolo/Main/CataPack.html`. It was developed by P. Montegriffo at INAF-OAS Bologna and it has been used by our group for more than 20 years.

typically going from the RGB-bump level down to about one magnitude below the cluster turn-off. Using these stars, a mean ridge line (MRL) was defined in the (B, B-I) CMD. Then, for all stars within 3σ (where σ is the color spread around the MRL), the geometric distance from the MRL (ΔX) was computed. For each star in the catalog, differential reddening was then obtained as the mean of the ΔX values of the 30 nearest (in space) selected stars. ΔX was then transformed into differential reddening $\delta E(B-V)$ using equation 1 from Dalessandro et al. (2018a), which was properly modified to account for the different extinction coefficients for the adopted filters. Differential reddening corrections turn out to be relatively small (< 0.1mag) for most GCs in the sample, with the most critical cases being NGC 3201 and NGC 5927, for which we find $\delta E(B-V)$ values larger than ~ 0.2 mag.

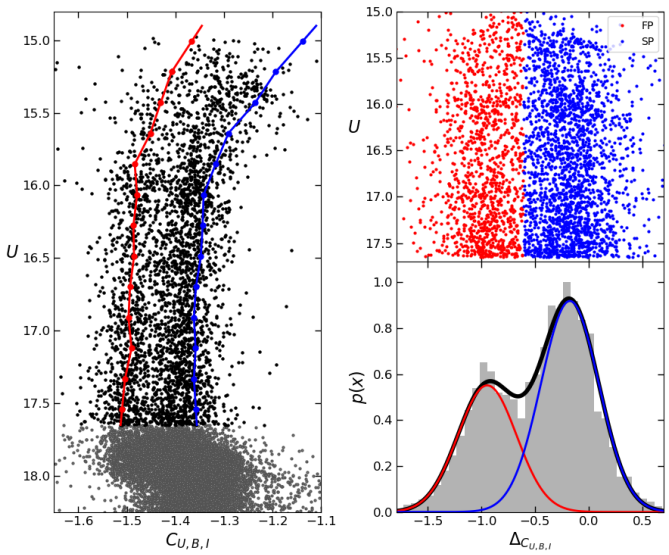

FIGURE 6.14: MP identification and selection for the case of 47 Tuc. Left panel: (U, $C_{U,B,I}$) CMD of likely 47 Tuc member stars. RGB stars adopted for the kinematic analysis are highlighted in black. The blue and red curves are the fiducial lines adopted to verticalize the color distribution. Right panels: Top panel displays verticalized color distribution of RGB stars, while the bottom panel shows the corresponding histograms. The red and blue curves represent the two best-fit Gaussians for the FP and SP, respectively, while the solid black curve is their sum.

MP classification

Starting from the sample of likely member stars and differential reddening corrected magnitudes, we identified MPs along the RGB by using their distribution in the (U, $C_{U,B,I}$) CMD (figure 6.14). It has been shown that this color combination is very effective to identify MPs along the RGB with different C and N (and possibly He) abundances (Sbordone et al., 2011; Monelli et al., 2013). RGB stars were verticalized in the (U, $C_{U,B,I}$) CMD with respect to two fiducial lines on the blue and red edges of the RGB, calculated as the 5th and 95th percentiles of the color distribution in different magnitude bins (figure 6.14 – see, e.g., Dalessandro et al. 2018b,a; Onorato et al. 2023 and Cadelano et al. 2023, for similar implementations of the same technique). In the resulting verticalized color distribution ($\Delta_{C_{U,B,I}}$; right panel in figure 6.14), stars on the red (blue) side are expected to be N-poor (-rich), that is FP (SP). We ran a two-component Gaussian mixture modeling[3] (GMM) analysis on the resulting $\Delta_{C_{U,B,I}}$ distribution, thus assigning a probability of belonging to the FP and SP subpopulations to each star. Stars with a probability of belonging to one of the two subpopulations larger than 50% were then flagged as FPs or SPs. Figure 6.14 shows the result of the MP identification and separation for the GC 47 Tuc. While this approach may introduce a few uncertainties

[3]We used the scikit-learn package (Pedregosa et al., 2011).

and over-simplifications in the MP classification as we are not directly deriving light-element chemical abundances, it secures statistically large samples of stars with MP tagging that are hard to obtain using only spectroscopic data.

6.5.2 Additional table

In table 6.3 we summarize the kinematical and structural properties inferred for the FP and SP in the GCs analyzed.

6.5.3 Incompleteness effects

We constrained the possible impact of the kinematic samples' size and of their (radially dependent) incompleteness (mainly caused by the intrinsically limited allocation efficiency of multi-object spectrographs) on the results obtained in this work by using the dynamical simulations described in sections 6.2.

In detail, we estimated the completeness (c) of the observed kinematic samples and their radial variation as the ratio between the number of RGB stars detected in the photometric catalogs and those with LOS velocities and/or PMs measures within concentric radial annuli at different cluster-centric distances. While we acknowledge that these estimates represent a lower limit to the real incompleteness, as photometric catalogs are not fully complete, we note that our targets are RGB stars, which are among the brightest stars in GC CMDs and therefore they are only moderately affected by incompleteness even when ground-based catalogs are adopted.

We then extracted randomly from the simulations sub-samples of stars with similar sizes as the observed ones for a large number of times. We applied the derived completeness curves to these sub-samples to make them as similar as possible to the observed catalogs. Finally, we run the same kinematic analysis described in section 6.1. We find that, while the limited sample sizes and incompleteness have an impact on the overall noise of the observed kinematic profiles and, as a consequence, on the uncertainties associated with the derived parameters, they do not have a significant impact on the final results.

6.5.4 Global kinematics and comparison with the literature

Figure 6.15 shows the distribution of the α values derived for the entire population along both the LOS and tangential velocity components, and of the $(\omega^{\rm TOT})_{\rm 3D}$, as a function of $n_{\rm h}$. As expected, both $\alpha^{\rm TOT}$ (for both LOS and T) and the $(\omega^{\rm TOT})_{\rm 3D}$ distributions show pretty clear anti-correlations with $n_{\rm h}$. In fact, while dynamically young GCs attain larger values of rotation parameters, with the only significant exception being M 3, the rotation strength progressively decreases as dynamical evolution proceeds. By performing a Spearman rank correlation test we find that such anti-correlations have a significance of $\sim 98\%$ for the LOS and $> 99.9\%$ for both the tangential and the 3D analysis, with the 3D case being the most significant. In general, these results are in very good agreement with previous analysis (e.g., Kamann et al. 2018; Sollima et al. 2019) and they further strengthen the conclusion that the present-day cluster rotation is the relic of that imprinted at the epoch of cluster formation, which has been then progressively dissipated via two-body relaxation.

TABLE 6.3: Best-fit values of the main MP kinematic properties.

Cluster	$\sigma_{0,\mathrm{LOS}}$ [km s^{-1}]	$\sigma_{0,\mathrm{R}}$ [km s^{-1}]	$\sigma_{0,\mathrm{T}}$ [km s^{-1}]	$A_{\mathrm{rot,LOS}}$ [km s^{-1}]	$R_{\mathrm{peak,LOS}}$ [arcsec]	PA$_0$ [deg]	$A_{\mathrm{rot,T}}$ [km s^{-1}]	$R_{\mathrm{peak,T}}$ [arcsec]	$A_{\mathrm{rot,3D}}$ [km s^{-1}]	i [deg]	θ_0 [deg]	β_∞	ϵ	POP
NGC 104	$11.4^{+1.7}_{-1.2}$	$10.5^{+0.9}_{-0.7}$	$12.3^{+1.1}_{-0.8}$	$-2.6^{+0.7}_{-0.6}$	$195.9^{+70.6}_{-120.5}$	53^{+7}_{-5}	$4.7^{+1.6}_{-1.5}$	$248.2^{+25.9}_{-28.7}$	$-6.5^{0.33}_{0.31}$	30^{+7}_{-6}	69^{+11}_{-12}	$-2.3^{+1.8}_{-1.8}$	$0.15^{+0.01}_{-0.01}$	FP
	$9.9^{+1.3}_{-0.7}$	$11.6^{+0.8}_{-0.6}$	$12.1^{+0.7}_{-0.8}$	$-3.0^{+0.3}_{-0.3}$	$283.0^{+58.1}_{-67.1}$	30^{+8}_{-6}	$6.3^{+0.8}_{-0.8}$	$222.0^{+22.1}_{-22.8}$	$-8.0^{+0.37}_{0.36}$	32^{+7}_{-6}	57^{+9}_{-9}	$0.3^{+0.1}_{-0.1}$	$0.26^{+0.01}_{-0.01}$	SP
NGC 288	$2.5^{+0.3}_{-0.2}$	$3.5^{+0.5}_{-0.3}$	$2.9^{+0.2}_{-0.2}$	$0.4^{+0.3}_{-0.3}$	$161.4^{+27.1}_{-32.8}$	-2^{+44}_{-24}	$-1.8^{+1.2}_{-1.1}$	$637.4^{+227.1}_{-219.8}$	$0.5^{+0.4}_{-0.2}$	41^{+23}_{-32}	332^{+18}_{-18}	$-0.8^{+2.8}_{-2.8}$	$0.19^{+0.08}_{-0.04}$	FP
	$3.3^{+0.7}_{-0.5}$	$4.8^{+2.4}_{-1.2}$	$5.6^{+2.4}_{-1.2}$	$0.5^{+0.3}_{-0.3}$	$151.6^{+32.4}_{-29.2}$	1^{+28}_{-36}	$-1.6^{+1.5}_{-1.4}$	$470.6^{+242.4}_{-182.2}$	$1.5^{+0.3}_{-0.3}$	18^{+26}_{-38}	35^{+24}_{-25}	$1.4^{+2.1}_{-2.8}$	$0.07^{+0.03}_{-0.03}$	SP
NGC 1261	$4.0^{+1.2}_{-0.6}$	$4.8^{+5.8}_{-1.8}$	$4.1^{+1.5}_{-0.8}$	$-1.8^{+1.0}_{-0.9}$	$46.4^{+97.3}_{-35.1}$	-31^{+20}_{-20}	$0.4^{+1.4}_{-1.1}$	$195.4^{+103.8}_{-90.7}$	$3.0^{+1.4}_{-1.4}$	78^{+12}_{-12}	43^{+27}_{-28}	$-0.7^{+3.4}_{-2.8}$	$0.24^{+0.13}_{-0.05}$	FP
	$3.3^{+0.6}_{-0.4}$	$5.8^{+5.4}_{-1.8}$	$3.3^{+1.6}_{-0.9}$	$-1.7^{+0.7}_{-0.6}$	$50.8^{+24.4}_{-19.7}$	-31^{+19}_{-17}	$0.8^{+0.9}_{-0.7}$	$110.0^{+138.2}_{-101.6}$	$2.5^{+1.3}_{-1.3}$	63^{+7}_{-6}	47^{+23}_{-23}	$0.2^{+2.3}_{-3.2}$	$0.27^{+0.03}_{-0.02}$	SP
NGC 1904	$3.8^{+0.7}_{-0.4}$	$4.2^{+1.1}_{-0.5}$	$5.5^{+1.8}_{-1.0}$	$1.6^{+0.7}_{-0.8}$	$31.9^{+39.3}_{-15.2}$	-8^{+15}_{-4}	$-1.1^{+1.6}_{-1.8}$	$101.4^{+71.2}_{-49.2}$	$1.5^{+1.2}_{-1.2}$	51^{+18}_{-19}	29^{+31}_{-29}	$0.3^{+2.7}_{-3.0}$	$0.06^{+0.05}_{-0.04}$	FP
	$4.4^{+1.0}_{-0.6}$	$5.5^{+2.4}_{-1.0}$	$5.8^{+1.6}_{-1.2}$	$0.9^{+0.6}_{-0.5}$	$58.8^{+50.7}_{-38.6}$	24^{+20}_{-30}	$-2.1^{+2.1}_{-1.9}$	$259.5^{+183.6}_{-113.6}$	$2.5^{+0.7}_{-0.7}$	23^{+26}_{-23}	36^{+26}_{-26}	$0.2^{+2.6}_{-2.6}$	$0.06^{+0.03}_{-0.03}$	SP
NGC 3201	$4.2^{+0.4}_{-0.3}$	$3.7^{+0.3}_{-0.2}$	$3.6^{+0.3}_{-0.2}$	$0.3^{+0.8}_{-1.0}$	$315.3^{+126.1}_{-159.6}$	20^{+52}_{-91}	$-0.6^{+1.0}_{-0.9}$	$345.3^{+78.1}_{-72.6}$	$1.2^{+0.5}_{-0.5}$	44^{+22}_{-21}	331^{+36}_{-37}	$-0.3^{+2.2}_{-2.5}$	$0.30^{+0.02}_{-0.04}$	FP
	$3.6^{+0.2}_{-0.2}$	$3.6^{+0.3}_{-0.2}$	$3.5^{+0.4}_{-0.3}$	$0.1^{+0.9}_{-0.6}$	$262.2^{+164.9}_{-168.2}$	-13^{+73}_{-50}	$-0.5^{+0.7}_{-0.8}$	$440.1^{+151.9}_{-92.2}$	$1.0^{+0.5}_{-0.5}$	41^{+28}_{-21}	345^{+32}_{-37}	$0.7^{+0.3}_{-0.2}$	$0.10^{+0.02}_{-0.02}$	SP
NGC 5272	$7.5^{+1.4}_{-0.9}$	$8.4^{+1.2}_{-0.8}$	$6.9^{+0.8}_{-0.6}$	$0.6^{+0.5}_{-0.5}$	$120.4^{+100.0}_{-100.2}$	46^{+24}_{-62}	$2.3^{+1.6}_{-1.8}$	$225.9^{+88.2}_{-78.8}$	$1.0^{+0.5}_{-0.5}$	33^{+27}_{-27}	78^{+18}_{-18}	$1.7^{+2.1}_{-1.7}$	$0.26^{+0.08}_{-0.08}$	FP
	$6.8^{+3.8}_{-1.2}$	$7.3^{+0.9}_{-0.7}$	$7.6^{+1.7}_{-0.9}$	$0.8^{+0.4}_{-0.4}$	$450.0^{+93.2}_{-238.3}$	34^{+18}_{-80}	$3.1^{+1.6}_{-1.2}$	$89^{+54.9}_{-57.4}$	$2.0^{+0.4}_{-0.4}$	56^{+21}_{-22}	61^{+16}_{-18}	$1.0^{+1.9}_{-0.9}$	$0.22^{+0.04}_{-0.07}$	SP
NGC 5904	$7.8^{+2.2}_{-1.2}$	$7.4^{+1.3}_{-0.9}$	$7.0^{+0.9}_{-0.7}$	$2.6^{+0.4}_{-0.4}$	$234.7^{+110.3}_{-68.7}$	-27^{+9}_{-10}	$-3.7^{+1.9}_{-1.6}$	$148.0^{+42.3}_{-33.7}$	$4.1^{+0.4}_{-0.5}$	49^{+6}_{-6}	27^{+16}_{-18}	$-2.3^{+1.5}_{-1.7}$	$0.36^{+0.02}_{-0.03}$	FP
	$7.2^{+1.5}_{-0.9}$	$6.7^{+0.9}_{-0.6}$	$7.5^{+0.9}_{-0.7}$	$2.1^{+0.3}_{-0.3}$	$237.6^{+92.5}_{-62.5}$	-58^{+6}_{-7}	$-3.2^{+1.6}_{-1.4}$	$240.3^{+68.5}_{-77.5}$	$5.5^{+0.5}_{-0.5}$	40^{+6}_{-6}	25^{+18}_{-19}	$0.5^{+2.0}_{-1.9}$	$0.36^{+0.02}_{-0.02}$	SP
NGC 5927	$5.3^{+1.1}_{-0.6}$	$6.8^{+0.3}_{-0.3}$	$6.7^{+0.4}_{-0.4}$	$-0.8^{+0.8}_{-0.5}$	$305.3^{+387.3}_{-167.8}$	-32^{+50}_{-30}	$0.5^{+1.6}_{-1.6}$	$56.6^{+125.3}_{-35.6}$	$1.0^{+0.8}_{-0.1}$	37^{+35}_{-29}	305^{+27}_{-27}	$-9.8^{+3.3}_{-3.2}$	$0.01^{+0.01}_{-0.01}$	FP
	$5.6^{+0.7}_{-0.5}$	$7.0^{+0.3}_{-0.3}$	$6.0^{+1.4}_{-0.8}$	$-0.2^{+1.8}_{-1.8}$	$320.4^{+396.1}_{-180.0}$	-6^{+80}_{-68}	$0.6^{+1.8}_{-1.8}$	$451.1^{+244.2}_{-214.6}$	$1.5^{+0.8}_{-0.8}$	58^{+33}_{-29}	315^{+36}_{-38}	$0.5^{+0.1}_{-0.2}$	$0.06^{+0.03}_{-0.03}$	SP
NGC 5986	$8.8^{+9.9}_{-2.9}$	$8.3^{+3.9}_{-2.6}$	$8.5^{+2.2}_{-2.2}$	$1.1^{+1.1}_{-1.0}$	$288.7^{+134.7}_{-188.1}$	14^{+40}_{-55}	$-1.9^{+2.8}_{-1.8}$	$210.7^{+120.1}_{-110.7}$	$1.9^{+0.5}_{-0.5}$	80^{+35}_{-32}	312^{+19}_{-19}	$3.0^{+2.8}_{-1.9}$	$0.35^{+0.06}_{-0.06}$	FP
	$8.3^{+3.5}_{-1.7}$	$9.6^{+1.5}_{-1.0}$	$8.5^{+0.8}_{-0.6}$	$1.6^{+1.5}_{-2.5}$	$309.4^{+120.3}_{-154.6}$	-40^{+88}_{-29}	$-3.0^{+2.2}_{-2.5}$	$40.5^{+54.7}_{-38.4}$	$1.2^{+0.5}_{-0.4}$	80^{+35}_{-33}	308^{+19}_{-19}	$-4.2^{+4.4}_{-6.1}$	$0.35^{+0.06}_{-0.06}$	SP
NGC 6093	$11.7^{+0.6}_{-0.5}$	$11.5^{+0.6}_{-0.5}$	$11.7^{+0.7}_{-0.6}$	$2.5^{+1.5}_{-1.4}$	$70.8^{+16.8}_{-13.8}$	76^{+30}_{-39}	$2.5^{+1.5}_{-1.4}$	$70.8^{+16.8}_{-13.8}$	$2.1^{+0.5}_{-0.5}$	117^{+34}_{-34}	122^{+9}_{-9}	$-0.88^{+0.58}_{-0.93}$	$0.11^{+0.04}_{-0.04}$	FP
	$10.8^{+0.7}_{-0.6}$	$11.0^{+0.4}_{-0.5}$	$10.8^{+0.7}_{-0.6}$	$2.1^{+1.2}_{-1.2}$	$80.8^{+12.5}_{-11.9}$	59^{+39}_{-37}	$2.1^{+1.2}_{-1.2}$	$70.8^{+12.5}_{-11.9}$	$1.6^{+0.5}_{-0.5}$	122^{+28}_{-29}	125^{+13}_{-7}	$-0.72^{+0.87}_{-1.02}$	$0.11^{+0.04}_{-0.04}$	SP
NGC 6171	$3.4^{+0.6}_{-0.4}$	$3.5^{+0.3}_{-0.3}$	$3.9^{+0.4}_{-0.3}$	$0.4^{+0.4}_{-0.3}$	$332.0^{+436.2}_{-205.2}$	4^{+60}_{-67}	$-0.7^{+1.4}_{-2.0}$	$91.7^{+136.3}_{-89.8}$	$-1.0^{+0.5}_{-0.5}$	30^{+55}_{-58}	23^{+41}_{-43}	$-2.0^{+3.3}_{-6.6}$	$0.11^{+0.02}_{-0.03}$	FP
	$3.5^{+0.8}_{-0.4}$	$4.7^{+1.2}_{-0.7}$	$4.2^{+0.8}_{-0.4}$	$0.4^{+0.3}_{-0.2}$	$171.5^{+204.9}_{-81.6}$	16^{+50}_{-73}	$-0.8^{+1.2}_{-1.3}$	$233.6^{+158.3}_{-136.8}$	$-0.5^{+0.6}_{-0.6}$	40^{+54}_{-55}	34^{+41}_{-43}	$-4.2^{+4.0}_{-6.4}$	$0.05^{+0.03}_{-0.03}$	SP
NGC 6205	$8.8^{+2.5}_{-1.9}$	$8.7^{+1.9}_{-1.6}$	$8.8^{+1.7}_{-1.4}$	$2.4^{+2.7}_{-1.7}$	$174.0^{+132.1}_{-102.2}$	53^{+48}_{-85}	$2.4^{+1.9}_{-2.2}$	174^{+111}_{-89}	$-1.6^{+0.7}_{-0.7}$	157^{+16}_{-19}	85^{+10}_{-12}	$0.02^{+0.98}_{-1.32}$	$0.34^{+0.04}_{-0.05}$	FP
	$6.1^{+0.9}_{-0.6}$	$6.3^{+1.2}_{-1.2}$	$6.1^{+0.9}_{-0.6}$	$2.9^{+0.9}_{-0.9}$	$113.6^{+90.6}_{-46.7}$	22^{+37}_{-45}	$2.9^{+0.9}_{-0.9}$	$113.6^{+90.6}_{-46.7}$	$-2.5^{+0.7}_{-0.7}$	173^{+16}_{-19}	78^{+10}_{-12}	$2.86^{+0.57}_{-0.76}$	$0.36^{+0.06}_{-0.05}$	SP
NGC 6362	$3.5^{+0.4}_{-0.3}$	$3.4^{+0.5}_{-0.5}$	$3.5^{+0.3}_{-0.4}$	$0.6^{+0.1}_{-0.1}$	$37.3^{+12.7}_{-22.8}$	102^{+40}_{-40}	$0.7^{+0.1}_{-0.1}$	$17.3^{+2.7}_{-2.8}$	$0.4^{+0.3}_{-0.3}$	62^{+34}_{-33}	140^{+38}_{-36}	$-0.11^{+1.58}_{-1.39}$	$0.02^{+0.02}_{-0.02}$	FP
	$3.6^{+0.4}_{-0.3}$	$3.7^{+0.3}_{-0.3}$	$3.6^{+0.3}_{-0.3}$	$1.2^{+0.2}_{-0.1}$	$32.3^{+22.5}_{-24.8}$	120^{+36}_{-36}	$1.2^{+0.2}_{-0.1}$	$17.3^{+2.7}_{-2.8}$	$0.7^{+0.1}_{-0.2}$	49^{+21}_{-24}	114^{+27}_{-28}	$0.53^{+1.25}_{-1.22}$	$0.11^{+0.02}_{-0.02}$	SP
NGC 6254	$5.4^{+0.6}_{-0.4}$	$4.8^{+0.6}_{-0.4}$	$5.3^{+0.6}_{-0.4}$	$0.7^{+0.5}_{-0.4}$	$649.7^{+292.2}_{-440.5}$	-1^{+64}_{-58}	$-0.3^{+1.2}_{-1.1}$	$465.7^{+397.2}_{-326.5}$	$1.5^{+0.5}_{-0.5}$	81^{+26}_{-27}	317^{+33}_{-31}	$-2.9^{+2.4}_{-5.8}$	$0.11^{+0.05}_{-0.03}$	FP
	$4.8^{+0.5}_{-0.3}$	$5.2^{+0.6}_{-0.4}$	$5.1^{+0.8}_{-0.5}$	$0.5^{+0.6}_{-0.4}$	$531.6^{+379.9}_{-391.3}$	3^{+53}_{-57}	$-0.1^{+1.0}_{-1.0}$	$418.6^{+428.9}_{-315.3}$	$1.0^{+0.5}_{-0.5}$	73^{+23}_{-27}	25^{+24}_{-21}	$3.1^{+3.1}_{-2.1}$	$0.09^{+0.03}_{-0.03}$	SP
NGC 6496	$2.9^{+0.6}_{-0.4}$	$4.2^{+0.6}_{-0.4}$	$4.3^{+1.6}_{-1.1}$	$0.9^{+1.0}_{-0.6}$	$307.7^{+167.1}_{-258.7}$	18^{+44}_{-75}	$0.4^{+1.2}_{-0.4}$	$150.7^{+120.1}_{-110.7}$	$0.5^{+0.6}_{-0.6}$	124^{+48}_{-55}	28^{+43}_{-41}	$5.6^{+5.9}_{-4.6}$	$0.34^{+0.06}_{-0.06}$	FP
	$2.4^{+0.6}_{-0.4}$	$3.9^{+0.9}_{-0.6}$	$3.4^{+1.0}_{-0.7}$	$1.0^{+1.1}_{-0.7}$	$315^{+160.7}_{-237.4}$	9^{+61}_{-74}	$0.8^{+0.8}_{-0.7}$	$65.5^{+54.7}_{-38.4}$	$1.0^{+0.7}_{-0.7}$	129^{+51}_{-52}	23^{+44}_{-21}	$0.4^{+5.3}_{-7.1}$	$0.34^{+0.06}_{-0.05}$	SP
NGC 6723	$4.6^{+0.8}_{-0.5}$	$6.2^{+1.5}_{-0.8}$	$6.8^{+1.9}_{-1.4}$	$0.7^{+0.5}_{-0.4}$	$161.0^{+269.1}_{-76.3}$	-28^{+53}_{-25}	$-0.1^{+1.1}_{-1.9}$	$277.2^{+251.5}_{-182.5}$	$2.4^{+0.4}_{-0.4}$	1^{+37}_{-35}	340^{+23}_{-22}	$0.5^{+2.6}_{-2.3}$	$0.26^{+0.04}_{-0.05}$	FP
	$4.6^{+0.9}_{-0.5}$	$5.3^{+0.3}_{-0.3}$	$5.9^{+0.3}_{-0.3}$	$0.5^{+0.5}_{-0.3}$	$155.1^{+275.6}_{-75.4}$	-19^{+72}_{-39}	3.3^{+2}_{-2}	$72.9^{+27.5}_{-27.5}$	$1.5^{+0.4}_{-0.5}$	80^{+27}_{-27}	350^{+21}_{-21}	$-1.8^{+1.9}_{-2.0}$	$0.05^{+0.03}_{-0.03}$	SP

Figure 6.16 shows the distribution of $(\alpha^{\rm TOT})_{\rm LOS}$ with the cluster ellipticity obtained as described in section 6.1. As expected (see discussion and references in section 6.2.2), a nice correlation between rotation and ellipticity is observed also for the total population in very good agreement with previous findings by Fabricius et al. (2014) and Kamann et al. (2018).

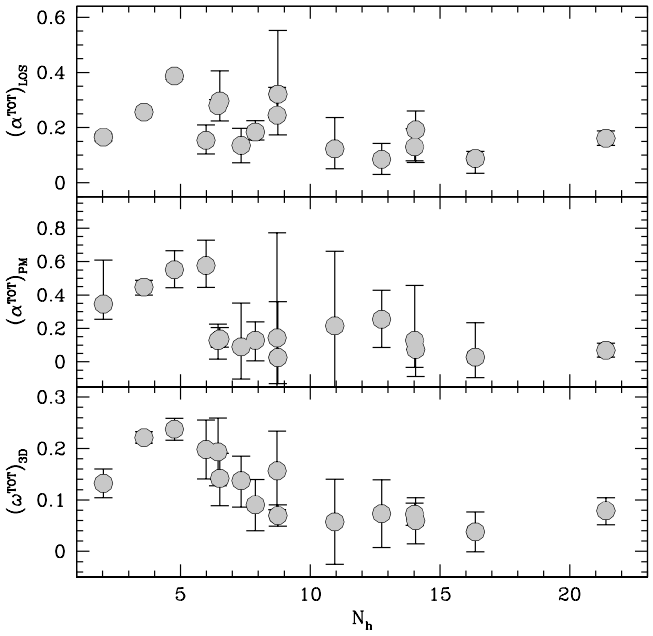

FIGURE 6.15: Distribution of the three rotation parameters defined in this work for the LOS, PM and 3D velocity components, as a function of the dynamical age ($n_{\rm h}$) for the total population (TOT) of GCs in our sample.

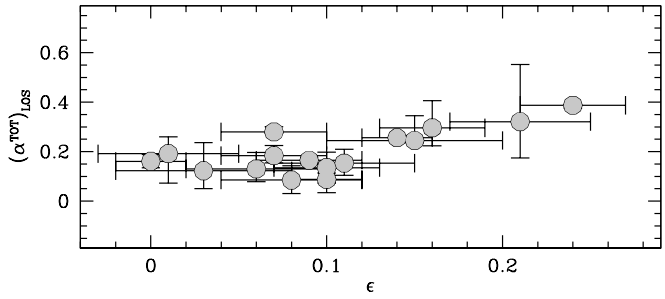

FIGURE 6.16: Distribution of the $(\alpha^{\rm TOT})_{\rm LOS}$ parameter for the total population as a function of the best-fit ellipticity values.

While the focus of this work is on the MP kinematics, nevertheless it is useful to compare the results obtained for the TOT population with those largely available in the literature to have an indication about the general performance of the adopted approach and data-sets. Detailed one-to-one comparisons with recent results obtained in the literature (Bellazzini et al., 2012; Ferraro et al., 2018b; Lanzoni et al., 2018a,b; Baumgardt et al., 2019; Sollima et al., 2019) for the TOT population are shown in figures 6.17 and 6.18. In general, a quite good agreement is observed with all the compilations considered here.

Our sample has 6 GCs in common with Bellazzini et al. (2012). A nice match is observed both in terms of σ_0 and $A_{\rm rot}$ (top row of figure 6.17) with the only exception being NGC 6171 for which Bellazzini et al. (2012) finds a rotation amplitude 4-5 times larger than the one obtained in this work. Given the estimate by Bellazzini et al. (2012), NGC 6171 would be a very fast rotator, with $A_{\rm rot}/\sigma_0 \sim 0.7$. However, it is important to note, that the sample

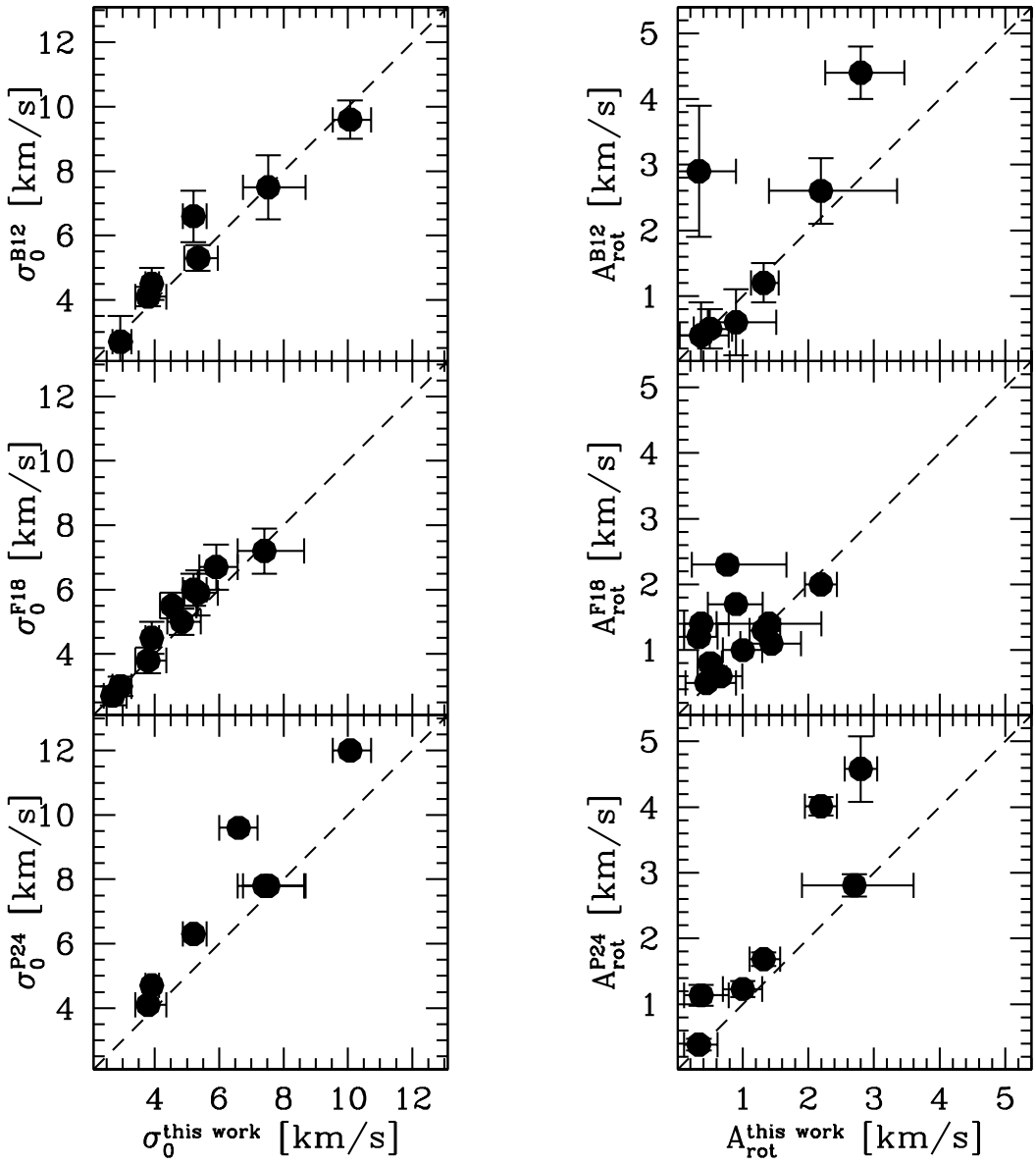

FIGURE 6.17: Comparison between the best-fit σ_0 and A_{rot} values obtained for the TOT sample for the clusters in common between the present work and Bellazzini et al. (2012) – B12, Ferraro et al. (2018b) – F18 and Petralia et al. (2024) – P24.

of LOS velocities used by Bellazzini et al. (2012) for this cluster includes only 31 stars in total, resulting the smallest sample of LOS velocities in their analysis. Here we sample the kinematic profile of NGC 6171 with 184 LOS velocities (see table 6.2). We note also that NGC 6171 results to have a significantly smaller rotation amplitude (1.2 km s^{-1}) than what found by Bellazzini et al. (2012) in the analysis by Ferraro et al. (2018b) and it is classified as non rotator by Sollima et al. (2019)

As for the comparison with results by Ferraro et al. (2018b), we stress that while the spectroscopic sample is largely similar, the adopted kinematic analysis (both the discrete and continuous ones) is significantly different for the rotation study in particular (see Ferraro et al. 2018b for details). Hence, it is not surprising that while the derived central velocity dispersion values are in excellent agreement for the entire sample (middle row of figure 6.17), the distribution of differences for $A_{\rm rot}$ is more scattered, while still showing a reasonable match within the errors. In this case, the most significant discrepancy is observed for NGC 5927, for which Ferraro et al. (2018b) derived $A_{\rm rot} = 2.3$ km s^{-1}, while we find $A_{\rm rot} = 0.76^{+0.90}_{-0.54}$ km s^{-1}. For this cluster also Sollima et al. (2019) derived a low probability of rotation.

In the bottom row of figure 6.17 we compare the results of this work with those recently obtained by Petralia et al. (2024) by using APOGEE spectra for a sample of Galactic GCs. For $A_{\rm rot}$ we use the semi-amplitude of the $A_{\rm fit}$ values reported in their work. A reasonable overall agreement is observed also in this case for the clusters in common, however 47 Tuc and NGC 5904 result to have larger central velocity dispersion values and peak of rotation than in our work.

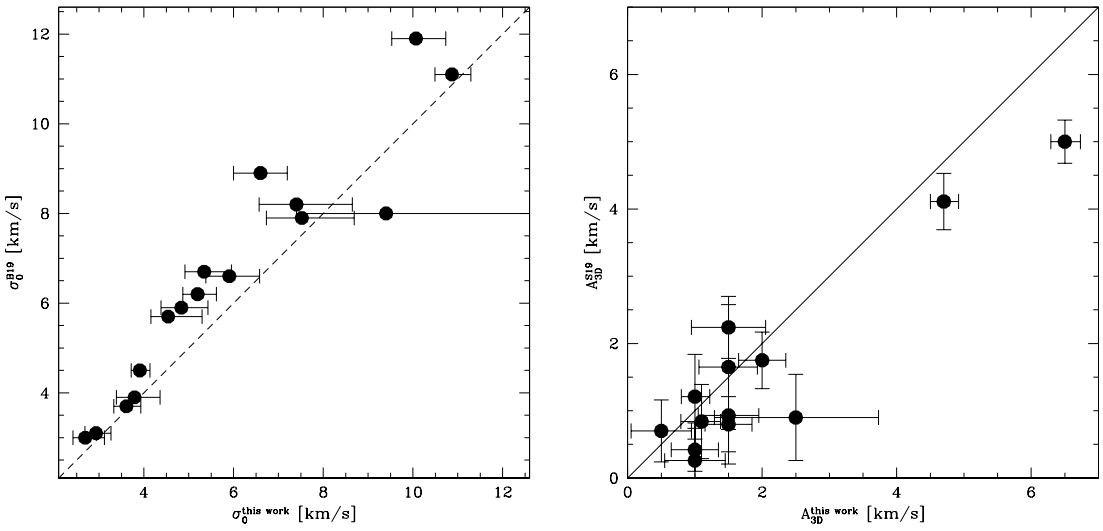

FIGURE 6.18: *Left panel:* Comparison with the best-fit σ_0 values obtained by Baumgardt et al. (2019) – B19 – for the total population of GCs in common with the present work. *Right panel:* One-to-one comparison of the 3D rotation amplitude values $A_{\rm 3D}$ found by Sollima et al. (2019) – S19 – and the present analysis.

Finally, as shown in figure 6.18 (left panel) a reasonably good match is also found with the σ_0 estimates by Baumgardt et al. (2019). Among the clusters in common with Sollima et al. (2019), the only significantly discrepant result is that of 47 Tuc, which results to have a $\sim 25\%$

larger rotation in this work. However, we note that in this case, as for the entire sample, both the i and θ_0 values are in very good agreement. In this respect, it is also interesting to highlight the nice match in terms of both the observed rotation amplitude and angles of the 3D rotation of 47 Tuc obtained in this work and those inferred by means of a detailed comparison between *HST* PMs and theoretical models of rotating clusters by Bellini et al. (2017).

Part III

The long-term evolution of massive stellar systems

Chapter 7

Black hole subsystems in Galactic globular clusters

> "Resterete una massa uniforme, seguace dei primi e persecutrice degli ultimi, capace di cambiare abiti piu' frequentemente di una indossatrice d'atelier."
>
> L'Organizzazione,
> CR Edizioni

The first direct BH detection through gravitational waves (Abbott et al., 2016) sparked a new interest in studying such elusive objects. In particular, within massive stellar systems, where dynamical interactions promise frequent gravitational wave emission and possibly detection. Also, the presence of BHs within stellar systems has a key role in their evolution (Breen & Heggie, 2013, see also discussion in section 1.3.5).

In this context, many studies addressed the inference of the total mass in stellar mass BHs harbored by GCs (Askar et al., 2018; Zocchi et al., 2019; Askar et al., 2019; Weatherford et al., 2020; Dickson et al., 2024). In particular, Askar et al. (2018) explored several correlations (obtained from Monte Carlo simulations, see Arca Sedda et al., 2018) to infer the properties of the potential BH subsystem, using as observational anchor the luminosity density within the half-mass radius. The authors shortlisted 29 GCs that could harbor a significant number (up to a few hundred) of BHs. Weatherford et al. (2020) used a theoretical correlation between the fraction of BHs and the degree of mass segregation (Weatherford et al., 2018) to infer the present-day BH population and their total mass in 50 Galactic GCs. Finally, Dickson et al. (2024) performed multi-mass modeling of several cluster observables (i.e., velocity dispersion profiles along the PM and LOS directions, number density profile, and mass function measurements) for 34 GCs, thereby being able to constrain the total dynamical mass in dark remnants at the cluster centers. Interestingly, they found typically lower BH mass fractions compared to Askar et al. (2018), and Weatherford et al. (2020, see e.g. Fig. 3 in Dickson et al. 2024).

However, as discussed by Askar et al. (2018, see their Sect. 2.6), the inference of the mass in BHs using a single observable can be strongly biased and dependent on the specific assumptions adopted in the analysis. In this Chapter, we address the degeneracies in the inference of the present-day BH population in GCs, possibly arising from multiple assumptions about the underlying physical processes that are still poorly constrained observationally. The purpose of this study presented in this Chapter is therefore dual: *i)* to point out that some observable structural quantities used in the literature to infer the mass fraction in BHs are consistent

both with systems with a significant mass fraction in BHs and systems with no (or a negligible fraction of) BHs; *ii)* to possibly identify the combination of dynamical parameters that allows unambiguous identification of the presence of a significant population of BHs.

The Chapter is organized as follows: in section 7.1 we present the simulation survey and its set of initial conditions, and in section 7.2 we discuss the parameters investigated and the implications for BH mass fraction-inference in real GCs. In section 7.3 we describe a detailed comparison between the observations and our set of simulations, trying to disentangle different scenarios. In section 7.4 we summarize the results and conclude. Additional material is presented in section 7.5.

The results presented in this Chapter are from Della Croce et al. (2024c, A&A, **690**, A179).

7.1 Monte Carlo simulations of star cluster evolution

In this work, we use a set of 101 Monte Carlo simulations (Hénon, 1971a,b) performed with the MOCCA[1] code (Giersz et al., 2013; Hypki & Giersz, 2013). The MOCCA code follows the evolution of star clusters including the effects of two-body relaxation, single and binary stellar evolution (modeled with the SSE and BSE prescriptions; Hurley et al., 2000, 2002), close stellar interactions (which were integrated by using the FEWBODY code Fregeau et al., 2004), and a spatial cut-off modeling the effect of the tidal truncation due to the host galaxy.

The set of simulations analyzed in this work was fully presented in Bhat et al. (2024) in the context of defining novel structural parameters to determine the stage reached by GCs in their evolution toward the core-collapse and post-core-collapse phases. Here we briefly summarize the initial conditions adopted and refer to Bhat et al. (2024) for further details. Each simulated cluster starts with an equilibrium configuration defined by a King (1966) distribution function, assuming a central dimensionless potential of $W_0 = 5$ or 7. The truncation radii of our models are equal to the tidal radii of clusters moving on circular orbits in a logarithmic potential for the Galaxy at galactocentric distances of 2, 4, and 6 kpc. A filling factor (defined as the ratio between the three-dimensional half-mass, $r_{\rm hm}$, and the tidal, $r_{\rm t}$, radii) of $0.025, 0.050$ or 0.1 was adopted. The number of particles, $N_{\rm p}$ (defined as the sum of the number of single stars and binaries), varies between 500k, 750k, and one million with a 10% primordial binary fraction. The initial distribution of binary properties was set following the eigenevolution procedure described in Kroupa (1995) and Kroupa et al. (2013). Finally, for each set of these initial conditions, two simulations were performed assuming a different prescription for the BH natal kicks: either a Maxwellian distribution with a dispersion of 265 km s^{-1}(i.e., the same as neutron stars, NSs, Hobbs et al., 2005), or a reduced kick velocity based on the fallback prescription by Belczynski et al. (2002). We adopted a Kroupa (2001) stellar initial mass function between 0.1 and 100 $M_\odot$ and a metallicity $Z = 10^{-3}$. Finally, we did not include 7 simulations in which an IMBH was formed. Studying the impact of IMBH formation on observable cluster properties is beyond the scope of this work, and will be the subject of future studies.

[1]The name MOCCA stands for MOnte Carlo Cluster simulAtor, see `https://moccacode.net/`.

7.2 Results from numerical simulations

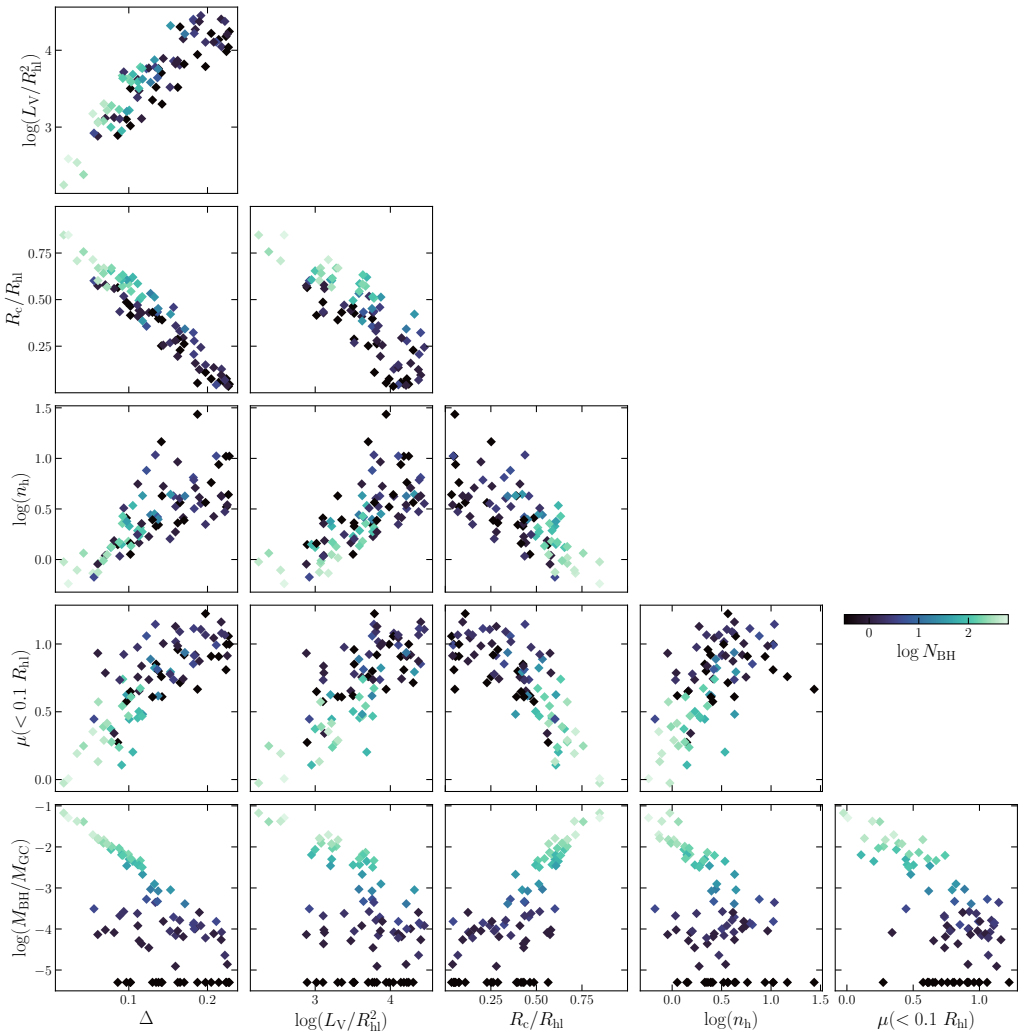

FIGURE 7.1: Simulation properties at 13 Gyr, each point representing a different simulation. Moving downwards on the $y-$axis: luminosity density (in units of $L_\odot$ pc^{-2}), core to half-light radius ratio (R_c/R_{hl}), dynamical age (n_h), inverse of the equipartition mass, $\mu(< 0.1R_{hl})$, BH mass fraction (M_{BH}/M_{GC}), and mass segregation parameter Δ. Simulations are color-coded according to the number of BHs (N_{BH}) at 13 Gyr . A value of $\log N_{BH} = -0.5$ was assigned to those with no BHs. Similarly, simulations that do not retain any BH at 13 Gyr are shown at $M_{BH}/M_{GC} = 5 \times 10^{-6}$ on the bottom row for visualization purposes only.

In this section, we present the analysis and the properties at 13 Gyr of the simulations in the survey. Firstly, for each simulation, we computed the total stellar mass (M_{GC}) and the BH mass fraction (defined as M_{BH}/M_{GC}, with M_{BH} being the total mass in BHs). We

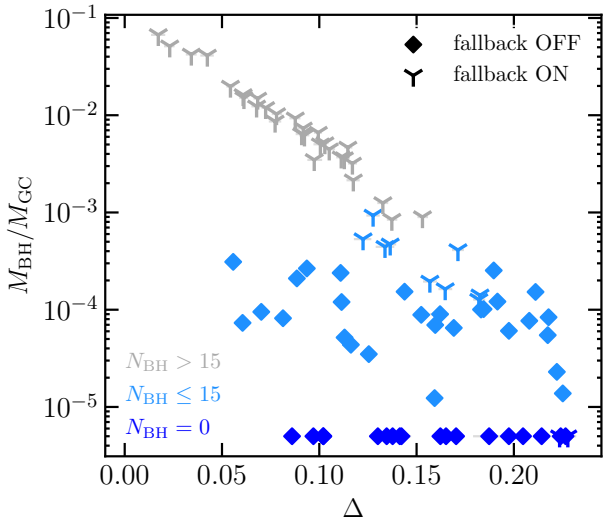

FIGURE 7.2: BH mass fraction as a function of Δ. Colors depict the number of BHs in the simulation at 13 Gyr , while different symbols show the adopted fallback prescription in the initial conditions. Simulations without BHs at 13 Gyr are shown at $M_{\rm BH}/M_{\rm GC} = 5 \times 10^{-6}$. To account for fluctuations in the estimates arising due to the discrete nature of the simulations, we performed 500 different projections along the LOS, and for each of them, we measured Δ. The values shown are the median ones. Errors obtained computing the 16% and 84% percentiles of the distribution are also shown although barely visible.

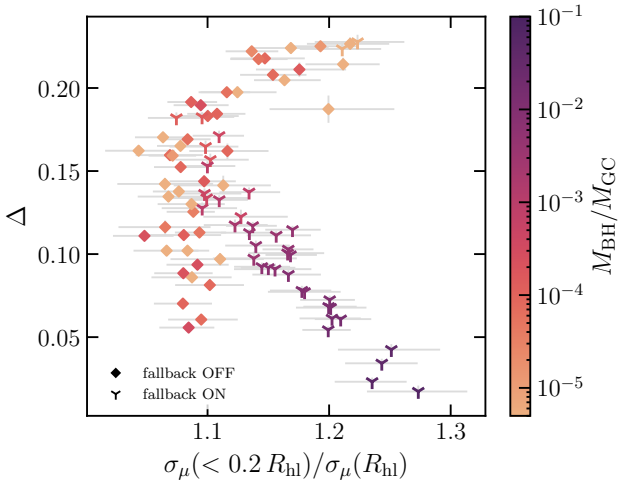

FIGURE 7.3: Mass segregation parameter as a function of the velocity dispersion ratio. Symbols show whether the simulation had (diamond) or had not (upside-down triangle) the fallback prescription for BH formation. Different colors depict the BH mass fraction (see the color bar on the side) Finally, error bars were obtained from multiple projections along the LOS.

then explored the impact of long-lived BH subsystems on the evolution of star clusters by computing several quantities, some of which were previously used to infer the presence of massive BH populations in Galactic GCs (see e.g., Mackey et al., 2008; Bianchini et al., 2016; Askar et al., 2018; Weatherford et al., 2020): the mass-segregation parameter (Δ), the average luminosity density, ($L_{\rm V}/R_{\rm hl}^2$, with $R_{\rm hl}$ the half-light radius and $L_{\rm V}$ the total V luminosity within $R_{\rm hl}$), the concentration ratio ($R_{\rm c}/R_{\rm hl}$ with $R_{\rm c}$ being the core radius), the dynamical age ($n_{\rm h}$), and the inverse of the equipartition mass (μ) estimated within $0.1R_{\rm hl}$.

The parameter Δ was defined as

$$\Delta = \int_0^1 {\rm nCRD}_{\rm pop1}(x) - {\rm nCRD}_{\rm pop2}(x)\, dx\,, \tag{7.1}$$

where nCRD is the normalized cumulative radial distribution computed for a more massive

(labeled as pop1) and a lower-mass (labeled as pop2) population. The integral is computed between the cluster center and a limiting distance $R_{\rm lim} = 2R_{\rm hl}$ with x corresponding to the projected distance of each star from the center, normalized to $R_{\rm lim}$. Similar parameters proved powerful tools in studying the properties and dynamical evolution of GCs (see e.g., Alessandrini et al., 2016; Lanzoni et al., 2016; Peuten et al., 2016; Ferraro et al., 2018a, 2019, 2023b,a; Raso et al., 2017; Dalessandro et al., 2019), and were already used in previous studies to investigate the role of BH subpopulations within GCs (see e.g., Weatherford et al., 2018). We exploited almost the full stellar mass range available at 13 Gyr to maximize the mass-segregation signal: for the more massive population, we selected stars within $[m_{\rm TO} - 0.025;\ m_{\rm TO}]$ $\rm M_\odot$ (with $m_{\rm TO} = 0.8155\,\rm M_\odot$ being the main-sequence turn-off mass at 13 Gyr for a simple stellar population with $Z = 10^{-3}$), whereas for pop2 we selected stars in the mass range $[0.1;\ 0.125]$ $\rm M_\odot$. According to the definition in equation 7.1, Δ is a dimensionless parameter that traces the relative spatial concentration of massive stars compared to lower-mass ones through their nCRDs: the larger the value, the more massive stars are spatially segregated compared to the lower-mass ones.

The proxy for the dynamical age, $n_{\rm h}$, was defined as the ratio between the cluster physical age and the half-mass relaxation time ($t_{\rm rh}$; Spitzer, 1987) calculated at that physical age; following Spitzer (1987):

$$t_{\rm rh} = 0.138 \frac{M_{\rm GC}^{1/2}\, r_{\rm hm}^{3/2}}{\langle m \rangle\, G^{1/2}\, \ln \Lambda}\,, \tag{7.2}$$

with G the gravitational constant, $\langle m \rangle$ the mean star mass, and Λ the Coulomb logarithm coefficient. We used $\Lambda = 0.02\, N_{\rm p}$, which accounts for the effects of a mass spectrum (Giersz & Heggie, 1996).

To compute $R_{\rm c}$, we fitted an analytical, multi-power law model to the surface brightness profile in the V band obtained using stars with $V < V_{\rm TO} + 2$, with $V_{\rm TO}$ being the turn-off magnitude. For each simulation, $V_{\rm TO}$ was estimated by dividing stars into magnitude bins (between $V = 17 - 23$ mag, 0.1 mag wide) and selecting the bin with the bluest $V - I$ color. Finally, the core radius was obtained as the radius at which the surface brightness is half the central one. The half-light radius ($R_{\rm hl}$) was defined as the radius enclosing half of the total projected light in the V band and computed directly from the simulation.

Finally, we computed the $\mu(< 0.1R_{\rm hl})$ parameter as presented in Aros & Vesperini (2023). This quantity represents the inverse of the equipartition mass (Bianchini et al., 2016) with the advantage of providing a simpler description of the stellar-mass-dependence of the velocity dispersion (see Aros & Vesperini, 2023, for further details).

In figure 7.1 we present all the possible combinations of the aforementioned parameters computed for each simulation. In particular, the bottom row in figure 7.1 shows the BH mass fraction as a function of different properties: the presence of a BH subsystem inhabiting the cluster central regions prevents the core collapse of visible stars thereby delaying the evolution of their structural properties (Mackey et al., 2007, 2008; Breen & Heggie, 2013; Morscher et al., 2015). This is in turn reflected in the $R_{\rm c}/R_{\rm hl}$ ratio (which increases for higher BH mass fractions, see e.g., Kremer et al., 2020), and the luminosity density (which decreases for increasing BH mass fractions, see the discussion in Arca Sedda et al., 2018).

In figure 7.2 we focus on the BH mass fraction as a function of Δ. When simulations with the fallback prescription are considered, it is possible to observe a nice correlation between the BH mass fraction and Δ, as expected based on the well-established role of binary BHs

in halting the mass segregation of massive visible stars (Breen & Heggie, 2013). A similar trend was also recovered by Weatherford et al. (2018). However, figure 7.2 also shows that clusters can exhibit little mass segregation (i.e., low values of Δ) without a sizeable population of BHs or even with no BHs at all. These systems have long initial relaxation times and BHs were ejected right after formation due to large natal kicks (for these simulations the fallback off prescription was adopted). Hence, while mass segregation can provide us with valuable information, the role of different initial conditions and physical assumptions should be carefully considered (see also, for instance, the discussion in section 2.6 of Askar et al., 2018). Also, a similar behavior is observed in all the quantities presented in figure 7.1. The fact that clusters with very different BH mass fractions might exhibit similar properties (in terms of mass segregation, concentration ratio, and luminosity density see figure 7.1) highlights the possible problems in inferring the BH mass fraction in real GCs using a single observable. Therefore, multiple physical properties should be jointly used to constrain the presence of BHs within GCs.

In this respect, we introduce a new observable parameter which in synergy with Δ turns out to be particularly useful in discriminating between BH retention and dynamical evolution. This is defined as $\sigma_\mu(< 0.2R_{\rm hl})/\sigma_\mu(R_{\rm hl})$, which is the ratio between the 1D velocity dispersion[2] computed within $0.2R_{\rm hl}$ and at $R_{\rm hl}$[3]. This parameter quantifies the steepness of the velocity dispersion profile, which directly reflects the radial variation of the gravitational potential.

In figure 7.3 we show the $\Delta - \sigma_\mu(< 0.2R_{\rm hl})/\sigma_\mu(R_{\rm hl})$ plot. Low mass segregation levels (roughly $\Delta < 0.15$) can be explained either by the presence of a massive BH subsystem (darker points in figure 7.3) or due to the system being dynamically younger, without requiring high BH mass fractions (lighter points in figure 7.3, but see also figure 7.1). However, these two classes depart in $\sigma_\mu(< 0.2R_{\rm hl})/\sigma_\mu(R_{\rm hl})$: the presence of a massive BH subsystem deepens the potential well in the central regions, increasing the velocity dispersion ratio. On the other hand, dynamically young systems without many BHs exhibit lower values.

Velocity dispersion ratios on the order of 1.15 are attained by systems with low BH mass fractions only if they are dynamically evolved (i.e., roughly $\Delta > 0.2$), effectively breaking the degeneracy between dynamically young GCs without large BH mass fractions and systems hosting a massive BH population which slowed down their dynamical aging.

7.3 Observations

In this section, we present the observational analyses carried out for a sample of Galactic GCs to compare their structural and kinematical properties with those from simulations.

[2]Following what is commonly done in PM studies, we used the two velocity components projected on the plane of the sky to determine the radial ($\sigma_{\rm R}$) and tangential ($\sigma_{\rm T}$) velocity dispersions for each cluster. We then defined $\sigma_\mu^2 \equiv (\sigma_{\rm R}^2 + \sigma_{\rm T}^2)/2$ according to equation 4.5.

[3]Computed from stars with projected distance from the center $\in [0.95; 1.05]\ R_{\rm hl}$.

7.3.1 Properties of Galactic GCs

We selected Galactic GCs with both photometric data from Sarajedini et al. (2007) and individual-stars PMs by Libralato et al. (2022)[4], covering at least the central $0.7R_{\rm hl}$. Such a selection included GCs proposed as promising candidates for hosting high BH mass fractions (including NGC 5053, NGC 6101, and NGC 6362, see Askar et al. 2018; Weatherford et al. 2020) while allowing to investigate a sufficiently large radial range. A large radial range enables better characterization of the system properties, such as mass segregation and the velocity dispersion profile. Finally, we empirically found that selecting stars down to three magnitudes below $V_{\rm TO}$ was the best compromise between keeping the mass gap between pop1 and pop2 as large as possible and ensuring photometric completeness of at least 0.5 over the whole radial range for a sizable fraction of GCs. In section 7.3.2 we present the calculation of the photometric completeness and we discuss those cases for which the incompleteness was too severe and the calculation of Δ-like quantities is not feasible with the dataset adopted in this work. Out of the 57 clusters in common between Sarajedini et al. (2007) and Libralato et al. (2022), 30 met all the aforementioned criteria. For cluster ages, masses, and characteristic radii, we used the catalog provided by Baumgardt et al. (2020, but see also Vasiliev & Baumgardt 2021; Baumgardt & Vasiliev 2021)[5].

To estimate $\sigma_\mu(< 0.2R_{\rm hl})/\sigma_\mu(R_{\rm hl})$, we used the recent astrometric catalog by Libralato et al. (2022). The catalog consists of PMs and multi-epoch photometry for stars in about the central 100″ of 56 Galactic GCs. We applied the same quality selections presented in section 4 of Libralato et al. (2022) retaining stars with $V < V_{\rm TO} + 1.25$ (as done for the simulations). Adopting the same spatial selections (section 7.2), and using $R_{\rm hl}$ from the catalog by Baumgardt et al. (2020, 4th version), we computed the 1D velocity dispersion accounting for errors on the n individual stars. In particular, we assumed the likelihood function (Pryor & Meylan, 1993)

$$\ln \mathcal{L} = \sum_{i=1}^{n} -\frac{1}{2}\left(\frac{(v_{i,\rm R} - \langle v_{\rm R}\rangle)^2}{\sigma_{\rm R}^2 + e_{i,\rm R}^2} + \ln\left(\sigma_{\rm R}^2 + e_{i,\rm R}^2\right)\right) + -\frac{1}{2}\left(\frac{(v_{i,\rm T} - \langle v_{\rm T}\rangle)^2}{\sigma_{\rm T}^2 + e_{i,\rm T}^2} + \ln\left(\sigma_{\rm T}^2 + e_{i,\rm T}^2\right)\right), \tag{7.3}$$

with $v_{i,\rm R}, v_{i,\rm T}$ being the radial and tangential velocity components for the $i-$th star, respectively. Each component had its error, namely $e_{i,\rm R}, e_{i,\rm T}$. All the values were computed in mas/yr, independent of any assumption on the cluster distance. Finally, the mean velocities $\langle v_{\rm R}\rangle$ and $\langle v_{\rm T}\rangle$, the velocity dispersion components $\sigma_{\rm R}$ and $\sigma_{\rm T}$, and the 1D velocity dispersion (σ_μ, see section 7.2) were computed through a MCM) exploration of the parameter space. In particular, we used the `emcee` package (Foreman-Mackey et al., 2013). The same analysis was carried out for stars within $0.2R_{\rm hl}$ and around $R_{\rm hl}$, and the 1D velocity dispersion ratio was computed. For clusters with field of view (FoV) coverage smaller than $R_{\rm hl}$, we opted for a hybrid approach. We estimated the inner 1D velocity dispersion using individual stars (see equation 7.3) whereas we relied on dynamical modeling for the outer one. Using a single-mass,

[4] publicy available at `https://archive.stsci.edu/hlsp/hacks`

[5] The catalog is publicly available at `https://people.smp.uq.edu.au/HolgerBaumgardt/globular/`. Values used in this work are from the 4th version of the catalog updated in March 2023.

King model (King, 1966, constructed via the LIMEPY[6] Python library developed by Gieles & Zocchi 2015) we fitted both the density (de Boer et al., 2019) and the 1D velocity dispersion (obtained by merging *HST* data from Libralato et al., 2022, , and *Gaia* DR3 data, Vasiliev & Baumgardt 2021) profiles. The former allowed us to constrain the structural parameters (such as W_0, and $r_{\rm hm}$), while the latter constrained the total cluster mass. We discuss the fitting procedure and present the results in section 7.5.1.

To quantify mass segregation, we defined the parameter $\Delta_{\rm obs}(< R_{\rm lim})$: similarly to equation 7.1, $\Delta_{\rm obs}(< R_{\rm lim})$ quantifies the degree of segregation via the area between the nCRDs of a bright (Bpop) and faint (Fpop) population computed within a given distance, $R_{\rm lim}$, from the center. We computed $\Delta_{\rm obs}(< R_{\rm lim})$ using the photometric catalog provided by Sarajedini et al. (2007).

A critical step in this regard was a proper assessment of the photometric incompleteness of the catalogs. Due to crowding, incompleteness mainly affects faint stars, preferentially in the center. Given that $\Delta_{\rm obs}(< R_{\rm lim})$ traces the mass segregation using the relative spatial distributions, incomplete catalogs bias the results in a non-trivial manner, possibly inflating the mass-segregation signal. We therefore estimated the completeness (c) for every star, accounting for its projected distance from the center and magnitude. Finally, each star contributed to the nCRD with a factor $1/c$.

7.3.2 Accounting for incompleteness

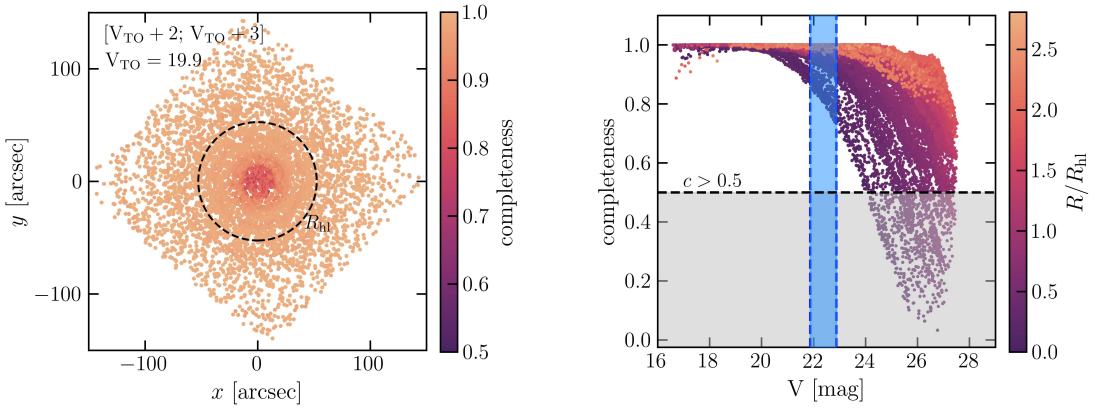

FIGURE 7.4: Photometric completeness for NGC 6584. Left panel: two-dimensional map of Fpop sources. Each star is color-coded according to the completeness in the V band. Right panel: V-magnitude dependence of the photometric completeness. Stars are color-coded according to their projected distance from the center normalized to $R_{\rm hl}$. The gray area marks $c < 0.5$ while the blue region shows the Fpop magnitude range ($[V_{\rm TO}+2; V_{\rm TO}+3]$).

In this section, we present the details of the photometric completeness calculation, carried out for all the clusters in the sample. In particular, we used the photometric catalog

[6]publicy available at `https://github.com/mgieles/limepy`

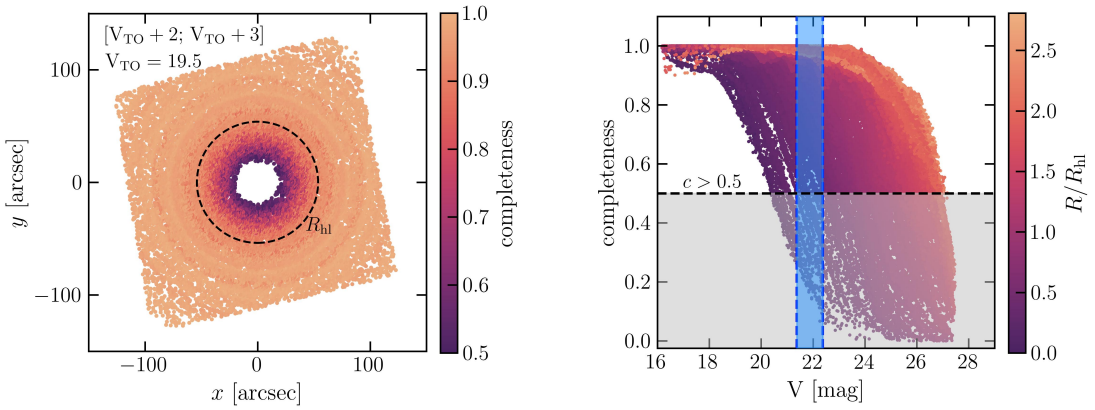

FIGURE 7.5: Same as figure 7.4 for NGC 7089.

by Sarajedini et al. (2007), and the artificial-star test catalog by Anderson et al. (2008) provided for each cluster. The latter catalog consists of 10^5 artificial stars, distributed uniformly within the core radius and with a density $\propto R^{-1}$ outside, with a flat luminosity function in the F606W filter and with colors along the cluster fiducial line (see Anderson et al., 2008, for further details).

To estimate the completeness we adopted the following procedure:

1. we determined quality selection criteria exploiting the `QFIT` parameter in both V and I bands as a function of magnitude. Stars with a `QFIT` higher than the 90th percentile of the distribution at the star magnitude were not considered in the subsequent analyses;

2. using stars with good photometry, we determined membership selection criteria in the color-magnitude diagram (V versus $V - I$). Dividing the stars in magnitude bins (0.5 magnitudes wide), we found the 10th and 90th percentiles of the color distribution. Stars outside this range were not included, as probably field interlopers;

3. we applied these selections to the observed and photometrically-calibrated artificial-star catalogs [7]. In this step, particular care was paid to keeping artificial stars without an output magnitude, which are those input stars not recovered by the data reduction pipeline;

4. for each observed star we selected artificial stars within a radial shell centered around the star position. The shell width was iteratively widened until at least 1000 artificial stars were selected. We then constructed the completeness curve as a function of the magnitude. For each magnitude bin, the completeness was directly computed as the ratio between the number of recovered and input artificial stars. We considered a star as recovered if the output and input V magnitudes were compatible with a tolerance

[7] For NGC 6144 we applied slightly different selections, adopting the 5th and 95th quantiles for the color-magnitude diagram and `QFIT` selections. Indeed, we found that the previous selections introduced systematics in the spatial distribution of the brightest stars thereby biasing the calculation of mass-segregation proxies through the nCRDs.

of 0.75 magnitudes, due to photometric blends (as suggested by Anderson et al., 2008). The final completeness value assigned to each star was obtained by interpolating this curve and evaluating it at the star magnitude.

We defined the Bpop as stars with V magnitude $[V_{\rm TO}; V_{\rm TO}+1]$, whereas Fpop stars have magnitudes in the range $[V_{\rm TO}+2; V_{\rm TO}+3]$. The limit of $V < V_{\rm TO}+3$ ensured that $c > 0.5$ over the whole FoV while keeping the mass gap between Bpop and Fpop stars as large as possible (see also discussion in section 7.3.1). Lower completeness estimates are indeed more uncertain as the completeness relative error roughly scales as the inverse of the square root of the number of recovered stars. Therefore, retaining stars with very low completeness makes the nCRD more uncertain. Also, evaluating the impact of pushing to very low completeness regimes is not straightforward, as one might over- or under-estimate the nCRD due to significant statistical fluctuations in the completeness estimate.

In figure 7.4 we show the completeness properties of Fpop stars in NGC 6584: as expected, the c decreases toward the center and for fainter magnitudes. However, the Fpop stars in this cluster are characterized by completeness levels $\gtrsim 75\%$ at all distances.

In figure 7.5 we show the 2D radial distribution (left panel) and completeness variation curves (right panel) for NGC 7089 as a prototypical case of a cluster excluded from our analysis. While this GC fulfills the radial coverage requirements (section 7.3.1), its Fpop is characterized by a strong incompleteness in the innermost regions. In fact, for this sub-sample of stars c decreases rapidly towards the center, dropping well below the critical threshold of 0.5 around $R_{\rm hl}$, and almost no stars are found within $< 0.5R_{\rm hl}$. Such severe incompleteness makes the calculation of $\Delta_{\rm obs}(< R_{\rm lim})$ practically unfeasible. We note that a few similar cases (for example NGC 2808, and NGC 6093) were included in the analysis by Weatherford et al. (2020) with a possible significant impact on the derived values of Δ for these systems.

7.3.3 Comparison with simulations

Here, we compare the results obtained from the simulations (section 7.2) and the state-of-the-art data presented in section 7.3.1.

figure 7.6 shows the BH mass fraction as a function of $\Delta_{\rm obs}(< R_{\rm lim})$ for $R_{\rm lim} = R_{\rm hl}$ (left panel) and $R_{\rm lim} = 0.7R_{\rm hl}$ (right panel). Values from both simulations and observations were computed according to the definition in section 7.3.1, adopting $R_{\rm lim} = R_{\rm hl}$ ($0.7R_{\rm hl}$ for those GCs with smaller FoV coverage), and using Bpop and Fpop stars to compute Δ. The simulations cover a similar range of $\Delta_{\rm obs}(< R_{\rm lim})$ as the observations. In addition, each value of $\Delta_{\rm obs}(< R_{\rm lim})$ could be reproduced by either simulation with high or low BH mass fractions. This further highlights the degeneracies and strengthens the need for a multi-dimensional approach.

figure 7.7 shows $\Delta_{\rm obs}(< R_{\rm lim})$-vs-$\sigma_\mu(< 0.2R_{\rm hl})/\sigma_\mu(R_{\rm hl})$. Simulations are color-coded according to the BH mass fraction, with different symbols depicting whether the fallback prescription was adopted for the BH natal kicks. Finally, blue points show the values obtained for Galactic GCs (see section 7.3.1). In particular, we show only those clusters for which at least 100 stars with kinematics were available in the radial ranges considered. Such a threshold ensures that the errors on $\sigma_\mu(< 0.2R_{\rm hl})/\sigma_\mu(R_{\rm hl})$ are small enough for a meaningful comparison with the simulations. Nonetheless, in table 7.1 we provide the values of

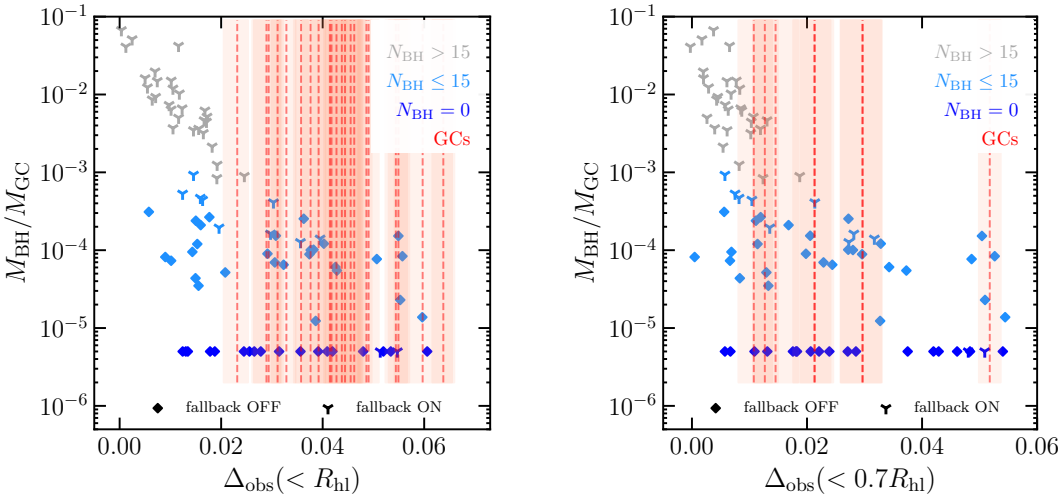

FIGURE 7.6: BH mass fraction as a function of $\Delta_{\rm obs}(< R_{\rm hl})$ (left panel) and $\Delta_{\rm obs}(< 0.7R_{\rm hl})$ (right panel). Points show the simulation properties recomputed according to the magnitude and spatial selections adopted for the observations (see section 7.3.1), whereas the vertical red lines show values obtained for the Galactic GCs studied in this work (along with errors as shaded areas). Simulations without BHs at 13 Gyr are shown at $M_{\rm BH}/M_{\rm GC} = 5 \times 10^{-6}$.

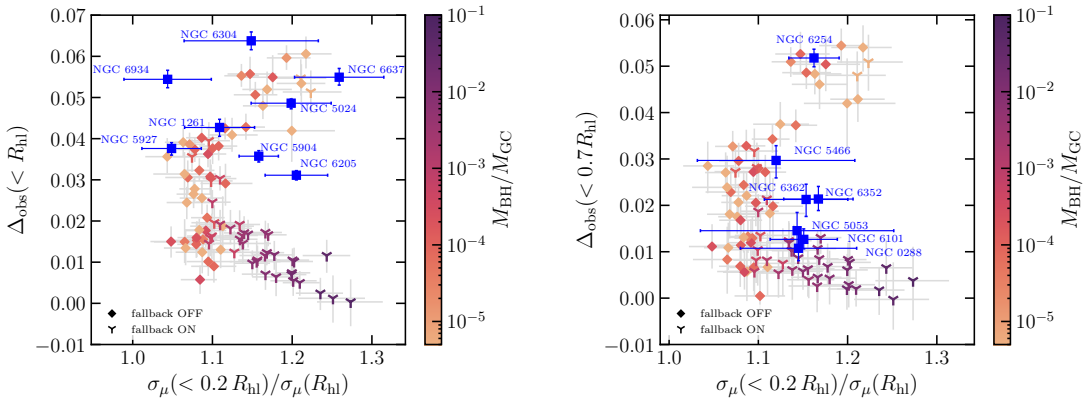

FIGURE 7.7: $\Delta_{\rm obs}(< R_{\rm hl})$ (left panel) and $\Delta_{\rm obs}(< 0.7R_{\rm hl})$ (right panel) as a function of the velocity dispersion ratio. Values from the simulations were recomputed according to the magnitude and spatial selections adopted for the observations (see section 7.3.1). Simulations are color-coded according to the BH mass fraction (see the color bar). Error bars were computed from multiple LOS projections. Finally, in blue we show the values (along with error bars) obtained for Galactic GCs (see section 7.3 for details). The observations shown in this plot are reported in table 7.1 and table 7.2.

$\Delta_{\rm obs}(< R_{\rm lim})$ for all the clusters, and $\sigma_\mu(< 0.2R_{\rm hl})/\sigma_\mu(R_{\rm hl})$ (and relative errors) for the clusters shown in figure 7.7.

The left panels of Figs. 7.6, and 7.7 show GCs for which the data coverage was $\geq R_{\rm hl}$. For these clusters the $\Delta_{\rm obs}(< R_{\rm hl})$ and $\sigma_\mu(< 0.2R_{\rm hl})/\sigma_\mu(R_{\rm hl})$ values are in reasonable agreement with numerical-simulation predictions except for a few cases that show discrepant values of $\Delta_{\rm obs}(< R_{\rm hl})$. Also, they typically show $\Delta_{\rm obs}(< R_{\rm hl}) \gtrsim 0.03$ (see also table 7.1). The mass segregation and the kinematic properties of these clusters could be thus reproduced either by systems in which BHs were ejected right after formation (due to high natal kicks) or that lose their BHs due to dynamical interactions in the center. In either case, the present-day BH mass fraction is likely low (similarly to what was found by Weatherford et al., 2020; Dickson et al., 2024).

As discussed in section 7.3.1, we also considered GCs with a FoV coverage smaller than $R_{\rm hl}$. Within this sample, a few notable clusters were indeed suggested to host massive BH populations at their center (e.g., NGC 5053, NGC 6101, and NGC 6362, see Askar et al. 2018; Weatherford et al. 2020). The right panel of figure 7.6 shows the $\Delta_{\rm obs}(< 0.7R_{\rm hl})$ values obtained for these GCs. As expected from previous works (Dalessandro et al., 2015; Peuten et al., 2016; Weatherford et al., 2020) some of these clusters exhibit little mass segregation. This feature could be interpreted as either the result of the BH burning phase (Kremer et al., 2020) or slow dynamical evolution, as already discussed in section 7.2.

In the right panel of figure 7.7, we delve more into the kinematic properties of these clusters using $\sigma_\mu(< 0.2R_{\rm hl})/\sigma_\mu(R_{\rm hl})$ introduced in this work: focussing on clusters with little mass segregation (roughly $\Delta_{\rm obs}(< 0.7R_{\rm hl}) < 0.02$, see the right panel of figure 7.7) we notice that while there might be hints of higher values of $\sigma_\mu(< 0.2R_{\rm hl})/\sigma_\mu(R_{\rm hl})$ (which would imply these GCs host a nonnegligible BH mass fraction), observational errors do not allow us to discriminate between the possible scenarios fully.

Finally, we highlight here that decreasing the radial and mass ranges for the calculation of Δ-like quantities almost hampers a proper distinction between systems with or without BHs using the $\sigma_\mu(< 0.2R_{\rm hl})/\sigma_\mu(R_{\rm hl})$ ratio (see Figs. 7.3, and 7.7). Hence, future surveys covering larger radial and mass ranges would be critical in this respect.

7.4 Summary and conclusions

In this work, we tackled the inference of the BH mass fraction in GCs through observable properties. We used a survey of Monte Carlo simulations exploring a large range of initial conditions and different prescriptions for the BH natal kicks. We demonstrated that single observables such as parameters measuring the degree of mass segregation are not suited for inferring the BH mass fraction in real GCs, because of significant degeneracies. This degeneracy naturally arises because clusters without a sizable BH population but being dynamically younger may exhibit similar features (e.g., in terms of mass segregation features) when compared to systems where the dynamical evolution was halted by the BH burning mechanism. This highlights that the role of possible different initial conditions and physical assumptions should be carefully considered when trying to obtain the present-day BH population in Galactic GCs.

We then explored multiple probes that could help us break this degeneracy. We introduced the combination Δ and $\sigma_\mu(< 0.2R_{\rm hl})/\sigma_\mu(R_{\rm hl})$ as a possible candidate pair. Δ traces the mass segregation of visible stars within the clusters, whereas $\sigma_\mu(< 0.2R_{\rm hl})/\sigma_\mu(R_{\rm hl})$

quantifies the steepness of the velocity dispersion profile: the presence of a massive BH subsystem increases $\sigma_\mu(< 0.2R_{\rm hl})/\sigma_\mu(R_{\rm hl})$ while halting the mass segregation of visible stars (i.e., keeping Δ low). At the same time, dynamically young clusters (i.e., exhibiting a low degree of mass segregation) that did not retain a massive BH population at 13 Gyr , have typically lower $\sigma_\mu(< 0.2R_{\rm hl})/\sigma_\mu(R_{\rm hl})$.

We therefore measured $\Delta_{\rm obs}(< R_{\rm lim})$ (assuming either $R_{\rm lim} = R_{\rm hl}$ or $R_{\rm lim} = 0.7R_{\rm hl}$, see section 7.3.3) and $\sigma_\mu(< 0.2R_{\rm hl})/\sigma_\mu(R_{\rm hl})$ for several Galactic GCs using the photometric and astrometric catalogs by Sarajedini et al. (2007) and Libralato et al. (2022) respectively, and we compared them with the same quantities computed from the simulations. We found that current state-of-the-art data do not provide stringent enough constraints to fully discriminate between different scenarios, likely due to the limited radial and mass ranges. Future astrometric and photometric data provided by, for instance, the *Roman* space telescope (WFIRST Astrometry Working Group et al., 2019) may allow us to shed light on the subject.

Finally, we also presented a detailed discussion on the calculation of the photometric completeness using artificial star tests. We found that for a non-negligible number of clusters, the calculation of $\Delta_{\rm obs}(< R_{\rm lim})$ was not feasible due to severe incompleteness in the center. Some of these clusters were previously studied using the same photometric catalog to infer the BH mass fraction (see e.g., Weatherford et al., 2020). We thus advise caution in interpreting those results.

In summary, we showed that the effects of BHs on the internal GC dynamics over their lifetime cannot be encapsulated in a single observable, thus multiple physical properties should be used to infer the present-day BH populations in real GCs.

7.5 Supplementary material

7.5.1 Density distribution and velocity dispersion profiles for nine GCs

In this section, we present the hybrid approach in the $\sigma_\mu(< 0.2R_{\rm hl})/\sigma_\mu(R_{\rm hl})$ calculation adopted for a subsample of GCs (see section 7.3). We used the number density profiles provided by de Boer et al. (2019). The authors stiched heterogeneous profiles from literature, such as surface brightness (Trager et al., 1995), and number density (Miocchi et al., 2013) profiles, complemented by *Gaia* data. For the 1D velocity dispersion profiles, we used the catalogs by Libralato et al. (2022) and Vasiliev & Baumgardt (2021) to ensure a larger radial coverage.

We fitted these profiles with a single-mass King model constructed using the LIMEPY (Gieles & Zocchi, 2015) Python library. Within a Bayesian framework, we assumed the likelihood function

$$\ln \mathcal{L} = \ln \mathcal{L}_{\rm profile} + \ln \mathcal{L}_{\rm vel.disp.} \,, \tag{7.4}$$

where the first and second terms of the right-hand side of equation 7.4 are the likelihoods for the density and the velocity dispersion profiles, respectively. Concerning the number density, the likelihood term is

$$\ln \mathcal{L}_{\rm profile} = -\frac{1}{2} \sum_{i=1}^{N_p} \frac{(n_i - \eta \Sigma(R_i|\boldsymbol{\theta}))^2}{\delta n_i^2} \,, \tag{7.5}$$

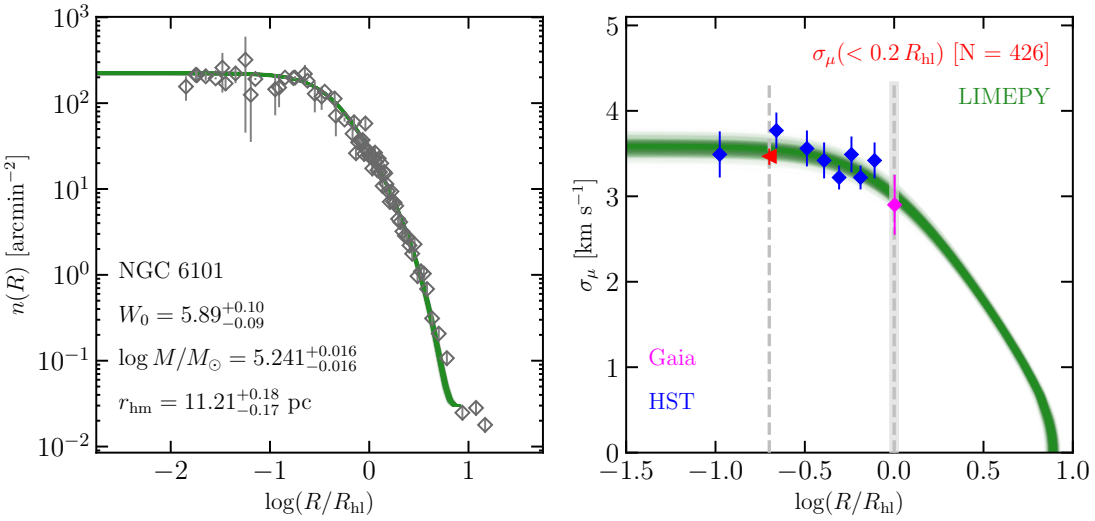

FIGURE 7.8: Structural and kinematical properties for NGC 6101. Left panel: number density profile from de Boer et al. (2019, in gray). Posterior values for the model's free parameters are reported. The green lines show 1000 model realizations from posterior samples. Right panel: 1D velocity dispersion profile in km s^{-1}. In blue are *HST* data from Libralato et al. (2022), whereas in purple are *Gaia* data from Vasiliev & Baumgardt (2021). Velocities were converted assuming the distance from Baumgardt & Vasiliev (2021). The red point shows the σ_μ obtained from single stars $< 0.2R_{\rm hl}$ plotted at $0.2R_{\rm hl}$ (the number of stars used in the calculation is also reported within square brackets). The vertical lines mark $0.2R_{\rm hl}$, and $R_{\rm hl}$ with the light-gray band depicting the radial range $[0.95;\ 1.05]\ R_{\rm hl}$.

with R_i, n_i, and δn_i being the projected cluster-centric distance, the number density, and the relative error for all N_p bins. The projected mass density (Σ) was computed at R_i for any given set of the model's free parameters, $\boldsymbol{\theta} = \{W_0, \log M_{\rm GC}, r_{r\rm hm}\}$, namely the dimensionless central potential, cluster mass, and half-mass radius (King, 1966). Finally, η is a nuisance parameter for scaling the mass-density profile into the number-density one. The velocity dispersion (σ_μ) term in equation 7.4

$$\ln \mathcal{L}_{\rm vel.disp.} = -\frac{1}{2}\sum_{i=1}^{N_\sigma} \frac{(\sigma_{\mu,i} - \sigma_{\mu,\rm model}(R_i|\boldsymbol{\theta}))^2}{\sigma^2_{\mu,i}}\,, \tag{7.6}$$

summed over the N_σ bins. The velocity dispersion from the model ($\sigma_{\mu,\rm model}$) was computed at any given radial position R_i for each set of the model's free parameters.

We explore the free parameters space using an MCMC approach exploiting the Python implementation provided by the `emcee` (Foreman-Mackey et al., 2013) library. For each cluster, we used 100 walkers, evolved for 500 steps. The first quarter was discarded for the sake of convergence and one sample every 50 was retained to account for correlations. In figure 7.8 we show the number density and velocity dispersion profiles for NGC 6101. Posterior values for the model's free parameters, as well as 1000 models constructed from posterior samples,

are also shown.

Within the hybrid approach, $\sigma_\mu(< 0.2R_{\rm hl})$ is computed using single stars (as presented in section 7.3, see equation 7.3), whereas $\sigma_\mu(R_{\rm hl})$ (and its relative error from the 16th and 84th percentiles of the posterior distribution on the velocity dispersion profile) is computed from the dynamical modeling at $R = R_{\rm hl}$. In doing so, we also verified that the value does not significantly change (within the errors) if computed at $R = 0.95R_{\rm hl}$ or $R = 1.05R_{\rm hl}$, which are the boundaries of the radial shell used in the single star analysis (see section 7.3). Finally, the 1D velocity dispersion ratio is computed.

7.5.2 Table of Δ and velocity dispersion ratio values

In this section, we report the results for the GC sample considered in this study. In particular, in table 7.1 we list the values $\Delta_{\rm obs}(< R_{\rm hl})$ and $\sigma_\mu(< 0.2R_{\rm hl})/\sigma_\mu(R_{\rm hl})$ obtained for the sample of 21 clusters with *HST* coverage of at least one half-light radius (see section 7.3 for the definition and calculation details of the parameters). Similarly, table 7.2 shows the results (namely $\Delta_{\rm obs}(< 0.7R_{\rm hl})$, and $\sigma_\mu(< 0.2R_{\rm hl})/\sigma_\mu(R_{\rm hl})$) for the nine clusters with *HST* coverage smaller than one half-light radius.

TABLE 7.1: Properties of the sample of 21 clusters analyzed in this study with FoV larger than $R_{\rm hl}$.

Cluster	$\Delta_{\rm obs}(< R_{\rm hl})$	$\sigma_\mu(< 0.2R_{\rm hl})/\sigma_\mu(R_{\rm hl})$
NGC 1261	$0.043^{+0.002}_{-0.002}$	1.11 ± 0.04
NGC 2298	$0.044^{+0.004}_{-0.003}$	–
NGC 4590	$0.049^{+0.002}_{-0.002}$	–
NGC 4833	$0.046^{+0.002}_{-0.002}$	–
NGC 5024	$0.049^{+0.001}_{-0.001}$	1.20 ± 0.05
NGC 5904	$0.036^{+0.001}_{-0.001}$	1.16 ± 0.02
NGC 5927	$0.038^{+0.001}_{-0.002}$	1.05 ± 0.04
NGC 5986	$0.039^{+0.001}_{-0.002}$	–
NGC 6144	$0.029^{+0.003}_{-0.003}$	–
NGC 6171	$0.044^{+0.003}_{-0.003}$	–
NGC 6205	$0.031^{+0.001}_{-0.001}$	1.21 ± 0.04
NGC 6218	$0.046^{+0.002}_{-0.002}$	–
NGC 6304	$0.064^{+0.002}_{-0.002}$	1.15 ± 0.08
NGC 6535	$0.042^{+0.006}_{-0.007}$	–
NGC 6584	$0.023^{+0.002}_{-0.003}$	–
NGC 6637	$0.055^{+0.002}_{-0.002}$	1.26 ± 0.06
NGC 6717	$0.060^{+0.006}_{-0.006}$	–
NGC 6723	$0.033^{+0.002}_{-0.002}$	–
NGC 6779	$0.041^{+0.002}_{-0.002}$	–
NGC 6934	$0.054^{+0.002}_{-0.002}$	1.04 ± 0.05
NGC 6981	$0.029^{+0.002}_{-0.003}$	–

Notes. $\Delta_{\rm obs}(< R_{\rm hl})$ and velocity dispersion ratio for the clusters with FoV coverage of at least one $R_{\rm hl}$. The velocity dispersion was computed directly from individual stars within $0.2R_{\rm hl}$ and around $R_{\rm hl}$. Only clusters with at least 100 stars within these ranges were considered.

TABLE 7.2: Properties of nine clusters with FoV coverage smaller than $R_{\rm hl}$.

Cluster	$\Delta_{\rm obs}(< 0.7R_{\rm hl})$	$\sigma_\mu(< 0.2R_{\rm hl})/\sigma_\mu(R_{\rm hl})$
NGC 0288	$0.011^{+0.003}_{-0.003}$	1.15 ± 0.07
NGC 6254	$0.052^{+0.002}_{-0.002}$	1.16 ± 0.03
NGC 6352	$0.021^{+0.003}_{-0.004}$	1.15 ± 0.05
NGC 6362	$0.021^{+0.003}_{-0.002}$	1.17 ± 0.04
NGC 6496	$0.030^{+0.003}_{-0.004}$	–
NGC 6752	$0.076^{+0.002}_{-0.002}$	1.35 ± 0.02
NGC 5053	$0.015^{+0.004}_{-0.004}$	1.14 ± 0.11
NGC 5466	$0.030^{+0.003}_{-0.004}$	1.12 ± 0.09
NGC 6101	$0.013^{+0.002}_{-0.002}$	1.15 ± 0.04

Notes. $\Delta_{\rm obs}(< 0.7R_{\rm hl})$ and velocity dispersion ratio for the clusters with FoV coverage $< R_{\rm hl}$. The velocity dispersion ratio was computed using individual stars (within $0.2R_{\rm hl}$) complemented by dynamical modeling around $R_{\rm hl}$. For NGC 6496 the $\sigma_\mu(< 0.2R_{\rm hl})/\sigma_\mu(R_{\rm hl})$ value was not computed due to large errors in the PMs that hindered a reliable calculation of σ_μ.

Chapter 8

Quest for an intermediate-mass BH in NGC 104

"Who knew the emptiness could be so cold?"
Monster,
Starset

The previous Chapter investigated the role of stellar-mass BHs in the long-term evolution of GCs and the observable features imprinted in the star distribution and kinematics. In addition to stellar-mass BHs, GCs are of interest in the hunt for IMBHs.

IMBHs are classified as BHs with masses in the range of 10^2-10^5 $M_\odot$ (Greene et al., 2020), setting them between stellar-mass BHs and of supermassive BHs (SMBHs). The discovery of SMBHs at $z = 7.5$, when the Universe was only 0.7 Gyrs old (Bañados et al., 2018), poses a challenge to theories of SMBH formation (Volonteri, 2010). Since IMBHs are thought to be the possible seeds from which SMBHs had grown at early times, finding evidence for IMBHs would provide insights into BH formation mechanisms. However, there has been no firm evidence presented for the existence of BHs in the range $10^2 - 10^5$ $M_\odot$ thus far (see e.g., den Brok et al., 2015; Nguyen et al., 2018; Abbott et al., 2020).

GCs are considered good candidates for hosting an IMBH because *i)* they are expected to be promising sites for IMBH formation (Miller & Hamilton, 2002; Portegies Zwart et al., 2004) and *ii)* extrapolating the empirical relation of Magorrian et al. (1998) between central BH and galaxy bulge masses predicts IMBH-like masses within GCs. The presence of IMBHs in GCs has been investigated by means of different techniques, such as radio emission (e.g., Strader et al., 2012; Tremou et al., 2018), constraining the gravitational field using the timing of radio pulsars (e.g., Kızıltan et al., 2017; Abbate et al., 2018), and kinematic studies of the innermost stars (e.g., Gerssen et al., 2002; Vitral et al., 2023). Interestingly in this respect, Häberle et al. (2024) reported the discovery of seven fast-moving stars in the center (innermost 0.08 pc) of the GC ω Centauri, suggesting that a BH as massive as > 8200 $M_\odot$ may be responsible of such high speeds.

Besides ω Centauri, the Galactic GC 47 Tucanae is arguably one of the best targets to look for an IMBH, because of its high density and mass (Miller & Hamilton, 2002; Portegies Zwart et al., 2004; Giersz et al., 2015). It is also relatively nearby ($\simeq 4.5$ kpc), which allows for detailed studies of the central kinematics. Thus, it has been studied using different approaches to investigate the possible presence of an IMBH. Some studies carried out radio observations of the core of 47 Tucanae (e.g., de Rijcke et al., 2006; Tremou et al., 2018), finding no evidence of a significant emission. Tremou et al. (2018) placed a 3σ upper limit at $M_{\rm BH} < 1040$ $M_\odot$,

while de Rijcke et al. (2006) found a broader limit of $M_{\rm BH} < 670 - 2060$ M$_\odot$, depending on different assumptions on the gas density, gas temperature, and the fraction of rest-mass energy of the infalling matter converted into radiation. Comparing spin-down measurements for 19 millisecond pulsars (MSPs) identified in 47 Tucanae, Kızıltan et al. (2017) found that an IMBH of mass $M_{\rm BH} = 2300^{+1500}_{-850}$ M$_\odot$ is required to reproduce the accelerations and the cumulative spatial distribution of MSPs. Hénault-Brunet et al. (2020) found that a total mass of 430^{+386}_{-301} M$_\odot$ in stellar-mass BHs could explain the stellar kinematics and spatial distribution (Hénault-Brunet et al., 2020, without IMBH). Exploiting a set of *HST* PM measurements of the central regions of 47 Tucanae, Mann et al. (2020) found that the stellar BH population cannot fully account for the observed velocity dispersion, even if a BH and neutron star retention fraction of the 100% is assumed. These authors concluded that an additional massive component with a mass $M_{\rm BH} = 808 - 4710$ M$_\odot$ (depending on the retention fraction) is favored.

The tension among some of the aforementioned results suggests that the question of the presence of an IMBH in 47 Tucanae requires further investigation. In the work presented in this Chapter, we addressed the problem by combining state-of-the-art data with flexible self-consistent models of stellar systems allowing for a central IMBH.

The Chapter is organized as follows: sections 8.1 and 8.2 introduce the dynamical models and the observational datasets, respectively. Section 8.3 presents the results, and section 8.4 compares them with previous works. In section 8.5 we summarize and conclude. Finally, section 8.6 provides supplementary material.

The results presented in this Chapter are part of the paper Della Croce et al. (2024b, A&A, **682**, A22). We also highlight in passing, that the recent study by Smith et al. (2024) nicely aligns with our results. The authors aimed at constraining the stellar-mass BH population within 47 Tuc and the bulge cluster Terzan 5 by modeling pulsar accelerations. Interestingly, they found that pulsars alone could provide valuable constraints on the cluster's internal dynamics. These findings are particularly relevant for systems where kinematics is hardly measured, such as the Galactic bulge.

8.1 Dynamical models

In this work, we use dynamical models based on DFs that depend on the action integrals **J** (see e.g. Binney & Tremaine, 2008a). Describing a stellar system as an ensemble of orbits, we can represent each orbit through its actions. Orbits with small $|\mathbf{J}|$ populate the internal regions of the clusters, whereas large $|\mathbf{J}|$ values describe orbits in the external regions (Binney & Tremaine, 2008a). This approach has a few important advantages: *i)* the model is physical since the DF is always non-negative by construction; *ii)* the velocity anisotropy, as well as any physical property of the system, are self-consistently computed directly from the DF (see section 8.1.3); and *iii)* the extension to multi-component systems, for instance galaxies with a stellar and dark matter component (Piffl et al., 2015; Binney & Piffl, 2015; Pascale et al., 2018) or GCs with a central BH (Pascale et al., 2019), is straightforward.

8.1.1 Model for the stellar component

We consider models where the stellar component of 47 Tucanae is described by the following DF

$$f(\mathbf{J}) = f_0\, M_{\rm GC} \left[1 + \left(\frac{J_0}{h(\mathbf{J})}\right)^{\zeta}\right]^{\Gamma/\zeta} \times \left[1 + \left(\frac{g(\mathbf{J})}{J_0}\right)^{\zeta}\right]^{-(B-\Gamma)/\zeta} \times \exp\left[-\left(\frac{g(\mathbf{J})}{J_{\rm cut}}\right)^{\alpha}\right], \tag{8.1}$$

which produces models whose spatial distributions closely follow a double-power law model (Vasiliev 2019a, but see also Evans & Williams 2014; Binney & Piffl 2015; Pascale et al. 2018, 2019) with an exponential cutoff in the system outskirts. Here, f_0 is such that the DF is normalized to the total stellar mass $M_{\rm GC} = (2\pi)^3 \int f(\mathbf{J}) d^3\mathbf{J}$.

The dimensionless free parameters Γ and B primarily determine the inner ($|\mathbf{J}| \lesssim J_0$) and outer ($|\mathbf{J}| \gtrsim J_0$) slopes in the action space, with J_0 being the typical action at which this transition takes place. In the case of the double power-law model, Γ and B can be converted in the slopes of the three-dimensional (3D) density profile (Posti et al., 2015). The transition regime ($|\mathbf{J}| \sim J_0$) is mainly regulated by ζ. Finally, the parameter α controls the sharpness of the exponential truncation for $|\mathbf{J}| \gtrsim J_{\rm cut}$, with $J_{\rm cut}$ ($> J_0$) being the typical action value above which the exponential cutoff dominates the stellar distribution. The functions $h(\mathbf{J})$ and $g(\mathbf{J})$ are linear combinations of the actions defined as

$$\begin{aligned} h(\mathbf{J}) &= (3-2h_z)J_r + h_z(J_z + |J_\phi|) \equiv (3-2h_z)J_r + h_z|\mathbf{L}|\,, \\ g(\mathbf{J}) &= (3-2g_z)J_r + g_z(J_z + |J_\phi|) \equiv (3-2g_z)J_r + g_z|\mathbf{L}|\,, \end{aligned} \tag{8.2}$$

where $|\mathbf{L}|$ is the total angular momentum. These functions depend only on the two free parameters h_z and g_z, which mainly control the inner and outer anisotropy of the system, respectively (see section 4.1 in Vasiliev, 2019a).

8.1.2 The gravitational potential

The total gravitational potential of the model cluster is the sum of the BH potential $\Phi_{\rm BH}$ and the stellar potential Φ. The BH potential is

$$\Phi_{\rm BH}(r) = -\frac{G\,M_{\rm BH}}{r}\,, \tag{8.3}$$

where $M_{\rm BH}$ is the BH mass and r is the radial spherical coordinate. The stellar potential is determined by numerically solving (in an iterative fashion) the Poisson equation. At each iteration, i, the stellar potential is updated according to

$$\begin{aligned} \nabla^2\Phi_{i+1} &= 4\pi G\,\rho_i \\ &= 4\pi G \int d^3\boldsymbol{v}\, f(\boldsymbol{J}[\boldsymbol{x},\boldsymbol{v}|\Phi_i + \Phi_{\rm BH}])\,, \end{aligned} \tag{8.4}$$

where $\rho = \int d^3\boldsymbol{v}\, f(\boldsymbol{J})$ is the 3D stellar density and we have made explicit the dependence of the conversion between actions and Cartesian phase-space coordinates $(\boldsymbol{x}, \boldsymbol{v})$ on the total potential $\Phi_i + \Phi_{\rm BH}$. This shows that, given a DF, the stellar density distribution, as well as any physical property derived for the visible component (see section 8.1.3), depends on the combination of stellar and BH potential. As an initial guess on Φ, we adopted the isochrone potential (Binney & Tremaine, 2008a), but we note that the final stellar potential does not depend on this specific choice (see Vasiliev, 2019a).

Since the BH potential is spherically symmetric, and the $h(\mathbf{J})$ and $g(\mathbf{J})$ functions are defined such that the DF depends only on the radial action and the angular momentum modulus, the overall system is also spherical. Any integral of the DF that involves conversion between actions and Cartesian phase-space coordinates was performed with the `AGAMA` library (Vasiliev, 2019a).

8.1.3 Observable properties from a DF

Given a DF, we can calculate the observable properties of the model based on suitable integrations of the DF that allow us to compare theoretical models against the observations. Throughout this work, the DF is normalized to the total system mass (see equation 8.1). The mass surface density distribution is then obtained via

$$\Sigma(R) = \int_{-\infty}^{+\infty} dz\, \rho(r)\,, \tag{8.5}$$

where z is the LOS direction and $R^2 = r^2 - z^2$ is the distance from the GC center on the plane of the sky. The stellar number density, n, is then simply defined by the relation $\Sigma \equiv m\, n$, where m is a nuisance parameter of the model with the dimension of a mass.

Furthermore, we can calculate projected velocity distributions as

$$\mathcal{V}_{\rm 3D}(\boldsymbol{v}_{\rm 3D}|R) \equiv \frac{\int dz\, f(\mathbf{J})}{\Sigma(R)}\,, \tag{8.6}$$

where $\boldsymbol{v}_{\rm 3D} = \{v_{\rm R}, v_{\rm T}, v_{\rm LOS}\}$ is the vector of 3D projected velocities (i.e., $v_{\rm R}$ and $v_{\rm T}$ on the plane of the sky, while $v_{\rm LOS}$ is the LOS component). Since for the majority of the stars the 3D velocity is not available, it is useful to define the marginalized velocity distributions. In particular, the LOS velocity distribution

$$\mathcal{V}_{\rm LOS}(v_{\rm LOS}|R) \equiv \frac{\int dz\, dv_{\rm R}\, dv_{\rm T}\, f(\mathbf{J})}{\Sigma(R)} \tag{8.7}$$

and the distribution in the plane-of-the-sky velocity components

$$\mathcal{V}_{\rm PM}(v_{\rm R},\, v_{\rm T}|R) \equiv \frac{\int dz\, dv_{\rm LOS}\, f(\mathbf{J})}{\Sigma(R)}\,, \tag{8.8}$$

such that they are normalized to unity in the velocity space. Finally, the velocity dispersion profile of the i-th velocity component (with $i \in$ {R, T, LOS}) is computed as

$$\sigma_i^2(R) \equiv \frac{\int dz\, d^3\mathbf{v}\, v_i^2\, f(\mathbf{J})}{\Sigma(R)}\,. \tag{8.9}$$

Equations 8.5 to 8.9 allow us to test our theoretical predictions against the data (see section 8.2).

8.2 The observable datasets

The family of dynamical models presented in section 8.1 has eleven free parameters: the total stellar and BH masses, $M_{\rm GC}$, and $M_{\rm BH}$; the scale actions, J_0, and $J_{\rm cut}$; the dimensionless free parameters, ζ, Γ, B, $g_{\rm z}$, $h_{\rm z}$, and α; and the nuisance parameter, m. We explored this parameter space by comparing the models with a set of observables in a fully Bayesian framework. Details on the likelihood and the Markov chain Monte Carlo method used to explore the model posterior and calculate uncertainties on the free parameters (and on any derived quantity) are given in Appendix 8.6.1.

As kinematic dataset, we used a combination of individual LOS velocities from Kamann et al. (2018, obtained using the *MUSE* spectrograph) and PMs from Libralato et al. (2022, derived from multi-epoch observations with *HST*).

Kamann et al. (2018) obtained individual LOS velocities using the *MUSE* spectrograph. This sample represents the largest compilation of LOS velocities covering the central regions of 47 Tucanae (up to 100″ from the GC center), with a typical velocity accuracy of $1 - 2$ km s^{-1}. To clean the sample of any possible contamination from binary systems, we selected only those stars with a probability of being an unresolved binary smaller than 50%, according to the criterion defined by Kamann et al. (2018). We also subtracted the average LOS velocity of the sample ($\langle v_{\rm LOS}\rangle = -18.6^{+0.2}_{-0.1}$ km s^{-1}) from individual velocities. The final sample of LOS velocities used in this work thus comprises 14,601 stars.

Similarly, the catalog of PM data from Libralato et al. (2022) represents the most complete, homogeneous collection of PMs of stars in the cores of stellar clusters to date. To select stars with reliable PM estimates, we applied the quality selections described in Libralato et al. (2022, see their section 4), retaining 68,954 stars. Moreover, we cleaned the sample of contaminants of the Small Magellanic Cloud by taking advantage of its high velocity ($\mu_{\alpha*} = -4.716 \pm 0.035$ mas yr^{-1} and $\mu_\delta = 1.325 \pm 0.021$ mas yr^{-1}, Anderson & King, 2003) relative to 47 Tucanae in the PM space. We thus removed all the stars further than 2.6 mas yr^{-1} from the cluster bulk velocity, corresponding to more than 50 km s^{-1} (i.e., larger than the central escape speed; Baumgardt & Hilker, 2018).

Finally, we used the number density profile provided by de Boer et al. (2019) to model the stellar density distribution of the GC. These authors combined Gaia DR2 data in the external regions (projected distances from the center larger than $\sim$ 20'), with ground-based and *HST* observations from Trager et al. (1995) and Miocchi et al. (2013), respectively.

The dataset covers the whole cluster extent, from $\sim$ 1″ to the cluster outskirts. In the fitting procedure, we adopted a fixed background level of 0.08 stars arcmin^{-2} (see e.g., Hénault-Brunet et al., 2020).

In particular, we fit individual stellar velocities within 12″ from the center. This distance would correspond to the radius of influence, defined by the implicit relation $R_{\rm infl} \equiv G\,M_{\rm BH}/\sigma^2_{\rm LOS}$ (where $\sigma_{\rm LOS} = \sigma_{\rm LOS}(R)$ is the LOS velocity dispersion, see equation 8.9) of a putative IMBH with mass $M_{\rm BH} = 10^4$ M$_\odot$. This is well above all previously claimed detections (Kızıltan et al., 2017; Mann et al., 2020) and the upper limits (McLaughlin et al., 2006). Our final kinematic sample consists of 260 stars, with either PM or LOS velocity, and 21 stars with the full 3D velocity. Beyond 12″, we used the velocity dispersion profiles computed using the same datasets.

Throughout the analysis, we adopted the center reported by Goldsbury et al. (2010) and the kinematic distance of 4.34 kpc (Libralato et al., 2022), without accounting for its 0.06 kpc error. The propagation of this error on PMs would contribute at 1% level, which is negligible compared to typical relative uncertainties on PM data around 16%.

Our models are non-rotating, though there is evidence that 47 Tucanae does rotate (Anderson & King, 2003; Bellini et al., 2017; Kamann et al., 2018). However, Kamann et al. (2018) derived the dispersion profiles we used accounting for a rotationally dependent mean velocity, and rotation is erased when deriving PMs due to local corrections. A residual differential rotation could be present in the LOS sample of central stars (i.e., within 12″). However, in the very central regions, the LOS rotation velocity is expected to be $\simeq 1$ km s^{-1}, which is a small fraction of the central LOS velocity dispersion (Kamann et al., 2018). We note that any residual rotation would likely bias the model toward higher IMBH masses, as it would increase the inferred central velocity dispersion.

8.3 Results from the dynamical model

The left panel of figure 8.1 shows the posterior distribution of the IMBH mass. According to our analysis, we find no evidence of an IMBH in 47 Tucanae. Instead, we set an upper limit of $M_{\rm BH} < 578$ M$_\odot$ at the 3σ level. This is the most stringent upper limit on the mass of a putative central dark component in 47 Tucanae ever achieved by any dynamical study. The right panel of figure 8.1 shows the 3σ upper limit on the IMBH $R_{\rm infl}$, overplotted to the on-sky distribution of stars closer than 12″ to the center. It is clear that the kinematics of these stars put a very tight constraint on $R_{\rm infl}$, whose upper limit is comparable to the distance from the center of the innermost stars. We further verified this point, by performing additional fits where first the individual stars inside 12″, and then the velocity dispersion profiles were also removed. We found that the upper limit on the IMBH mass increases to a few thousand and to several hundred thousand solar masses, respectively.

Figure 8.2 shows the PM and LOS velocity distributions for stars within 12″ from the center. Overplotted to the observations, we show the median model, and the 68% and 99.7% credible intervals (CIs) for the corresponding velocity distributions. Each model was convolved with a Gaussian distribution with a standard deviation equal to the observational median error in each component and was integrated over the radial extent covered by the datasets. The model reproduces the observed velocity distributions out to the tails (figure 8.2). We emphasize though that we did not fit the binned histograms, whereas we used an individual-star approach fully exploiting the datasets (see equation 8.12).

The very good agreement between the model and the data can be further observed in figures 8.3 and 8.4, which show the projected velocity dispersion profiles and the stellar density

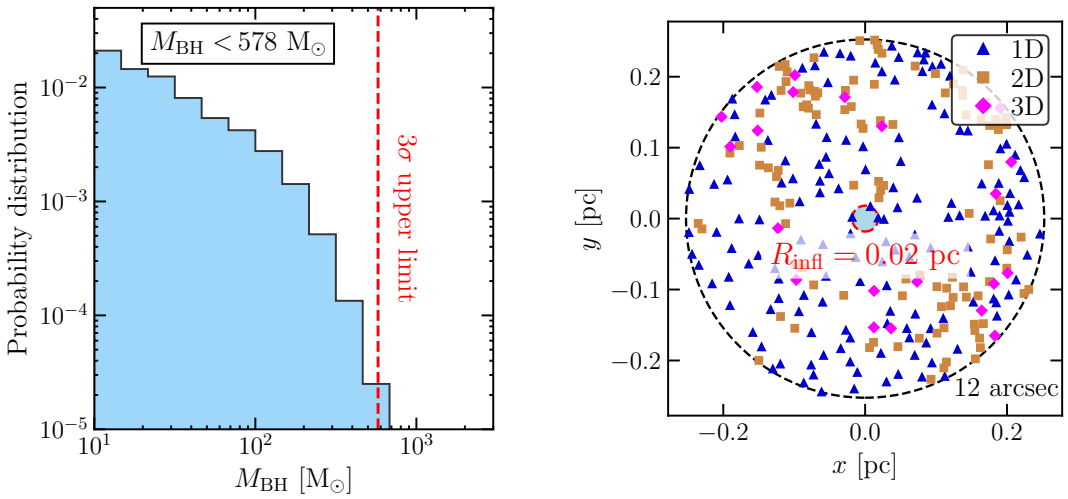

FIGURE 8.1: Posterior distributions on the IMBH mass and region of influence in 47 Tucanae. Left: Posterior distribution on the BH mass (blue histogram). The vertical line indicates the upper limit on the BH mass (578 M$_\odot$) containing 99.7% (3σ) of the posterior distribution. Right: Spatial distribution of the kinematic sample of individual stars inside a circumference of radius of 12″ (black curve). Each star is color-coded according to the available kinematic information: LOS velocity (i.e., 1D velocity) in dark blue, PM (2D) in brown, and full kinematic information (PM and LOS velocity, i.e., 3D) in magenta. The blue shaded area indicates the region that would be influenced by a central BH with mass 578 $M_\odot$ (our 3σ upper limit), which has a radius of influence $R_{\rm infl} = 0.02$ pc (red curve).

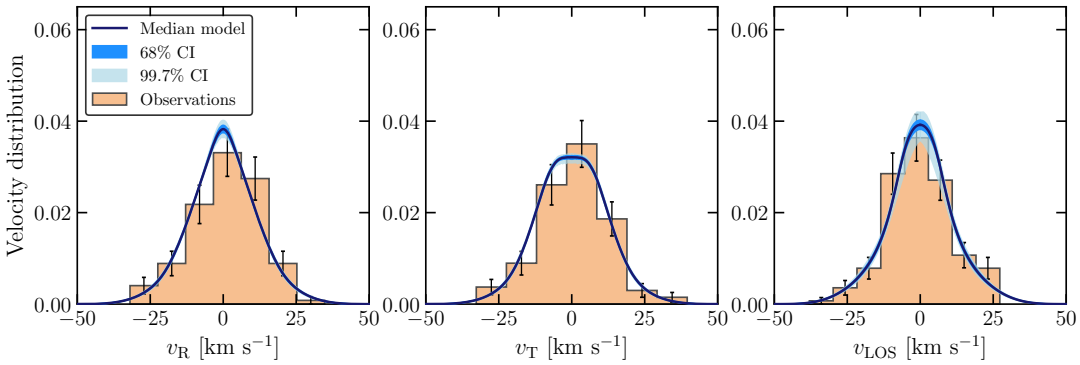

FIGURE 8.2: Observed velocity distribution within 12″ from the cluster center, along the radial (left panel), tangential (central panel), and LOS (right panel) directions. The bars indicate uncertainties estimated as Poissonian errors on the bin counts. The median models (solid line), 68% (1σ), and 99.7% (3σ) CIs (shaded areas) are shown in blue (see text for details).

profile, compared with the median and CIs of the corresponding theoretical profiles. We also

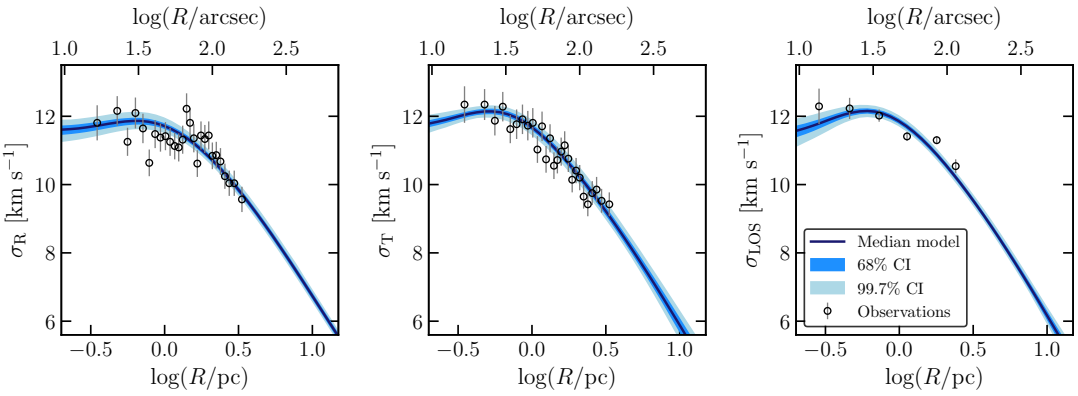

FIGURE 8.3: Projected velocity dispersion profiles along the radial (left panel), tangential (central panel), and LOS (right panel) directions. Observations are shown as black points along with 1σ error bars. The blue line is the median model, while the shaded areas represent the 68% and the 99.7% CIs.

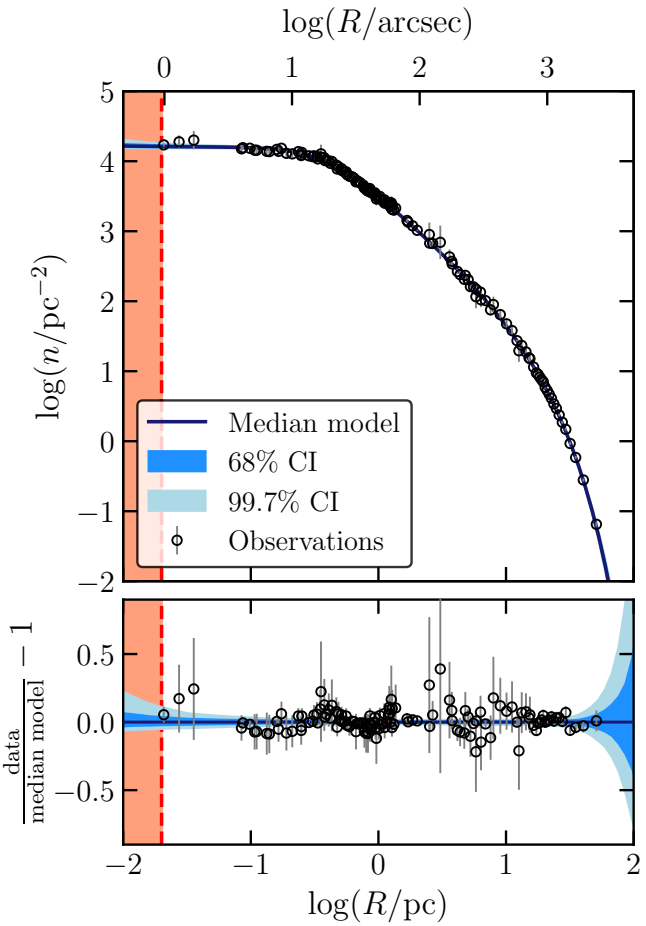

FIGURE 8.4: Surface number density as a function of the projected distance from the cluster center. Observations are shown as black points (with 1σ error bars), whereas the model is shown in blue. The 68% and 99.7% CIs are also shown as shaded areas. The vertical dashed line represents the 3σ upper limit (0.02 pc) on the BH $R_{\rm infl}$.

compared (see figure 8.5) our model with measurements of the projected velocity anisotropy

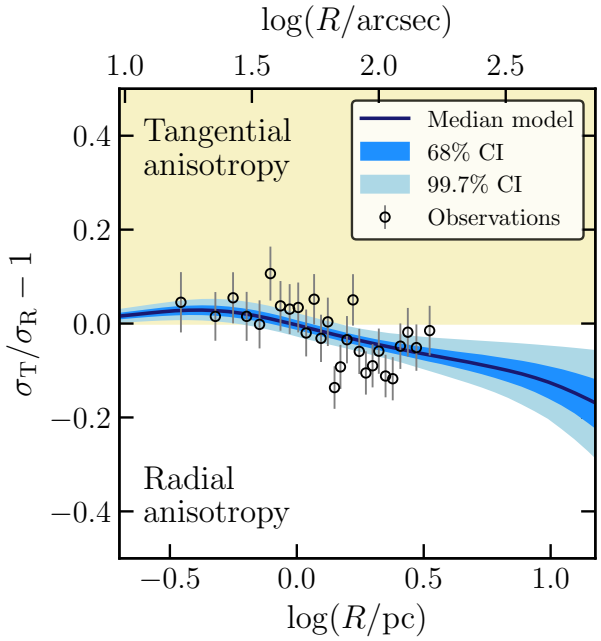

FIGURE 8.5: Projected velocity anisotropy. Positive values of the anisotropy parameter correspond to tangential anisotropy, whereas negative ones to radial anisotropy. The median model is shown in blue and the corresponding CIs are shown as shaded areas. The black points are observational data from Libralato et al. (2022) with 1σ error bars.

(data from Libralato et al., 2022), defined as $\sigma_T/\sigma_R - 1$, with σ_R and σ_T the radial and tangential velocity dispersion components, respectively (see equation 8.9). Figure 8.5 shows that our model can reproduce the system velocity anisotropy remarkably well also compared to previous studies (see e.g., Dickson et al., 2023).

8.4 Comparisons with previous works

Our result is in tension with some previous studies claiming the presence of a massive IMBH in 47 Tucanae (see e.g., Kızıltan et al., 2017; Mann et al., 2020). In this section, we delve into the possible reasons for such discrepancies.

Kızıltan et al. (2017) used spin-down measurements for nineteen MSPs identified in 47 Tucanae. Comparing acceleration data with N-body simulations, they found evidence for a massive central BH with mass $M_{BH} = 2300^{+1500}_{-850}$ $M_\odot$. While a direct comparison with the study of Kızıltan et al. (2017) is not straightforward, as different dynamical models and data were used, we note that it is in general hard to perform a large exploration of possible initial conditions using N-body simulations. Dynamical models of equilibrium, on the other hand, allow us to perform a systematic exploration of the parameter space. In addition, in our model-data comparison, we fit simultaneously the spatial distribution and the full velocity distribution using individual stars, while Kızıltan et al. (2017) analyzed only those N-body simulations that better reproduced the density profile and the LOS velocity dispersion, which may not be representative of the full cluster kinematics.

However, as a further check, we verified whether our best-fit model is able to reproduce the measurements of MSPs. Figure 8.6 shows the cluster LOS acceleration data from the MSP sample (data from Ridolfi et al., 2016, and Freire et al. 2017) used by Kızıltan

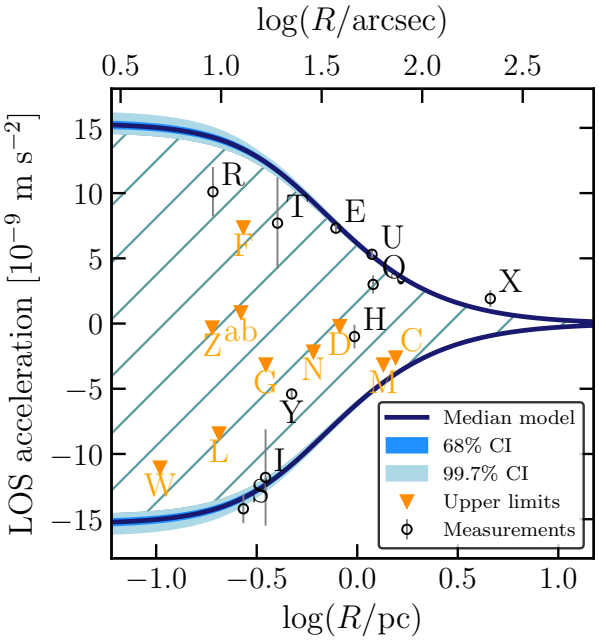

FIGURE 8.6: LOS acceleration as a function of the projected distance from the center of 47 Tucanae. Black points are measurements, while orange ones are upper limits. Both were obtained from pulsars (data from Ridolfi et al., 2016; Freire et al., 2017). The label of each pulsar is shown either in orange or black. The blue line shows the maximum (if positive) and minimum (if negative) LOS acceleration allowed by our dynamical model at a given distance from the center. Similarly, the 68% and 99.7% CIs on the maximum and minimum LOS acceleration are shown as shaded areas. The hatched area is the allowed LOS acceleration space.

et al. (2017), as well as the maximum and minimum LOS acceleration allowed by our dynamical model. This quantity was computed as the maximum projection along the LOS of the radial acceleration, $a(r)$, at any given projected distance from the center, R, namely, $\max\left(a(r)\sqrt{1-(R/r)^2}\right)\forall r \geq R$. Interestingly, our model is compatible with all the upper limits and also with the central pulsars showing the highest accelerations (such as 47 Tuc-E, 47 Tuc-U, 47 Tuc-I, and 47 Tuc-S) without the need for an IMBH more massive than 578 $M_\odot$ (at the 3σ level). The only outlier might be 47 Tuc-X, still compatible within 2σ with the median model.

Using dynamical models based on the Jeans equations coupled with PM data of the cluster center from *HST*, Mann et al. (2020) found that a massive IMBH with mass $808 - 4610$ $M_\odot$ is required to explain the central kinematics. While employing the same dataset would be the best approach to understand the possible reasons that lead to a discrepancy, we note that the work of Mann et al. (2020) focused on reproducing the system velocity dispersion. On the contrary, our DF-based models and individual-star approach (see Appendix 8.6.1) make the most of the kinematic sample, since it does not condense the kinematic information into few radial bins. Instead, our approach is to model, in a continuous way, the full shape of the cluster's velocity distribution in the center. This approach provides more stringent constraints on the presence of a putative massive dark component in the center (see Pascale et al., 2019). Furthermore, we also used LOS data to probe the 3D kinematics.

Finally, we note that our result is consistent with the findings of McLaughlin et al. (2006) and Hénault-Brunet et al. (2020). Using *HST* data and Jeans modeling, McLaughlin et al. (2006) put an upper limit of about 1578 $M_\odot$ at the 1σ level, compatible with the much more stringent upper limit set by this study (578 $M_\odot$ at 3σ). Moreover, Hénault-Brunet et al. (2020) constrained the overall mass budget in dark remnants (stellar-mass BH, neutron stars, and white dwarfs) possibly harbored at the center of 47 Tucanae. The upper limit set by

the current work is consistent with the mass budget of $M_{\rm remnant} = 430^{+386}_{-301}$ $M_\odot$ found by Hénault-Brunet et al. (2020). Although our analysis only considers a point-like central mass, such as an IMBH, the upper limit on the central mass we have found would also apply to an extended spherical central object.

8.5 Summary and conclusions

In this work, we address the problem of the presence of a putative IMBH at the center of the GC 47 Tucanae, using dynamical models based on DFs depending on the action integrals. We modeled state-of-the-art data providing information on the spatial distribution, along with both the LOS and on-sky kinematics up to the very central regions of the cluster. Also, we employed a star-by-star approach in the central region to fully exploit the data and model the full shape of the velocity distribution. According to our analysis, we ruled out (at the 3σ level) the presence of a dark central component more massive than 578 $M_\odot$. To date, this is the most stringent upper limit that has been set in 47 Tucanae by any dynamical study. While this result is consistent with other studies (e.g., McLaughlin et al., 2006; Hénault-Brunet et al., 2020), it is in tension with those studies claiming the detection of an IMBH in 47 Tucanae (see e.g., Mann et al., 2020; Kızıltan et al., 2017). Despite the very stringent upper limit we set in this study, more sophisticated dynamical models and novel data with greater precision would shed further light on the nature of a putative central dark component in 47 Tucanae, as well as in other GCs. For instance, multi-mass modeling would allow us to account for stellar evolution and mass segregation (Gieles & Zocchi, 2015).

From the point of view of the data, more extensive coverage of the central regions and progressively better-defined cluster centers and distances would certainly provide more robust results. Future facilities, such as the Extremely Large Telescope, will measure the stellar kinematics of GC centers with unprecedented accuracy, likely providing new and exciting data for this area of research.

Finally, we note that the methodology presented in this work could be applied to any GC in our Galaxy, regardless of the particular data available, whether pertaining to either PMs or LOS velocities only or full 3D kinematic information, as done in the present study. In addition, this approach is not limited to GCs and could be also used to explore the presence of central BHs in external galaxies (Pascale et al. in preparation).

8.6 Supplementary material

8.6.1 Model and data comparison

We inferred the model's free parameters in a Bayesian framework. In particular, this was done by defining the vector of 11 free parameters $\boldsymbol{\theta} \equiv \{\log M_{\rm GC}, \log J_0, \zeta, \Gamma, B, g_z, h_z, \log J_{\rm cut}, \alpha, \log M_{\rm BH}, m\}$, namely the nine DF parameters (see equation 8.1), the logarithm of the IMBH mass ($\log M_{\rm BH}$), and the normalization factor of the density profile (m). Thus, we can express the posterior distribution as

$$p(\boldsymbol{\theta}|\boldsymbol{D}) \propto p(\boldsymbol{\theta})\, p(\boldsymbol{D}|\boldsymbol{\theta})\,, \tag{8.10}$$

where $\boldsymbol{D}$ is the data vector, including both the kinematic sample and the surface density profile. The $p(\boldsymbol{\theta})$ and $p(\boldsymbol{D}|\boldsymbol{\theta}) \equiv \mathcal{L}(\boldsymbol{D})$ terms on the right-hand side of the equation are, respectively, the prior on the free parameters and the likelihood.

Assuming that all the data sets are independent of each other, we decompose the logarithm of the likelihood into the sum of the different terms

$$\ln \mathcal{L}(\boldsymbol{D}) = \ln \mathcal{L}_v + \ln \mathcal{L}_{\sigma_{\rm R}} + \ln \mathcal{L}_{\sigma_{\rm T}} + \ln \mathcal{L}_{\sigma_{\rm LOS}} + \ln \mathcal{L}_n \,. \tag{8.11}$$

We stress that for the cluster central region, we adopt a star-by-star approach modeling the velocity and error of each of the $N_{\rm stars}$ stars. The resulting likelihood is

$$\ln \mathcal{L}_v \equiv \sum_{j=1}^{N_{\rm stars}} \ln \mathcal{F}(\boldsymbol{v}_j | R_j\, \boldsymbol{e}_j) \,, \tag{8.12}$$

where $\mathcal{F} \equiv \mathcal{V} * \mathcal{N}$. Therefore, for each star j, the velocity distribution ($\mathcal{V}$, see equations 8.6 through 8.8, computed at the observed projected distance, R_j) is convolved ($*$) with observational errors, represented by a zero-mean, multivariate Gaussian ($\mathcal{N}$). The Gaussian covariance matrix has diagonal elements equal to the errors squared, $\boldsymbol{e}_j^2$, and zero off-diagonal terms. The resulting function is evaluated at the observed velocity ($\boldsymbol{v}_j$). When the full kinematic information (PM and LOS velocity) is not available for the j-th star, we marginalize over the missing velocity components (see equations 8.7, and 8.8).

For the velocity dispersions outside the central 12″, we define

$$\ln \mathcal{L}_{\sigma_i} \equiv -\frac{1}{2} \sum_{k=1}^{N_{\rm bin,\,i}} \frac{(\sigma_{i,\,k} - \sigma_i(R_k))^2}{\delta\sigma_{i,\,k}^2} \quad i \in \{\rm R, T, LOS\} \,, \tag{8.13}$$

with $\sigma_{i,\,k}$ being the velocity dispersion of the i-th component in the k-th radial bin (centered in $R_{\rm k}$), $\delta\sigma_{i,\,k}$ the corresponding error, and $\sigma_i(R_k)$ the model prediction. Also, $N_{\rm bin,\,i}$ is the total number of bins in which the velocity dispersion was obtained. Similarly, for the density profile, we have

$$\ln \mathcal{L}_n \equiv -\frac{1}{2} \sum_{l=1}^{N_{\rm prof}} \frac{(n_l - n(R_l))^2}{\delta n_l^2} \,, \tag{8.14}$$

where $n_{\rm l}$, $\delta n_{\rm l}$, and $N_{\rm prof}$ are the observed number density, the corresponding error, and the number of bins of the surface density profile, respectively.

All the physical quantities of the model are self-consistently computed from the DF (see section 8.1.3). For all the parameters, we assumed uniform priors (table 8.1 for the specific prior ranges adopted). In particular, for the IMBH mass, we adopted a lower limit of 10 $\rm M_\odot$, well below the nominal definition of IMBH. Also, a less massive BH would have $R_{\rm infl} < 10^{-3}$ pc, with a negligible impact on observables. We explored the free-parameter space by means of a MCMC algorithm, using the `emcee` Python package (Foreman-Mackey et al., 2013). The algorithm was run with 112 walkers for about 7000 steps each. We used a mixture of moves developed by ter Braak & Vrugt (2008), and Nelson et al. (2014) to achieve a more efficient exploration of the parameter space. For each walker, we discarded the first 2500 steps to account for the initial convergence phase, while exploring the prior. Afterward,

we accounted for the correlation between subsequent samples, taking one sample every 100. Finally, we obtained about 5000 independent posterior samples. In figure 8.7, we show the corner plot with both the marginalized posterior distributions (diagonal panels) and 2D joint distributions (lower-diagonal panels).

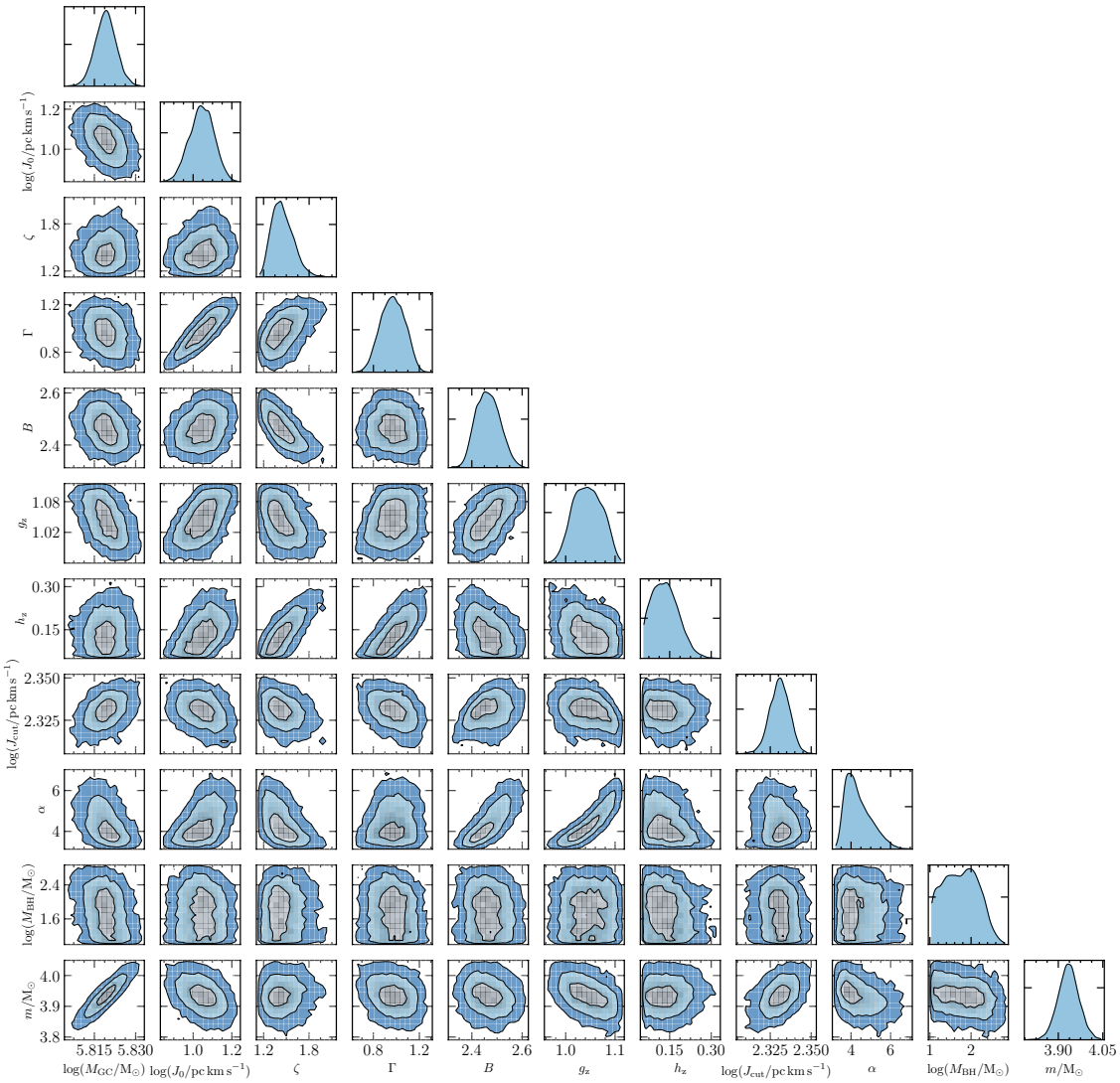

FIGURE 8.7: 1D (diagonal panels) and 2D (lower-diagonal panels) marginalized, posterior distributions over the model's free parameters. See section 8.1 for a description of the parameters. Prior ranges, median values, 68%, and 99.7% CIs for each parameter are reported in table 8.1.

In table 8.1, we list the parameter prior ranges and the posterior values from the MCMC fitting. For each model free parameter, we report the median value, as well as the 68% (1σ) and 99.7% (3σ) CIs, computed from posterior samples. We note that all the free parameters are well constrained within the prior ranges. This indicates that the adopted intervals were well suited for a thorough exploration of the free-parameters space and there is no evidence for any need to extend these ranges.

TABLE 8.1: Free parameters of the model.

Parameter	Prior range	Posterior		
		Median	68% CI	99.7% CI
$\log(M_{\rm GC}/{\rm M}_\odot)$	[5.0; 7.0]	5.819	[5.815; 5.823]	[5.807; 5.831]
$\log(J_0/{\rm pc\,km\,s^{-1}})$	[0.3; 1.5]	1.05	[0.98; 1.11]	[0.87; 1.2]
ζ	[0.5; 5.0]	1.43	[1.31; 1.59]	[1.15; 1.96]
Γ	[0.0; 2.0]	0.97	[0.86; 1.08]	[0.69; 1.22]
B	[1.0; 4.0]	2.46	[2.42; 2.51]	[2.32; 2.6]
$g_{\rm z}$	[0.05; 1.45]	1.04	[1.01; 1.08]	[0.97; 1.11]
$h_{\rm z}$	[0.05; 1.45]	0.13	[0.08; 0.18]	[0.05; 0.29]
$\log(J_{\rm cut}/{\rm pc\,km\,s^{-1}})$	[1.5; 3.0]	2.331	[2.325; 2.337]	[2.311; 2.348]
α	[2.0; 10.0]	4.23	[3.75; 5.04]	[3.27; 6.55]
$\log(M_{\rm BH}/{\rm M}_\odot)$	[1.0; 5.5]	1.74	[1.27; 2.19]	[1.0; 2.76]
$m/{\rm M}_\odot$	[2.0; 7.0]	3.93	[3.9; 3.97]	[3.83; 4.04]

Notes. The central column shows the adopted prior ranges in each parameter. The rightmost columns report the median values, the 68%, and 99.7% CIs of the posterior distributions. We note that the 3σ lower limit on the IMBH mass coincides with the lower boundary of the prior (10 $\rm M_\odot$).

Part IV

Conclusions

Chapter 9

Final remarks

" 'cause it not too late, it's never too late"
Never too late,
Three Days Grace

9.1 Thesis summary and conclusions

It is widely accepted that most (70%-90%) stars form in groups, clusters, or hierarchies, and spend some time gravitationally bound with their siblings when still embedded in their progenitor molecular cloud. Most of such systems will be disrupted in their first few million years of existence, due to mechanisms possibly involving gas loss driven or encounters with GMCs. Nonetheless, a fraction of proto-clusters will survive the embedded phase and remain bound over longer timescales. In the Milky Way, this evidence comes from the clustered structure of the disk and the similar star formation rates observed in embedded clusters and the field. On a larger scale, this indication is supported by the good agreement between the mass density in stellar clusters and the average co-moving stellar density at the peak of the universal star formation density at redshift ~ 2.

The implications of clustered star formation touch a wide range of astrophysical disciplines: from the star formation process and the effectiveness of gas-expulsion as a mechanism for cluster disruption to the fundamental properties of young star clusters.

Star clusters are tracers of intense star formation episodes across cosmic time and rich cradles of stellar-mass BHs which are prime gravitational wave sources. They are also important witnesses of the epoch of cosmic reionization, of the dark matter's role in forming the first structures and its present-day distribution in galaxies. Finally, star clusters potentially trace the assembly process of galaxies in a cosmological context. Major star-forming episodes in galaxies are typically accompanied by significant star cluster formation, and their main properties are thus strictly linked with those of their hosts, making them valuable probes across a wide range of disciplines in astronomy from cosmology to stellar evolution.

However, a major limitation hampers the full exploitation of star clusters: we have a yet crude understanding of their formation and early evolution. Star cluster formation is indeed a multi-scale, multi-physics process: star clusters emerge from GMCs whose formation and evolution are regulated by galactic scale processes and dynamics, while, at the other side of the scale ladder, star formation is set by turbulence-driven, small-scale density enhancements.

In the local Universe, studies of the early phases of cluster formation have been limited due to the lack of adequate observations, in particular at infrared wavelengths. Also, only

recently we have started to observe proto, massive star cluster candidates at high-redshift in gravitationally lensed galaxies thanks to *JWST* observations. Similarly, simulations of star cluster formation in cosmological contexts that account for star formation and internal stellar dynamics are well beyond reach even with modern computational facilities.

In this thesis, we tackle open questions about cluster formation and evolution using stellar kinematics and a rigorous combination of observations and simulations as key *modus operandi*. The thesis complementary traces and follows *i)* the early phases of cluster formation, survival, and evolution by focusing on the properties of young stellar clusters, and *ii)* the long-term evolution of massive clusters with particular attention on the role of massive compact objects, such as BHs. The main thesis results can be schematically summarized as follows.

Concerning the cluster's formation and early evolution, we first investigated the internal dynamical state of virtually all known young (< 300 Myr) star clusters, focussing, in particular, on their expansion. Thanks to the introduction of a simple, yet informative, parameter (i.e., the ratio between the mean radial velocity and the velocity dispersion, $\langle v_{\rm R} \rangle / \sigma_{\rm R}$) **we were able for the first time to constrain the fraction of expanding clusters as a function of their age and thus the typical time scale in which star clusters undergo expansion**, which we find to be $\simeq 30$ Myr (Della Croce et al., 2024b, presented in Chapter 3). Older systems likely survived this phase and are evolving toward equilibrium.

We then **found evidence of possibly the second massive hierarchical system in the Milky Way: LISCA II .** LISCA II is a large ($\simeq 150$ pc) hierarchical structure encompassing nine young star clusters embedded in a more diffuse stellar halo (the total mass of the system is estimated in the range $0.6 - 1.2 \times 10^5$ $M_\odot$). The detection of such structure allowed us to characterize in great detail the process of hierarchical cluster formation (thanks to *Gaia* and high-resolution spectroscopic data). The system shows prominent out-of-equilibrium dynamics, mass segregation on both local and global scales, and mass-dependent dynamics. Such observations are consistent with tailored numerical simulations performed by our group following the violent relaxation of hierarchical systems (Della Croce et al., 2023, see Chapter 4).

We also comprehensively studied the complex hosting LISCA II (together with the other hierarchical structure LISCA I , see Dalessandro et al. 2021b). First, we studied the kinematics of the extremely young (~ 5 Myr) star clusters in the star-forming W345 region, some of which are still partially embedded in the gas. We also explored the YSO kinematics, offering the intriguing chance to trace the parent gas kinematics. Finally, we could follow the evolution of the Perseus complex and assess its formation conditions thanks to the 6D information available for star clusters while accounting for spiral arms and bar perturbations of the Galactic potential (Della Croce et al. 2025, submitted to A&A, see Chapter 5).

To possibly constrain the formation conditions of present-day GCs we investigated the internal kinematical differences among MPs in Galactic GCs. **For the first time, we constrained the rotational properties of MPs using 3D kinematics for a representative sample**

of Galactic GCs. Our results are consistent with SP stars forming more centrally concentrated and rapidly rotating than FP ones, adding another (possible key) piece to the complex puzzle of MP formation and evolution (see Chapter 6 as part of the study by Dalessandro et al., 2024).

On the long-term evolution of massive stellar systems, we first studied the role of a population of BHs within massive stellar systems by means of Monte Carlo simulations. **We addressed the degeneracies in inferring the present-day population of BHs harbored in Galactic GCs, proving that stellar kinematics coupled with a multi-diagnostic approach is key in breaking such degeneracies.** We also tested our predictions against observations finding that we still lack the precision and sample size necessary to firmly disentangle between multiple interpretations. Nonetheless, our results provide guidelines for future observational campaigns and studies (Della Croce et al., 2024c, and Chapter 7).

Finally, we delved into the debated topic of the presence of an IMBH within 47 tuc. **We put a stringent upper limit ($< 578\ M_\odot$) on the total dark mass possibly hiding at the center of NGC 104** through novel dynamical models constrained against central 3D kinematics on a star-to-star basis (Della Croce et al., 2024a, discussed in Chapter 8). Our results rule out the possibility of a massive IMBH (as claimed by Kızıltan et al., 2017) leaving though room for lower BH masses. Interestingly, our results are consistent with more recent studies (e.g., Smith et al., 2024).

9.2 Future instruments

Young star cluster observations are mainly limited to gas-free configurations when studying their internal kinematics. While *Gaia* has been instrumental in many recent developments of cluster early evolution, it is practically blind to embedded clusters and highly obscured regions due to foreground extinction (e.g., the Galactic bulge). To overcome these limitations a new mission is being proposed to ESA, *GaiaNIR* (Hobbs et al., 2021). The mission proposes *Gaia*-like instrumentation but in the NIR, thus allowing the study of embedded cluster kinematics. This would be particularly relevant for the work presented in Chapter 3, as we could observe only the consequences of gas expulsion, instead of probing it while in place.

Complementary to future astrometric missions, upcoming spectroscopic surveys, like *WEAVE* (Jin et al., 2024), *4MOST* (de Jong et al., 2012), *MOONS* (Cirasuolo et al., 2011), and *WST* (Mainieri et al., 2024), will further enlarge the sample of stars with known LOS velocity allowing for 3D kinematic studies of star clusters and star-forming regions, and disentangling projection effects. Besides kinematic information, chemical abundances will be thoroughly available, probing possible chemical gradients in star-forming regions. Within this context, we will further study the LISCA I, and LISCA II systems using *WEAVE* GTO observations, which would provide us with LOS velocities and chemical abundances for thousands of stars belonging both to star clusters and their surrounding halo.

Looking at GCs, the *Roman* space telescope (WFIRST Astrometry Working Group et al., 2019) will provide invaluable data to study their internal kinematics. Combining ground-based-like FoV and *HST*-like astrometry, most Galactic GCs will fit into a single observation, and internal kinematics for lower mass stars could be obtained (for instance to study

equipartition effects). On the spectroscopic side, the *BlueMUSE* spectrograph (Richard et al., 2019) is being built at VLT complementing *MUSE* observations on the blue side (350 − 600 nm) of the optical spectrum. *BlueMUSE* will extend investigations of MPs from red giants to main sequence stars, strongly increasing the number of accessible stars. The higher spectral resolution (on average 3600) secured by the bluer spectral range will also improve the LOS precision. Finally, looking ahead, the *Etremely Large Telescope* will probe deeper into GC centers to look for stellar-mass BH populations and IMBHs in Galactic GCs, possibly shedding light on this long-standing quest.

9.3 Future projects

In this last section of the thesis, we would like to provide a quick overview of future projects on cluster formation and evolution that will be pursued.

9.3.1 Probing rotation in young clusters

Several processes could contribute to imprint a coherent rotational motion in star clusters: *i)* the primordial gas cloud rotation could be inherited by the nascent star cluster (as argued from extra-galactic gas clouds rotation, e.g., Braine et al. 2020); *ii)* dynamical friction within dark matter haloes characterized by asymmetric velocity distributions could lead to an increase in the cluster angular momentum over time (Moreno et al., 2022); *iii)* stars escape through the Lagrangian points of the cluster-host galaxy system. This process is intrinsically asymmetric and may result in rotational signatures in the clusters (Jerabkova et al., 2021; Kroupa et al., 2022); *iv)* tidal interactions between stellar clumps originating from the same gas cloud or flybys (Piatti & Malhan, 2022) could induce rotation.

Internal cluster rotation is therefore a key process in cluster evolution. Also, as presented in Chapter 6, rotational signatures could provide us with novel insights into the formation of GCs. Rotational patterns were observed in both embedded clusters (e.g., Hénault-Brunet et al., 2012), and several Galactic GCs (e.g., Anderson & King, 2003; van de Ven et al., 2006; Bellini et al., 2017; Bianchini et al., 2018; Kamann et al., 2018; Sollima et al., 2019; Vasiliev & Baumgardt, 2021; Szigeti et al., 2021b; Dalessandro et al., 2024). However, the evolution of rotation in OCs remains largely unexplored due to the lack of precise kinematic data (either PM or LOS velocities) for a large sample of cluster members. Recently, Guilherme-Garcia et al. (2023); Jadhav et al. (2024) carried out large explorations of the OC internal kinematics attempting to trace rotation. In particular, Guilherme-Garcia et al. (2023) applied a vector field reconstruction algorithm to PM data from *Gaia*, while Jadhav et al. (2024) used *Gaia* in synergy with LOS velocity measurements (collected from *Gaia* RVS and the homogenized collection by Tsantaki et al. 2022). The combination of PM and LOS velocity measurements allows us to break the degeneracy between rotation amplitude and the inclination of the rotation axis (see discussion in Jadhav et al., 2024). Despite recent efforts though, these studies struggled to identify rotation in Galactic OCs and provided a list of candidate rotating clusters (besides a list of rotators). This suggests that further investigations are necessary to firmly confirm or reject those clusters as rotating. To this aim, we are expanding the study presented in Chapter 3 to internal cluster rotation. In particular, we are testing the use of the same diagnostic adopted in Chapter 6 to trace rotation also in younger systems, given the

promising results obtained for GCs. We will study internal rotation in virtually all known clusters in the Galaxy and adopt different membership catalogs (e.g., Hunt & Reffert 2023, 2024; Della Croce et al. 2024b) to assess the possible impact of different compilations. In this context, we already extended the preliminary work on cluster members presented in Chapter 3 to all clusters known in the Galaxy. Our results will be first compared with previous studies that identified rotating OCs (e.g., Guilherme-Garcia et al., 2023; Jadhav et al., 2024). Then, we shall focus on the candidate rotating clusters. Finally, on a broader view, we will explore several aspects linked to cluster rotation: *i)* the possible evolution of rotational amplitude with cluster age and the link with the cluster dynamical state and age; *ii)* the connection between cluster spin (and spin axis) with its position and orbit within the Galaxy; *iii)* finally, the evolution of putative peculiar clusters could be explored through numerical simulations.

9.3.2 The search for hierarchical structures in the Galaxy

The fraction of star clusters forming bound pairs, groups or, more in general, hierarchical structures is a long-standing question. Cluster pairs or groups with higher multiplicity could form in several ways (de la Fuente Marcos & de la Fuente Marcos, 2009): *i)* many star clusters could form out of the same molecular cloud. Those clusters likely share similar positions and velocities and have similar ages and chemical compositions. Also, they may be the result of clump mergers and suffer tidal interactions from nearby stellar clumps; *ii)* massive stars in young star clusters are expected to shape the surrounding left-over gas through radiative feedback, winds, and ultimately supernova. These processes likely compress the gas, possibly triggering star formation (Brown et al., 1995). In the so-called sequential scenario, clusters are expected to have small age differences and possibly different chemical compositions due to the enrichment process of massive stars; *iii)* van den Bergh (1996) suggested that star cluster binaries could form due to tidal captures. In this case, the clusters are not necessarily formed within the same cloud and may have very different properties (see e.g., Piatti & Malhan 2022); *iv)* finally, orbital resonances due to non-axisymmetric perturbations (such as spiral arms or the bar) produce overdensities in the phase-space possibly trapping star clusters (Dehnen, 1998; De Simone et al., 2004; Quillen & Minchev, 2005; Chakrabarty, 2007). Resonantly trapped clusters would have similar phase-space properties but likely different chemical compositions and ages.

Several studies searched for star cluster pairs and groups in past years adopting different datasets and approaches. Table 9.1 summarizes the results of these previous works (adapted from Palma et al. 2025). In particular, a critical leap forward in the field was enabled by precise cluster distances and LOS velocities.

Despite the number of studies, the link between the cluster aggregates (regardless of whether they form a pair or group) and the surrounding Galactic environment is largely unexplored, although theoretical studies showed that the Galactic tidal field has a major role in determining the system survival chances (Priyatikanto et al., 2016). Also, the presence of surrounding stellar halos was investigated only in the LISCA I (Dalessandro et al. 2021b, but see also Zhong et al. 2019 for an earlier investigation on the pair NGC 869, NGC 884) and LISCA II (Della Croce et al., 2023) systems. In a future study, we thus plan to improve the search for candidate cluster binary systems and groups accounting for the tidal boundary set by the Galaxy in which these systems orbit. We will then compare with previous detections,

TABLE 9.1: Summary of the results from previous studies on the search of cluster binary and group candidates (adapted from Palma et al. 2025)

Reference	# binary systems	# groups
Pavlovskaya & Filippova (1989)	–	5
Subramaniam et al. (1995)	18	–
de la Fuente Marcos & de la Fuente Marcos (2009)	43	–
Conrad et al. (2017)	14	5
Soubiran et al. (2018)	8	4
Liu & Pang (2019)	39	16
Zhong et al. (2019)	1	–
Piecka & Paunzen (2021)	50	10
Casado (2021b)	11	11
Casado (2021a)	1	–
Angelo et al. (2022)	5	2
Song et al. (2022)	14	–
Palma et al. (2025)	617	261

Notes. The first column provides the reference to the study while the other two columns briefly summarize the results concerning the numbers of candidate cluster binaries and groups in the Galaxy.

refining and possibly extending the catalog. The presence of a diffuse stellar halo that is co-moving and shares similar properties with the clusters will be a matter of investigation for all the candidate systems (as previously done for the LISCAs, Dalessandro et al. 2021b; Della Croce et al. 2023). Such a study would likely provide us with a more complete picture of the formation of multiple cluster systems together with the chance to study the role of the Galaxy in their evolution.

9.3.3 Cluster formation and evolution: from high-z to the local Universe

The last project aims to investigate the possible evolutionary links between the old GCs in the local Universe and the high-redshift (z) massive cluster candidates recently observed by *JWST* (e.g., Vanzella et al. 2023a,c; Adamo et al. 2024). Indeed, while local massive clusters could provide insights into the formation mechanisms and dynamical history of old GCs, their different formation environment likely plays a role in the early dynamical evolution of proto-GCs (e.g., Kruijssen, 2015; Krumholz et al., 2019; Li & Gnedin, 2019).

Recent studies have shown that in the first Gyr of their evolution, GCs evolve in a much stronger (and highly time-varying) tidal field than that experienced later in their evolution (e.g., Li & Gnedin, 2019; Keller et al., 2020). Such a strong and lively tidal field significantly impacts the early dynamical evolution of GCs, possibly leading to their complete dissolution.

While these studies pointed out the central role of the strong tidal field at high redshift, tailored numerical simulations, accounting for the interplay between internal dynamical processes and the external tidal field, are required to properly assess the cluster survival along with the dynamical and structural responses of the nascent GC to the tidal field.

Such an ambitious project requires combining high-resolution, zoom-in cosmological simulations (e.g., those already performed by Calura et al. 2022) with direct N-body simulations accounting for stellar interactions. The former would allow us to model the cosmological environment in which the cluster is forming, while the latter accounts for internal dynamical interactions and the cluster response to the time-dependent tidal field. Also, other physical processes such as stellar evolution, formation of binaries, initial fractal configurations, and left-over gas expulsion could be accounted for. Including all these elements will produce the physical conditions closest to the formation environments and conditions ever simulated so far for GCs.

This simulation set would thus allow us to address several timely questions: *i)* the co-evolution between the host galaxy and the proto-GCs; *ii)* the fraction of proto-GCs surviving these initial lively phases and *iii)* the role of cosmological tidal fields in shaping the cluster internal dynamics and structure; *iv)* the interplay between the lively tidal field and the degree of sub-structures and their evolution.

Finally, we plan to investigate the long-term evolution of the emerging cluster properties until the present day. We will study the evolution of structural (e.g., Lagrangian radii, concentration parameters, total mass, and density), and dynamical (e.g., velocity dispersion, equipartition, and anisotropy) properties through Monte Carlo simulations, thus building a comprehensive catalog of cluster present-day properties starting from the proto-GC ones. This will ultimately yield the connection between high-z *JWST* observations of proto-GC and local, old ones.

Bibliography

Aarseth S. J., 1963, "Dynamical evolution of clusters of galaxies, I" MNRAS, 126, 223

Aarseth S. J., 2003, Gravitational N-Body Simulations, by Sverre J. Aarseth. Cambridge University Press, November, Cambridge, UK

Aarseth S. J., 2012, "Mergers and ejections of black holes in globular clusters" MNRAS, 422, 841 (arXiv:1202.4688)

Aarseth S. J., Heggie D. C., 1998, "Basic N-body modelling of the evolution of globular clusters - I. Time scaling" MNRAS, 297, 794 (arXiv:astro-ph/9805344)

Abbate F., Possenti A., Ridolfi A., Freire P. C. C., Camilo F., Manchester R. N., D'Amico N., 2018, "Internal gas models and central black hole in 47 Tucanae using millisecond pulsars" MNRAS, 481, 627 (arXiv:1808.06621)

Abbott B. P., et al., 2016, "Binary Black Hole Mergers in the First Advanced LIGO Observing Run" Physical Review X, 6, 041015 (arXiv:1606.04856)

Abbott R., et al., 2020, "GW190521: A Binary Black Hole Merger with a Total Mass of 150 $M_\odot$" Phys. Rev. Lett., 125, 101102 (arXiv:2009.01075)

Abel T., Bryan G. L., Norman M. L., 2002, "The Formation of the First Star in the Universe" Science, 295, 93 (arXiv:astro-ph/0112088)

Adamo A., et al., 2020, "Star Clusters Near and Far; Tracing Star Formation Across Cosmic Time" Space Sci. Rev., 216, 69 (arXiv:2005.06188)

Adamo A., et al., 2024, "Bound star clusters observed in a lensed galaxy 460 Myr after the Big Bang" Nature, 632, 513 (arXiv:2401.03224)

Adams F. C., Lada C. J., Shu F. H., 1987, "Spectral Evolution of Young Stellar Objects" ApJ, 312, 788

Alessandrini E., Lanzoni B., Ferraro F. R., Miocchi P., Vesperini E., 2016, "Investigating the Mass Segregation Process in Globular Clusters with Blue Straggler Stars: The Impact of Dark Remnants" ApJ, 833, 252 (arXiv:1610.04562)

Alessi B. S., Moitinho A., Dias W. S., 2003, "Searching for unknown open clusters in the Tycho-2 catalog" A&A, 410, 565 (arXiv:astro-ph/0309232)

Allen L. E., et al., 2004, "Infrared Array Camera (IRAC) Colors of Young Stellar Objects" ApJS, 154, 363

Allison R. J., Goodwin S. P., Parker R. J., de Grijs R., Portegies Zwart S. F., Kouwenhoven M. B. N., 2009, "Dynamical Mass Segregation on a Very Short Timescale" ApJ, 700, L99 (arXiv:0906.4806)

Almeida A., Monteiro H., Dias W. S., 2023, "Revisiting the mass of open clusters with Gaia data" MNRAS, 525, 2315 (arXiv:2307.15182)

Anderson J., King I. R., 2003, "The Rotation of the Globular Cluster 47 Tucanae in the Plane of the Sky" AJ, 126, 772

Anderson J., et al., 2008, "The Acs Survey of Globular Clusters. V. Generating a Comprehensive Star Catalog for each Cluster" AJ, 135, 2055 (arXiv:0804.2025)

Andrews J. J., Kalogera V., 2022, "Constraining Black Hole Natal Kicks with Astrometric Microlensing" ApJ, 930, 159 (arXiv:2203.15156)

Angelo M. S., Santos J. F. C., Maia F. F. S., Corradi W. J. B., 2022, "Investigating Galactic binary cluster candidates with Gaia EDR3" MNRAS, 510, 5695 (arXiv:2112.15247)

Antoja T., et al., 2018, "A dynamically young and perturbed Milky Way disk" Nature, 561, 360 (arXiv:1804.10196)

Antonini F., Rasio F. A., 2016, "Merging Black Hole Binaries in Galactic Nuclei: Implications for Advanced-LIGO Detections" ApJ, 831, 187 (arXiv:1606.04889)

Antonov V. A., 1962, Solution of the problem of stability of stellar system Emden's density law and the spherical distribution of velocities

Arca Sedda M., Askar A., Giersz M., 2018, "MOCCA-Survey Database - I. Unravelling black hole subsystems in globular clusters" MNRAS, 479, 4652 (arXiv:1801.00795)

Arca Sedda M., Kamlah A. W. H., Spurzem R., Rizzuto F. P., Naab T., Giersz M., Berczik P., 2023, "The DRAGON-II simulations - II. Formation mechanisms, mass, and spin of intermediate-mass black holes in star clusters with up to 1 million stars" MNRAS, 526, 429 (arXiv:2307.04806)

Arca Sedda M., et al., 2024a, "The DRAGON-II simulations - I. Evolution of single and binary compact objects in star clusters with up to 1 million stars" MNRAS, 528, 5119 (arXiv:2307.04805)

Arca Sedda M., Kamlah A. W. H., Spurzem R., Rizzuto F. P., Giersz M., Naab T., Berczik P., 2024b, "The DRAGON-II simulations - III. Compact binary mergers in clusters with up to 1 million stars: mass, spin, eccentricity, merger rate, and pair instability supernovae rate" MNRAS, 528, 5140 (arXiv:2307.04807)

Armstrong J. J., Wright N. J., Jeffries R. D., Jackson R. J., 2020, "The dynamics of the γ Vel cluster and nearby Vela OB2 association" MNRAS, 494, 4794 (arXiv:2003.14209)

Armstrong J. J., Wright N. J., Jeffries R. D., Jackson R. J., Cantat-Gaudin T., 2022, "The structure and 3D kinematics of vela OB2" MNRAS, 517, 5704 (arXiv:2208.05277)

Aros F. I., Vesperini E., 2023, "Effects of massive central objects on the degree of energy equipartition of globular clusters" MNRAS, 525, 3136 (arXiv:2308.03845)
Arsenault R., et al., 2008, in Hubin N., Max C. E., Wizinowich P. L., eds, Society of Photo-Optical Instrumentation Engineers (SPIE) Conference Series Vol. 7015, Adaptive Optics Systems. p. 701524, doi:10.1117/12.790359
Askar A., Szkudlarek M., Gondek-Rosińska D., Giersz M., Bulik T., 2017, "MOCCA-SURVEY Database - I. Coalescing binary black holes originating from globular clusters" MNRAS, 464, L36 (arXiv:1608.02520)
Askar A., Arca Sedda M., Giersz M., 2018, "MOCCA-SURVEY Database I: Galactic globular clusters harbouring a black hole subsystem" MNRAS, 478, 1844 (arXiv:1802.05284)
Askar A., Askar A., Pasquato M., Giersz M., 2019, "Finding black holes with black boxes - using machine learning to identify globular clusters with black hole subsystems" MNRAS, 485, 5345 (arXiv:1811.06473)
Audit E., Hennebelle P., 2005, "Thermal condensation in a turbulent atomic hydrogen flow" A&A, 433, 1 (arXiv:astro-ph/0410062)
Bañados E., et al., 2018, "An 800-million-solar-mass black hole in a significantly neutral Universe at a redshift of 7.5" Nature, 553, 473 (arXiv:1712.01860)
Baba J., Morokuma-Matsui K., Miyamoto Y., Egusa F., Kuno N., 2016, "Gas velocity patterns in simulated galaxies: observational diagnostics of spiral structure theories" MNRAS, 460, 2472 (arXiv:1604.06879)
Bacon R., et al., 2010, in McLean I. S., Ramsay S. K., Takami H., eds, Society of Photo-Optical Instrumentation Engineers (SPIE) Conference Series Vol. 7735, Ground-based and Airborne Instrumentation for Astronomy III. p. 773508 (arXiv:2211.16795), doi:10.1117/12.856027
Ballesteros-Paredes J., Klessen R. S., Mac Low M. M., Vazquez-Semadeni E., 2007, in Reipurth B., Jewitt D., Keil K., eds, Protostars and Planets V. p. 63 (arXiv:astro-ph/0603357), doi:10.48550/arXiv.astro-ph/0603357
Ballone A., Mapelli M., Di Carlo U. N., Torniamenti S., Spera M., Rastello S., 2020, "Evolution of fractality and rotation in embedded star clusters" MNRAS, 496, 49 (arXiv:2001.10003)
Bally J., 2016, "Protostellar Outflows" ARA&A, 54, 491
Banerjee S., Kroupa P., 2013, "Did the Infant R136 and NGC 3603 Clusters Undergo Residual Gas Expulsion?" ApJ, 764, 29 (arXiv:1301.3491)
Banerjee S., Kroupa P., 2014, "A Perfect Starburst Cluster made in One Go: The NGC 3603 Young Cluster" ApJ, 787, 158 (arXiv:1403.4601)
Banerjee S., Kroupa P., 2015, "The formation of NGC 3603 young starburst cluster: 'prompt' hierarchical assembly or monolithic starburst?" MNRAS, 447, 728 (arXiv:1412.1473)
Banerjee R., Vázquez-Semadeni E., Hennebelle P., Klessen R. S., 2009, "Clump morphology and evolution in MHD simulations of molecular cloud formation" MNRAS, 398, 1082 (arXiv:0808.0986)
Banerjee S., Baumgardt H., Kroupa P., 2010, "Stellar-mass black holes in star clusters: implications for gravitational wave radiation" MNRAS, 402, 371 (arXiv:0910.3954)
Bastian N., Lardo C., 2018, "Multiple Stellar Populations in Globular Clusters" ARA&A, 56, 83 (arXiv:1712.01286)
Bastian N., Ercolano B., Gieles M., Rosolowsky E., Scheepmaker R. A., Gutermuth R., Efremov Y., 2007, "Hierarchical star formation in M33: fundamental properties of the star-forming regions" MNRAS, 379, 1302 (arXiv:0706.0495)
Bastian N., et al., 2011, "Evidence for environmentally dependent cluster disruption in M83" MNRAS, 417, L6 (arXiv:1106.2427)
Bastian N., Lamers H. J. G. L. M., de Mink S. E., Longmore S. N., Goodwin S. P., Gieles M., 2013, "Early disc accretion as the origin of abundance anomalies in globular clusters" MNRAS, 436, 2398 (arXiv:1309.3566)
Baumgardt H., Hilker M., 2018, "A catalogue of masses, structural parameters, and velocity dispersion profiles of 112 Milky Way globular clusters" MNRAS, 478, 1520 (arXiv:1804.08359)
Baumgardt H., Kroupa P., 2007, "A comprehensive set of simulations studying the influence of gas expulsion on star cluster evolution" MNRAS, 380, 1589 (arXiv:0707.1944)
Baumgardt H., Makino J., 2003, "Dynamical evolution of star clusters in tidal fields" MNRAS, 340, 227 (arXiv:astro-ph/0211471)
Baumgardt H., Vasiliev E., 2021, "Accurate distances to Galactic globular clusters through a combination of Gaia EDR3, HST, and literature data" MNRAS, 505, 5957 (arXiv:2105.09526)
Baumgardt H., Hut P., Heggie D. C., 2002, "Long-term evolution of isolated N-body systems" MNRAS, 336, 1069 (arXiv:astro-ph/0206258)
Baumgardt H., Hilker M., Sollima A., Bellini A., 2019, "Mean proper motions, space orbits, and velocity dispersion profiles of Galactic globular clusters derived from Gaia DR2 data" MNRAS, 482, 5138 (arXiv:1811.01507)
Baumgardt H., Sollima A., Hilker M., 2020, "Absolute V-band magnitudes and mass-to-light ratios of Galactic globular clusters" PASA, 37, e046 (arXiv:2009.09611)
Becker W., Fenkart R., 1971, "A catalogue of galactic star clusters observed in three colours" A&AS, 4, 241
Bekki K., 2010, "Rotation and Multiple Stellar Population in Globular Clusters" ApJ, 724, L99 (arXiv:1010.3841)
Bekki K., 2011, "Secondary star formation within massive star clusters: origin of multiple stellar populations in globular clusters" MNRAS, 412, 2241 (arXiv:1011.5956)
Belczynski K., Kalogera V., Bulik T., 2002, "A Comprehensive Study of Binary Compact Objects as Gravitational Wave Sources: Evolutionary Channels, Rates, and Physical Properties" ApJ, 572, 407 (arXiv:astro-ph/0111452)
Bellazzini M., Bragaglia A., Carretta E., Gratton R. G., Lucatello S., Catanzaro G., Leone F., 2012, "Na-O anticorrelation and HB. IX. Kinematics of the program clusters A link between systemic rotation and HB morphology?" A&A, 538, A18 (arXiv:1111.2688)

Bellini A., et al., 2015, "The Hubble Space Telescope UV Legacy Survey of Galactic Globular Clusters: The Internal Kinematics of the Multiple Stellar Populations in NGC 2808" ApJ, 810, L13 (arXiv:1508.01804)
Bellini A., Bianchini P., Varri A. L., Anderson J., Piotto G., van der Marel R. P., Vesperini E., Watkins L. L., 2017, "Hubble Space Telescope Proper Motion (HSTPROMO) Catalogs of Galactic Globular Clusters. V. The Rapid Rotation of 47 Tuc Traced and Modeled in Three Dimensions" ApJ, 844, 167 (arXiv:1706.08974)
Bennett M., Bovy J., 2021, "Did Sgr cause the vertical waves in the solar neighbourhood?" MNRAS, 503, 376 (arXiv:2010.04165)
Bergin E. A., Tafalla M., 2007, "Cold Dark Clouds: The Initial Conditions for Star Formation" ARA&A, 45, 339 (arXiv:0705.3765)
Bertoldi F., 1989, "The Photoevaporation of Interstellar Clouds. I. Radiation-driven Implosion" ApJ, 346, 735
Bertoldi F., McKee C. F., 1990, "The Photoevaporation of Interstellar Clouds. II. Equilibrium Cometary Clouds" ApJ, 354, 529
Bhat B., Lanzoni B., Vesperini E., Ferraro F. R., Aros F. I., Askar A., Hypki A., 2024, "New Parameters for Star Cluster Dynamics: The Role of Clusters' Initial Conditions" ApJ, 968, 2 (arXiv:2404.06992)
Bianchini P., Varri A. L., Bertin G., Zocchi A., 2013, "Rotating Globular Clusters" ApJ, 772, 67 (arXiv:1305.6025)
Bianchini P., van de Ven G., Norris M. A., Schinnerer E., Varri A. L., 2016, "A novel look at energy equipartition in globular clusters" MNRAS, 458, 3644 (arXiv:1603.00878)
Bianchini P., van der Marel R. P., del Pino A., Watkins L. L., Bellini A., Fardal M. A., Libralato M., Sills A., 2018, "The internal rotation of globular clusters revealed by Gaia DR2" MNRAS, 481, 2125 (arXiv:1806.02580)
Binney J., Piffl T., 2015, "The distribution function of the Galaxy's dark halo" MNRAS, 454, 3653 (arXiv:1509.06877)
Binney J., Tremaine S., 2008a, Galactic Dynamics: Second Edition
Binney J., Tremaine S., 2008b, Galactic Dynamics: Second Edition. Princeton University Press, Princeton, NJ
Bland-Hawthorn J., et al., 2019, "The GALAH survey and Gaia DR2: dissecting the stellar disc's phase space by age, action, chemistry, and location" MNRAS, 486, 1167 (arXiv:1809.02658)
Blitz L., 1993, in Levy E. H., Lunine J. I., eds, Protostars and Planets III. p. 125
Boberg O. M., Vesperini E., Friel E. D., Tiongco M. A., Varri A. L., 2017, "Internal Rotation in the Globular Cluster M53" ApJ, 841, 114
Bobylev V. V., Bajkova A. T., 2014, "The Milky Way spiral structure parameters from data on masers and selected open clusters" MNRAS, 437, 1549 (arXiv:1310.3974)
Bobylev V. V., Bajkova A. T., 2023, "Determination of the Spiral Pattern Speed in the Milky Way from Young Open Star Clusters" Astronomy Letters, 49, 320 (arXiv:2309.12097)
Boley A. C., Lake G., Read J., Teyssier R., 2009, "Globular Cluster Formation Within a Cosmological Context" ApJ, 706, L192 (arXiv:0908.1254)
Bonnell I. A., Bate M. R., Clarke C. J., Pringle J. E., 2001, "Competitive accretion in embedded stellar clusters" MNRAS, 323, 785 (arXiv:astro-ph/0102074)
Bonnell I. A., Bate M. R., Vine S. G., 2003, "The hierarchical formation of a stellar cluster" MNRAS, 343, 413 (arXiv:astro-ph/0305082)
Bontemps S., Motte F., Csengeri T., Schneider N., 2010, "Fragmentation and mass segregation in the massive dense cores of Cygnus X" A&A, 524, A18 (arXiv:0909.2315)
Bossini D., et al., 2019, "Age determination for 269 Gaia DR2 open clusters" A&A, 623, A108 (arXiv:1901.04733)
Bottema R., 2003, "Simulations of normal spiral galaxies" MNRAS, 344, 358 (arXiv:astro-ph/0303257)
Bovy J., Hogg D. W., Roweis S. T., 2011, "Extreme deconvolution: Inferring complete distribution functions from noisy, heterogeneous and incomplete observations" Annals of Applied Statistics, 5, 1657 (arXiv:0905.2979)
Bragaglia A., Carretta E., D'Orazi V., Sollima A., Donati P., Gratton R. G., Lucatello S., 2017, "NGC 6535: the lowest mass Milky Way globular cluster with a Na-O anti-correlation? Cluster mass and age in the multiple population context" A&A, 607, A44 (arXiv:1708.07705)
Braine J., Hughes A., Rosolowsky E., Gratier P., Colombo D., Meidt S., Schinnerer E., 2020, "Rotation of molecular clouds in M 51" A&A, 633, A17 (arXiv:1911.08977)
Bravi L., et al., 2018, "The Gaia-ESO Survey: a kinematical and dynamical study of four young open clusters" A&A, 615, A37 (arXiv:1803.01908)
Breen P. G., Heggie D. C., 2013, "Dynamical evolution of black hole subsystems in idealized star clusters" MNRAS, 432, 2779 (arXiv:1304.3401)
Bressan A., Marigo P., Girardi L., Salasnich B., Dal Cero C., Rubele S., Nanni A., 2012, "PARSEC: stellar tracks and isochrones with the PAdova and TRieste Stellar Evolution Code" MNRAS, 427, 127 (arXiv:1208.4498)
Bressert E., et al., 2010, "The spatial distribution of star formation in the solar neighbourhood: do all stars form in dense clusters?" MNRAS, 409, L54 (arXiv:1009.1150)
Briley M. M., Harbeck D., Smith G. H., Grebel E. K., 2004, "On the Carbon and Nitrogen Abundances of 47 Tucanae's Main-Sequence Stars" AJ, 127, 1588 (arXiv:astro-ph/0312316)
Brinkmann N., Banerjee S., Motwani B., Kroupa P., 2017, "The bound fraction of young star clusters" A&A, 600, A49 (arXiv:1611.05871)
Brodie J. P., Strader J., 2006, "Extragalactic Globular Clusters and Galaxy Formation" ARA&A, 44, 193 (arXiv:astro-ph/0602601)
Bromm V., Coppi P. S., Larson R. B., 2002, "The Formation of the First Stars. I. The Primordial Star-forming Cloud" ApJ, 564, 23 (arXiv:astro-ph/0102503)

Brown A. G. A., 2021, "Microarcsecond Astrometry: Science Highlights from Gaia" ARA&A, 59, 59 (arXiv:2102.11712)
Brown A. G. A., Hartmann D., Burton W. B., 1995, "The Orion OB1 association. II. The Orion-Eridanus Bubble." A&A, 300, 903 (arXiv:astro-ph/9503016)
Buckner A. S. M., et al., 2020, "The spatial evolution of young massive clusters. II. Looking for imprints of star formation in NGC 2264 with Gaia DR2" A&A, 636, A80 (arXiv:2002.12673)
Cadelano M., Saracino S., Dalessandro E., Ferraro F. R., Lanzoni B., Massari D., Pallanca C., Salaris M., 2020, "Digging for Relics of the Past: The Ancient and Obscured Bulge Globular Cluster NGC 6256" ApJ, 895, 54 (arXiv:2004.06131)
Cadelano M., Dalessandro E., Salaris M., Bastian N., Mucciarelli A., Saracino S., Martocchia S., Cabrera-Ziri I., 2022, "Expanding the Time Domain of Multiple Populations: Evidence of Nitrogen Variations in the 1.5 Gyr Old Star Cluster NGC 1783" ApJ, 924, L2 (arXiv:2112.06964)
Cadelano M., et al., 2023, "JWST uncovers helium and water abundance variations in the bulge globular cluster NGC 6440" A&A, 679, L13 (arXiv:2310.13056)
Calura F., D'Ercole A., Vesperini E., Vanzella E., Sollima A., 2019, "Formation of second-generation stars in globular clusters" MNRAS, 489, 3269 (arXiv:1906.09137)
Calura F., et al., 2022, "Sub-parsec resolution cosmological simulations of star-forming clumps at high redshift with feedback of individual stars" MNRAS, 516, 5914 (arXiv:2206.13538)
Cannon R. D., Croke B. F. W., Bell R. A., Hesser J. E., Stathakis R. A., 1998, "Carbon and nitrogen abundance variations on the main sequence of 47 Tucanae" MNRAS, 298, 601
Cantat-Gaudin T., 2022, "Milky Way Star Clusters and Gaia: A Review of the Ongoing Revolution" Universe, 8, 111
Cantat-Gaudin T., Anders F., 2020, "Clusters and mirages: cataloguing stellar aggregates in the Milky Way" A&A, 633, A99 (arXiv:1911.07075)
Cantat-Gaudin T., et al., 2018, "A Gaia DR2 view of the open cluster population in the Milky Way" A&A, 618, A93 (arXiv:1805.08726)
Cantat-Gaudin T., Mapelli M., Balaguer-Núñez L., Jordi C., Sacco G., Vallenari A., 2019a, "A ring in a shell: the large-scale 6D structure of the Vela OB2 complex" A&A, 621, A115 (arXiv:1808.00573)
Cantat-Gaudin T., et al., 2019b, "Gaia DR2 unravels incompleteness of nearby cluster population: new open clusters in the direction of Perseus" A&A, 624, A126 (arXiv:1810.05494)
Cantat-Gaudin T., et al., 2019c, "Expanding associations in the Vela-Puppis region. 3D structure and kinematics of the young population" A&A, 626, A17 (arXiv:1812.08114)
Cantat-Gaudin T., et al., 2020, "Painting a portrait of the Galactic disc with its stellar clusters" A&A, 640, A1 (arXiv:2004.07274)
Cantat-Gaudin T., et al., 2023, "An empirical model of the Gaia DR3 selection function" A&A, 669, A55 (arXiv:2208.09335)
Cappellari M., Copin Y., 2003, "Adaptive spatial binning of integral-field spectroscopic data using Voronoi tessellations" MNRAS, 342, 345 (arXiv:astro-ph/0302262)
Cardelli J. A., Clayton G. C., Mathis J. S., 1989, "The Relationship between Infrared, Optical, and Ultraviolet Extinction" ApJ, 345, 245
Carnerero M. I., et al., 2023, "Gaia Data Release 3. The first Gaia catalogue of variable AGN" A&A, 674, A24 (arXiv:2207.06849)
Carpenter J. M., Heyer M. H., Snell R. L., 2000, "Embedded Stellar Clusters in the W3/W4/W5 Molecular Cloud Complex" ApJS, 130, 381 (arXiv:astro-ph/0005237)
Carretta E., Bragaglia A., Gratton R., et al., 2009 A&A, 505, 139
Cartwright A., Whitworth A. P., 2004, "The statistical analysis of star clusters" MNRAS, 348, 589 (arXiv:astro-ph/0403474)
Casado J., 2021a, "New open clusters found by manual mining of data based on Gaia DR2" Research in Astronomy and Astrophysics, 21, 117 (arXiv:2009.04751)
Casado J., 2021b, "The List of Possible Double and Multiple Open Clusters between Galactic Longitudes 240º and 270º" Astronomy Reports, 65, 755 (arXiv:2107.12036)
Casamiquela L., et al., 2021, "Abundance-age relations with red clump stars in open clusters" A&A, 652, A25 (arXiv:2103.14692)
Casertano S., Hut P., 1985, "Core radius and density measurements in N-body experiments Connections with theoretical and observational definitions" ApJ, 298, 80
Castro-Ginard A., Jordi C., Luri X., Julbe F., Morvan M., Balaguer-Núñez L., Cantat-Gaudin T., 2018, "A new method for unveiling open clusters in Gaia. New nearby open clusters confirmed by DR2" A&A, 618, A59 (arXiv:1805.03045)
Castro-Ginard A., Jordi C., Luri X., Cantat-Gaudin T., Balaguer-Núñez L., 2019, "Hunting for open clusters in Gaia DR2: the Galactic anticentre" A&A, 627, A35 (arXiv:1905.06161)
Castro-Ginard A., et al., 2020, "Hunting for open clusters in Gaia DR2: 582 new open clusters in the Galactic disc" A&A, 635, A45 (arXiv:2001.07122)
Castro-Ginard A., et al., 2021, "Milky Way spiral arms from open clusters in Gaia EDR3" A&A, 652, A162 (arXiv:2105.04590)
Castro-Ginard A., et al., 2022, "Hunting for open clusters in Gaia EDR3: 628 new open clusters found with OCfinder" A&A, 661, A118 (arXiv:2111.01819)

Cautun M., et al., 2020, "The milky way total mass profile as inferred from Gaia DR2" MNRAS, 494, 4291 (arXiv:1911.04557)
Cavallo L., et al., 2024, "Parameter Estimation for Open Clusters using an Artificial Neural Network with a QuadTree-based Feature Extractor" AJ, 167, 12 (arXiv:2311.03009)
Chakrabarty D., 2007, "Phase space structure in the solar neighbourhood" A&A, 467, 145 (arXiv:astro-ph/0703242)
Chambers K. C., et al., 2016, "The Pan-STARRS1 Surveys" arXiv e-prints, p. arXiv:1612.05560 (arXiv:1612.05560)
Chandar R., Whitmore B. C., Calzetti D., Di Nino D., Kennicutt R. C., Regan M., Schinnerer E., 2011, "New Constraints on Mass-dependent Disruption of Star Clusters in M51" ApJ, 727, 88 (arXiv:1101.2869)
Chandrasekhar S., 1969, "The Instability of the Congruent Darwin Ellipsoids" ApJ, 157, 1419
Chatterjee S., Umbreit S., Fregeau J. M., Rasio F. A., 2013, "Understanding the dynamical state of globular clusters: core-collapsed versus non-core-collapsed" MNRAS, 429, 2881 (arXiv:1207.3063)
Chauhan N., Ogura K., Pandey A. K., Samal M. R., Bhatt B. C., 2011a, "Stars at the Tip of Peculiar Elephant Trunk-Like Clouds in IC 1848E: A Possible Third Mechanism of Triggered Star Formation" PASJ, 63, 795 (arXiv:1107.3358)
Chauhan N., Pandey A. K., Ogura K., Jose J., Ojha D. K., Samal M. R., Mito H., 2011b, "Star formation in bright-rimmed clouds and clusters associated with the W5 E H II region" MNRAS, 415, 1202 (arXiv:1103.3396)
Chernoff D. F., Shapiro S. L., 1987, "Globular Cluster Evolution in the Galaxy: A Global View" ApJ, 322, 113
Chernoff D. F., Weinberg M. D., 1990, "Evolution of Globular Clusters in the Galaxy" ApJ, 351, 121
Chernoff D. F., Kochanek C. S., Shapiro S. L., 1986, "Tidal Heating of Globular Clusters" ApJ, 309, 183
Chevance M., et al., 2016, "A milestone toward understanding PDR properties in the extreme environment of LMC-30 Doradus" A&A, 590, A36 (arXiv:1603.03573)
Chevance M., et al., 2020, "The CO-dark molecular gas mass in 30 Doradus" MNRAS, 494, 5279 (arXiv:2004.09516)
Chomiuk L., Strader J., Maccarone T. J., Miller-Jones J. C. A., Heinke C., Noyola E., Seth A. C., Ransom S., 2013, "A Radio-selected Black Hole X-Ray Binary Candidate in the Milky Way Globular Cluster M62" ApJ, 777, 69 (arXiv:1306.6624)
Chung C., Yoon S.-J., Lee Y.-W., 2011, "The Effect of Helium-enhanced Stellar Populations on the Ultraviolet-upturn Phenomenon of Early-type Galaxies" ApJ, 740, L45 (arXiv:1109.3463)
Cirasuolo M., Afonso J., Bender R., Bonifacio P., Evans C., Kaper L., Oliva E., Vanzi L., 2011, "MOONS: The Multi-Object Optical and Near-infrared Spectrograph" The Messenger, 145, 11
Combes F., Leon S., Meylan G., 1999, "N-body simulations of globular cluster tides" A&A, 352, 149 (arXiv:astro-ph/9910148)
Conrad C., et al., 2017, "A RAVE investigation on Galactic open clusters . II. Open cluster pairs, groups and complexes" A&A, 600, A106
Cordero M. J., Hénault-Brunet V., Pilachowski C. A., Balbinot E., Johnson C. I., Varri A. L., 2017, "Differences in the rotational properties of multiple stellar populations in M13: a faster rotation for the 'extreme' chemical subpopulation" MNRAS, 465, 3515 (arXiv:1610.09374)
Cordoni G., Milone A. P., Mastrobuono-Battisti A., Marino A. F., Lagioia E. P., Tailo M., Baumgardt H., Hilker M., 2020, "Three-component Kinematics of Multiple Stellar Populations in Globular Clusters with Gaia and VLT" ApJ, 889, 18 (arXiv:1905.09908)
Cosentino R., et al., 2014, in Ramsay S. K., McLean I. S., Takami H., eds, Society of Photo-Optical Instrumentation Engineers (SPIE) Conference Series Vol. 9147, Ground-based and Airborne Instrumentation for Astronomy V. p. 91478C, doi:10.1117/12.2055813
Cournoyer-Cloutier C., Karam J., Sills A., Portegies Zwart S., Wilhelm M., 2024a, "Binary Disruption and Ejected Stars from Hierarchical Star Cluster Assembly" arXiv e-prints, p. arXiv:2409.13564 (arXiv:2409.13564)
Cournoyer-Cloutier C., et al., 2024b, "Massive Star Cluster Formation with Binaries. I. Evolution of Binary Populations" arXiv e-prints, p. arXiv:2410.07433 (arXiv:2410.07433)
Cox D. P., Gómez G. C., 2002, "Analytical Expressions for Spiral Arm Gravitational Potential and Density" ApJS, 142, 261 (arXiv:astro-ph/0207635)
Crowther P. A., et al., 2016, "The R136 star cluster dissected with Hubble Space Telescope/STIS. I. Far-ultraviolet spectroscopic census and the origin of He II λ1640 in young star clusters" MNRAS, 458, 624 (arXiv:1603.04994)
Cunha K., et al., 2016, "Chemical abundance gradients from open clusters in the Milky Way disk: Results from the APOGEE survey" Astronomische Nachrichten, 337, 922 (arXiv:1601.03099)
Curran P. A., 2015, MCSpearman: Monte Carlo error analyses of Spearman's rank test
Cutri R. M., et al., 2013, Explanatory Supplement to the AllWISE Data Release Products, Explanatory Supplement to the AllWISE Data Release Products, by R. M. Cutri et al.
Cutri R. M., et al., 2021, VizieR Online Data Catalog: AllWISE Data Release (Cutri+ 2013), VizieR On-line Data Catalog: II/328. Originally published in: IPAC/Caltech (2013)
D'Antona F., Vesperini E., D'Ercole A., Ventura P., Milone A. P., Marino A. F., Tailo M., 2016, "A single model for the variety of multiple-population formation(s) in globular clusters: a temporal sequence" MNRAS, 458, 2122 (arXiv:1602.05412)
D'Ercole A., Vesperini E., D'Antona F., McMillan S. L. W., Recchi S., 2008, "Formation and dynamical evolution of multiple stellar generations in globular clusters" MNRAS, 391, 825 (arXiv:0809.1438)

Da Rio N., et al., 2017, "IN-SYNC. V. Stellar Kinematics and Dynamics in the Orion A Molecular Cloud" ApJ, 845, 105 (arXiv:1702.04113)
Dale J. E., 2015, "The modelling of feedback in star formation simulations" New A Rev., 68, 1 (arXiv:1508.06054)
Dale J. E., Bonnell I., 2011, "Ionizing feedback from massive stars in massive clusters: fake bubbles and untriggered star formation" MNRAS, 414, 321 (arXiv:1103.1532)
Dalessandro E., Salaris M., Ferraro F. R., Cassisi S., Lanzoni B., Rood R. T., Fusi Pecci F., Sabbi E., 2011, "The peculiar horizontal branch of NGC 2808" MNRAS, 410, 694 (arXiv:1008.4478)
Dalessandro E., et al., 2013, "Double Blue Straggler Sequences in Globular Clusters: The Case of NGC 362" ApJ, 778, 135 (arXiv:1310.2389)
Dalessandro E., et al., 2014, "First Evidence of Fully Spatially Mixed First and Second Generations in Globular Clusters: The Case of NGC 6362" ApJ, 791, L4 (arXiv:1407.0484)
Dalessandro E., Ferraro F. R., Massari D., Lanzoni B., Miocchi P., Beccari G., 2015, "No Evidence of Mass Segregation in the Low-mass Galactic Globular Cluster NGC 6101" ApJ, 810, 40 (arXiv:1507.04776)
Dalessandro E., Lapenna E., Mucciarelli A., Origlia L., Ferraro F. R., Lanzoni B., 2016, "Multiple Populations in the Old and Massive Small Magellanic Cloud Globular Cluster NGC 121" ApJ, 829, 77 (arXiv:1607.05736)
Dalessandro E., et al., 2018a, "IC 4499 revised: Spectro-photometric evidence of small light-element variations" A&A, 618, A131 (arXiv:1807.07618)
Dalessandro E., et al., 2018b, "The Peculiar Radial Distribution of Multiple Populations in the Massive Globular Cluster M80" ApJ, 859, 15 (arXiv:1804.03222)
Dalessandro E., et al., 2018c, "The Unexpected Kinematics of Multiple Populations in NGC 6362: Do Binaries Play a Role?" ApJ, 864, 33 (arXiv:1807.07918)
Dalessandro E., et al., 2019, "A Family Picture: Tracing the Dynamical Path of the Structural Properties of Multiple Populations in Globular Clusters" ApJ, 884, L24 (arXiv:1910.00613)
Dalessandro E., Raso S., Kamann S., Bellazzini M., Vesperini E., Bellini A., Beccari G., 2021a, "3D core kinematics of NGC 6362: central rotation in a dynamically evolved globular cluster" MNRAS, 506, 813 (arXiv:2105.02246)
Dalessandro E., et al., 2021b, "First Phase Space Portrait of a Hierarchical Stellar Structure in the Milky Way" ApJ, 909, 90 (arXiv:2101.04133)
Dalessandro E., et al., 2024, "A 3D view of multiple populations kinematics in Galactic globular clusters" arXiv e-prints, p. arXiv:2409.03827 (arXiv:2409.03827)
Damiani F., Prisinzano L., Pillitteri I., Micela G., Sciortino S., 2019, "Stellar population of Sco OB2 revealed by Gaia DR2 data" A&A, 623, A112 (arXiv:1807.11884)
Danielski C., Babusiaux C., Ruiz-Dern L., Sartoretti P., Arenou F., 2018, "The empirical Gaia G-band extinction coefficient" A&A, 614, A19 (arXiv:1802.01670)
De Simone R., Wu X., Tremaine S., 2004, "The stellar velocity distribution in the solar neighbourhood" MNRAS, 350, 627 (arXiv:astro-ph/0310906)
Decressin T., Meynet G., Charbonnel C., Prantzos N., Ekström S., 2007, "Fast rotating massive stars and the origin of the abundance patterns in galactic globular clusters" A&A, 464, 1029 (arXiv:astro-ph/0611379)
Deharveng L., et al., 2012, "Interstellar matter and star formation in W5-E. A Herschel view" A&A, 546, A74 (arXiv:1209.2907)
Dehnen W., 1998, "The Distribution of Nearby Stars in Velocity Space Inferred from HIPPARCOS Data" AJ, 115, 2384 (arXiv:astro-ph/9803110)
Dehnen W., Odenkirchen M., Grebel E. K., Rix H.-W., 2004, "Modeling the Disruption of the Globular Cluster Palomar 5 by Galactic Tides" AJ, 127, 2753 (arXiv:astro-ph/0401422)
Delbo' M., Gayon-Markt J., Busso G., Brown A., Galluccio L., Ordenovic C., Bendjoya P., Tanga P., 2012, "Asteroid spectroscopy with Gaia" Planet. Space Sci., 73, 86
Della Croce A., et al., 2023, "Ongoing hierarchical massive cluster assembly: The LISCA II structure in the Perseus complex" A&A, 674, A93 (arXiv:2303.15501)
Della Croce A., Pascale R., Giunchi E., Nipoti C., Cignoni M., Dalessandro E., 2024a, "The most stringent upper limit set on the mass of a central black hole in 47 Tucanae using dynamical models" A&A, 682, A22 (arXiv:2310.15221)
Della Croce A., Dalessandro E., Livernois A., Vesperini E., 2024b, "Young, wild, and free: The early expansion of star clusters" A&A, 683, A10
Della Croce A., Aros F. I., Vesperini E., Dalessandro E., Lanzoni B., Ferraro F. R., Bhat B., 2024c, "Inference of black-hole mass fraction in Galactic globular clusters: A multi-dimensional approach to break the initial-condition degeneracies" A&A, 690, A179 (arXiv:2409.01400)
Dias W. S., Lépine J. R. D., Alessi B. S., 2002, "Proper motions of open clusters based on the TYCHO2 Catalogue. II. Clusters farther than 1 kpc" A&A, 388, 168
Dias W. S., Monteiro H., Lépine J. R. D., Barros D. A., 2019, "The spiral pattern rotation speed of the Galaxy and the corotation radius with Gaia DR2" MNRAS, 486, 5726 (arXiv:1905.08133)
Dias W. S., Monteiro H., Moitinho A., Lépine J. R. D., Carraro G., Paunzen E., Alessi B., Villela L., 2021, "Updated parameters of 1743 open clusters based on Gaia DR2" MNRAS, 504, 356 (arXiv:2103.12829)
Dickson N., Hénault-Brunet V., Baumgardt H., Gieles M., Smith P. J., 2023, "Multimass modelling of Milky Way globular clusters - I. Implications on their stellar initial mass function above 1 $M_\odot$" MNRAS, 522, 5320 (arXiv:2303.01637)

Dickson N., Smith P. J., Hénault-Brunet V., Gieles M., Baumgardt H., 2024, "Multimass modelling of milky way globular clusters - II. Present-day black hole populations" MNRAS, 529, 331 (arXiv:2308.13037)
Dinnbier F., Kroupa P., 2020a, "Tidal tails of open star clusters as probes of early gas expulsion. I. A semi-analytic model" A&A, 640, A84 (arXiv:2006.14087)
Dinnbier F., Kroupa P., 2020b, "Tidal tails of open star clusters as probes to early gas expulsion. II. Predictions for Gaia" A&A, 640, A85 (arXiv:2007.00036)
Dinnbier F., Kroupa P., Anderson R. I., 2022, "Do the majority of stars form as gravitationally unbound?" A&A, 660, A61 (arXiv:2201.06582)
Dobbs C., Baba J., 2014, "Dawes Review 4: Spiral Structures in Disc Galaxies" PASA, 31, e035 (arXiv:1407.5062)
Donor J., et al., 2020, "The Open Cluster Chemical Abundances and Mapping Survey. IV. Abundances for 128 Open Clusters Using SDSS/APOGEE DR16" AJ, 159, 199 (arXiv:2002.08980)
Dorval J., Boily C. M., Moraux E., Roos O., 2017, "Wide- and contact-binary formation in substructured young stellar clusters" MNRAS, 465, 2198
Dotter A., et al., 2010, "The ACS Survey of Galactic Globular Clusters. IX. Horizontal Branch Morphology and the Second Parameter Phenomenon" ApJ, 708, 698 (arXiv:0911.2469)
Drimmel R., et al., 2023, "A new resonance-like feature in the outer disc of the Milky Way" A&A, 670, A10 (arXiv:2207.12977)
Eadie G. M., Harris W. E., Widrow L. M., 2015, "Estimating the Galactic Mass Profile in the Presence of Incomplete Data" ApJ, 806, 54 (arXiv:1503.07176)
Einsel C., Spurzem R., 1999, "Dynamical evolution of rotating stellar systems - I. Pre-collapse, equal-mass system" MNRAS, 302, 81
El-Badry K., 2024, "On the formation of a 33 solar-mass black hole in a low-metallicity binary" The Open Journal of Astrophysics, 7, 38 (arXiv:2404.13047)
Elmegreen B. G., 1983, "Quiescent formation of bound galactic clusters." MNRAS, 203, 1011
Elmegreen B. G., Falgarone E., 1996, "A Fractal Origin for the Mass Spectrum of Interstellar Clouds" ApJ, 471, 816
Elmegreen B. G., Hunter D. A., 2010, "On the Disruption of Star Clusters in a Hierarchical Interstellar Medium" ApJ, 712, 604 (arXiv:1002.2823)
Elson R., Hut P., Inagaki S., 1987, "Dynamical evolution of globular clusters." ARA&A, 25, 565
Erkal D., Koposov S. E., Belokurov V., 2017, "A sharper view of Pal 5's tails: discovery of stream perturbations with a novel non-parametric technique" MNRAS, 470, 60 (arXiv:1609.01282)
Ernst A., Just A., Spurzem R., 2009, "On the dissolution of star clusters in the Galactic Centre - I. Circular orbits" MNRAS, 399, 141 (arXiv:0906.4459)
Evans N. W., Oh S., 2022, "Mass segregation in the hyades cluster" MNRAS, 512, 3846 (arXiv:2202.06973)
Evans N. W., Williams A. A., 2014, "A very simple cusped halo model" MNRAS, 443, 791 (arXiv:1406.3730)
Everall A., Boubert D., 2022, "Completeness of the Gaia verse - V. Astrometry and radial velocity sample selection functions in Gaia EDR3" MNRAS, 509, 6205 (arXiv:2111.04127)
Everall A., Boubert D., Koposov S. E., Smith L., Holl B., 2021, "Completeness of the Gaia-verse - IV. The astrometry spread function of Gaia DR2" MNRAS, 502, 1908 (arXiv:2101.01723)
Fabricius M. H., et al., 2014, "Central Rotations of Milky Way Globular Clusters" ApJ, 787, L26 (arXiv:1405.1722)
Fall S. M., Krumholz M. R., Matzner C. D., 2010, "Stellar Feedback in Molecular Clouds and its Influence on the Mass Function of Young Star Clusters" ApJ, 710, L142 (arXiv:0910.2238)
Fanelli C., Origlia L., Oliva E., Dalessandro E., Mucciarelli A., Sanna N., 2022, "Stellar population astrophysics (SPA) with the TNG. The chemical content of the red supergiant population in the Perseus complex" A&A, 660, A7 (arXiv:2112.08402)
Farias J. P., Tan J. C., 2023, "Star cluster formation from turbulent clumps - III. Across the mass spectrum" MNRAS, 523, 2083 (arXiv:2301.08997)
Farias J. P., Smith R., Fellhauer M., Goodwin S., Candlish G. N., Blaña M., Dominguez R., 2015, "The difficult early stages of embedded star clusters and the importance of the pre-gas expulsion virial ratio" MNRAS, 450, 2451 (arXiv:1504.02474)
Farias J. P., Tan J. C., Chatterjee S., 2017, "Star Cluster Formation from Turbulent Clumps. I. The Fast Formation Limit" ApJ, 838, 116 (arXiv:1701.00701)
Farias J. P., Fellhauer M., Smith R., Domínguez R., Dabringhausen J., 2018, "Gas expulsion in highly substructured embedded star clusters" MNRAS, 476, 5341 (arXiv:1803.00581)
Feigelson E. D., Townsley L. K., 2008, "The Diverse Stellar Populations of the W3 Star-forming Complex" ApJ, 673, 354 (arXiv:0710.0090)
Fellhauer M., Wilkinson M. I., Kroupa P., 2009, "Merging time-scales of stellar subclumps in young star-forming regions" MNRAS, 397, 954 (arXiv:0905.0399)
Ferraro F. R., et al., 2018a, "The Hubble Space Telescope UV Legacy Survey of Galactic Globular Clusters. XV. The Dynamical Clock: Reading Cluster Dynamical Evolution from the Segregation Level of Blue Straggler Stars" ApJ, 860, 36 (arXiv:1805.00968)
Ferraro F. R., et al., 2018b, "MIKiS: The Multi-instrument Kinematic Survey of Galactic Globular Clusters. I. Velocity Dispersion Profiles and Rotation Signals of 11 Globular Clusters" ApJ, 860, 50 (arXiv:1804.08618)
Ferraro F. R., Lanzoni B., Dalessandro E., Cadelano M., Raso S., Mucciarelli A., Beccari G., Pallanca C., 2019, "Size diversity of old Large Magellanic Cloud clusters as determined by internal dynamical evolution" Nature Astronomy, 3, 1149 (arXiv:1909.02049)

Ferraro F. R., et al., 2023a, "Fast rotating blue stragglers prefer loose clusters" Nature Communications, 14, 2584 (arXiv:2305.08478)
Ferraro F. R., Lanzoni B., Vesperini E., Cadelano M., Deras D., Pallanca C., 2023b, "Empirical Measurement of the Dynamical Ages of Three Globular Clusters and Some Considerations on the Use of the Dynamical Clock" ApJ, 950, 145 (arXiv:2304.08140)
Field G. B., 1965, "Thermal Instability." ApJ, 142, 531
Forbes D. A., et al., 2018a, "Globular cluster formation and evolution in the context of cosmological galaxy assembly: open questions" Proceedings of the Royal Society of London Series A, 474, 20170616 (arXiv:1801.05818)
Forbes D. A., Read J. I., Gieles M., Collins M. L. M., 2018b, "Extending the globular cluster system-halo mass relation to the lowest galaxy masses" MNRAS, 481, 5592 (arXiv:1809.07831)
Foreman-Mackey D., Hogg D. W., Lang D., Goodman J., 2013, "emcee: The MCMC Hammer" PASP, 125, 306 (arXiv:1202.3665)
Fragione G., Kocsis B., 2018, "Black Hole Mergers from an Evolving Population of Globular Clusters" Phys. Rev. Lett., 121, 161103 (arXiv:1806.02351)
Frank A., et al., 2014, in Beuther H., Klessen R. S., Dullemond C. P., Henning T., eds, Protostars and Planets VI. pp 451–474 (arXiv:1402.3553), doi:10.2458/azu_uapress_9780816531240-ch020
Fregeau J. M., Cheung P., Portegies Zwart S. F., Rasio F. A., 2004, "Stellar collisions during binary-binary and binary-single star interactions" MNRAS, 352, 1 (arXiv:astro-ph/0401004)
Freire P. C. C., et al., 2017, "Long-term observations of the pulsars in 47 Tucanae - II. Proper motions, accelerations and jerks" MNRAS, 471, 857 (arXiv:1706.04908)
Fujii M. S., Saitoh T. R., Portegies Zwart S. F., 2012, "The Formation of Young Dense Star Clusters through Mergers" ApJ, 753, 85 (arXiv:1205.1434)
Fujii M. S., Wang L., Tanikawa A., Hirai Y., Saitoh T. R., 2024, "Simulations predict intermediate-mass black hole formation in globular clusters" Science, 384, 1488 (arXiv:2406.06772)
Fukushige T., Heggie D. C., 1995, "Pre-collapse evolution of galactic globular clusters" MNRAS, 276, 206 (arXiv:astro-ph/9405058)
Fukushige T., Heggie D. C., 2000, "The time-scale of escape from star clusters" MNRAS, 318, 753 (arXiv:astro-ph/9910468)
GRAVITY Collaboration et al., 2019, "A geometric distance measurement to the Galactic center black hole with 0.3% uncertainty" A&A, 625, L10 (arXiv:1904.05721)
Gaia Collaboration 2016a, "The Gaia mission" A&A, 595, A1 (arXiv:1609.04153)
Gaia Collaboration 2016b, "Gaia Data Release 1. Summary of the astrometric, photometric, and survey properties" A&A, 595, A2 (arXiv:1609.04172)
Gaia Collaboration 2018, "Gaia Data Release 2. Summary of the contents and survey properties" A&A, 616, A1 (arXiv:1804.09365)
Gaia Collaboration 2021, "Gaia Early Data Release 3. Summary of the contents and survey properties" A&A, 649, A1 (arXiv:2012.01533)
Gaia Collaboration 2023a, "Gaia Data Release 3. Summary of the content and survey properties" A&A, 674, A1 (arXiv:2208.00211)
Gaia Collaboration 2023b, "Gaia Data Release 3. Reflectance spectra of Solar System small bodies" A&A, 674, A35 (arXiv:2206.12174)
Gaia Collaboration 2023c, "Gaia Data Release 3. Mapping the asymmetric disc of the Milky Way" A&A, 674, A37 (arXiv:2206.06207)
Gaia Collaboration 2023d, "Gaia Data Release 3. Chemical cartography of the Milky Way" A&A, 674, A38 (arXiv:2206.05534)
Gaia Collaboration et al., 2018, "Gaia Data Release 2. Observational Hertzsprung-Russell diagrams" A&A, 616, A10 (arXiv:1804.09378)
Gaia Collaboration et al., 2023, "Gaia Data Release 3. Summary of the content and survey properties" A&A, 674, A1 (arXiv:2208.00211)
Gavagnin E., Mapelli M., Lake G., 2016, "A critical look at the merger scenario to explain multiple populations and rotation in iron-complex globular clusters" MNRAS, 461, 1276 (arXiv:1606.02743)
Geen S., Rosdahl J., Blaizot J., Devriendt J., Slyz A., 2015a, "A detailed study of feedback from a massive star" MNRAS, 448, 3248 (arXiv:1412.0484)
Geen S., Hennebelle P., Tremblin P., Rosdahl J., 2015b, "Photoionization feedback in a self-gravitating, magnetized, turbulent cloud" MNRAS, 454, 4484 (arXiv:1507.02981)
Gennaro M., Brandner W., Stolte A., Henning T., 2011, "Mass segregation and elongation of the starburst cluster Westerlund 1" MNRAS, 412, 2469 (arXiv:1011.5223)
Gerssen J., van der Marel R. P., Gebhardt K., Guhathakurta P., Peterson R. C., Pryor C., 2002, "Hubble Space Telescope Evidence for an Intermediate-Mass Black Hole in the Globular Cluster M15. II. Kinematic Analysis and Dynamical Modeling" AJ, 124, 3270 (arXiv:astro-ph/0209315)
Getman K. V., Feigelson E. D., Kuhn M. A., Bate M. R., Broos P. S., Garmire G. P., 2018, "Intracluster age gradients in numerous young stellar clusters" MNRAS, 476, 1213 (arXiv:1804.05077)
Getman K. V., Feigelson E. D., Kuhn M. A., Garmire G. P., 2019, "Gaia stellar kinematics in the head of the Orion A cloud: runaway stellar groups and gravitational infall" MNRAS, 487, 2977 (arXiv:1905.10251)

Giacobbo N., Mapelli M., 2020, "Revising Natal Kick Prescriptions in Population Synthesis Simulations" ApJ, 891, 141 (arXiv:1909.06385)
Gieles M., Baumgardt H., 2008, "Lifetimes of tidally limited star clusters with different radii" MNRAS, 389, L28 (arXiv:0806.2327)
Gieles M., Zocchi A., 2015, "A family of lowered isothermal models" MNRAS, 454, 576 (arXiv:1508.02120)
Gieles M., Portegies Zwart S. F., Baumgardt H., Athanassoula E., Lamers H. J. G. L. M., Sipior M., Leenaarts J., 2006, "Star cluster disruption by giant molecular clouds" MNRAS, 371, 793 (arXiv:astro-ph/0606451)
Gieles M., et al., 2018, "Concurrent formation of supermassive stars and globular clusters: implications for early self-enrichment" MNRAS, 478, 2461 (arXiv:1804.04682)
Gieles M., Erkal D., Antonini F., Balbinot E., Peñarrubia J., 2021, "A supra-massive population of stellar-mass black holes in the globular cluster Palomar 5" Nature Astronomy, 5, 957 (arXiv:2102.11348)
Giersz M., 1998, "Monte Carlo simulations of star clusters - I. First Results" MNRAS, 298, 1239 (arXiv:astro-ph/9804127)
Giersz M., Heggie D. C., 1996, "Statistics of N-body simulations - III. Unequal masses" MNRAS, 279, 1037 (arXiv:astro-ph/9506143)
Giersz M., Heggie D. C., Hurley J. R., Hypki A., 2013, "MOCCA code for star cluster simulations - II. Comparison with N-body simulations" MNRAS, 431, 2184 (arXiv:1112.6246)
Giersz M., Leigh N., Hypki A., Lützgendorf N., Askar A., 2015, "MOCCA code for star cluster simulations - IV. A new scenario for intermediate mass black hole formation in globular clusters" MNRAS, 454, 3150 (arXiv:1506.05234)
Giesers B., et al., 2018, "A detached stellar-mass black hole candidate in the globular cluster NGC 3201" MNRAS, 475, L15 (arXiv:1801.05642)
Girichidis P., Federrath C., Banerjee R., Klessen R. S., 2011, "Importance of the initial conditions for star formation - I. Cloud evolution and morphology" MNRAS, 413, 2741 (arXiv:1008.5255)
Girichidis P., et al., 2020, "Physical Processes in Star Formation" Space Sci. Rev., 216, 68 (arXiv:2005.06472)
Gnedin O. Y., Lee H. M., Ostriker J. P., 1999, "Effects of Tidal Shocks on the Evolution of Globular Clusters" ApJ, 522, 935 (arXiv:astro-ph/9806245)
Goldreich P., Kwan J., 1974, "Molecular Clouds" ApJ, 189, 441
Goldsbury R., Richer H. B., Anderson J., Dotter A., Sarajedini A., Woodley K., 2010, "The ACS Survey of Galactic Globular Clusters. X. New Determinations of Centers for 65 Clusters" AJ, 140, 1830 (arXiv:1008.2755)
Goodwin S. P., Bastian N., 2006, "Gas expulsion and the destruction of massive young clusters" MNRAS, 373, 752 (arXiv:astro-ph/0609477)
Goodwin S. P., Whitworth A. P., 2004, "The dynamical evolution of fractal star clusters: The survival of substructure" A&A, 413, 929 (arXiv:astro-ph/0310333)
Gouliermis D., Keller S. C., Kontizas M., Kontizas E., Bellas-Velidis I., 2004, "Mass segregation in young Magellanic Cloud star clusters: Four clusters observed with HST" A&A, 416, 137 (arXiv:astro-ph/0311477)
Gratton R., Bragaglia A., Carretta E., D'Orazi V., Lucatello S., Sollima A., 2019, "What is a globular cluster? An observational perspective" A&A Rev., 27, 8 (arXiv:1911.02835)
Greene J. E., Strader J., Ho L. C., 2020, "Intermediate-Mass Black Holes" ARA&A, 58, 257 (arXiv:1911.09678)
Grillmair C. J., Dionatos O., 2006, "Detection of a 63° Cold Stellar Stream in the Sloan Digital Sky Survey" ApJ, 643, L17 (arXiv:astro-ph/0604332)
Grudić M. Y., Hopkins P. F., Faucher-Giguère C.-A., Quataert E., Murray N., Kereš D., 2018a, "When feedback fails: the scaling and saturation of star formation efficiency" MNRAS, 475, 3511 (arXiv:1612.05635)
Grudić M. Y., Guszejnov D., Hopkins P. F., Lamberts A., Boylan-Kolchin M., Murray N., Schmitz D., 2018b, "From the top down and back up again: star cluster structure from hierarchical star formation" MNRAS, 481, 688 (arXiv:1708.09065)
Grudić M. Y., Hafen Z., Rodriguez C. L., Guszejnov D., Lamberts A., Wetzel A., Boylan-Kolchin M., Faucher-Giguère C.-A., 2023, "Great balls of FIRE - I. The formation of star clusters across cosmic time in a Milky Way-mass galaxy" MNRAS, 519, 1366 (arXiv:2203.05732)
Güdel M., Telleschi A., 2007, "The X-ray soft excess in classical T Tauri stars" A&A, 474, L25 (arXiv:0709.0881)
Guilherme-Garcia P., Krone-Martins A., Moitinho A., 2023, "Detection of open cluster rotation fields from Gaia EDR3 proper motions" A&A, 673, A128
Guszejnov D., Markey C., Offner S. S. R., Grudić M. Y., Faucher-Giguère C.-A., Rosen A. L., Hopkins P. F., 2022, "Cluster assembly and the origin of mass segregation in the STARFORGE simulations" MNRAS, 515, 167 (arXiv:2201.01781)
Gutermuth R. A., et al., 2008, "Spitzer Observations of NGC 1333: A Study of Structure and Evolution in a Nearby Embedded Cluster" ApJ, 674, 336 (arXiv:0710.1860)
Häberle M., et al., 2024, "Fast-moving stars around an intermediate-mass black hole in ω Centauri" Nature, 631, 285 (arXiv:2405.06015)
Hachisuka K., et al., 2006, "Water Maser Motions in W3(OH) and a Determination of Its Distance" ApJ, 645, 337 (arXiv:astro-ph/0512226)
Halbwachs J.-L., et al., 2023, "Gaia Data Release 3. Astrometric binary star processing" A&A, 674, A9 (arXiv:2206.05726)
Hao C. J., et al., 2021, "Evolution of the local spiral structure of the Milky Way revealed by open clusters" A&A, 652, A102 (arXiv:2107.06478)

Harayama Y., Eisenhauer F., Martins F., 2008, "The Initial Mass Function of the Massive Star-forming Region NGC 3603 from Near-Infrared Adaptive Optics Observations" ApJ, 675, 1319 (arXiv:0710.2882)
Harris W. E., 1996, "A Catalog of Parameters for Globular Clusters in the Milky Way" AJ, 112, 1487
Harris W. E., Harris G. L., Hudson M. J., 2015, "Dark Matter Halos in Galaxies and Globular Cluster Populations. II. Metallicity and Morphology" ApJ, 806, 36 (arXiv:1504.03199)
He Z.-H., Xu Y., Hou L.-G., 2021, "Search for age pattern across spiral arms of the Milky Way" Research in Astronomy and Astrophysics, 21, 009
Heggie D. C., 2001, in Deiters S., Fuchs B., Just A., Spurzem R., Wielen R., eds, Astronomical Society of the Pacific Conference Series Vol. 228, Dynamics of Star Clusters and the Milky Way. p. 29 (arXiv:astro-ph/0007336), doi:10.48550/arXiv.astro-ph/0007336
Heggie D. C., Giersz M., 2014, "MOCCA code for star cluster simulations - III. Stellar-mass black holes in the globular cluster M22" MNRAS, 439, 2459 (arXiv:1401.3657)
Heggie D., Hut P., 2003, The Gravitational Million-Body Problem: A Multidisciplinary Approach to Star Cluster Dynamics
Heitsch F., Burkert A., Hartmann L. W., Slyz A. D., Devriendt J. E. G., 2005, "Formation of Structure in Molecular Clouds: A Case Study" ApJ, 633, L113 (arXiv:astro-ph/0507567)
Heitsch F., Slyz A. D., Devriendt J. E. G., Hartmann L. W., Burkert A., 2006, "The Birth of Molecular Clouds: Formation of Atomic Precursors in Colliding Flows" ApJ, 648, 1052 (arXiv:astro-ph/0605435)
Helmi A., 2020, "Streams, Substructures, and the Early History of the Milky Way" ARA&A, 58, 205 (arXiv:2002.04340)
Hénault-Brunet V., et al., 2012, "The VLT-FLAMES Tarantula Survey. VI. Evidence for rotation of the young massive cluster R136" A&A, 545, L1 (arXiv:1207.7071)
Hénault-Brunet V., Gieles M., Agertz O., Read J. I., 2015, "Multiple populations in globular clusters: the distinct kinematic imprints of different formation scenarios" MNRAS, 450, 1164 (arXiv:1503.07532)
Hénault-Brunet V., Gieles M., Strader J., Peuten M., Balbinot E., Douglas K. E. K., 2020, "On the black hole content and initial mass function of 47 Tuc" MNRAS, 491, 113 (arXiv:1908.08538)
Hennebelle P., Falgarone E., 2012, "Turbulent molecular clouds" A&A Rev., 20, 55 (arXiv:1211.0637)
Hennebelle P., Banerjee R., Vázquez-Semadeni E., Klessen R. S., Audit E., 2008, "From the warm magnetized atomic medium to molecular clouds" A&A, 486, L43 (arXiv:0805.1366)
Hénon M., 1961, "Sur l'évolution dynamique des amas globulaires" Annales d'Astrophysique, 24, 369
Hénon M., 1971a, "Monte Carlo Models of Star Clusters (Part of the Proceedings of the IAU Colloquium No. 10, held in Cambridge, England, August 12-15, 1970.)" Ap&SS, 13, 284
Hénon M. H., 1971b, "The Monte Carlo Method (Papers appear in the Proceedings of IAU Colloquium No. 10 Gravitational N-Body Problem (ed. by Myron Lecar), R. Reidel Publ. Co. , Dordrecht-Holland.)" Ap&SS, 14, 151
Heyl J., Caiazzo I., Richer H., Anderson J., Kalirai J., Parada J., 2017, "Deep HST Imaging in 47 Tucanae: A Global Dynamical Model" ApJ, 850, 186 (arXiv:1710.10666)
Hillenbrand L. A., Hartmann L. W., 1998, "A Preliminary Study of the Orion Nebula Cluster Structure and Dynamics" ApJ, 492, 540
Hobbs G., Lorimer D. R., Lyne A. G., Kramer M., 2005, "A statistical study of 233 pulsar proper motions" MNRAS, 360, 974 (arXiv:astro-ph/0504584)
Hobbs D., et al., 2021, "All-sky visible and near infrared space astrometry" Experimental Astronomy, 51, 783 (arXiv:1907.12535)
Hofner P., Delgado H., Whitney B., Churchwell E., Linz H., 2002, "X-Ray Detection of the Ionizing Stars in Ultracompact H II Regions" ApJ, 579, L95
Holl B., et al., 2023, "Gaia Data Release 3. Astrometric orbit determination with Markov chain Monte Carlo and genetic algorithms: Systems with stellar, sub-stellar, and planetary mass companions" A&A, 674, A10 (arXiv:2206.05439)
Hong J., Kim E., Lee H. M., Spurzem R., 2013, "Comparative study between N-body and Fokker-Planck simulations for rotating star clusters - II. Two-component models" MNRAS, 430, 2960 (arXiv:1211.6527)
Hong J., et al., 2017, "The dynamical origin of multiple populations in intermediate-age clusters in the Magellanic Clouds" MNRAS, 472, 67 (arXiv:1707.09153)
Hong J., Vesperini E., Askar A., Giersz M., Szkudlarek M., Bulik T., 2018, "Binary black hole mergers from globular clusters: the impact of globular cluster properties" MNRAS, 480, 5645 (arXiv:1808.04514)
Hong J., Askar A., Giersz M., Hypki A., Yoon S.-J., 2020, "MOCCA-SURVEY Database I: Binary black hole mergers from globular clusters with intermediate mass black holes" MNRAS, 498, 4287 (arXiv:2008.10823)
Horner D. J., Lada E. A., Lada C. J., 1997, "A Near-Infrared Imaging Survey of NGC 2282" AJ, 113, 1788
Howard C. S., Pudritz R. E., Sills A., Harris W. E., 2019, "On the origin of multiple populations during massive star cluster formation" MNRAS, 486, 1146 (arXiv:1808.07081)
Hudson M. J., Harris G. L., Harris W. E., 2014, "Dark Matter Halos in Galaxies and Globular Cluster Populations" ApJ, 787, L5 (arXiv:1404.1920)
Hunt E. L., Reffert S., 2021, "Improving the open cluster census. I. Comparison of clustering algorithms applied to Gaia DR2 data" A&A, 646, A104 (arXiv:2012.04267)
Hunt E. L., Reffert S., 2023, "Improving the open cluster census. II. An all-sky cluster catalogue with Gaia DR3" A&A, 673, A114 (arXiv:2303.13424)

Hunt E. L., Reffert S., 2024, "Improving the open cluster census. III. Using cluster masses, radii, and dynamics to create a cleaned open cluster catalogue" A&A, 686, A42 (arXiv:2403.05143)
Hurley J. R., Pols O. R., Tout C. A., 2000, "Comprehensive analytic formulae for stellar evolution as a function of mass and metallicity" MNRAS, 315, 543 (arXiv:astro-ph/0001295)
Hurley J. R., Tout C. A., Pols O. R., 2002, "Evolution of binary stars and the effect of tides on binary populations" MNRAS, 329, 897 (arXiv:astro-ph/0201220)
Hurley J. R., Sippel A. C., Tout C. A., Aarseth S. J., 2016, "A Dynamical Gravitational Wave Source in a Dense Cluster" PASA, 33, e036 (arXiv:1607.00641)
Hypki A., Giersz M., 2013, "MOCCA code for star cluster simulations - I. Blue stragglers, first results" MNRAS, 429, 1221 (arXiv:1207.6700)
Ibata R. A., Bellazzini M., Malhan K., Martin N., Bianchini P., 2019a, "Identification of the long stellar stream of the prototypical massive globular cluster ω Centauri" Nature Astronomy, 3, 667 (arXiv:1902.09544)
Ibata R. A., Malhan K., Martin N. F., 2019b, "The Streams of the Gaping Abyss: A Population of Entangled Stellar Streams Surrounding the Inner Galaxy" ApJ, 872, 152 (arXiv:1901.07566)
Iorio G., et al., 2023, "Compact object mergers: exploring uncertainties from stellar and binary evolution with SEVN" MNRAS, 524, 426 (arXiv:2211.11774)
Jadhav V. V., Kroupa P., Wu W., Pflamm-Altenburg J., Thies I., 2024, "The spin, expansion, and contraction of open star clusters" A&A, 687, A89 (arXiv:2404.05327)
Jaehnig K., Bird J., Holley-Bockelmann K., 2021, "Membership Lists for 431 Open Clusters in Gaia DR2 Using Extreme Deconvolution Gaussian Mixture Models" ApJ, 923, 129 (arXiv:2108.02783)
Janka H.-T., 2013, "Natal kicks of stellar mass black holes by asymmetric mass ejection in fallback supernovae" MNRAS, 434, 1355 (arXiv:1306.0007)
Jeans J. H., 1902, "The Stability of a Spherical Nebula" Philosophical Transactions of the Royal Society of London Series A, 199, 1
Jeans J. H., 1913, "On the "kinetic theory" of star-clusters" MNRAS, 74, 109
Jerabkova T., Boffin H. M. J., Beccari G., de Marchi G., de Bruijne J. H. J., Prusti T., 2021, "The 800 pc long tidal tails of the Hyades star cluster. Possible discovery of candidate epicyclic overdensities from an open star cluster" A&A, 647, A137 (arXiv:2103.12080)
Jin S., et al., 2024, "The wide-field, multiplexed, spectroscopic facility WEAVE: Survey design, overview, and simulated implementation" MNRAS, 530, 2688 (arXiv:2212.03981)
Jordi C., et al., 2010, "Gaia broad band photometry" A&A, 523, A48 (arXiv:1008.0815)
Jose J., Kim J. S., Herczeg G. J., Samal M. R., Bieging J. H., Meyer M. R., Sherry W. H., 2016, "Star Formation in W3—AFGL 333: Young Stellar Content, Properties, and Roles of External Feedback" ApJ, 822, 49 (arXiv:1602.06212)
Joshi Y. C., Malhotra S., 2023, "Revisiting Galactic Disk and Spiral Arms Using Open Clusters" AJ, 166, 170 (arXiv:2212.09384)
Junqueira T. C., Chiappini C., Lépine J. R. D., Minchev I., Santiago B. X., 2015, "A new method for estimating the pattern speed of spiral structure in the Milky Way" MNRAS, 449, 2336 (arXiv:1503.00926)
Kamann S., et al., 2018, "A stellar census in globular clusters with MUSE: The contribution of rotation to cluster dynamics studied with 200 000 stars" MNRAS, 473, 5591 (arXiv:1710.07257)
Kamann S., et al., 2020, "The peculiar kinematics of the multiple populations in the globular cluster Messier 80 (NGC 6093)" MNRAS, 492, 966 (arXiv:1912.06158)
Kamlah A. W. H., et al., 2022, "The impact of stellar evolution on rotating star clusters: the gravothermal-gravogyro catastrophe and the formation of a bar of black holes" MNRAS, 516, 3266 (arXiv:2205.04470)
Karam J., Sills A., 2022, "Modelling star cluster formation: mergers" MNRAS, 513, 6095 (arXiv:2205.03265)
Karam J., Sills A., 2024, "Dynamics of Star Cluster Formation: Mergers in Gas-rich Environments" ApJ, 967, 86 (arXiv:2404.06348)
Karr J. L., Martin P. G., 2003, "Triggered Star Formation in the W5 H II Region" ApJ, 595, 900
Katz D., et al., 2019, "Gaia Data Release 2. Properties and validation of the radial velocities" A&A, 622, A205 (arXiv:1804.09372)
Katz D., et al., 2023, "Gaia Data Release 3. Properties and validation of the radial velocities" A&A, 674, A5 (arXiv:2206.05902)
Kawata D., Baba J., Hunt J. A. S., Schönrich R., Ciucă I., Friske J., Seabroke G., Cropper M., 2021, "Galactic bar resonances inferred from kinematically hot stars in Gaia EDR3" MNRAS, 508, 728 (arXiv:2012.05890)
Keller B. W., Kruijssen J. M. D., Pfeffer J., Reina-Campos M., Bastian N., Trujillo-Gomez S., Hughes M. E., Crain R. A., 2020, "Where did the globular clusters of the Milky Way form? Insights from the E-MOSAICS simulations" MNRAS, 495, 4248 (arXiv:2005.05342)
Kennicutt R. C., Evans N. J., 2012, "Star Formation in the Milky Way and Nearby Galaxies" ARA&A, 50, 531 (arXiv:1204.3552)
Khalisi E., Amaro-Seoane P., Spurzem R., 2007, "A comprehensive NBODY study of mass segregation in star clusters: energy equipartition and escape" MNRAS, 374, 703 (arXiv:astro-ph/0602570)
Kharchenko N. V., Piskunov A. E., Röser S., Schilbach E., Scholz R. D., 2005a, "Astrophysical parameters of Galactic open clusters" A&A, 438, 1163 (arXiv:astro-ph/0501674)
Kharchenko N. V., Piskunov A. E., Röser S., Schilbach E., Scholz R. D., 2005b, "109 new Galactic open clusters" A&A, 440, 403 (arXiv:astro-ph/0505019)

Kharchenko N. V., Piskunov A. E., Schilbach E., Röser S., Scholz R. D., 2012, "Global survey of star clusters in the Milky Way. I. The pipeline and fundamental parameters in the second quadrant" A&A, 543, A156 (arXiv:1207.4001)
Kharchenko N. V., Piskunov A. E., Schilbach E., Röser S., Scholz R. D., 2013, "Global survey of star clusters in the Milky Way. II. The catalogue of basic parameters" A&A, 558, A53 (arXiv:1308.5822)
King I., 1962, "The structure of star clusters. I. an empirical density law" AJ, 67, 471
King I. R., 1966, "The structure of star clusters. III. Some simple dynamical models" AJ, 71, 64
Kirk H., Offner S. S. R., Redmond K. J., 2014, "The formation and evolution of small star clusters" MNRAS, 439, 1765 (arXiv:1401.4510)
Kızıltan B., Baumgardt H., Loeb A., 2017, "An intermediate-mass black hole in the centre of the globular cluster 47 Tucanae" Nature, 542, 203 (arXiv:1702.02149)
Klessen R. S., Burkert A., 2000, "The Formation of Stellar Clusters: Gaussian Cloud Conditions. I." ApJS, 128, 287 (arXiv:astro-ph/9904090)
Klessen R. S., Hennebelle P., 2010, "Accretion-driven turbulence as universal process: galaxies, molecular clouds, and protostellar disks" A&A, 520, A17 (arXiv:0912.0288)
Klessen R. S., Heitsch F., Mac Low M.-M., 2000, "Gravitational Collapse in Turbulent Molecular Clouds. I. Gasdynamical Turbulence" ApJ, 535, 887 (arXiv:astro-ph/9911068)
Koenig X. P., Allen L. E., Gutermuth R. A., Hora J. L., Brunt C. M., Muzerolle J., 2008, "Clustered and Triggered Star Formation in W5: Observations with Spitzer" ApJ, 688, 1142 (arXiv:0808.3284)
Kos J., et al., 2018, "The GALAH survey and Gaia DR2: (non-)existence of five sparse high-latitude open clusters" MNRAS, 480, 5242 (arXiv:1807.00822)
Krause M. G. H., et al., 2018, "Surround and Squash: the impact of superbubbles on the interstellar medium in Scorpius-Centaurus OB2" A&A, 619, A120 (arXiv:1808.04788)
Krause M. G. H., et al., 2020, "The Physics of Star Cluster Formation and Evolution" Space Sci. Rev., 216, 64 (arXiv:2005.00801)
Kravtsov A. V., Gnedin O. Y., 2005, "Formation of Globular Clusters in Hierarchical Cosmology" ApJ, 623, 650 (arXiv:astro-ph/0305199)
Kremer K., Ye C. S., Chatterjee S., Rodriguez C. L., Rasio F. A., 2018, "How Black Holes Shape Globular Clusters: Modeling NGC 3201" ApJ, 855, L15 (arXiv:1802.09553)
Kremer K., et al., 2020, "Modeling Dense Star Clusters in the Milky Way and Beyond with the CMC Cluster Catalog" ApJS, 247, 48 (arXiv:1911.00018)
Kroupa P., 1995, "Inverse dynamical population synthesis and star formation" MNRAS, 277, 1491 (arXiv:astro-ph/9508117)
Kroupa P., 2001, "On the variation of the initial mass function" MNRAS, 322, 231 (arXiv:astro-ph/0009005)
Kroupa P., Aarseth S., Hurley J., 2001, "The formation of a bound star cluster: from the Orion nebula cluster to the Pleiades" MNRAS, 321, 699 (arXiv:astro-ph/0009470)
Kroupa P., Weidner C., Pflamm-Altenburg J., Thies I., Dabringhausen J., Marks M., Maschberger T., 2013, in Oswalt T. D., Gilmore G., eds, , Vol. 5, Planets, Stars and Stellar Systems. Volume 5: Galactic Structure and Stellar Populations. p. 115, doi:10.1007/978-94-007-5612-0_4
Kroupa P., et al., 2022, "Asymmetrical tidal tails of open star clusters: stars crossing their cluster's práh challenge Newtonian gravitation" MNRAS, 517, 3613 (arXiv:2210.13472)
Kruijssen J. M. D., 2012, "On the fraction of star formation occurring in bound stellar clusters" MNRAS, 426, 3008 (arXiv:1208.2963)
Kruijssen J. M. D., 2015, "Globular clusters as the relics of regular star formation in 'normal' high-redshift galaxies" MNRAS, 454, 1658 (arXiv:1509.02163)
Kruijssen J. M. D., Pelupessy F. I., Lamers H. J. G. L. M., Portegies Zwart S. F., Icke V., 2011, "Modelling the formation and evolution of star cluster populations in galaxy simulations" MNRAS, 414, 1339 (arXiv:1102.1013)
Kruijssen J. M. D., Maschberger T., Moeckel N., Clarke C. J., Bastian N., Bonnell I. A., 2012, "The dynamical state of stellar structure in star-forming regions" MNRAS, 419, 841 (arXiv:1109.0986)
Krumholz M. R., Matzner C. D., 2009, "The Dynamics of Radiation-pressure-dominated H II Regions" ApJ, 703, 1352 (arXiv:0906.4343)
Krumholz M. R., McKee C. F., Bland-Hawthorn J., 2019, "Star Clusters Across Cosmic Time" ARA&A, 57, 227 (arXiv:1812.01615)
Kuhn M. A., Hillenbrand L. A., Sills A., Feigelson E. D., Getman K. V., 2019a, "Kinematics in Young Star Clusters and Associations with Gaia DR2" ApJ, 870, 32 (arXiv:1807.02115)
Kuhn M. A., Hillenbrand L. A., Sills A., Feigelson E. D., Getman K. V., 2019b, "Kinematics in Young Star Clusters and Associations with Gaia DR2" ApJ, 870, 32 (arXiv:1807.02115)
Kuhn M. A., Hillenbrand L. A., Carpenter J. M., Avelar Menendez A. R., 2020, "The Formation of a Stellar Association in the NGC 7000/IC 5070 Complex: Results from Kinematic Analysis of Stars and Gas" ApJ, 899, 128 (arXiv:2006.08622)
Küpper A. H. W., MacLeod A., Heggie D. C., 2008, "On the structure of tidal tails" MNRAS, 387, 1248 (arXiv:0804.2476)
Lacchin E., Calura F., Vesperini E., Mastrobuono-Battisti A., 2022, "The role of rotation on the formation of second generation stars in globular clusters" MNRAS, 517, 1171 (arXiv:2209.05178)
Lada C. J., Lada E. A., 2003, "Embedded Clusters in Molecular Clouds" ARA&A, 41, 57 (arXiv:astro-ph/0301540)

Lada C. J., Margulis M., Dearborn D., 1984, "The formation and early dynamical evolution of bound stellar systems." ApJ, 285, 141
Lada C. J., Alves J., Lada E. A., 1996, "Near-Infrared Imaging of Embedded Clusters: NGC 1333" AJ, 111, 1964
Lamers H. J. G. L. M., Cassinelli J. P., 1999, Introduction to Stellar Winds
Langer N., 2012, "Presupernova Evolution of Massive Single and Binary Stars" ARA&A, 50, 107 (arXiv:1206.5443)
Lanzoni B., Ferraro F. R., Alessandrini E., Dalessandro E., Vesperini E., Raso S., 2016, "Refining the Dynamical Clock for Star Clusters" ApJ, 833, L29
Lanzoni B., et al., 2018a, "The Strong Rotation of M5 (NGC 5904) as Seen from the MIKiS Survey of Galactic Globular Clusters" ApJ, 861, 16 (arXiv:1804.10509)
Lanzoni B., et al., 2018b, "The ESO Multi-instrument Kinematic Survey (MIKiS) of Galactic Globular Clusters: Solid-body Rotation and Anomalous Velocity Dispersion Profile in NGC 5986" ApJ, 865, 11 (arXiv:1808.01194)
Larsen S. S., Strader J., Brodie J. P., 2012, "Constraints on mass loss and self-enrichment scenarios for the globular clusters of the Fornax dSph" A&A, 544, L14 (arXiv:1207.5792)
Larsen S. S., Brodie J. P., Wasserman A., Strader J., 2018, "Detailed abundance analysis of globular clusters in the Local Group. NGC 147, NGC 6822, and Messier 33" A&A, 613, A56 (arXiv:1801.03140)
Leanza S., et al., 2022, "The ESO-VLT MIKiS Survey Reloaded: Velocity Dispersion Profile and Rotation Curve of NGC 1904" ApJ, 929, 186 (arXiv:2203.07294)
Leanza S., et al., 2023, "The ESO-VLT MIKiS Survey Reloaded: Exploring the Internal Kinematics of NGC 6440" ApJ, 944, 162 (arXiv:2212.07373)
Lefloch B., Lazareff B., 1994, "Cometary globules I. Formation, evolution and morphology." A&A, 289, 559
Lefloch B., Lazareff B., 1995, "Cometary globules. II. Observational tests of radiation-driven implosion: the case of CG7S." A&A, 301, 522
Leon S., Meylan G., Combes F., 2000, "Tidal tails around 20 Galactic globular clusters. Observational evidence for gravitational disk/bulge shocking" A&A, 359, 907 (arXiv:astro-ph/0006100)
Leveque A., Giersz M., Paolillo M., 2021, "MOCCA Survey Database: extra Galactic globular clusters. I. Method and first results" MNRAS, 501, 5212 (arXiv:2006.05887)
Leveque A., Giersz M., Banerjee S., Vesperini E., Hong J., Portegies Zwart S., 2022a, "A Monte Carlo study of early gas expulsion and evolution of star clusters: new simulations with the MOCCA code in the AMUSE framework" MNRAS, 514, 5739 (arXiv:2206.03404)
Leveque A., Giersz M., Arca-Sedda M., Askar A., 2022b, "MOCCA-survey data base: extra galactic globular clusters - II. Milky Way and Andromeda" MNRAS, 514, 5751 (arXiv:2206.03967)
Leveque A., Giersz M., Askar A., Arca-Sedda M., Olejak A., 2023, "MOCCA-Survey Database: extra galactic globular clusters - III. The population of black holes in Milky Way and Andromeda-like galaxies" MNRAS, 520, 2593 (arXiv:2209.01564)
Levine E. S., Blitz L., Heiles C., 2006, "The Spiral Structure of the Outer Milky Way in Hydrogen" Science, 312, 1773 (arXiv:astro-ph/0605728)
Li H., Gnedin O. Y., 2019, "Star cluster formation in cosmological simulations - III. Dynamical and chemical evolution" MNRAS, 486, 4030 (arXiv:1810.11036)
Li H., Vogelsberger M., Marinacci F., Gnedin O. Y., 2019a, "Disruption of giant molecular clouds and formation of bound star clusters under the influence of momentum stellar feedback" MNRAS, 487, 364 (arXiv:1904.11987)
Li C., Sun W., de Grijs R., Deng L., Wang K., Cordoni G., Milone A. P., 2019b, "Extended Main-sequence Turnoffs in the Double Cluster h and χ Persei: The Complex Role of Stellar Rotation" ApJ, 876, 65 (arXiv:1904.02005)
Libralato M., et al., 2018, "Hubble Space Telescope Proper Motion (HSTPROMO) Catalogs of Galactic Globular Cluster. VI. Improved Data Reduction and Internal-kinematic Analysis of NGC 362" ApJ, 861, 99 (arXiv:1805.05332)
Libralato M., Bellini A., Piotto G., Nardiello D., van der Marel R. P., Anderson J., Bedin L. R., Vesperini E., 2019, "The Hubble Space Telescope UV Legacy Survey of Galactic Globular Clusters. XVIII. Proper-motion Kinematics of Multiple Stellar Populations in the Core Regions of NGC 6352" ApJ, 873, 109 (arXiv:1902.02787)
Libralato M., et al., 2022, "The Hubble Space Telescope UV Legacy Survey of Galactic Globular Clusters. XXIII. Proper-motion Catalogs and Internal Kinematics" ApJ, 934, 150 (arXiv:2206.09924)
Libralato M., et al., 2023, "The Hubble Space Telescope UV Legacy Survey of Galactic Globular Clusters. XXIV. Differences in Internal Kinematics of Multiple Stellar Populations" ApJ, 944, 58 (arXiv:2301.04148)
Lim B., Hong J., Yun H.-S., Hwang N., Kim J. S., Lee J.-E., Park B.-G., Park S., 2020, "The Origin of a Distributed Stellar Population in the Star-forming Region W4" ApJ, 899, 121 (arXiv:2006.15262)
Lim B., et al., 2021, "A Kinematic Perspective on the Formation Process of the Stellar Groups in the Rosette Nebula" AJ, 162, 56 (arXiv:2105.03698)
Lim B., Nazé Y., Hong J., Yoon S.-y., Lee J., Hwang N., Park B.-G., Lee J.-E., 2022, "A Gaia View on the Star Formation in the Monoceros OB1 and R1 Associations" AJ, 163, 266 (arXiv:2204.00444)
Lin C. C., Shu F. H., 1964, "On the Spiral Structure of Disk Galaxies." ApJ, 140, 646
Lindegren L., et al., 2021a, "Gaia Early Data Release 3. The astrometric solution" A&A, 649, A2 (arXiv:2012.03380)
Lindegren L., et al., 2021b, "Gaia Early Data Release 3. Parallax bias versus magnitude, colour, and position" A&A, 649, A4 (arXiv:2012.01742)
Lindegren L., et al., 2021c, "Gaia Early Data Release 3. Parallax bias versus magnitude, colour, and position" A&A, 649, A4 (arXiv:2012.01742)

Liszt H. S., Wilson R. W., Penzias A. A., Jefferts K. B., Wannier P. G., Solomon P. M., 1974, "CO and CS in the Orion Nebula" ApJ, 190, 557
Littlefair S. P., Naylor T., Jeffries R. D., Devey C. R., Vine S., 2003, "Mass segregation in the young open cluster NGC 2547" MNRAS, 345, 1205 (arXiv:astro-ph/0308320)
Liu L., Pang X., 2019, "A Catalog of Newly Identified Star Clusters in Gaia DR2" ApJS, 245, 32 (arXiv:1910.12600)
Livernois A., Vesperini E., Tiongco M., Varri A. L., Dalessandro E., 2021, "Early dynamics and violent relaxation of multimass rotating star clusters" MNRAS, 506, 5781 (arXiv:2107.11394)
Livernois A. R., Vesperini E., Varri A. L., Hong J., Tiongco M., 2022, "Long-term evolution of multimass rotating star clusters" MNRAS, 512, 2584 (arXiv:2204.06578)
Longmore S. N., et al., 2014, in Beuther H., Klessen R. S., Dullemond C. P., Henning T., eds, Protostars and Planets VI. pp 291–314 (arXiv:1401.4175), doi:10.2458/azu_uapress_9780816531240-ch013
Lynden-Bell D., 1967, "Statistical mechanics of violent relaxation in stellar systems" MNRAS, 136, 101
Mac Low M.-M., Klessen R. S., 2004, "Control of star formation by supersonic turbulence" Reviews of Modern Physics, 76, 125 (arXiv:astro-ph/0301093)
MacLean B. T., De Silva G. M., Lattanzio J., 2015, "O, Na, Ba and Eu abundance patterns in open clusters" MNRAS, 446, 3556 (arXiv:1411.1185)
Maccarone T. J., Kundu A., Zepf S. E., Rhode K. L., 2007, "A black hole in a globular cluster" Nature, 445, 183 (arXiv:astro-ph/0701310)
Mackey A. D., Wilkinson M. I., Davies M. B., Gilmore G. F., 2007, "The effect of stellar-mass black holes on the structural evolution of massive star clusters" MNRAS, 379, L40 (arXiv:0704.2494)
Mackey A. D., Wilkinson M. I., Davies M. B., Gilmore G. F., 2008, "Black holes and core expansion in massive star clusters" MNRAS, 386, 65 (arXiv:0802.0513)
Magorrian J., et al., 1998, "The Demography of Massive Dark Objects in Galaxy Centers" AJ, 115, 2285 (arXiv:astro-ph/9708072)
Mainieri V., et al., 2024, "The Wide-field Spectroscopic Telescope (WST) Science White Paper" arXiv e-prints, p. arXiv:2403.05398 (arXiv:2403.05398)
Maíz Apellániz J., Pantaleoni González M., Barbá R. H., Weiler M., 2022, "Escape from the Bermuda cluster: Orphanization by multiple stellar ejections" A&A, 657, A72 (arXiv:2110.01484)
Makino J., 1996, in Hut P., Makino J., eds, IAU Symposium Vol. 174, Dynamical Evolution of Star Clusters: Confrontation of Theory and Observations. p. 151
Makino J., Funato Y., 1993, "The GRAPE Software System" PASJ, 45, 279
Makino J., Taiji M., 1998, Scientific Simulations with Special-Purpose Computers–the GRAPE Systems
Makino J., Taiji M., Ebisuzaki T., Sugimoto D., 1997, "GRAPE-4: A Massively Parallel Special-Purpose Computer for Collisional N-Body Simulations" ApJ, 480, 432
Makino J., Fukushige T., Koga M., Namura K., 2003, "GRAPE-6: Massively-Parallel Special-Purpose Computer for Astrophysical Particle Simulations" PASJ, 55, 1163 (arXiv:astro-ph/0310702)
Malhan K., Ibata R. A., Martin N. F., 2018, "Ghostly tributaries to the Milky Way: charting the halo's stellar streams with the Gaia DR2 catalogue" MNRAS, 481, 3442 (arXiv:1804.11339)
Mandel I., 2016, "Estimates of black hole natal kick velocities from observations of low-mass X-ray binaries" MNRAS, 456, 578 (arXiv:1510.03871)
Mann H., Whitney D., 1947, "On a Test of Whether One of Two Random Variables is Stochastically Larger Than The Other" Annals of Mathematical Statistics, 18, 50
Mann C. R., et al., 2020, "Erratum: "A Multimass Velocity Dispersion Model of 47 Tucanae Indicates No Evidence for an Intermediate-mass Black Hole" (2019, ApJ, 875, 1)" ApJ, 893, 86
Mapelli M., 2017, "Rotation in young massive star clusters" MNRAS, 467, 3255 (arXiv:1702.00415)
Marín Pina D., Rastello S., Gieles M., Kremer K., Fitzgerald L., Rando Forastier B., 2024, "Dynamical formation of Gaia BH3 in the progenitor globular cluster of the ED-2 stream" A&A, 688, L2 (arXiv:2404.13036)
Martell S. L., Smolinski J. P., Beers T. C., Grebel E. K., 2011, "Building the Galactic halo from globular clusters: evidence from chemically unusual red giants" A&A, 534, A136 (arXiv:1109.3916)
Martens S., et al., 2023, "Kinematic differences between multiple populations in Galactic globular clusters" A&A, 671, A106 (arXiv:2301.08675)
Martocchia S., et al., 2018a, "Age as a major factor in the onset of multiple populations in stellar clusters" MNRAS, 473, 2688 (arXiv:1710.00831)
Martocchia S., et al., 2018b, "The search for multiple populations in Magellanic Cloud clusters - IV. Coeval multiple stellar populations in the young star cluster NGC 1978" MNRAS, 477, 4696 (arXiv:1804.04141)
Massari D., Koppelman H. H., Helmi A., 2019, "Origin of the system of globular clusters in the Milky Way" A&A, 630, L4 (arXiv:1906.08271)
Massey P., Johnson K. E., Degioia-Eastwood K., 1995, "The Initial Mass Function and Massive Star Evolution in the OB Associations of the Northern Milky Way" ApJ, 454, 151
Mastrobuono-Battisti A., Di Matteo P., Montuori M., Haywood M., 2012, "Clumpy streams in a smooth dark halo: the case of Palomar 5" A&A, 546, L7 (arXiv:1209.0466)
Mathieu R. D., 1983, "Dynamical constraints on star formation efficiency." ApJ, 267, L97
McBride A., Kounkel M., 2019, "Runaway Young Stars near the Orion Nebula" ApJ, 884, 6 (arXiv:1908.07550)
McInnes L., Healy J., Astels S., 2017, "hdbscan: Hierarchical density based clustering" The Journal of Open Source Software, 2, 205

McKee C. F., Ostriker E. C., 2007, "Theory of Star Formation" ARA&A, 45, 565 (arXiv:0707.3514)
McLaughlin D. E., Anderson J., Meylan G., Gebhardt K., Pryor C., Minniti D., Phinney S., 2006, "Hubble Space Telescope Proper Motions and Stellar Dynamics in the Core of the Globular Cluster 47 Tucanae" ApJS, 166, 249 (arXiv:astro-ph/0607597)
McLeod A. F., Reiter M., Kuiper R., Klaassen P. D., Evans C. J., 2018, "A parsec-scale optical jet from a massive young star in the Large Magellanic Cloud" Nature, 554, 334 (arXiv:1801.08147)
McMillan S. L. W., 2008, "Gravitational dynamics of large stellar systems" Classical and Quantum Gravity, 25, 114007 (arXiv:0804.3987)
McMillan P. J., 2017, "The mass distribution and gravitational potential of the Milky Way" MNRAS, 465, 76 (arXiv:1608.00971)
McMillan S. L. W., Vesperini E., Portegies Zwart S. F., 2007, "A Dynamical Origin for Early Mass Segregation in Young Star Clusters" ApJ, 655, L45 (arXiv:astro-ph/0609515)
Megeath S. T., Townsley L. K., Oey M. S., Tieftrunk A. R., 2008, in Reipurth B., ed., , Vol. 4, Handbook of Star Forming Regions, Volume I. p. 264
Meingast S., Alves J., 2019, "Extended stellar systems in the solar neighborhood. I. The tidal tails of the Hyades" A&A, 621, L3 (arXiv:1811.04931)
Meingast S., Alves J., Rottensteiner A., 2021, "Extended stellar systems in the solar neighborhood. V. Discovery of coronae of nearby star clusters" A&A, 645, A84 (arXiv:2010.06591)
Meingast S., et al., 2023, "VISIONS: the VISTA Star Formation Atlas. I. Survey overview" A&A, 673, A58 (arXiv:2303.08831)
Miller M. C., Hamilton D. P., 2002, "Production of intermediate-mass black holes in globular clusters" MNRAS, 330, 232 (arXiv:astro-ph/0106188)
Miller-Jones J. C. A., et al., 2015, "Deep radio imaging of 47 Tuc identifies the peculiar X-ray source X9 as a new black hole candidate" MNRAS, 453, 3918 (arXiv:1509.02579)
Milone A. P., et al., 2017, "The Hubble Space Telescope UV Legacy Survey of Galactic globular clusters - IX. The Atlas of multiple stellar populations" MNRAS, 464, 3636 (arXiv:1610.00451)
Milone A. P., Marino A. F., Mastrobuono-Battisti A., Lagioia E. P., 2018, "Gaia unveils the kinematics of multiple stellar populations in 47 Tucanae" MNRAS, 479, 5005 (arXiv:1807.03511)
Miocchi P., et al., 2013, "Star Count Density Profiles and Structural Parameters of 26 Galactic Globular Clusters" ApJ, 774, 151 (arXiv:1307.6035)
Miret-Roig N., Galli P. A. B., Olivares J., Bouy H., Alves J., Barrado D., 2022, "The star formation history of Upper Scorpius and Ophiuchus. A 7D picture: positions, kinematics, and dynamical traceback ages" A&A, 667, A163 (arXiv:2209.12938)
Moeckel N., Bonnell I. A., 2009, "Does subcluster merging accelerate mass segregation in local clusters?" MNRAS, 400, 657 (arXiv:0908.0253)
Monelli M., et al., 2013, "The SUMO project I. A survey of multiple populations in globular clusters" MNRAS, 431, 2126 (arXiv:1303.5187)
Moody K., Sigurdsson S., 2009, "Modeling the Retention Probability of Black Holes in Globular Clusters: Kicks and Rates" ApJ, 690, 1370 (arXiv:0809.1617)
Moreno E., Fernández-Trincado J. G., Pérez-Villegas A., Chaves-Velasquez L., Schuster W. J., 2022, "Orbits of globular clusters computed with dynamical friction in the Galactic anisotropic velocity dispersion field" MNRAS, 510, 5945 (arXiv:2112.11589)
Morgan L. K., Thompson M. A., Urquhart J. S., White G. J., Miao J., 2004, "A radio and mid-infrared survey of northern bright-rimmed clouds" A&A, 426, 535
Morgan L. K., Urquhart J. S., Thompson M. A., 2009, "CO observations towards bright-rimmed clouds" MNRAS, 400, 1726
Morscher M., Umbreit S., Farr W. M., Rasio F. A., 2013, "Retention of Stellar-mass Black Holes in Globular Clusters" ApJ, 763, L15 (arXiv:1211.3372)
Morscher M., Pattabiraman B., Rodriguez C., Rasio F. A., Umbreit S., 2015, "The Dynamical Evolution of Stellar Black Holes in Globular Clusters" ApJ, 800, 9 (arXiv:1409.0866)
Mucciarelli A., Origlia L., Ferraro F. R., Pancino E., 2009, "Looking Outside the Galaxy: The Discovery of Chemical Anomalies in Three Old Large Magellanic Cloud Clusters" ApJ, 695, L134 (arXiv:0902.4778)
Myers N., et al., 2022, "The Open Cluster Chemical Abundances and Mapping Survey. VI. Galactic Chemical Gradient Analysis from APOGEE DR17" AJ, 164, 85 (arXiv:2206.13650)
Naoz S., Shaviv N. J., 2007, "Open cluster birth analysis and multiple spiral arm sets in the Milky Way" New A, 12, 410 (arXiv:astro-ph/0503127)
Nardiello D., et al., 2015, "The Hubble Space Telescope UV Legacy Survey of Galactic Globular Clusters - IV. Helium content and relative age of multiple stellar populations within NGC 6352" MNRAS, 451, 312 (arXiv:1504.07876)
Nardiello D., et al., 2018, "The Hubble Space Telescope UV Legacy Survey of Galactic Globular Clusters - XVII. Public Catalogue Release" MNRAS, 481, 3382 (arXiv:1809.04300)
Nelson B., Ford E. B., Payne M. J., 2014, "RUN DMC: An Efficient, Parallel Code for Analyzing Radial Velocity Observations Using N-body Integrations and Differential Evolution Markov Chain Monte Carlo" ApJS, 210, 11 (arXiv:1311.5229)

Nguyen D. D., et al., 2018, "Nearby Early-type Galactic Nuclei at High Resolution: Dynamical Black Hole and Nuclear Star Cluster Mass Measurements" ApJ, 858, 118 (arXiv:1711.04314)
Niederhofer F., et al., 2017, "The search for multiple populations in Magellanic Cloud clusters - II. The detection of multiple populations in three intermediate-age SMC clusters" MNRAS, 465, 4159 (arXiv:1612.00400)
Nitadori K., Aarseth S. J., 2012 MNRAS, 424, 545
Niwa T., Tachihara K., Itoh Y., Oasa Y., Sunada K., Sugitani K., Mukai T., 2009, "Millimeter-wave survey of molecular clouds around the <ASTROBJ>W5</ASTROBJ>-East triggered star-forming region" A&A, 500, 1119
Odenkirchen M., et al., 2003, "The Extended Tails of Palomar 5: A 10° Arc of Globular Cluster Tidal Debris" AJ, 126, 2385 (arXiv:astro-ph/0307446)
Offner S. S. R., Klein R. I., McKee C. F., Krumholz M. R., 2009a, "The Effects of Radiative Transfer on Low-Mass Star Formation" ApJ, 703, 131 (arXiv:0904.2004)
Offner S. S. R., Hansen C. E., Krumholz M. R., 2009b, "Stellar Kinematics of Young Clusters in Turbulent Hydrodynamic Simulations" ApJ, 704, L124 (arXiv:0909.4304)
Oh S. H., Kim W.-T., Lee H. M., Kim J., 2008, "Physical Properties of Tidal Features in Interacting Disk Galaxies" ApJ, 683, 94 (arXiv:0803.1893)
Oliva E., et al., 2012, in McLean I. S., Ramsay S. K., Takami H., eds, Society of Photo-Optical Instrumentation Engineers (SPIE) Conference Series Vol. 8446, Ground-based and Airborne Instrumentation for Astronomy IV. p. 84463T, doi:10.1117/12.925274
Onorato S., Cadelano M., Dalessandro E., Vesperini E., Lanzoni B., Mucciarelli A., 2023, "The structural properties of multiple populations in the dynamically young globular cluster NGC 2419" A&A, 677, A8 (arXiv:2307.09508)
Palma T., Coenda V., Baume G., Feinstein C., 2025, "Binary and grouped open clusters: A new catalogue" A&A, 693, A218 (arXiv:2412.05376)
Pang X., Li Y., Yu Z., Tang S.-Y., Dinnbier F., Kroupa P., Pasquato M., Kouwenhoven M. B. N., 2021a, "3D Morphology of Open Clusters in the Solar Neighborhood with Gaia EDR 3: Its Relation to Cluster Dynamics" ApJ, 912, 162 (arXiv:2102.10508)
Pang X., Li Y., Yu Z., Tang S.-Y., Dinnbier F., Kroupa P., Pasquato M., Kouwenhoven M. B. N., 2021b, "3D Morphology of Open Clusters in the Solar Neighborhood with Gaia EDR 3: Its Relation to Cluster Dynamics" ApJ, 912, 162 (arXiv:2102.10508)
Panwar N., et al., 2017, "Low-mass young stellar population and star formation history of the cluster IC 1805 in the W4 H II region" MNRAS, 468, 2684 (arXiv:1703.03604)
Panwar N., Samal M. R., Pandey A. K., Singh H. P., Sharma S., 2019, "Understanding Formation of Young, Distributed Low-mass Stars and Clusters in the W4 Cloud Complex" AJ, 157, 112 (arXiv:1901.00888)
Parker R. J., Wright N. J., 2016, "Dynamical evolution of star-forming regions - II. Basic kinematics" MNRAS, 457, 3430 (arXiv:1601.02606)
Parker R. J., Dale J. E., Ercolano B., 2015, "Primordial mass segregation in simulations of star formation?" MNRAS, 446, 4278 (arXiv:1411.3002)
Parker R. J., Goodwin S. P., Wright N. J., Meyer M. R., Quanz S. P., 2016, "Mass segregation in star clusters is not energy equipartition" MNRAS, 459, L119 (arXiv:1604.00394)
Parmentier G., Pfalzner S., Grebel E. K., 2014, "Stellar Age Spreads in Clusters as Imprints of Cluster-parent Clump Densities" ApJ, 791, 132 (arXiv:1407.4119)
Pascale R., Posti L., Nipoti C., Binney J., 2018, "Action-based dynamical models of dwarf spheroidal galaxies: application to Fornax" MNRAS, 480, 927 (arXiv:1802.02606)
Pascale R., Binney J., Nipoti C., Posti L., 2019, "Action-based models for dwarf spheroidal galaxies and globular clusters" MNRAS, 488, 2423 (arXiv:1904.08447)
Pavlovskaya E. D., Filippova A. A., 1989, "Groups of Stars with Common Motion in the Galaxy - Groups of Stars in Luminosity Classes i and II - Comparison with Groups of Longperiod Cepheids and Open Clusters" Soviet Ast., 33, 602
Pedregosa F., et al., 2011, "Scikit-learn: Machine Learning in Python" Journal of Machine Learning Research, 12, 2825 (arXiv:1201.0490)
Pelupessy F. I., Portegies Zwart S., 2012, "The evolution of embedded star clusters" MNRAS, 420, 1503 (arXiv:1111.0992)
Penoyre Z., Belokurov V., Wyn Evans N., Everall A., Koposov S. E., 2020, "Binary deviations from single object astrometry" MNRAS, 495, 321 (arXiv:2003.05456)
Penoyre Z., Belokurov V., Evans N. W., 2022a, "Astrometric identification of nearby binary stars - I. Predicted astrometric signals" MNRAS, 513, 2437 (arXiv:2111.10380)
Penoyre Z., Belokurov V., Evans N. W., 2022b, "Astrometric identification of nearby binary stars - II. Astrometric binaries in the Gaia Catalogue of Nearby Stars" MNRAS, 513, 5270 (arXiv:2202.06963)
Peters T., Klessen R. S., Mac Low M.-M., Banerjee R., 2010, "Limiting Accretion onto Massive Stars by Fragmentation-induced Starvation" ApJ, 725, 134 (arXiv:1005.3271)
Petralia I., Minniti D., Fernández-Trincado J. G., Lane R. R., Schiavon R. P., 2024, "Signature of systemic rotation in 21 galactic globular clusters from APOGEE-2" A&A, 688, A92 (arXiv:2404.10902)
Peuten M., Zocchi A., Gieles M., Gualandris A., Hénault-Brunet V., 2016, "A stellar-mass black hole population in the globular cluster NGC 6101?" MNRAS, 462, 2333 (arXiv:1609.01720)
Pfalzner S., Kaczmarek T., 2013, "The expansion of massive young star clusters - observation meets theory" A&A, 559, A38 (arXiv:1309.0315)

Pfalzner S., Parmentier G., Steinhausen M., Vincke K., Menten K., 2014, "The Evolutionary Tracks of Young Massive Star Clusters" ApJ, 794, 147 (arXiv:1408.6021)
Piatti A. E., Carballo-Bello J. A., 2020, "The tidal tails of Milky Way globular clusters" A&A, 637, L2 (arXiv:2004.11747)
Piatti A. E., Malhan K., 2022, "First evidence of a collision between two unrelated open clusters in the Milky Way" MNRAS, 511, L1 (arXiv:2112.03786)
Piche F., 1993, "A Near-Infrared Survey of the Star Forming Region NGC 2264" PASP, 105, 324
Piecka M., Paunzen E., 2021, "Aggregates of clusters in the Gaia data" A&A, 649, A54 (arXiv:2106.08920)
Piffl T., Penoyre Z., Binney J., 2015, "Bringing the Galaxy's dark halo to life" MNRAS, 451, 639 (arXiv:1502.02916)
Piotto G., et al., 2007, "A Triple Main Sequence in the Globular Cluster NGC 2808" ApJ, 661, L53 (arXiv:astro-ph/0703767)
Piotto G., et al., 2015, "The Hubble Space Telescope UV Legacy Survey of Galactic Globular Clusters. I. Overview of the Project and Detection of Multiple Stellar Populations" AJ, 149, 91 (arXiv:1410.4564)
Plummer H. C., 1911, "On the problem of distribution in globular star clusters" MNRAS, 71, 460
Polak B., et al., 2024, "Massive star cluster formation III. Early mass segregation during cluster assembly" arXiv e-prints, p. arXiv:2408.14592 (arXiv:2408.14592)
Portail M., Gerhard O., Wegg C., Ness M., 2017, "Dynamical modelling of the galactic bulge and bar: the Milky Way's pattern speed, stellar and dark matter mass distribution" MNRAS, 465, 1621 (arXiv:1608.07954)
Portegies Zwart S. F., Baumgardt H., Hut P., Makino J., McMillan S. L. W., 2004, "Formation of massive black holes through runaway collisions in dense young star clusters" Nature, 428, 724 (arXiv:astro-ph/0402622)
Posti L., Binney J., Nipoti C., Ciotti L., 2015, "Action-based distribution functions for spheroidal galaxy components" MNRAS, 447, 3060 (arXiv:1411.7897)
Prantzos N., Charbonnel C., Iliadis C., 2007, "Light nuclei in galactic globular clusters: constraints on the self-enrichment scenario from nucleosynthesis" A&A, 470, 179 (arXiv:0704.3331)
Prantzos N., Charbonnel C., Iliadis C., 2017, "Revisiting nucleosynthesis in globular clusters. The case of NGC 2808 and the role of He and K" A&A, 608, A28 (arXiv:1709.05819)
Priyatikanto R., Kouwenhoven M. B. N., Arifyanto M. I., Wulandari H. R. T., Siregar S., 2016, "The dynamical fate of binary star clusters in the Galactic tidal field" MNRAS, 457, 1339 (arXiv:1601.01752)
Pryor C., Meylan G., 1993, in Djorgovski S. G., Meylan G., eds, Astronomical Society of the Pacific Conference Series Vol. 50, Structure and Dynamics of Globular Clusters. p. 357
Quillen A. C., Minchev I., 2005, "The Effect of Spiral Structure on the Stellar Velocity Distribution in the Solar Neighborhood" AJ, 130, 576 (arXiv:astro-ph/0502205)
Rantala A., Naab T., Lahén N., 2024, "FROST-CLUSTERS - I. Hierarchical star cluster assembly boosts intermediate-mass black hole formation" MNRAS, 531, 3770 (arXiv:2403.10602)
Raso S., Ferraro F. R., Dalessandro E., Lanzoni B., Nardiello D., Bellini A., Vesperini E., 2017, "The "UV-route" to Search for Blue Straggler Stars in Globular Clusters: First Results from the HST UV Legacy Survey" ApJ, 839, 64 (arXiv:1704.01453)
Raso S., et al., 2020, "A Kinematic View of NGC 1261: Structural Parameters, Internal Dispersion, Absolute Proper Motion, and Blue Straggler Stars" ApJ, 895, 15 (arXiv:2004.09540)
Rauw G., Nazé Y., 2016, "X-ray and optical spectroscopy of the massive young open cluster IC 1805" A&A, 594, A82 (arXiv:1608.04499)
Ray A. E., Frinchaboy P. M., Donor J., Chojnowski S. D., Melendez M., 2022, "The Open Cluster Chemical Abundances and Mapping Survey. V. Chemical Abundances of CTIO/Hydra Clusters Using The Cannon" AJ, 163, 195 (arXiv:2202.05759)
Reddy A. B. S., Lambert D. L., Giridhar S., 2016, "The evolution of the Milky Way: new insights from open clusters" MNRAS, 463, 4366 (arXiv:1609.02619)
Reid M. J., Brunthaler A., 2020, "The Proper Motion of Sagittarius A*. III. The Case for a Supermassive Black Hole" ApJ, 892, 39 (arXiv:2001.04386)
Reid M. J., et al., 2019, "Trigonometric Parallaxes of High-mass Star-forming Regions: Our View of the Milky Way" ApJ, 885, 131 (arXiv:1910.03357)
Reina-Campos M., Sills A., Bichon G., 2023, "Initial sizes of star clusters: implications for cluster dissolution during galaxy evolution" MNRAS, 524, 968 (arXiv:2306.17701)
Renaud F., 2018, "Star clusters in evolving galaxies" New A Rev., 81, 1 (arXiv:1801.04278)
Repetto S., Davies M. B., Sigurdsson S., 2012, "Investigating stellar-mass black hole kicks" MNRAS, 425, 2799 (arXiv:1203.3077)
Repetto S., Igoshev A. P., Nelemans G., 2017, "The Galactic distribution of X-ray binaries and its implications for compact object formation and natal kicks" MNRAS, 467, 298 (arXiv:1701.01347)
Richard J., et al., 2019, "BlueMUSE: Project Overview and Science Cases" arXiv e-prints, p. arXiv:1906.01657 (arXiv:1906.01657)
Richer H. B., Heyl J., Anderson J., Kalirai J. S., Shara M. M., Dotter A., Fahlman G. G., Rich R. M., 2013, "A Dynamical Signature of Multiple Stellar Populations in 47 Tucanae" ApJ, 771, L15 (arXiv:1306.1226)
Ridolfi A., et al., 2016, "Long-term observations of the pulsars in 47 Tucanae - I. A study of four elusive binary systems" MNRAS, 462, 2918 (arXiv:1607.07248)
Roberts W. W., 1969, "Large-Scale Shock Formation in Spiral Galaxies and its Implications on Star Formation" ApJ, 158, 123

Robichon N., Arenou F., Mermilliod J. C., Turon C., 1999, "Open clusters with Hipparcos. I. Mean astrometric parameters" A&A, 345, 471 (arXiv:astro-ph/9903131)
Robin A. C., Reylé C., Derrière S., Picaud S., 2003, "A synthetic view on structure and evolution of the Milky Way" A&A, 409, 523
Rodriguez C. L., Morscher M., Pattabiraman B., Chatterjee S., Haster C.-J., Rasio F. A., 2015, "Binary Black Hole Mergers from Globular Clusters: Implications for Advanced LIGO" Phys. Rev. Lett., 115, 051101 (arXiv:1505.00792)
Rodriguez C. L., Haster C.-J., Chatterjee S., Kalogera V., Rasio F. A., 2016a, "Dynamical Formation of the GW150914 Binary Black Hole" ApJ, 824, L8 (arXiv:1604.04254)
Rodriguez C. L., Zevin M., Pankow C., Kalogera V., Rasio F. A., 2016b, "Illuminating Black Hole Binary Formation Channels with Spins in Advanced LIGO" ApJ, 832, L2 (arXiv:1609.05916)
Rodriguez C. L., Amaro-Seoane P., Chatterjee S., Kremer K., Rasio F. A., Samsing J., Ye C. S., Zevin M., 2018, "Post-Newtonian dynamics in dense star clusters: Formation, masses, and merger rates of highly-eccentric black hole binaries" Phys. Rev. D, 98, 123005 (arXiv:1811.04926)
Rodríguez M. J., Baume G., Feinstein C., 2019, "The young stellar population in NGC 247. Main properties and hierarchical clustering" A&A, 626, A35 (arXiv:1904.09926)
Rogers H., Pittard J. M., 2013, "Feedback from winds and supernovae in massive stellar clusters - I. Hydrodynamics" MNRAS, 431, 1337 (arXiv:1302.2443)
Román-Zúñiga C. G., Ybarra J. E., Megías G. D., Tapia M., Lada E. A., Alves J. F., 2015, "Star Formation Across the W3 Complex" AJ, 150, 80 (arXiv:1507.00016)
Román-Zúñiga C. G., Roman-Lopes A., Tapia M., Hernández J., Ramírez-Preciado V., 2019, "Evidence of Hubble Flow-like Motion of Young Stellar Populations away from the Perseus Arm" ApJ, 871, L12 (arXiv:1812.11102)
Röser S., Schilbach E., Goldman B., 2019, "Hyades tidal tails revealed by Gaia DR2" A&A, 621, L2 (arXiv:1811.03845)
Salpeter E. E., 1955, "The Luminosity Function and Stellar Evolution." ApJ, 121, 161
Sampedro L., Dias W. S., Alfaro E. J., Monteiro H., Molino A., 2017, "A multimembership catalogue for 1876 open clusters using UCAC4 data" MNRAS, 470, 3937 (arXiv:1706.05581)
Samsing J., D'Orazio D. J., 2018, "Black Hole Mergers From Globular Clusters Observable by LISA I: Eccentric Sources Originating From Relativistic N-body Dynamics" MNRAS, 481, 5445 (arXiv:1804.06519)
Samsing J., Askar A., Giersz M., 2018, "MOCCA-SURVEY Database. I. Eccentric Black Hole Mergers during Binary-Single Interactions in Globular Clusters" ApJ, 855, 124 (arXiv:1712.06186)
Sana H., et al., 2012, "Binary Interaction Dominates the Evolution of Massive Stars" Science, 337, 444 (arXiv:1207.6397)
Saracino S., et al., 2020, "Chromosome maps of young LMC clusters: an additional case of coeval multiple populations" MNRAS, 493, 6060 (arXiv:2003.01780)
Sarajedini A., et al., 2007, "The ACS Survey of Galactic Globular Clusters. I. Overview and Clusters without Previous Hubble Space Telescope Photometry" AJ, 133, 1658 (arXiv:astro-ph/0612598)
Saydjari A. K., et al., 2023, "The Dark Energy Camera Plane Survey 2 (DECaPS2): More Sky, Less Bias, and Better Uncertainties" ApJS, 264, 28 (arXiv:2206.11909)
Sbordone L., Salaris M., Weiss A., Cassisi S., 2011, "Photometric signatures of multiple stellar populations in Galactic globular clusters" A&A, 534, A9 (arXiv:1103.5863)
Scally A., Clarke C., 2002, "Primordial substructure in the Orion Nebula Cluster" MNRAS, 334, 156
Schiavon R. P., Caldwell N., Conroy C., Graves G. J., Strader J., MacArthur L. A., Courteau S., Harding P., 2013, "Star Clusters in M31. V. Evidence for Self-enrichment in Old M31 Clusters from Integrated Spectroscopy" ApJ, 776, L7 (arXiv:1308.6590)
Schlafly E. F., Finkbeiner D. P., 2011, "Measuring Reddening with Sloan Digital Sky Survey Stellar Spectra and Recalibrating SFD" ApJ, 737, 103 (arXiv:1012.4804)
Schlafly E. F., et al., 2018, "The DECam Plane Survey: Optical Photometry of Two Billion Objects in the Southern Galactic Plane" ApJS, 234, 39 (arXiv:1710.01309)
Schlegel D. J., Finkbeiner D. P., Davis M., 1998, "Maps of Dust Infrared Emission for Use in Estimation of Reddening and Cosmic Microwave Background Radiation Foregrounds" ApJ, 500, 525 (arXiv:astro-ph/9710327)
Schmeja S., Kharchenko N. V., Piskunov A. E., Röser S., Schilbach E., Froebrich D., Scholz R. D., 2014, "Global survey of star clusters in the Milky Way. III. 139 new open clusters at high Galactic latitudes" A&A, 568, A51 (arXiv:1406.6267)
Schoettler C., de Bruijne J., Vaher E., Parker R. J., 2020, "Runaway and walkaway stars from the ONC with Gaia DR2" MNRAS, 495, 3104 (arXiv:2004.13730)
Schoettler C., Parker R. J., de Bruijne J., 2022, "Constraining the initial conditions of NGC 2264 using ejected stars found in Gaia DR2" MNRAS, 510, 3178 (arXiv:2111.14892)
Scholz R. D., Kharchenko N. V., Piskunov A. E., Röser S., Schilbach E., 2015, "Global survey of star clusters in the Milky Way. IV. 63 new open clusters detected by proper motions" A&A, 581, A39 (arXiv:1507.02125)
Schönrich R., Binney J., Dehnen W., 2010, "Local kinematics and the local standard of rest" MNRAS, 403, 1829 (arXiv:0912.3693)
Sellwood J. A., Carlberg R. G., 1984, "Spiral instabilities provoked by accretion and star formation" ApJ, 282, 61
Shu F. H., 2016, "Six Decades of Spiral Density Wave Theory" ARA&A, 54, 667

Shukirgaliyev B., Parmentier G., Berczik P., Just A., 2017, "Impact of a star formation efficiency profile on the evolution of open clusters" A&A, 605, A119 (arXiv:1706.03228)
Shukirgaliyev B., et al., 2021, "Bound mass of Dehnen models with a centrally peaked star formation efficiency" A&A, 654, A53 (arXiv:2105.09510)
Sills A., Rieder S., Scora J., McCloskey J., Jaffa S., 2018, "Dynamical evolution of stars and gas of young embedded stellar sub-clusters" MNRAS, 477, 1903 (arXiv:1803.04301)
Sills A., Dalessandro E., Cadelano M., Alfaro-Cuello M., Kruijssen J. M. D., 2019, "Light element variations within the different age-metallicity populations in the nucleus of the Sagittarius dwarf" MNRAS, 490, L67 (arXiv:1910.00080)
Sippel A. C., Hurley J. R., 2013, "Multiple stellar-mass black holes in globular clusters: theoretical confirmation." MNRAS, 430, L30 (arXiv:1211.6608)
Sirianni M., et al., 2005, "The Photometric Performance and Calibration of the Hubble Space Telescope Advanced Camera for Surveys" PASP, 117, 1049 (arXiv:astro-ph/0507614)
Sivia D. S., Skilling J., 2006, Data Analysis - A Bayesian Tutorial, 2nd edn. Oxford Science Publications, Oxford University Press
Smartt S. J., 2009, "Progenitors of Core-Collapse Supernovae" ARA&A, 47, 63 (arXiv:0908.0700)
Smith R., Goodwin S., Fellhauer M., Assmann P., 2013, "Infant mortality in the hierarchical merging scenario: dependence on gas expulsion time-scales" MNRAS, 428, 1303 (arXiv:1210.0908)
Smith P. J., Hénault-Brunet V., Dickson N., Gieles M., Baumgardt H., 2024, "Probing populations of dark stellar remnants in the globular clusters 47 Tuc and Terzan 5 using pulsar timing" arXiv e-prints, p. arXiv:2407.06274 (arXiv:2407.06274)
Snider K. D., Hester J. J., Desch S. J., Healy K. R., Bally J., 2009, "Spitzer Observations of The H II Region NGC 2467: An Analysis of Triggered Star Formation" ApJ, 700, 506 (arXiv:0711.1515)
Sollima A., 2021, "Monte Carlo simulations of multiple populations in globular clusters: constraints on the cooling flow versus accretion scenario using million bodies simulations" MNRAS, 502, 1974 (arXiv:2102.01707)
Sollima A., Baumgardt H., Hilker M., 2019, "The eye of Gaia on globular clusters kinematics: internal rotation" MNRAS, 485, 1460 (arXiv:1902.05895)
Song F., Esamdin A., Hu Q., Zhang M., 2022, "Binary open clusters in the Gaia data" A&A, 666, A75 (arXiv:2208.12935)
Sormani M. C., Gerhard O., Portail M., Vasiliev E., Clarke J., 2022, "The stellar mass distribution of the Milky Way's bar: an analytical model" MNRAS, 514, L1 (arXiv:2204.13114)
Soubiran C., et al., 2018, "Open cluster kinematics with Gaia DR2" A&A, 619, A155 (arXiv:1808.01613)
Spina L., et al., 2021, "The GALAH survey: tracing the Galactic disc with open clusters" MNRAS, 503, 3279 (arXiv:2011.02533)
Spitler L. R., Forbes D. A., 2009, "A new method for estimating dark matter halo masses using globular cluster systems" MNRAS, 392, L1 (arXiv:0809.5057)
Spitzer Lyman J., 1958, "Disruption of Galactic Clusters." ApJ, 127, 17
Spitzer Lyman J., 1969, "Equipartition and the Formation of Compact Nuclei in Spherical Stellar Systems" ApJ, 158, L139
Spitzer L., 1978, Physical processes in the interstellar medium, doi:10.1002/9783527617722.
Spitzer L., 1987, Dynamical evolution of globular clusters
Spurzem R., Kamlah A., 2023, "Computational methods for collisional stellar systems" Living Reviews in Computational Astrophysics, 9, 3 (arXiv:2305.11606)
Stahler S. W., Shu F. H., Taam R. E., 1980, "The evolution of protostars. I - Global formulation and results" ApJ, 241, 637
Stetson P. B., Pancino E., Zocchi A., Sanna N., Monelli M., 2019, "Homogeneous photometry - VII. Globular clusters in the Gaia era" MNRAS, 485, 3042 (arXiv:1902.09925)
Stodolkiewicz J. S., 1986, "Dynamical evolution of globular clusters. II - Binaries Method" Acta Astron., 36, 19
Stolte A., Brandner W., Brandl B., Zinnecker H., 2006, "The Secrets of the Nearest Starburst Cluster. II. The Present-Day Mass Function in NGC 3603" AJ, 132, 253 (arXiv:astro-ph/0604333)
Strader J., Chomiuk L., Maccarone T. J., Miller-Jones J. C. A., Seth A. C., 2012, "Two stellar-mass black holes in the globular cluster M22" Nature, 490, 71 (arXiv:1210.0901)
Ströbele S., et al., 2012, in Ellerbroek B. L., Marchetti E., Véran J.-P., eds, Society of Photo-Optical Instrumentation Engineers (SPIE) Conference Series Vol. 8447, Adaptive Optics Systems III. p. 844737, doi:10.1117/12.926110
Strömgren B., 1939, "The Physical State of Interstellar Hydrogen." ApJ, 89, 526
Subramaniam A., Gorti U., Sagar R., Bhatt H. C., 1995, "Probable binary open star clusters in the Galaxy." A&A, 302, 86
Sugitani K., Ogura K., 1994, "A Catalog of Bright-rimmed Clouds with IRAS Point Sources: Candidates for Star Formation by Radiation-driven Implosion. II. The Southern Hemisphere" ApJS, 92, 163
Sugitani K., Fukui Y., Ogura K., 1991, "A Catalog of Bright-rimmed Clouds with IRAS Point Sources: Candidates for Star Formation by Radiation-driven Implosion. I. The Northern Hemisphere" ApJS, 77, 59
Sun N.-C., et al., 2018, "The VMC Survey. XXIX. Turbulence-controlled Hierarchical Star Formation in the Small Magellanic Cloud" ApJ, 858, 31 (arXiv:1804.01652)
Sung H., et al., 2017, "An Optical and Infrared Photometric Study of the Young Open Cluster IC 1805 in the Giant H II Region W4 " ApJS, 230, 3 (arXiv:1704.04592)

Swiggum C., et al., 2021, "Evidence for Radial Expansion at the Core of the Orion Complex with Gaia EDR3" ApJ, 917, 21 (arXiv:2101.10380)
Szigeti L., Mészáros S., Szabó G. M., Fernández-Trincado J. G., Lane R. R., Cohen R. E., 2021a, "The rotation of selected globular clusters and the differential rotation of M3 in multiple populations from the SDSS-IV APOGEE-2 survey" MNRAS, 504, 1144 (arXiv:2104.04524)
Szigeti L., Mészáros S., Szabó G. M., Fernández-Trincado J. G., Lane R. R., Cohen R. E., 2021b, "The rotation of selected globular clusters and the differential rotation of M3 in multiple populations from the SDSS-IV APOGEE-2 survey" MNRAS, 504, 1144 (arXiv:2104.04524)
Tanga P., Mignard F., 2012, "The Solar System as seen by Gaia: The asteroids and their accuracy budget" Planet. Space Sci., 73, 5
Tanga P., et al., 2023, "Gaia Data Release 3. The Solar System survey" A&A, 674, A12 (arXiv:2206.05561)
Tarricq Y., et al., 2021, "3D kinematics and age distribution of the open cluster population" A&A, 647, A19 (arXiv:2012.04017)
Tchernyshyov K., Peek J. E. G., Zasowski G., 2018, "Kinetic Tomography. II. A Second Method for Mapping the Velocity Field of the Milky Way Interstellar Medium and a Comparison with Spiral Structure Models" AJ, 156, 248 (arXiv:1808.01286)
Theuns T., 1991, "Interactions between star clusters and molecular clouds" Mem. Soc. Astron. Italiana, 62, 909
Thomas G. F., Famaey B., Monari G., Laporte C. F. P., Ibata R., de Laverny P., Hill V., Boily C., 2023, "Impact of the Galactic bar on tidal streams within the Galactic disc. The case of the tidal stream of the Hyades" A&A, 678, A180 (arXiv:2309.05733)
Thompson M. A., White G. J., Morgan L. K., Miao J., Fridlund C. V. M., Huldtgren-White M., 2004, "Searching for signs of triggered star formation toward IC 1848" A&A, 414, 1017 (arXiv:astro-ph/0311034)
Tiongco M. A., Vesperini E., Varri A. L., 2017, "Kinematical evolution of tidally limited star clusters: rotational properties" MNRAS, 469, 683 (arXiv:1704.05918)
Tiongco M. A., Vesperini E., Varri A. L., 2019, "Kinematical evolution of multiple stellar populations in star clusters" MNRAS, 487, 5535 (arXiv:1907.05901)
Toomre A., 1964, "On the gravitational stability of a disk of stars." ApJ, 139, 1217
Toomre A., Toomre J., 1972, "Galactic Bridges and Tails" ApJ, 178, 623
Townsley L. K., Broos P. S., Garmire G. P., Povich M. S., 2019, "The Massive Star-forming Regions Omnibus X-ray Catalog, Third Installment" ApJS, 244, 28 (arXiv:1907.13126)
Tozzi A., et al., 2016, in Evans C. J., Simard L., Takami H., eds, Society of Photo-Optical Instrumentation Engineers (SPIE) Conference Series Vol. 9908, Ground-based and Airborne Instrumentation for Astronomy VI. p. 99086C, doi:10.1117/12.2231898
Trager S. C., King I. R., Djorgovski S., 1995, "Catalogue of Galactic Globular-Cluster Surface-Brightness Profiles" AJ, 109, 218
Tremou E., et al., 2018, "The MAVERIC Survey: Still No Evidence for Accreting Intermediate-mass Black Holes in Globular Clusters" ApJ, 862, 16 (arXiv:1806.00259)
Trenti M., van der Marel R., 2013, "No energy equipartition in globular clusters" MNRAS, 435, 3272 (arXiv:1302.2152)
Tsantaki M., et al., 2022, "Survey of Surveys. I. The largest compilation of radial velocities for the Galaxy" A&A, 659, A95 (arXiv:2110.09316)
Tully R. B., 1974, "The Kinematics and Dynamics of M51. III. The Spiral Structure" ApJS, 27, 449
Vanzella E., et al., 2022a, "High star cluster formation efficiency in the strongly lensed Sunburst Lyman-continuum galaxy at z = 2.37" A&A, 659, A2 (arXiv:2106.10280)
Vanzella E., et al., 2022b, "Early Results from GLASS-JWST. VII. Evidence for Lensed, Gravitationally Bound Proto-globular Clusters at z = 4 in the Hubble Frontier Field A2744" ApJ, 940, L53 (arXiv:2208.00520)
Vanzella E., et al., 2023a, "An extremely metal-poor star complex in the reionization era: Approaching Population III stars with JWST" A&A, 678, A173 (arXiv:2305.14413)
Vanzella E., et al., 2023b, "JWST/NIRCam Probes Young Star Clusters in the Reionization Era Sunrise Arc" ApJ, 945, 53 (arXiv:2211.09839)
Vanzella E., et al., 2023c, "JWST/NIRCam Probes Young Star Clusters in the Reionization Era Sunrise Arc" ApJ, 945, 53 (arXiv:2211.09839)
Varri A. L., Bertin G., 2012, "Self-consistent models of quasi-relaxed rotating stellar systems" A&A, 540, A94 (arXiv:1201.1899)
Vasiliev E., 2018, "Internal dynamics of the Large Magellanic Cloud from Gaia DR2" MNRAS, 481, L100 (arXiv:1805.08157)
Vasiliev E., 2019a, "AGAMA: action-based galaxy modelling architecture" MNRAS, 482, 1525 (arXiv:1802.08239)
Vasiliev E., 2019b, "Proper motions and dynamics of the Milky Way globular cluster system from Gaia DR2" MNRAS, 484, 2832 (arXiv:1807.09775)
Vasiliev E., 2019c, "Systematic errors in Gaia DR2 astrometry and their impact on measurements of internal kinematics of star clusters" MNRAS, 489, 623 (arXiv:1811.05345)
Vasiliev E., Baumgardt H., 2021, "Gaia EDR3 view on galactic globular clusters" MNRAS, 505, 5978 (arXiv:2102.09568)
Vázquez-Semadeni E., Ryu D., Passot T., González R. F., Gazol A., 2006, "Molecular Cloud Evolution. I. Molecular Cloud and Thin Cold Neutral Medium Sheet Formation" ApJ, 643, 245 (arXiv:astro-ph/0509127)

Vázquez-Semadeni E., Gómez G. C., Jappsen A. K., Ballesteros-Paredes J., González R. F., Klessen R. S., 2007, "Molecular Cloud Evolution. II. From Cloud Formation to the Early Stages of Star Formation in Decaying Conditions" ApJ, 657, 870 (arXiv:astro-ph/0608375)
Vázquez-Semadeni E., González-Samaniego A., Colín P., 2017, "Hierarchical star cluster assembly in globally collapsing molecular clouds" MNRAS, 467, 1313 (arXiv:1611.00088)
Vázquez-Semadeni E., Palau A., Ballesteros-Paredes J., Gómez G. C., Zamora-Avilés M., 2019, "Global hierarchical collapse in molecular clouds. Towards a comprehensive scenario" MNRAS, 490, 3061 (arXiv:1903.11247)
Vesperini E., 2010, "Star cluster dynamics" Philosophical Transactions of the Royal Society of London Series A, 368, 829 (arXiv:0911.0793)
Vesperini E., Chernoff D. F., 1996, "Truncation of the Binary Distribution Function in Globular Cluster Formation" ApJ, 458, 178 (arXiv:astro-ph/9510135)
Vesperini E., Heggie D. C., 1997, "On the effects of dynamical evolution on the initial mass function of globular clusters" MNRAS, 289, 898 (arXiv:astro-ph/9705073)
Vesperini E., McMillan S. L. W., D'Antona F., D'Ercole A., 2013, "Dynamical evolution and spatial mixing of multiple population globular clusters" MNRAS, 429, 1913 (arXiv:1212.2651)
Vesperini E., Varri A. L., McMillan S. L. W., Zepf S. E., 2014, "Kinematical fingerprints of star cluster early dynamical evolution." MNRAS, 443, L79 (arXiv:1406.3634)
Vesperini E., Hong J., Giersz M., Hypki A., 2021, "Dynamical evolution of multiple-population globular clusters" MNRAS, 502, 4290 (arXiv:2102.01717)
Vishniac E. T., 1978, "A necessary condition for equilibrium in stellar systems with a continuous mass spectrum." ApJ, 223, 986
Vitral E., Libralato M., Kremer K., Mamon G. A., Bellini A., Bedin L. R., Anderson J., 2023, "An elusive dark central mass in the globular cluster M4" arXiv e-prints, p. arXiv:2305.12702 (arXiv:2305.12702)
Volonteri M., 2010, "Formation of supermassive black holes" A&A Rev., 18, 279 (arXiv:1003.4404)
WFIRST Astrometry Working Group et al., 2019, "Astrometry with the Wide-Field Infrared Space Telescope" Journal of Astronomical Telescopes, Instruments, and Systems, 5, 044005 (arXiv:1712.05420)
Wang L., Spurzem R., Aarseth S., Nitadori K., Berczik P., Kouwenhoven M. B. N., Naab T., 2015, "NBODY6++GPU: ready for the gravitational million-body problem" MNRAS, 450, 4070 (arXiv:1504.03687)
Wang L., et al., 2016, "The DRAGON simulations: globular cluster evolution with a million stars" MNRAS, 458, 1450 (arXiv:1602.00759)
Ward J. L., Kruijssen J. M. D., 2018, "Not all stars form in clusters - measuring the kinematics of OB associations with Gaia" MNRAS, 475, 5659 (arXiv:1801.03938)
Ward J. L., Kruijssen J. M. D., Rix H.-W., 2020, "Not all stars form in clusters - Gaia-DR2 uncovers the origin of OB associations" MNRAS, 495, 663 (arXiv:1910.06974)
Watkins L. L., van der Marel R. P., Bellini A., Anderson J., 2015, "Hubble Space Telescope Proper Motion (HSTPROMO) Catalogs of Galactic Globular Cluster. II. Kinematic Profiles and Maps" ApJ, 803, 29 (arXiv:1502.00005)
Watkins L. L., van der Marel R. P., Libralato M., Bellini A., Anderson J., Alfaro-Cuello M., 2022, "Hubble Space Telescope Proper Motion (HSTPROMO) Catalogs of Galactic Globular Clusters. VII. Energy Equipartition" ApJ, 936, 154 (arXiv:2206.05300)
Weatherford N. C., Chatterjee S., Rodriguez C. L., Rasio F. A., 2018, "Predicting Stellar-mass Black Hole Populations in Globular Clusters" ApJ, 864, 13 (arXiv:1712.03979)
Weatherford N. C., Chatterjee S., Kremer K., Rasio F. A., 2020, "A Dynamical Survey of Stellar-mass Black Holes in 50 Milky Way Globular Clusters" ApJ, 898, 162 (arXiv:1911.09125)
Weinberg M. D., 1994, "Adiabatic Invariants in Stellar Dynamics. II. Gravitational Shocking" AJ, 108, 1403 (arXiv:astro-ph/9404016)
Whitney B. A., Wood K., Bjorkman J. E., Wolff M. J., 2003a, "Two-dimensional Radiative Transfer in Protostellar Envelopes. I. Effects of Geometry on Class I Sources" ApJ, 591, 1049 (arXiv:astro-ph/0303479)
Whitney B. A., Wood K., Bjorkman J. E., Cohen M., 2003b, "Two-dimensional Radiative Transfer in Protostellar Envelopes. II. An Evolutionary Sequence" ApJ, 598, 1079 (arXiv:astro-ph/0309007)
Whitney B. A., et al., 2004, "A GLIMPSE of Star Formation in the Giant H II Region RCW 49" ApJS, 154, 315 (arXiv:astro-ph/0406100)
Wilson R. W., Jefferts K. B., Penzias A. A., 1970, "Carbon Monoxide in the Orion Nebula" ApJ, 161, L43
Wright E. L., et al., 2010, "The Wide-field Infrared Survey Explorer (WISE): Mission Description and Initial On-orbit Performance" AJ, 140, 1868 (arXiv:1008.0031)
Wright N. J., et al., 2019, "The Gaia-ESO Survey: asymmetric expansion of the Lagoon Nebula cluster NGC 6530 from GES and Gaia DR2" MNRAS, 486, 2477 (arXiv:1903.12176)
Xu Y., Reid M. J., Zheng X. W., Menten K. M., 2006, "The Distance to the Perseus Spiral Arm in the Milky Way" Science, 311, 54 (arXiv:astro-ph/0512223)
Yadav R. K., et al., 2016, "A multiwavelength investigation of the H II region S311: young stellar population and star formation" MNRAS, 461, 2502
Yang Y., Zhao J.-K., Ishigaki M. N., Chiba M., Yang C.-Q., Xue X.-X., Ye X.-H., Zhao G., 2022, "Existence of tidal tails for the globular cluster NGC 5824" A&A, 667, A37 (arXiv:2208.05197)
Yong D., Carney B. W., Friel E. D., 2012, "Elemental Abundance Ratios in Stars of the Outer Galactic Disk. IV. A New Sample of Open Clusters" AJ, 144, 95 (arXiv:1206.6931)

Yoshida N., Omukai K., Hernquist L., Abel T., 2006, "Formation of Primordial Stars in a ΛCDM Universe" ApJ, 652, 6 (arXiv:astro-ph/0606106)
Zeidler P., et al., 2018, "The Young Massive Star Cluster Westerlund 2 Observed with MUSE. I. First Results on the Cluster Internal Motion from Stellar Radial Velocities" AJ, 156, 211 (arXiv:1809.06866)
Zeidler P., Sabbi E., Nota A., McLeod A. F., 2021, "The Young Massive Star Cluster Westerlund 2 Observed with MUSE. III. A Cluster in Motion—The Complex Internal Dynamics" AJ, 161, 140 (arXiv:2101.01694)
Zemp M., Gnedin O. Y., Gnedin N. Y., Kravtsov A. V., 2011, "On Determining the Shape of Matter Distributions" ApJS, 197, 30 (arXiv:1107.5582)
Zevin M., Samsing J., Rodriguez C., Haster C.-J., Ramirez-Ruiz E., 2019, "Eccentric Black Hole Mergers in Dense Star Clusters: The Role of Binary-Binary Encounters" ApJ, 871, 91 (arXiv:1810.00901)
Zhong J., Chen L., Kouwenhoven M. B. N., Li L., Shao Z., Hou J., 2019, "Substructure and halo population of Double Cluster h and χ Persei" A&A, 624, A34 (arXiv:1902.06892)
Zocchi A., Gieles M., Hénault-Brunet V., 2019, "The effect of stellar-mass black holes on the central kinematics of ω Cen: a cautionary tale for IMBH interpretations" MNRAS, 482, 4713 (arXiv:1806.02157)
Zuckerman B., Evans N. J. I., 1974, "Models of Massive Molecular Clouds" ApJ, 192, L149
Zuckerman B., Palmer P., 1974, "Radio radiation from interstellar molecules." ARA&A, 12, 279
de Boer T. J. L., Gieles M., Balbinot E., Hénault-Brunet V., Sollima A., Watkins L. L., Claydon I., 2019, "Globular cluster number density profiles using Gaia DR2" MNRAS, 485, 4906 (arXiv:1901.08072)
de Grijs R., Gilmore G. F., Mackey A. D., Wilkinson M. I., Beaulieu S. F., Johnson R. A., Santiago B. X., 2002, "Mass segregation in young compact clusters in the Large Magellanic Cloud - III. Implications for the initial mass function" MNRAS, 337, 597 (arXiv:astro-ph/0208150)
de Jong R. S., et al., 2012, in McLean I. S., Ramsay S. K., Takami H., eds, Society of Photo-Optical Instrumentation Engineers (SPIE) Conference Series Vol. 8446, Ground-based and Airborne Instrumentation for Astronomy IV. p. 84460T (arXiv:1206.6885), doi:10.1117/12.926239
de Mink S. E., Pols O. R., Langer N., Izzard R. G., 2009, "Massive binaries as the source of abundance anomalies in globular clusters" A&A, 507, L1 (arXiv:0910.1086)
de Oliveira M. R., Dottori H., Bica E., 1998, "Dynamical studies of cluster pairs in the Magellanic Clouds" MNRAS, 295, 921
de Rijcke S., Buyle P., Dejonghe H., 2006, "Upper limits on the central black hole masses of 47Tuc and NGC 6397 from radio continuum emission" MNRAS, 368, L43 (arXiv:astro-ph/0601450)
de la Fuente Marcos R., de la Fuente Marcos C., 2009, "Hierarchical Star Formation in the Milky Way Disk" ApJ, 700, 436 (arXiv:0905.1889)
den Brok M., et al., 2015, "Measuring the Mass of the Central Black Hole in the Bulgeless Galaxy NGC 4395 from Gas Dynamical Modeling" ApJ, 809, 101 (arXiv:1507.04358)
ter Braak C., Vrugt J., 2008, "Differential Evolution Markov Chain with snooker updater and fewer chains." Statistics and Computing, 18, 435
van Leeuwen F., 2009, "Parallaxes and proper motions for 20 open clusters as based on the new Hipparcos catalogue" A&A, 497, 209 (arXiv:0902.1039)
van de Ven G., van den Bosch R. C. E., Verolme E. K., de Zeeuw P. T., 2006, "The dynamical distance and intrinsic structure of the globular cluster ω Centauri" A&A, 445, 513 (arXiv:astro-ph/0509228)
van den Bergh S., 1996, "Mergers of Globular Clusters" ApJ, 471, L31 (arXiv:astro-ph/9609095)
van den Bergh S., 2008 AJ, 135, 1731
van der Kruit P. C., Freeman K. C., 2011, "Galaxy Disks" ARA&A, 49, 301 (arXiv:1101.1771)